UNIVERSIDADE ESTADUAL DE CAMPINAS

Faculdade de Engenharia Mecânica

HEITOR NIGRO LOPES

High-frequency vibroacoustic topology optimization considering natural frequency separation and sound insulation

Otimização topológica vibro-acústica em alta frequência considerando separação de frequências naturais e isolação sonora

CAMPINAS

2024

HEITOR NIGRO LOPES

High-frequency vibroacoustic topology optimization considering natural frequency separation and sound insulation

Otimização topológica vibro-acústica em alta frequência considerando separação de frequências naturais e isolação sonora

Thesis presented to the School of Mechanical Engineering of the University of Campinas in partial fulfillment of the requirements for the degree of Doctor in Mechanical Engineering, in the area of Solid Mechanics and Mechanical Design.

Tese apresentada à Faculdade de Engenharia Mecânica da Universidade Estadual de Campinas como parte dos requisitos exigidos para a obtenção do título de Doutor em Engenharia Mecânica, na Área de Mecânica dos Sólidos e Projeto Mecânico.

Orientador: Prof. Dr. Renato Pavanello

ESTE TRABALHO CORRESPONDE À VERSÃO FINAL DA TESE DE DOUTORADO DEFENDIDA PELO ALUNO HEITOR NIGRO LOPES, E ORIENTADA PELO PROF. DR. RENATO PAVANELLO.

CAMPINAS

2024

Ficha catalográfica
Universidade Estadual de Campinas
Biblioteca da Área de Engenharia e Arquitetura
Rose Meire da Silva - CRB 8/5974

L881h

Lopes, Heitor Nigro, 1994-
High-frequency vibroacoustic topology optimization considering natural frequency separation and sound insulation / Heitor Nigro Lopes. – Campinas, SP : [s.n.], 2024.

Orientador: Renato Pavanello.
Tese (doutorado) – Universidade Estadual de Campinas, Faculdade de Engenharia Mecânica.

1. Otimização topológica. 2. Vibração. 3. Acústica. 4. Isolamento acústico. I. Pavanello, Renato, 1959-. II. Universidade Estadual de Campinas. Faculdade de Engenharia Mecânica. III. Título.

Informações Complementares

Título em outro idioma: Otimização topológica vibro-acústica em alta frequência considerando separação de frequências naturais e isolação sonora
Palavras-chave em inglês:
Topology optimization
Vibration
Acoustics
Acoustic insulation
Área de concentração: Mecânica dos Sólidos e Projeto Mecânico
Titulação: Doutor em Engenharia Mecânica
Banca examinadora:
Renato Pavanello [Orientador]
Alberto Luiz Serpa
Marco Lúcio Bittencourt
Daniel Milbrath De Leon
Eduardo Lenz Cardoso
Data de defesa: 01-03-2024
Programa de Pós-Graduação: Engenharia Mecânica

Identificação e informações acadêmicas do(a) aluno(a)
- ORCID do autor: https://orcid.org/0000-0001-6113-7324
- Currículo Lattes do autor: http://lattes.cnpq.br/1477667441597329

UNIVERSIDADE ESTADUAL DE CAMPINAS
FACULDADE DE ENGENHARIA MECÂNICA

TESE DE DOUTORADO ACADÊMICO

High-frequency vibroacoustic topology optimization considering natural frequency separation and sound insulation

Otimização topológica vibro-acústica em alta frequência considerando separação de frequências naturais e isolação sonora

Autor: Heitor Nigro Lopes

Orientador: Prof. Dr. Renato Pavanello

A Banca Examinadora composta pelos membros abaixo aprovou esta Tese:

Prof. Dr. Renato Pavanello
ENG. MECÂNICA / UNICAMP

Prof. Dr. Alberto Luiz Serpa
ENG. MECÂNICA / UNICAMP

Prof. Dr. Marco Lúcio Bittencourt
ENG. MECÂNICA / UNICAMP

Prof. Dr. Daniel Milbrath De Leon
ENG. MECÂNICA / UFRGS

Prof. Dr. Eduardo Lenz Cardoso
ENG. MECÂNICA / UDESC

A Ata de Defesa com as respectivas assinaturas dos membros encontra-se no SIGA/Sistema de Fluxo de Dissertação/Tese e na Secretaria do Programa da Unidade.

Campinas, 01 de março de 2024

ACKNOWLEDGEMENTS

To my parents, Antonio Carlos and Cecilia, who have always supported me and guaranteed my well-being. To my brother, Daniel, for his friendship. To my grandparents Vera and José. To my aunts Francine, Gláucia and Silvia.

To my advisor, professor Renato Pavanello, without which none of this work would have been possible. For his guidance, suggestions, commentaries, criticisms, and for every opportunity that I had thanks to him.

To the external professors who received me in their institutions. To professor Jarir Mahfoud, for receiving me at INSA-Lyon. To professor Mattias Schevenels, for receiving me and guiding me during my stay at KU Leuven. To professor Edwin Reynders and Daniele Giannini, who guided me during my research at KU Leuven.

To my great friend and colleague Rodrigo Lima Pereira. Without his moral and academic support, I wouldn't have been able to conclude this work. To my great friends who have always supported me and with whom I have always had fun moments. My friends Arlindo, Yugo, and Tanabe; with whom I hope to enjoy many more moments.

To my friends and colleagues from Laboratory of Topology Optimization and Multiphysical Analysis, for all the relaxing moments and for the academic experience that we shared. To my colleagues Daniel, Breno, Marcela, Vinicius, Claudia, Gisele, Vitor Hugo, João, Evandro, Valter, Rafael, Márcio, Luis.

To my friends and colleagues from KU Leuven, who were essential during my stay in Belgium, and who I hope to see again and spend more moments together (and coffee-breaks). To my colleagues Tomas, Tobias, Nick, Damien, Lise, Delphine, Arta, Ayu, Fabian, Daan, Willem, Els, Simon, Evelien, Nazanin.

To the School of Mechanical Engineering of UNICAMP, for the necessary infrastructure for this work.

This study was financed in part by the São Paulo Research Foundation (FAPESP), grant 2019/05393-7, part of a Research, Innovation and Dissemination Center (RIDC), grant 2013/08293-7. This study was financed in part by The Brazilian National Council for Scientific and Technological Development (CNPq), grant 130636/2019-3.

RESUMO

Vibração excessiva é normalmente acompanhada por fenômenos indesejados ou, ocasionalmente, catastróficos. Seja para minimizar a propagação de ruídos, seja para evitar falhas mecânicas devido a esforços elevados, controlar o comportamento dinâmico de estruturas é um aspecto importante em projetos de engenharia. Esta tese tem como objetivo desenvolver e melhorar técnicas de otimização topológica em problemas dinâmicos estruturais e acústico-estruturais. A otimização de separação de frequências naturais em alta frequência é formulada e resolvida pelo método *Bi-directional Evolutionary Structural Optimization* (BESO). Um algoritmo de rastreamento de autovetores é proposto para evitar instabilidades devido a modos locais e para uma melhor organização dos modos. Este problema de otimização resulta em topologias quase-periódicas com alternância de materiais, em acordo com a teoria de cristais fonônicos. Para viabilizar esse problema em formulações com um material e vazio, um método garantidor de conectividade, o *Virtual Flux Method* (VFM) é proposto. O VFM utiliza a solução de um problema auxiliar como medida de conectividade. Essa formulação foi validada experimentalmente através da medição da resposta harmônica de uma topologia otimizada. O modelo acústico-estrutura é baseado na formulação de Helmholtz e nas equações da elasticidade linear. Dois diferentes casos de interação acústico-estrutura são analisados. O primeiro é a otimização de frequências naturais em sistemas fortemente acoplados. Neste caso, a análise de sensibilidade teve que ser expandida para contemplar os novos termos. O segundo é a maximização da isolação acústica por impactos em pisos. Neste caso, devido ao acoplamento fraco entre os domínios acústico e estrutural, um acoplamento unilateral é usado. O campo de pressão no domínio acústico é considerado como difuso. A minimização da transmissão sonora de impactos indicou uma sinergia entre a estrutura otimizada e mecanismos convencionais de laje flutuante.

Palavras–chave: Otimização topológica, Vibração, Acústica, Isolamento acústico.

ABSTRACT

Excessive vibration is usually accompanied by undesirable or sometimes catastrophic phenomena. Whether to minimize the propagation of excessive noise or avoid failure due to high mechanical loads, controlling the dynamic behavior of structures is a substantial aspect of engineering design. This thesis aims at developing and improving topology optimization techniques for structural and acoustic-structural dynamic problems. The optimization for natural frequency separation in the high-frequency domain is formulated and solved with the Bi-directional Evolutionary Structural Optimization (BESO) method. An eigenvector tracking algorithm is proposed to avoid instabilities due to local modes and for more proper management of modes. This optimization problem leads to quasi-periodic topologies of alternating material, following the phenomena behind phononic crystals. To make this problem work on one-material and void formulations, a method to enforce connectivity, the Virtual Flux Method (VFM), is proposed. The VFM uses the solution of an auxiliary problem as a connectivity measure. This formulation was validated experimentally by measuring the harmonic response of an optimized topology. The acoustic-structure model is based on the Helmholtz formulation and the linear elastic equations. Two different instances of acoustic-structure interaction problems are analyzed. The first one is the natural frequency optimization of natural frequencies of strongly coupled systems. In this case, the sensitivity analysis had to be expanded to include terms introduced by this formulation. The second type of problem is the maximization of impact sound insulation on floors. In this case, due to the weak coupling between the acoustic and the structural domains, a one-way coupling formulation is used. The pressure field in the acoustic domain is assumed to be diffuse. The minimization of sound impact transmission indicated the synergy between the optimized structure and the transmissibility properties of conventional floating floor mechanisms.

Keywords: Topology optimization, Vibration, Acoustics, Acoustic insulation.

LIST OF FIGURES

LIST OF TABLES

LIST OF ABBREVIATIONS AND ACRONYMS

BESO	Bi-directional Evolutionary Structural Optimization
DKT	Discrete Kirchhoff Triangle
ESO	Evolutionary Structural Optimization
FEA	Finite Element Analysis
FEM	Finite Element Method
FPTO	Floating Projection Topology Optimization
FRF	Frequency Response Function
GC-MMA	Globally Convergent Method of Moving Asymptotes
MAC	Modal Assurance Criterion
NCO	Normalized Cross Orthogonality
N-VTM	Nonlinear Virtual Temperature Method
PETSc	Portable, Extensible Toolkit for Scientific Computations
SEA	Statistical Energy Analysis
SIMP	Solid Isotropic Material with Penalization
SLEPc	Scalable Library for Eigenvalue Problem Computations
SNQ	Single Number Quantity
SPL	Sound Pressure Level
TO	Topology Optimization
TOBS	Topology Optimization of Binary Structures
UNICAMP	Universidade Estadual de Campinas
VFM	Virtual Flux Method

VSF	Virtual Scalar Field
VTM	Virtual Temperature Method

LIST OF SYMBOLS

Latin Letters

b	Fixed base of ribbed shell element
c_e	Elemental connectivity parameter
c_f	Speed of sound in acoustic domain
$c(\mathbf{r})$	Connectivity parameter in VFM
$f(x_e)$	Objective function
f'	Floating floor resonance frequency based on Cremer's model
f_0	Operating frequency
f_k	kth natural frequency
f_s	Surface force
g	Elastic constant of springs in interlayer
h_e	Variable section of eth ribbed shell element
i	Imaginary unit ($\sqrt{-1}$)
j	Iteration counter
k	Thermal conductivity
k_a	Acoustic wave number
k_x, k_y, k_z	Wave number projections in cartesian coordinates
m	Order of generalized mean
m_s	Mean normal heat flux in solid domain
m_s	Mean normal heat flux in void domain
n	Objective function parameter

n_x, n_y, n_z	Integers
p	Penalization exponent
p_0	Reference pressure
$p(\mathbf{r})$	Pressure field
q_e	Norm of heat flux per unit area in eth element
q_k	Modal displacement of the kth mode
q_{act}	Activation heat flux norm
q_{in}	Input heat flux in VFM
q_{lim}	Limit heat flux norm
q_{out}	Output heat flux in VFM
$q_V(\mathbf{r})$	Volumetric heat source
r_{en}	Distance between the centroid of e and n
r_{min}	Filter radius
r_{dil}	Dilate filter radius
s	Degree of activation in VFM
s'	Dynamic stiffness of the interlayer
t	Time
t_e	Thickness of the eth element
t_{max}	Maximum admissible thickness
t_{min}	Minimum admissible thickness
u_n	Normal displacement
x, y, z	Cartesian coordinates
x_e	Design variable of the eth element

$x_{\min}$	Design variable of void elements
y_e	Fluid design variable of the eth element
A	Total absorption area in the receiving room
A_0	Reference absorption area
A_{act}	Activation area
A_{lim}	Limit area
A_{s}	Solid surface area of S
A_{v}	Void surface area of S
AR	Addition ratio
$\text{AR}_{\max}$	Maximum addition ratio
C_{I}	Spectral adaptation term
E	Young's modulus
E_{B}	Band integrated total mean acoustic energy
E_{tot}	Total mean acoustic energy
ER	Evolutionary rate
$J_{\square}$	Bessel function of first kind with $\square$th order
L_x, L_y, L_z	Cell dimensions in cartesian coordinates
$L_{\text{n,B}}$	Band integrated normalized sound pressure level
$L_{\text{n,sum}}$	Average unweighted normalized sound pressure level
$L_{\text{n},\omega}$	Weighted impact sound insulation single number quantity
N	BESO historical convergence criterion
N_{cell}	Number of cells
N_{con}	Number of imposed connectivities

N_{dof}	Number of degrees of freedom
N_{el}	Number of elements in mesh
$N_{\text{el}n}$	Number of elements with the nth node
N_{in}	Number of degrees of freedom in input domain of VFM
N_{modes}	Number of modes
N_{nd}	Number of nodes
N_{out}	Number of degrees of freedom in output domain of VFM
N_{p}	Excitation degrees of freedom when calculating the SNQ
R	Distance between pressure location and displacement location in Rayleigh integral
S	VFM section
T_{in}	Temperature in input domain of VFM
T_{out}	Temperature in output domain of VFM
$T(\mathbf{r})$	Temperature field
V	Volume
W_{diss}	Dissipated power
W_{in}	Input power
$\mathbf{a}$	Nodal displacement vector
$\mathbf{b}$	Body force field
$\mathbf{d}$	Nodal periodic displacement vector
$\mathbf{e}_1, \mathbf{e}_2, \mathbf{e}_3$	Unit vectors
$\mathbf{f}$	Nodal force vector
$\mathbf{f}_\omega$	Amplitude of harmonic excitation at frequency ω

$\mathbf{f_{fs}}$	Force in structural domain due to acoustic-structure coupling
$\mathbf{k}(\mathbf{r})$	Wave number
$\mathbf{n}$	Unit normal vector
$\mathbf{p}$	Nodal pressure vector
$\mathbf{q}$	Modal displacement vector
$\mathbf{q}''$	Heat flux per unit area
$\mathbf{q_h}$	Nodal heat source vector
$\mathbf{q_p}$	Nodal pressure source vector
$\mathbf{q_{fs}}$	Pressure source in acoustic domain due to acoustic-structure coupling
$\mathbf{r}$	Position vector
$\mathbf{r}'$	Position vector for baffled surface in Rayleigh integral
$\mathbf{t}$	Nodal temperature vector
$\mathbf{u}(\mathbf{r})$	Displacement field
$\mathbf{u}_\Upsilon(\mathbf{r})$	Periodic displacement field
$\mathbf{w}$	Nodal force and pressure source vector
$\mathbf{x}$	Vector of design variables
$\mathbf{y}$	Nodal displacement and pressure vector
$\mathbf{A}$	Acoustic-structure coupled stiffness matrix
$\mathbf{B}$	Matrix of shape function derivatives
$\mathbf{C}$	Constitutive tensor
$\mathbf{D}$	Dynamic stiffness matrix
$\mathbf{D}_{\text{dir}}$	Direct field dynamic stiffness matrix
$\mathbf{D}_{\text{tot}}$	Total dynamic stiffness matrix

$\mathbf{E}$	Matrix for sensitivity analysis of repeated modes
$\mathbf{G}$	Acoustic-structure coupled mass matrix
$\mathbf{H}$	Kinetic matrix
$\mathbf{I}_{\square}$	Identity matrix of size $\square$
$\mathbf{I}_{\mathrm{MAC}}$	MAC matrix
$\mathbf{K}$	Stiffness matrix
$\mathbf{K}_{\boldsymbol{\Upsilon}}$	Dispersion analysis stiffness matrix
$\mathbf{L}$	Acoustic-structure coupling matrix
$\mathbf{L}_1, \mathbf{L}_2$	Localization matrices
$\mathbf{M}$	Mass matrix
$\mathbf{N}$	Matrix of shape functions
$\mathbf{P}$	Coupling matrix on the interlayer
$\mathbf{Q}$	Compressibility matrix
$\mathbf{R}$	Heat conductivity matrix
$\mathbf{S}_{\mathbf{ff,ext}}$	Cross-spectrum of the external force
$\mathbf{S}_{\mathbf{qq}}$	Cross-spectrum of the displacement
$\mathbf{T}$	Cauchy stress tensor
$\mathbf{Y}$	Auxiliary matrix

Greek Letters

α	Sensitivity
β	Structural damping
γ	MAC modal parameter
ϵ	Objective function historical variation

η	Acoustic loss factor
λ	First Lamé's parameter
μ	Second Lamé's parameter
ν	Poisson's ratio
ρ	Density
ξ	Conductivity of 1D element
φ	Shape function in wavelet formulation
ω	Frequency
ω_0	Operating angular frequency
ω_k	kth angular natural frequency
θ, ϕ	Rotations of a shell
ζ	Eigenvector of repeated mode calculation
$\Delta\Box$	Variation of $\Box$
Γ_{b}	Boundary between acoustic and structural domains
Γ_{fd}	Boundary of acoustic domain with Dirichlet boundary condition
Γ_{fn}	Boundary of acoustic domain with Neumann boundary condition
Γ_{sd}	Boundary of structural domain with Dirichlet boundary condition
Γ_{sn}	Boundary of structural domain with Neumann boundary condition
Ω_{s}	Structural domain
$\boldsymbol{\phi}_k$	kth left eigenvector
$\boldsymbol{\psi}_k$	kth right eigenvector
$\boldsymbol{\Lambda}$	Matrix of eigenvalues
$\boldsymbol{\Phi}$	Matrix of left eigenvectors

$\boldsymbol{\Psi}$	Matrix of right eigenvectors

Subscripts

$\square_b$	Related to the base floor
$\square_c$	Related to the cth periodic cell
$\square_e$	Related to the eth finite element
$\square_{\mathrm{f}}$	On the fluid domain
$\square_g$	Related to a global variable
$\square_{\mathrm{in}}$	Related to the input of the VFM
$\square_j$	Related to the jth iteration
$\square_k$	Related to the kth eigenmode
$\square_n$	Related to the nth node
$\square_{\mathrm{out}}$	Related to the input of the VFM
$\square_p$	Related to the floating screed
$\square_{\mathrm{s}}$	On the structural domain

Superscripts

$\square^T$	Transpose
$\square^H$	Hermitian (transpose conjugate)
$\square^0$	Of the solid element
$\square^1$	Of material 1
$\square^{-1}$	Inverse of matrix
$\square^{-T}$	Inverse of transpose
$\square^{-H}$	Inverse of hermitian
$\square^{(j)}$	Related to the jth iteration

$\square^{(b)}$	Related to the bth frequency band
$\square^{(p)}$	Related to the pth excitation location
$\square^{*}$	Target or prescribed value

Other Notations

$\dot{\square}$	First time-derivative
$\ddot{\square}$	Second time-derivative
$\mathbb{A}$	Finite element assembly operator
$\nabla\square$	Gradient of a function
$\nabla\cdot\square$	Divergent of a vector function
$\nabla^2\square$	Laplacian of a vector function (divergent of gradient)
$\langle\square,\square\rangle_F$	Frobenius inner product of two matrices
$\square\otimes\square$	Outer product of two vectors
$\tilde{\square}$	Parameter after applying boundary conditions
$\bar{\square}$	Parameter projected to the eigenvector basis
$\hat{\square}$	Reference value of $\square$
$\mathbb{R}_+^*$	Set of positive real numbers
Re $\{\square\}$	Real part of $\square$
Im $\{\square\}$	Imaginary part of $\square$

CONTENTS

1 INTRODUCTION

1.1 Motivation

Excessive vibration of mechanical components is usually associated with undesirable consequences, such as failure. Likewise, it can also cause the excessive propagation of sound, which could be a nuisance or unhealthy to occupants of a vehicle or a building. To mitigate these effects, engineers either: apply active control, modify the boundary conditions of these components, or modify their stiffness or mass characteristics. With the advancement of computational methods, such as the Topology Optimization (TO) method, we can produce light and efficient structures that satisfy those dynamic restrictions.

In high-frequency optimization problems, difficulties may arise when simulating them. Particularly, the high modal density of this frequency domain may prevent the use of traditional TO algorithms. Additionally, for elongated structures such as aircraft wings, bridges, and rockets, the optimization can degenerate into trivial solutions that reduce the length of the component or can converge to local optima with disconnected regions.

Finally, when optimizing acoustic-structure systems, there are challenges in modeling the interaction between both phases accurately and efficiently. For example, the type of coupling can be completely different depending on the materials for the structural and fluid domains.

This thesis investigates some of these challenges regarding topology optimization of dynamic systems for structural and acoustic-structural applications.

1.2 Scientific literature review

Designing more efficient structures for dynamic and acoustic applications has been a widely studied field in engineering. This section aims to briefly review studies in this area, focusing on topology optimization procedures. The following sections are divided according to their subjects, and their reviews are chronological.

1.2.1 Topology optimization method

The Topology Optimization (TO) method is a procedure based on designing an optimal structure by changing both its shape and topology within a given design domain (Figure 1.1). Introduced by Bendsøe and Kikuchi (1988), it was initially based on Homogenization, although its application has been widely extended ever since.

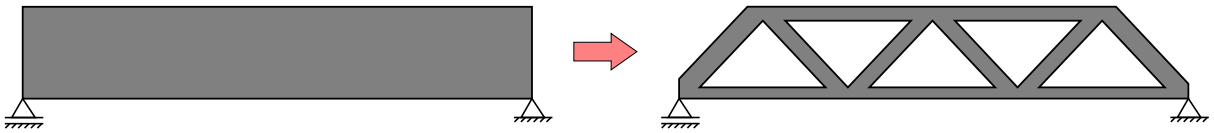

Figure 1.1 – Example of a structure optimized by the Topology Optimization method.

Unlike shape optimization methods, which can only optimize certain features of a predefined structure, TO requires few assumptions before being applied. These are usually the dimensions of the design domain, its boundary conditions, and external forces. As such, its application is usually limited to the initial steps of the design process.

This method was then adapted by Bendsøe (1989) to function based on the interpolation schemes of the material properties. It not only widened the possibilities of application but also simplified its theoretical and numerical analyses. However, it also came with the downside of often generating "gray" areas, that is, sections neither filled with material nor void. This challenge, though, was mostly solved by Zhou and Rozvany (1991), who proposed penalizing the stiffness of these areas, causing the algorithm to prefer full and void elements. Rozvany *et al.* (1992) formalized this procedure, calling it Solid Isotropic Material with Penalization (SIMP).

Although the implementation of penalization parameters was usually enough to solve the problem of "gray" elements, they still appear throughout the procedure. This led to the development of discrete TO algorithms, such as the Evolutionary Structural Optimization (ESO) method. Proposed by Xie and Steven (1993), the ESO is a method that, although based on the SIMP, only allows the presence of fully solid or void elements. At each iteration, some finite elements are removed, based on a given user-inputted parameter. The procedure stops after reaching the desired final volume.

The ESO was subsequently extended to its bidirectional successor, the Bidirectional Evolutionary Structural Optimization (BESO) algorithm (Querin *et al.*, 1998). This method presents the advantages of the ESO while also allowing the addition of previously removed elements. Although the ESO and BESO are purely heuristic, their results are comparable to those obtained by the SIMP.

Among all the aforementioned methods, some numerical errors are usually found. The main problem is the appearance of a "checkerboard pattern" due to shear locking in bilinear elements or elements connected solely by one node (Díaz; Sigmund, 1995). Based on image filtering techniques, Sigmund (1994) proposed a filter that helps to mitigate this problem and guarantees mesh independence of the final solution (Sigmund, 1997). Despite its heuristic features, the proponents of this method show that solutions obtained with this method are similar to those obtained by other optimization methods. Huang and Xie (2007) then adapted this procedure and implemented it on the ESO and BESO algorithms.

These methods have since been widely used in a variety of problems. The works presented in the next sections mostly apply one of the above-mentioned methods. The BESO method has become one of the main algorithms for TO procedures, even being the inspiration of other discrete optimization methods, such as the Floating Projection Topology Optimization (FPTO) (Huang, 2020) and the Topology Optimization of Binary Structures (TOBS) (Sivapuram; Picelli, 2018).

1.2.2 Optimization of dynamic systems

The optimization problem for natural frequencies is usually a way to produce a system whose dynamics must be passively controlled in a certain way, such as attenuating its vibration. To achieve this goal in a TO framework, a sensitivity analysis on natural frequencies must be performed. Haug and Rousselet (1980) were the first to develop such a study, by differentiating the Rayleigh quotient. This procedure is used to assign a value to each element that represents the estimated change in the eigenvalues given a small change in the topology. They also note the difficulty of working with systems that have eigenvalues with geometric multiplicity higher than one. In this case, these eigenvalues are not Fréchet differentiable, only Gateaux differentiable. That is, whenever an eigenvalue has a geometric multiplicity higher than one, it only has directional derivatives.

Regarding the repeated eigenvalues problem, Seyranian *et al.* (1994) showed that their sensitivities cannot be defined similarly to the simple eigenvalue case, requiring an alternative procedure. Krog and Olho (1999) then proposed a solution by imposing an additional constraint, subsequently used by Xia *et al.* (2011) to optimize the first natural frequency, simple or repeated.

However, according to Sun (1990), performing the sensitivity analysis as if the re-

peated eigenvalues were single, has the meaning of using the directional derivative in a direction represented by unitary vectors for all variables. Torii and Faria (2017) uses a smooth p-norm approximation for the smallest eigenvalue to obtain a differentiable expression for the first eigenvalue of a system. Discussions regarding the sensitivity analysis of eigenvalues are summarized in Lin *et al.* (2020).

Parallel to the development of sensitivity analyses was its application on topology optimization. As discussed previously, topology optimization methods such as the SIMP and BESO methods are powerful tools to obtain lightweight efficient structures. Díaz and Kikuchi (1992) maximized the first natural frequency of select linear elastic structures. Ma *et al.* (1993) proposed another method for dynamic system optimization, by minimizing the response of harmonically excited systems. Subsequently, Ma *et al.* (1994) proposed an efficient procedure for either optimizing one natural frequency or a combination of multiple ones. Although a complete and efficient proposition, this procedure has since been abandoned by the following researchers, being replaced by simpler and less extensive approaches.

With the advancement of topology optimization procedures, so did the formulation for natural frequency maximization. Xie and Steven (1994) performed the maximization of natural frequencies using the ESO method, which was further explored by Xie and Steven (1996). Zhao *et al.* (1997) analyzed the influence of non-structural mass on the optimization results. They concluded that, while their addition can be used in some cases to maintain connectivity, it is not guaranteed. They also formulated a mathematical approach to estimate the influence of lumped non-structural mass on the natural frequencies. Finally, Yang *et al.* (1999) extended the optimization of eigenvalues to the BESO method.

Besides the aforementioned problem of repeated eigenvalues, topology optimization can also present problems due to void finite elements. These elements can either alter the natural frequencies or the mode shapes in a non-physical way. Pedersen (2000) explored this phenomenon, proposing an interpolation scheme for stiffness and mass properties to avoid this problem. Huang and Xie (2010) then adapted this procedure for the BESO method. Zuo *et al.* (2011) implemented this procedure with periodicity constraints introduced by Huang and Xie (2008). Zuo *et al.* (2010) proposed another procedure for avoiding local modes from void elements, based on altering the element removal procedure.

Most initial works maximize the first few natural frequencies or by implemented simpler mathematical models for the structure. Jensen and Pedersen (2006) optimized the nat-

ural frequency separation of one and two-dimensional structures, the latter being modeled by the Helmholtz equation. Their results indicated periodicity in optimal topologies for high-frequency ranges. Olhoff *et al.* (2012) extended this analysis, optimizing Euler-Bernoulli beams and verifying the resulting periodicity. Their study also showed the presence of a band gap in the maximized interval. These assessments indicate that periodic optimization might be sufficient in frequency separation maximization problems.

These results sparked the area of TO of phononic crystals, which are periodic elastic components made of two or more materials, that prevent the propagation of elastic waves at certain frequency intervals (Brillouin, 1953; Kittel, 1976). These methods are highly inspired by the optimization of photonic crystals (Joannopoulos *et al.*, 1997). They are based on Bloch's Theorem, which asserts that, for infinitely periodic structures, any variable that is a function of position (such as displacement or pressure) can be solely described by a periodic function with the same period as the repeated cell (Sigalas; Economou, 1992; Kushwaha *et al.*, 1993). Structures such as these present frequency bands where wave propagation is prohibited, which are known as band gaps (Vasseur *et al.*, 1998).

Sigmund and Jensen (2003) performed the first TO assessment of a phononic crystal, obtaining structures that attenuated wave propagation at a given frequency. Since then, a large number of TO studies on this methodology have been performed (Li *et al.*, 2019). Despite that, there is a recent tendency of trying to avoid the perspective of phononic crystals, as it limits the applicability of the method, due to the hypothesis of an infinitely periodic domain. For instance, Liu *et al.* (2020) studied a method to control the propagation of waves in a one-dimensional structure, not only increasing the band gap width but also decreasing the wave propagation speed.

Parallel to the phononic crystal analysis is the dynamic compliance study. The dynamic response of the structure has been recently used as a way to avoid the eigenproblem that must be solved at each iteration (Andreassen *et al.*, 2018; Ferrari *et al.*, 2018). This type of analysis is mainly motivated by the high computational costs of solving eigenproblems compared to the costs of solving linear systems. Although it is only being applied, to this moment, to the fundamental frequency or a few frequencies above it, it is an important alternative to natural frequency optimization. Olhoff and Du (2016) uses the TO method to optimize the dynamic compliance of structure up to the 6^{th} natural frequency. They implemented an incremental method, updating the frequency at which the compliance is calculated by following the

movement of the resonance.

Finally, Li *et al.* (2021) proposed a methodology for adding frequency band constraints. That is, they maximized the fundamental frequency of structures while imposing that no natural frequency is within given frequency bands. They then extended their work for the maximization of nonlinear eigenvalue problems (Li *et al.*, 2022).

1.2.3 Fluid-structure modeling

Be it an oil applied for lubrication purposes or water completely engulfing the structure, engineering devices usually involve some fluid-structure interaction. Though important, it is not necessarily easy to take this phenomenon into account, as at least two different equations are required to describe it. As proposed by Zienkiewicz and Bettess (1978), both systems can be solved simultaneously, coupling them by their common boundaries via the inclusion of a coupling matrix. As this method involves the solution of the system by dividing it into two different domains, it is usually identified as the segregated formulation.

As the aforementioned method requires a clear boundary between domains, it is not readily available for the SIMP method. Wang and Bathe (1997) proposed a solution for this in the mixed formulation. With this method, the elastic stiffness matrix is defined by its bulk and shear moduli, and the fluid stiffness matrix is defined solely by the bulk modulus (as fluids can only resist compression forces). This modeling strategy not only enables solving both domains with the same equation, but also makes it possible to interpolate between solid and fluid phases since they are defined by the same properties: density, bulk, and shear moduli. With this formulation, Yoon *et al.* (2007) optimized acoustic-structure coupled systems using the SIMP method. It proved to be effective in pressure and vibration minimization problems, despite presenting some fluctuation due to local modes. Sigmund and Clausen (2007) used this formulation on pressure load compliance optimization problems. Kook and Jensen (2017) applied it in the optimization of periodic microstructures, minimizing their loss factor. Kook (2019) performed the optimization of the mean pressure using the BESO method. Hu *et al.* (2020) optimized the mean pressure, displacement of a degree of freedom, and sound transmission loss of acoustic-structure interaction domains using the FPTO method.

Alternatively, the segregated formulation also showed its viability in studies parallel to the mixed formulation. Chen and Kikuchi (2001) presented a technique to apply design-dependent hydro-static loads. This way, the fluid-structure boundary is easily identified along

with the iterations. Picelli *et al.* (2015a) then provided a simple implementation that automatically assigns the correct values to the boundary matrices. Picelli *et al.* (2015b) then used this coupling to optimize the first natural frequency of acoustic-structure coupled systems. Likewise, Vicente *et al.* (2015) used this formulation on the harmonic response optimization of coupled systems. They neglected, however, the sensitivity terms due to the acoustic and coupling matrices. Jensen (2019) presented an interpolation scheme for structural and acoustic elements in the segregated u/p formulation. They implement this methodology in the optimization of dynamic compliance.

Regarding the optimization of dynamic fluid-structure systems, there are many difficulties in optimizing their natural frequencies. The mixed u/p formulation mass matrix is singular, and the fluid domain is highly susceptible to local modes. The first point could cause problems on eigenproblem solvers that require a positive definite mass matrix, while the second one can cause instabilities in the evolutionary procedure.

These approaches work very effectively in low frequency, however, they are not viable in high frequency domains. In this type of formulation, the modal density may become too high, requiring the calculation of an immense number of eigenvalues and eigenvectors; furthermore, more refined finite element meshes are required, due to lower wavelengths (Hopkins, 2007).

For the structural domain, as mentioned before, one may use a periodic wave propagation analysis. However, an alternative formulation involving an additional kinematic hypothesis for the sound pressure field or the velocity field can be employed. One such methodology is to assume a diffuse pressure field, meaning that it is composed of several independent plane waves, all propagating towards random directions and with random phases. This hypothesis vastly simplifies the calculations in high frequency, but its main drawback is its lack of accuracy in lower frequency domains (Reynders *et al.*, 2019). One of the common applications for this methodology is the Statistical Energy Analysis (SEA) (Lyon *et al.*, 1995; Fahy, 1994).

The diffuse field model has been applied in cases involving the simulation of either airborne or structure-borne excitation systems. Reynders *et al.* (2019) presents the formulation for impact sound transmission between two rooms. This work is validated by Wang *et al.* (2020), where they verify this model numerically and analytically for lightweight timber joist floors. Gao *et al.* (2019) uses a Boundary Element-Statistical Energy Analysis procedure (Gao *et al.*, 2018) to minimize the sound pressure level by redistributing sound-absorbing materials

within a vibroacoustic domain. Gao *et al.* (2020) optimizes the ensemble average energy of both single excitation and frequency band systems. Van den Wyngaert *et al.* (2020) models a double-leaf wall system with the SEA and minimizes their airborne sound transmission by designing their acoustic studs. Then, they expanded this work for multi-objective formulations that consider material usage (Van den Wyngaert *et al.*, 2021). Yao *et al.* (2019) maximized the sound transmission loss in floating floor railway systems. Giannini *et al.* (2023) used the diffuse formulation to optimize single and double panels for minimum airborne sound transmission.

1.2.4 Connectivity constraint

When optimizing the natural frequency, the process often results in structures with no physical meaning or that violate certain geometric restrictions. For instance, if we decrease the length of a cantilever beam, we will increase its fundamental frequency. However, that is usually not a possible solution for many applications. Furthermore, optimizing higher natural frequencies usually leads to disconnected isles of solid regions. These cases are illustrated in Figure 1.2.

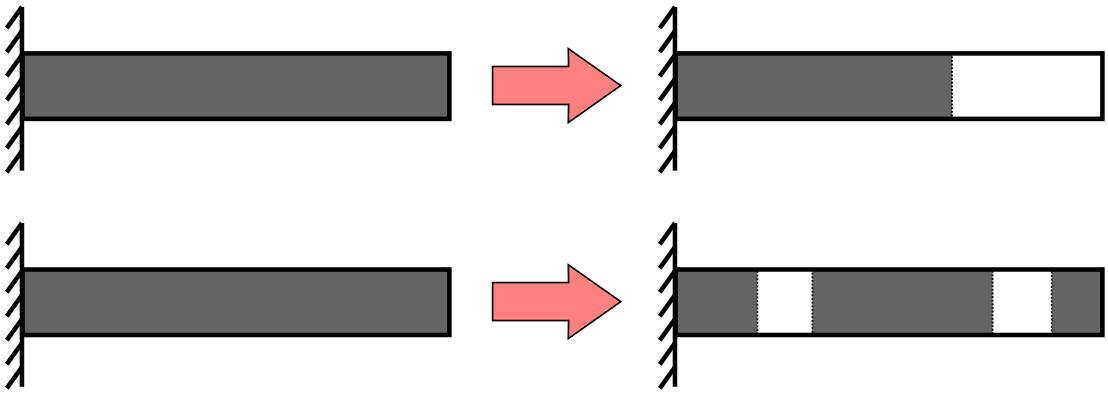

Figure 1.2 – Examples of an optimization leading to impractical solutions.

Several propositions have been made in the literature to avoid this behavior. The first alternative is to use a multi-objective function, with a term to minimize compliance. Zuo *et al.* (2010) applied this method by subtracting the compliance into the function that is maximized. Since disconnected regions are associated with low-frequency local modes, it could also be used for that end. Leon *et al.* (2015) added stress constraints to the optimization to avoid hinges on the topology. They later expanded this analysis considering both geometric and material nonlinearities (Leon *et al.*, 2020). Pereira and Cardoso (2018) assessed stress constraints on this kind of problem, comparing both local and global stress constraints. Finally, Emmendoerfer *et*

al. (2022) implemented these stress constraints to the optimization of multi-material compliant mechanisms to avoid hinges.

The second method is to include additional masses to the structure (Zhao *et al.*, 1997). For instance, if we add a mass at the free edge of a cantilever beam, the optimization process will not disconnect it, as it would decrease the first natural frequency. This method, however, changes the dynamic behavior of the system. It is also difficult to control its influence over the optimization process.

The third alternative is to perform changes to the optimization algorithm itself. Munk *et al.* (2017) proposed a connectivity matrix to guarantee connectivity between all solid elements. This is done by creating a square matrix whose size is the number of solid elements at that iteration. If it is filled with 1 wherever there is a connected pair and 0 elsewhere, connectivity can be directly seen from this matrix. This method manages to guarantee connectivity in rough meshes, such as the Zhou-Rozvany problem (Zhou; Rozvany, 2001), but not for practical applications. It is highly mesh-dependent, and could often result in connections with one element of width.

Du *et al.* (2018) proposed a way to calculate a connectivity index for multi-scale optimization studies. They presented a methodology to guarantee connectivity at the interfaces between distinct cells. Xiong *et al.* (2020) used graphs to identify the location of enclosed voids (which can be troublesome to manufacture). A hierarchical graph scheme is used to identify the shortest path between these enclosed voids and the boundaries. Tunnels are generated between them and are chosen based on the ones which affect the least the objective function.

More recently, Nejat *et al.* (2022) performed modifications to the level-set optimization method to guarantee connectivity and a stable evolution. They illustrate this by minimizing the compliance of an elongated cantilever beam.

The last possibility involves performing an auxiliary Finite Element Analysis (FEA). Enclosed voids can be identified by solving a heat conduction problem where void elements generate heat and are conductive, while solid ones are insulators. This is the basis of the Virtual Temperature Method (VTM) proposed by Liu *et al.* (2015), which can also be known as the Virtual Scalar Field (VSF) method (Li *et al.*, 2016). The VTM has been since studied and extended; Luo *et al.* (2020) proposed its nonlinear variant, the N-VTM, which limits the maximum temperature, rendering the process more stable.

The VTM has also been widely used in the literature, Wang *et al.* (2021) applied

it on electric fields and studied its effects when it is imposed alongside volume and stress constraints. Pereira *et al.* (2022) used the VTM in acoustic optimization to avoid the presence of holes in rigid structures and to facilitate the manufacturing of poro-rigid structures.

1.3 Goals and contributions

The main goal of this work is to contribute to methods of structural optimization in problems of natural frequency optimization in low and medium to high-frequency domains. Four different optimization problems are studied:

- Topology optimization of natural frequency separation of high natural frequencies;
- Development of a connectivity constraint to avoid convergence to trivial solutions or disconnected topologies;
- Topology optimization of natural frequencies of acoustic-structure interaction problems;
- Optimization of sound insulation of ribbed floors using a diffuse pressure field formulation.

The following conference presentations were derived from this research:

- Topology optimization of frequency gap for composite materials. In **14$^{\text{th}}$ World Congress on Computational Mechanics**;
- Topology optimization with connectivity constraint to separate natural frequencies of a ring structure. In **8$^{\text{th}}$ International Symposium on Solid Mechanics**;
- Broadband optimization of ribbed floors for impact sound insulation. In **16$^{\text{th}}$ World Congress on Structural and Multidisciplinary Optimization**.

The following journal papers have been derived from the work presented in this thesis:

- High natural frequency gap topology optimization of bi-material elastic structures and band gap analysis. **Structural and Multidisciplinary Optimization**, v. 63, n. 5, 2325–2340, Lopes *et al.* (2021);

- Numerical and experimental investigation on topology optimization of an elongated dynamic system. **Mechanical Systems and Signal Processing**, v. 165, 108356, Lopes *et al.* (2022b).

At the time of writing this thesis, another paper is under review at *Building and Environment*.

Furthermore, three papers have also been co-authored by the author. They contributed to the programming of the BESO algorithm, as well as complementing the vibroacoustic optimization analyses from this work. The papers are the following:

- Finite variation sensitivity analysis for discrete topology optimization of continuum structures. **Structural and Multidisciplinary Optimization**, v. 64, 3877–3909, Cunha *et al.* (2021);
- Topology optimization of acoustic systems with a multiconstrained BESO approach. **Finite Elements in Analysis and Design**, v. 201, p. 10370, Pereira *et al.* (2022);
- Multi-domain acoustic topology optimization based on the BESO approach: applications on the design of multi-phase material mufflers. **Structural and Multidisciplinary Optimization**, v. 66, n. 1, p. 25, Pereira *et al.* (2023).

1.4 Layout of the thesis

This thesis is divided into six chapters. The first chapter introduces the motivation of this work, describes the state of the art in problems of Topology Optimization, and presents the goals of this work.

Chapter 2 discusses natural frequency optimization without acoustic domain. The formulation for two-material natural frequency separation optimization is presented. Finally, some results are examined.

Chapter 3 presents a way to perform the natural frequency optimization for one material and void domains. This is done by introducing a novel method, entitled the Virtual Flux Method (VFM).

Chapter 4 analyzes acoustic-structure optimization problems, describing the formulation of the acoustic domain and its coupling with the structural one via the Helmholtz equations. Here, a study on the sensitivity analysis, as well as on an optimization case are done.

Chapter 5 presents the optimization formulation and optimization results of a weakly coupled system, more specially, the maximization of impact sound insulation. Here, the base floor is optimized, while the fluid domain is modeled via a diffuse field formulation.

Finally, Chapter 6 contains the conclusions of this thesis and suggestions for future research.

Appendix A presents the validation of the Finite Element Analysis. Appendix B shows the validation of the sensitivity analysis. Appendix C deduces the analytical expressions for the heat flux of linear quadrilateral elements. Appendix D illustrates the assembly and update process of the acoustic-structure coupling matrix.

2 HIGH NATURAL FREQUENCY SEPARATION MAXIMIZATION

In the literature, it is quite common to optimize the first few natural frequencies of a structure. However, additional procedures must be included to do the same in higher frequency domains. An eigenvector tracking mechanism is added to avoid local modes and to stabilize the optimization procedure. A less common objective function is chosen to account for the contribution of several modes simultaneously. The computational costs of the eigenvalue solver is studied in order to decrease it. The contribution from this section was presented at the 14th World Congress on Computational Mechanics and published at *Structural and Multidisciplinary Optimization* (Lopes *et al.*, 2021).

2.1 Formulation of structural natural frequency problem

In this section, the structural domain is defined based on the theories of continuum mechanics. The finite element formulation is presented, as well as the eigenproblem that returns the natural frequencies and modes of the system. Finally, the dispersion analysis that is used to study the numerical results is presented.

2.1.1 Structural domain formulation

The optimization problem presented here is initially performed on a solely structural domain, indicated by Figure 2.1.

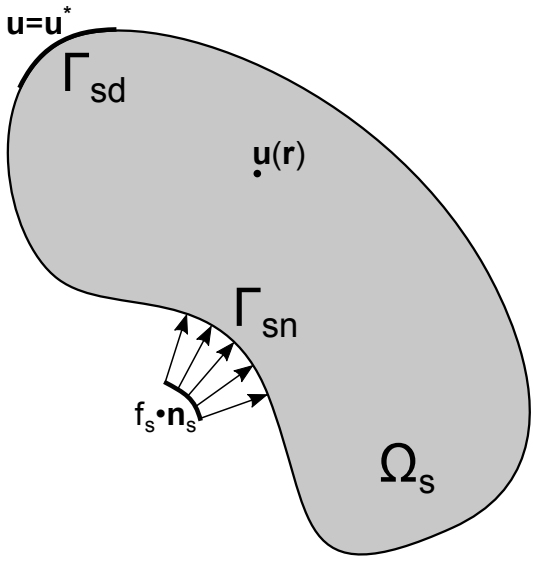

Figure 2.1 – Structural domain.

The domain is modeled as linear elastic and isotropic, the dissipative and damping effects are neglected. Its displacement field can be obtained from the solution of the Navier's equation, along with the appropriate Dirichlet and Neumann boundary conditions:

$$\begin{cases} \rho_s \ddot{\mathbf{u}} - (\lambda + \mu) \nabla (\nabla \cdot \mathbf{u}) - \mu \nabla^2 \mathbf{u} = \mathbf{b_s} & \text{, on } \Omega_s \\ \mathbf{u}(\mathbf{r}) = \mathbf{u}^* & \text{, on } \Gamma_{sd} \\ \mathbf{T}\mathbf{n_s} = f_s \mathbf{n_s} & \text{, on } \Gamma_{sn}, \end{cases} \tag{2.1}$$

where $\mathbf{T}$ is the Cauchy stress tensor, $\mathbf{b}$ is the body force vector, $\mathbf{u}$ is the displacement field, and $\ddot{\mathbf{u}}$ is the acceleration. The values λ and μ are the Lamé parameters, and ρ_s is the density of the material. The surface forces are represented by f_s and $\mathbf{n_s}$ is the normal vector at the surfaces of the domain.

The displacement field can be approximated via the Finite Element Method (FEM) by discretizing the domain and applying the shape functions:

$$\mathbf{u}_e \approx \mathbf{N_s} \mathbf{a}, \tag{2.2}$$

where $\mathbf{N_s}$ is the matrix of shape functions, $\mathbf{a}$ is the nodal displacement vector and $\mathbf{u}_e$ is the displacement field within the domain of the eth element.

Applying the Weighted Residual Method of and the Galerkin method, Eq. (2.1) becomes:

$$\mathbf{M}_g \ddot{\mathbf{a}} + \mathbf{K}_g \mathbf{a} = \mathbf{f}_g, \tag{2.3}$$

where $\mathbf{M}_g$, $\mathbf{K}_g$ and $\mathbf{f}_g$ are the global mass and stiffness matrices and the global force vector, which are assembled from the elemental ones:

$$\mathbf{M}_g = \bigwedge_{e=1}^{N_{el}} \mathbf{M}_e, \tag{2.4}$$

$$\mathbf{K}_g = \bigwedge_{e=1}^{N_{el}} \mathbf{K}_e, \tag{2.5}$$

$$\mathbf{f}_g = \bigwedge_{e=1}^{N_{el}} \mathbf{f}_e, \tag{2.6}$$

where N_{el} is the number of elements of the domain, and $\mathbb{A}$ is the assembly operator.

The elemental matrices of the eth element can be obtained by integrating along its domain:

$$\mathbf{M}_e = \int_{\Omega_e} \rho_s \mathbf{N_s}^T \mathbf{N_s} d\Omega, \tag{2.7}$$

$$\mathbf{K}_e = \int_{\Omega_e} \mathbf{B_s}^T \mathbf{C_s} \mathbf{B_s} d\Omega, \tag{2.8}$$

$$\mathbf{f}_e = \int_{\Gamma_{sn}} \mathbf{N_s}^T \left(\mathbf{f_s} \cdot \mathbf{n_s}\right) d\Gamma + \int_{\Omega_s} \mathbf{N_s}^T \mathbf{b_s} d\Omega, \tag{2.9}$$

where $\mathbf{B_s}$ is the matrix of shape function derivatives and $\mathbf{C_s}$ is the linear elastic constitutive matrix.

In this section, all problems are modeled either as two-dimensional under plane stress hypothesis or under three-dimensional linear elastic hypothesis. For plane stress problems, the domain is discretized into 4-node isoparametric quadrilateral elements with the following matrices:

$$\mathbf{N}_s = \begin{bmatrix} N_1 & 0 & N_2 & 0 & N_3 & 0 & N_4 & 0 \\ 0 & N_1 & 0 & N_2 & 0 & N_3 & 0 & N_4 \end{bmatrix}, \tag{2.10}$$

$$\mathbf{B}_s = \begin{bmatrix} \frac{\partial N_1}{\partial x} & 0 & \frac{\partial N_2}{\partial x} & 0 & \frac{\partial N_3}{\partial x} & 0 & \frac{\partial N_4}{\partial x} & 0 \\ 0 & \frac{\partial N_1}{\partial y} & 0 & \frac{\partial N_2}{\partial y} & 0 & \frac{\partial N_3}{\partial y} & 0 & \frac{\partial N_4}{\partial y} \\ \frac{\partial N_1}{\partial y} & \frac{\partial N_1}{\partial x} & \frac{\partial N_2}{\partial y} & \frac{\partial N_2}{\partial x} & \frac{\partial N_3}{\partial y} & \frac{\partial N_3}{\partial x} & \frac{\partial N_4}{\partial y} & \frac{\partial N_4}{\partial x} \end{bmatrix}, \tag{2.11}$$

$$\mathbf{C}_s = \frac{E}{1-\nu^2} \begin{bmatrix} 1 & \nu & 0 \\ \nu & 1 & 0 \\ 0 & 0 & \frac{1-\nu}{2} \end{bmatrix}, \tag{2.12}$$

where E is the Young's modulus and ν is the Poisson's ratio.

For the three dimensional cases, the mesh is discretized using 8-node hexahedral elements with the following matrices:

$$\mathbf{N}_s = \begin{bmatrix} N_1 & 0 & 0 & & N_8 & 0 & 0 \\ 0 & N_1 & 0 & \cdots & 0 & N_8 & 0 \\ 0 & 0 & N_1 & & 0 & 0 & N_8 \end{bmatrix}, \tag{2.13}$$

$$\mathbf{B}_s = \begin{bmatrix} \frac{\partial N_1}{\partial x} & 0 & 0 & & \frac{\partial N_8}{\partial x} & 0 & 0 \\ 0 & \frac{\partial N_1}{\partial y} & 0 & & 0 & \frac{\partial N_8}{\partial y} & 0 \\ 0 & 0 & \frac{\partial N_1}{\partial z} & & 0 & 0 & \frac{\partial N_8}{\partial z} \\ \frac{\partial N_1}{\partial y} & \frac{\partial N_1}{\partial x} & 0 & \cdots & \frac{\partial N_8}{\partial y} & \frac{\partial N_8}{\partial x} & 0 \\ \frac{\partial N_1}{\partial z} & 0 & \frac{\partial N_1}{\partial x} & & \frac{\partial N_8}{\partial z} & 0 & \frac{\partial N_8}{\partial x} \\ 0 & \frac{\partial N_1}{\partial z} & \frac{\partial N_1}{\partial y} & & 0 & \frac{\partial N_8}{\partial z} & \frac{\partial N_8}{\partial y} \end{bmatrix}, \tag{2.14}$$

$$\mathbf{C}_s = \frac{E}{(1-2\nu)(1+\nu)} \begin{bmatrix} 1-\nu & \nu & \nu & 0 & 0 & 0 \\ \nu & 1-\nu & \nu & 0 & 0 & 0 \\ \nu & \nu & 1-\nu & 0 & 0 & 0 \\ 0 & 0 & 0 & \frac{1-2\nu}{2} & 0 & 0 \\ 0 & 0 & 0 & 0 & \frac{1-2\nu}{2} & 0 \\ 0 & 0 & 0 & 0 & 0 & \frac{1-2\nu}{2} \end{bmatrix}. \tag{2.15}$$

The matrices are assembled via numerical integration using the Gauss-Legendre quadrature, ensuring the necessary number of integration points for an exact integration on the regular elements that are employed here.

2.1.2 Eigenvalue problem

The response of a dynamic system subjected to a harmonic excitation at a frequency of ω is given by:

$$-\omega^2 \mathbf{M}_g \mathbf{a}_\omega + \mathbf{K}_g \mathbf{a}_\omega = \mathbf{f}_\omega, \tag{2.16}$$

where $\mathbf{f}_\omega$ is the amplitude of the force and $\mathbf{a}_\omega$ is the amplitude of the displacement, both at a frequency ω.

In an undamped system, resonances occur when the excitation frequency is equal to one of their natural frequencies. These natural frequencies can be obtained by finding the non-trivial solutions of Eq. 2.3 when the force is zero. This leads to the following eigenproblem:

$$\omega_k^2 \mathbf{M}_g \boldsymbol{\phi}_{\boldsymbol{k}} = \mathbf{K}_g \boldsymbol{\phi}_{\boldsymbol{k}}, \tag{2.17}$$

where ω_k is the kth angular natural frequency and $\boldsymbol{\phi}_{\boldsymbol{k}}$ is the kth eigenvector.

Eq. (2.3) can be rewritten in matrix representation as:

$$\mathbf{M}_g \boldsymbol{\Phi} \boldsymbol{\Lambda} = \mathbf{K}_g \boldsymbol{\Phi}, \tag{2.18}$$

where the matrices $\boldsymbol{\Lambda}$ and $\boldsymbol{\Phi}$ are the eigenvalue and eigenvector matrices, defined as:

$$\boldsymbol{\Lambda} = \begin{bmatrix} \omega_1^2 & 0 & \cdots & 0 \\ 0 & \omega_2^2 & \cdots & 0 \\ \vdots & \vdots & \ddots & \vdots \\ 0 & 0 & \cdots & \omega_{N_{\text{dof}}}^2 \end{bmatrix}, \tag{2.19}$$

$$\boldsymbol{\Phi} = \begin{bmatrix} \boldsymbol{\phi_1} & \boldsymbol{\phi_2} & \cdots & \boldsymbol{\phi}_{\boldsymbol{N}_{\text{dof}}} \end{bmatrix}, \tag{2.20}$$

where N_{dof} is the total number of eigenvalues and eigenvectors, also corresponding to the size of the $\mathbf{M}_g$ and $\mathbf{K}_g$ matrices.

In this work, the eigenproblems are solved using the SLEPc (Scalable Library for Eigenvalue Problem Computations) (Hernandez *et al.*, 2005) open library, which is an extension of the PETSc (Portable, Extensible Toolkit for Scientific Computation) (Balay *et al.*, 2022) open library. The Krylov-Schur algorithm is employed, and intermediate linear systems are solved by the Cholesky factorization from the Intel® MKL PARDISO library. For faster computational times during the optimization, the eigenvectors obtained from the previous iteration are used as the initial space at the next iteration.

Additionally, the eigenvectors are normalized with respect to the mass matrix. Therefore, the following properties are true:

$$\mathbf{I}_{N_{\text{dof}}} = \boldsymbol{\Phi}^T \mathbf{M}_g \boldsymbol{\Phi}, \tag{2.21}$$

$$\boldsymbol{\Lambda} = \boldsymbol{\Phi}^T \mathbf{K}_g \boldsymbol{\Phi}, \tag{2.22}$$

where $\mathbf{I}_{N_{\text{dof}}}$ is the identity matrix of size N_{dof}.

This FEA and eigenproblem was validated by comparing their results with the commercial software COMSOL Multiphysics®. This validation is shown in Appendix A. Note that it is done with the acoustic-structure formulation from Chapter 4.

2.1.3 Dispersion analysis

The results from the optimization of high natural frequencies are usually periodic or quasi-periodic (Jensen; Pedersen, 2006; Lopes *et al.*, 2021). With that in mind, a way to analyze these topologies is to perform a wave dispersion analysis. This type of analysis aims to obtain the wave modes and their frequency of propagation on an infinitely periodic structure, such as Figure 2.2.

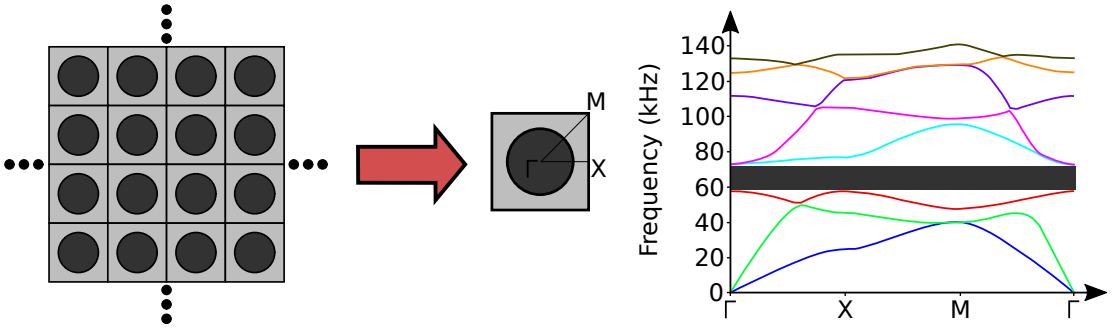

Figure 2.2 – Illustration of an infinitely periodic structure and dispersion analysis.

Due to this periodicity, Bloch's theorem can be applied (Floquet, 1883; Sigalas; Economou, 1992). It states that the free-vibration response of this system can be written as:

$$\mathbf{u}(\mathbf{r},t) = \mathbf{u}_\Upsilon(\mathbf{r}) e^{\mathrm{i}\mathbf{k}\cdot\mathbf{r}} e^{\mathrm{i}\omega t}, \tag{2.23}$$

where i is the imaginary unit ($\sqrt{-1}$), $\mathbf{k}$ is the wave number ($\mathbf{k} = k_x\mathbf{e_1} + k_y\mathbf{e_2} + k_z\mathbf{e_3}$) and ω is the natural frequency. $\mathbf{u}_\Upsilon(\mathbf{r})$ is a periodic displacement field in a given unit cell, that is, it has the following property:

$$\mathbf{u}_\Upsilon(\mathbf{r} + n_x L_x\mathbf{e_1} + n_y L_y\mathbf{e_2} + n_z L_z\mathbf{e_3}) = \mathbf{u}_\Upsilon(\mathbf{r}), \tag{2.24}$$

where $\mathbf{e_1}$, $\mathbf{e_2}$ and $\mathbf{e_3}$ are the unit vectors and L_x, L_y and L_z are the cell size at the X, Y and Z directions. The values n_x, n_y and n_z are integers.

This relation is substituted into the Navier's Equation (Eq. (2.1)), and its solution is approximated by the FEM using the same shape functions from Section 2.1.1:

$$\mathbf{u}_\Upsilon(\mathbf{r}) \approx \mathbf{N_s}\mathbf{d}. \tag{2.25}$$

Applying the weighted residuals and Galerkin methods results in the following eigenproblem (Sigmund; Jensen, 2003):

$$-\omega^2 \mathbf{M}_g \mathbf{d} + \mathbf{K}_{\Upsilon_g}(k_x, k_y)\mathbf{d} = \mathbf{0}, \tag{2.26}$$

where $\mathbf{M}_g$ is equal to the one previously obtained (Eq. (2.7)), and $\mathbf{K}_{\Upsilon_g}$ is assembled from the corresponding elemental stiffness matrix $\mathbf{K}_{\Upsilon_e}$. For a two-dimensional analysis, it is given as:

$$\mathbf{K}_{\Upsilon_e} = \mathbf{K}_e - i\left(\mathbf{K}_1 k_x + \mathbf{K}_2 k_y\right) + \mathbf{K}_3 k_x^2 + \mathbf{K}_4 k_x k_y + \mathbf{K}_5 k_y^2, \tag{2.27}$$

where $\mathbf{K}_e$ is given by Eq. (2.8) and the other components are given by:

$$\mathbf{K}_1 = \int_{\Omega_e} \left(\mathbf{N_s}^T \mathbf{L_1}^T \mathbf{C_s} \mathbf{B_s} - \mathbf{B_s}^T \mathbf{C_s} \mathbf{L_1} \mathbf{N_s}\right) d\Omega, \tag{2.28}$$

$$\mathbf{K}_2 = \int_{\Omega_e} \left(\mathbf{N_s}^T \mathbf{L_2}^T \mathbf{C_s} \mathbf{B_s} - \mathbf{B_s}^T \mathbf{C_s} \mathbf{L_2} \mathbf{N_s}\right) d\Omega, \tag{2.29}$$

$$\mathbf{K}_3 = \int_{\Omega_e} \mathbf{N_s}^T \mathbf{L_1}^T \mathbf{C_s} \mathbf{L_1} \mathbf{N_s} d\Omega, \tag{2.30}$$

$$\mathbf{K}_4 = \int_{\Omega_e} \left(\mathbf{N_s}^T \mathbf{L_1}^T \mathbf{C_s} \mathbf{L_2} \mathbf{N_s} - \mathbf{N_s}^T \mathbf{L_2}^T \mathbf{C_s} \mathbf{L_1} \mathbf{N_s}\right) d\Omega, \tag{2.31}$$

$$\mathbf{K}_5 = \int_{\Omega_s} \mathbf{N_s}^T \mathbf{L_2}^T \mathbf{C_s} \mathbf{L_2} \mathbf{N_s} d\Omega, \tag{2.32}$$

where the $\mathbf{L_1}$ and $\mathbf{L_2}$ are localization matrices defined as:

$$\mathbf{L}_1 = \begin{bmatrix} 1 & 0 \\ 0 & 0 \\ 0 & 1 \end{bmatrix}, \tag{2.33}$$

$$\mathbf{L}_2 = \begin{bmatrix} 0 & 0 \\ 0 & 1 \\ 1 & 0 \end{bmatrix}. \tag{2.34}$$

With these matrices, the dispersion curve can be obtained by varying k_x and k_y and solving the eigensystem on Eq. (2.26). Due to the periodicity of the system, we can restrict the wave vector to the first Brillouin zone (Brillouin, 1953). Furthermore, assuming the

symmetries of the unit cell allows us to reduce it even further, such as the triangle from Figure 2.2. Additionally, we can investigate only the edges of this region. This yields the frequencies of the wave modes that can propagate within this domain. Intervals without wave modes are called band gaps.

2.2 Formulation of the optimization problem

This section presents the overall formulation of the optimization problem, along with the necessary procedures for this end. First, the optimization problem is formulated, then the sensitivity analysis is performed by differentiating the objective function. An eigenvector tracking procedure is presented to follow the modes throughout the optimization and to mitigate the effects of local modes.

2.2.1 Objective function

Concerning the optimizing natural frequencies, different objective functions may be desired, such as maximizing or minimizing a certain combination of natural frequencies, maximizing the separation between consecutive ones, or assigning target values to them. Traditionally, the maximization of the kth natural frequency is formulated as (Xie; Steven, 1996):

$$\begin{aligned} \max \quad & f(\mathbf{x}) = \omega_k^2, \\ \text{s.t.} \quad & V^* - \textstyle\sum_{e=1}^{N_{\text{el}}} V_e x_e = 0, \\ & x_e = 1 \text{ or } x_{\text{min}}, \end{aligned} \tag{2.35}$$

where ω_k is the kth angular natural frequency. The vector $\mathbf{x}$ contains the design variables of each element, being x_e the design variable of the eth element. Each x_e can be either 1, for full elements, or x_{min}, for void elements. V^* is the final volume of the domain, V_e is the volume of the eth element, and N_{el} is the number of elements in the domain.

Concerning the optimization of natural frequency separation, two common formulations are (Jensen; Pedersen, 2006):

$$\begin{aligned} \max \quad & f(\mathbf{x}) = \omega_k^2 - \omega_{k-1}^2, \\ \text{s.t.} \quad & V^* - \textstyle\sum_{e=1}^{N_{\text{el}}} V_e x_e = 0, \\ & x_e = 1 \text{ or } x_{\text{min}}, \end{aligned} \tag{2.36}$$

and:

$$\begin{aligned} \max \quad & f(\mathbf{x}) = \frac{\omega_k^2}{\omega_{k-1}^2}, \\ \text{s.t.} \quad & V^* - \sum_{e=1}^{N_{\text{el}}} V_e x_e = 0, \\ & x_e = 1 \text{ or } x_{\text{min}}. \end{aligned} \tag{2.37}$$

These formulations are extremely useful in continuous optimization methods. However, some undesirable effects may appear in high-frequency domain that must be addressed. In discrete optimization algorithms, their presence is even more critical. Due to the higher modal density around the kth mode, its natural frequency can cross with other ones, which is called mode-shifting. As a result, two problems appear: the ordering of the modes gets scrambled, and a discontinuity appears on the derivatives of the mode shapes (Haug; Rousselet, 1980).

To ensure proper consideration of the natural frequencies, an objective function that encapsulates multiple modes simultaneously must be used. The formulation proposed by Ma *et al.* (1994) is implemented, as it not only considers multiple modes but can also solve different natural frequency optimization problems by changing a parameter n:

$$\begin{aligned} \max \quad & f(\mathbf{x}) = \omega_0^2 + \left[\frac{1}{N_{\text{modes}}} \sum_{k=1}^{N_{\text{modes}}} \left(\omega_k^2 - \omega_0^2\right)^n \right]^{\frac{1}{n}}, \\ \text{s.t.} \quad & V^* - \sum_{e=1}^{N_{\text{el}}} V_e x_e = 0, \\ & x_e = 1 \text{ or } x_{\text{min}}, \end{aligned} \tag{2.38}$$

where ω_0 is the angular operating frequency, N_{modes} is the number of natural frequencies considered in the analysis. The parameter n is responsible for modifying the goal of the optimization.

This objective function allows different possibilities by altering the parameter n. If it is an odd number, then it represents a natural frequency maximization problem. In this case, if n is positive, the farthest eigenvalues from ω_0 have the highest contribution. On the other hand, if it is negative, the closest ones to ω_0 have the highest contribution. If n is a negative even number, then the function maximizes the distance of eigenvalues from ω_0. The closest eigenvalues from the operating frequency have the highest contribution. Increasing n magnifies this effect. As the goal of this work is to analyze problems of maximization of natural frequency

separation, the formulation with $n = -2$ is employed:

$$\begin{aligned} \max \quad & f(\mathbf{x}) = \omega_0^2 + \left[\frac{1}{N_{\text{modes}}} \sum_{k=1}^{N_{\text{modes}}} \frac{1}{\left(\omega_k^2 - \omega_0^2\right)^2} \right]^{-\frac{1}{2}}, \\ \text{s.t.} \quad & V^* - \sum_{e=1}^{N_{\text{el}}} V_e x_e = 0, \\ & x_e = 1 \text{ or } x_{\text{min}}. \end{aligned} \tag{2.39}$$

2.2.2 Sensitivity analysis

At each iteration of the topology optimization process, elements must have their design variable changed according to its effect on the objective function. This study is done based on a sensitivity analysis.

In discrete topology optimization procedures, such as the BESO method, ideally, such an analysis would be made by comparing the values of the objective function at each configuration. This is, however, not a computationally viable procedure. Nonetheless, studies in the last few years have attempted to provide a feasible method for discrete sensitivity analyses (Cunha *et al.*, 2021).

The usual procedure followed by density-based topology optimization procedures corresponds to relaxing the discrete objective function into a continuous one. That is, the design variables x_e are assumed to be in the interval $[x_{\text{min}},1]$ instead of the set $\{x_{\text{min}},1\}$. This allows us to perform a Taylor series expansion on the objective function:

$$f(\mathbf{x}) = f(\mathbf{x}^*) + \sum_{e=1}^{N_{\text{el}}} \left. \frac{\partial f(\mathbf{x})}{\partial x_e} \right|_{x_e = x_e^*} (x_e - x_e^*) + O\left(\|\Delta \mathbf{x}\|^2\right) \tag{2.40}$$

where x_e^* indicates the current eth design variable, and $O\left(\|\Delta \mathbf{x}\|^2\right)$ represents higher order terms.

From the Taylor series, one way to measure the changes in the objective function is by evaluating its derivatives. Traditionally, only the first derivative is used due to its simplicity. Despite that, the feasibility of using higher-order terms has been studied in several works. However, to the best of the authors' knowledge, these terms cannot be feasibly calculated in dynamic problems.

From this procedure, the sensitivity analysis can be performed by differentiating the

objective function:

$$\alpha_e = \frac{\partial f(\mathbf{x})}{\partial x_e} = \left[\sum_{k=1}^{N_{\text{modes}}} \frac{1}{\left(\omega_k^2 - \omega_0^2\right)^2}\right]^{-\frac{3}{2}} \sum_{k=1}^{N_{\text{modes}}} \frac{1}{\left(\omega_k^2 - \omega_0^2\right)^3} \frac{\partial(\omega_k^2)}{\partial x_e} \tag{2.41}$$

where the term $\frac{\partial(\omega_k^2)}{\partial x_e}$ is the derivative of the eigenvalue, which can be obtained from the Rayleigh quotient (Haftka; Gürdal, 1993):

$$\omega_k^2 = \frac{\phi_k^T \mathbf{K}_g \phi_k}{\phi_k^T \mathbf{M}_g \phi_k} \tag{2.42}$$

With this expression, the derivative of the eigenvalue can be calculated as:

$$\frac{\partial(\omega_k^2)}{\partial x_e} = \phi_k^T \left(\frac{\partial \mathbf{K}_g}{\partial x_e} - \omega_k^2 \frac{\partial \mathbf{M}_g}{\partial x_e}\right) \phi_k \tag{2.43}$$

where the derivatives of the system matrices $\frac{\partial \mathbf{K}_g}{\partial x_e}$ and $\frac{\partial \mathbf{M}_g}{\partial x_e}$ are defined from the material interpolation scheme that will be presented shortly. Moreover, this expression assumes the normalization of the eigenvectors from Eq. (2.21).

From Eq. (2.41), the first term, despite being equal for all elements, is maintained due to its influence on the historical average procedure, which will be discussed in Section 2.2.5. The coefficient inside the second summation functions as a weighting factor for each mode. If the natural frequency ω_k is less than the operating frequency ω_0, this term is negative. Otherwise, if it is greater than the operating frequency, this term is positive. Finally, the closer it is to the operating frequency, the greater this coefficient, increasing the influence of the corresponding mode. Numerically, the natural frequencies are assumed different from the operating frequency.

To perform the differentiation of the system matrices, an interpolation scheme must be defined between both configurations $x_e = 1$ and $x_e = x_{\text{min}}$. In this chapter, as only two-material optimization problems are defined, only the interpolation scheme for this kind of system is presented. The density and Young's Modulus of a given element is defined as:

$$\rho(x_e) = (\rho_1 - \rho_2)x_e + \rho_2 \tag{2.44}$$

$$E(x_e) = (E_1 - E_2)x_e^p + E_2 \tag{2.45}$$

where E_1 and E_2 are the Young's modulus, and ρ_1 and ρ_2 are the density of the first and second materials. These materials are ordered so $E_1 > E_2$. The parameter p is the penalization exponent and is usually defined based on the Hashin-Shtrikman bounds (Hashin; Shtrikman, 1963). On discrete optimization formulations, such as the BESO, this is a heuristically defined parameter, whose value is chosen based on the user experience.

The derivatives of the mass and stiffness matrices with respect to the design variables are:

$$\frac{\partial \mathbf{M}_g}{\partial x_e} = \left(1 - \frac{\rho_2}{\rho_1}\right) \mathbf{M}_e^1 \tag{2.46}$$

$$\frac{\partial \mathbf{K}_g}{\partial x_e} = p x_e^{p-1} \left(1 - \frac{E_2}{E_1}\right) \mathbf{K}_e^1 \tag{2.47}$$

where $\mathbf{M}_e^1$ and $\mathbf{K}_e^1$ are the mass and stiffness matrices of the eth element, assuming it is made of material 1.

The sensitivity analysis was validated using the finite difference method, as shown in Appendix B.

2.2.3 Treatment of repeated eigenvalues

In some cases, an eigenvalue can have a geometric multiplicity higher than one, that is, multiple linearly independent eigenvectors can be attributed to a single eigenvalue. The main drawback when that happens is that the eigenvalues become indifferentiable in the traditional sense, meaning that Eq. (2.43) is no longer valid for those specific modes. Haug and Rousselet (1980) explain that while they are not Fréchet differentiable, they are Gateaux differentiable; that is, they have directional derivatives, but no gradient vector.

In this case, Seyranian *et al.* (1994) proposed a method to better estimate the directional derivative on a given topological change. That is, for the eth term of the sensitivity vector, the directional derivative on the direction of x_e is calculated. They propose applying an infinitesimal perturbation on the structural matrices and substituting it into the original eigenproblem (Eq. (2.17)). This results in another eigenproblem, indicated below:

$$(\mathbf{E} - \alpha_e \mathbf{I})\, \zeta = 0, \tag{2.48}$$

where α_e are the eigenvalues of this system, representing the eth term of the sensitivity component of the repeated modes. The vector ζ is the eigenvector of this system. Finally, $\mathbf{E}$ is a square matrix of $N_\mathrm{r} \times N_\mathrm{r}$, being N_r the multiplicity of the eigenvalue. This matrix is defined as:

$$\mathbf{E} = \begin{bmatrix} \phi_1^T \left(\frac{\partial \mathbf{K}_g}{\partial x_e} - \omega^2 \frac{\partial \mathbf{M}_g}{\partial x_e} \right) \phi_1 & \phi_1^T \left(\frac{\partial \mathbf{K}_g}{\partial x_e} - \omega^2 \frac{\partial \mathbf{M}_g}{\partial x_e} \right) \phi_2 & \cdots & \phi_1^T \left(\frac{\partial \mathbf{K}_g}{\partial x_e} - \omega^2 \frac{\partial \mathbf{M}_g}{\partial x_e} \right) \phi_{N_\mathrm{r}} \\ \phi_2^T \left(\frac{\partial \mathbf{K}_g}{\partial x_e} - \omega^2 \frac{\partial \mathbf{M}_g}{\partial x_e} \right) \phi_1 & \phi_2^T \left(\frac{\partial \mathbf{K}_g}{\partial x_e} - \omega^2 \frac{\partial \mathbf{M}_g}{\partial x_e} \right) \phi_2 & \cdots & \phi_2^T \left(\frac{\partial \mathbf{K}_g}{\partial x_e} - \omega^2 \frac{\partial \mathbf{M}_g}{\partial x_e} \right) \phi_{N_\mathrm{r}} \\ \vdots & \vdots & \ddots & \vdots \\ \phi_{N_\mathrm{r}}^T \left(\frac{\partial \mathbf{K}_g}{\partial x_e} - \omega^2 \frac{\partial \mathbf{M}_g}{\partial x_e} \right) \phi_1 & \phi_{N_\mathrm{r}}^T \left(\frac{\partial \mathbf{K}_g}{\partial x_e} - \omega^2 \frac{\partial \mathbf{M}_g}{\partial x_e} \right) \phi_2 & \cdots & \phi_{N_\mathrm{r}}^T \left(\frac{\partial \mathbf{K}_g}{\partial x_e} - \omega^2 \frac{\partial \mathbf{M}_g}{\partial x_e} \right) \phi_{N_\mathrm{r}} \end{bmatrix}, \tag{2.49}$$

where ω is the eigenvalue and $\phi_1, \phi_2, \cdots, \phi_{N_\mathrm{r}}$ is a set of $\mathbf{M}_g$-orthogonal eigenvectors.

For a set of repeated modes, we must solve the eigenproblem from Eq. (2.48), for each finite element. The eigenvalues of this problem represent the derivatives of the natural frequencies of the original problem. In the end, they are inserted into Eq. (2.41), alongside the sensitivities from the single natural frequencies.

2.2.4 Eigenvector tracking algorithm

As mentioned in Section 2.2.1, the mode-shifting problem is an important aspect to be considered during the optimization process. Additionally, local modes may appear during the evolution. These usually correspond to thin bars and disconnected regions in the domain. If a flexible or disconnected feature appears during an iteration, the algorithm would tend to add mass to it, instead of removing it, further increasing the problem. This phenomenon is particularly more critical in discrete optimization analyses, as sudden removal of bars or creation of isles of solid material are frequent. This is illustrated in Figure 2.3.

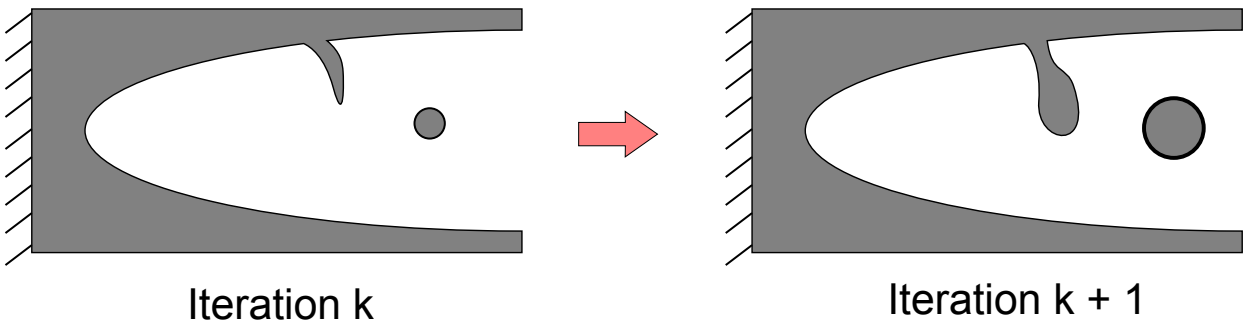

Figure 2.3 – Illustration of a topology optimization procedure adding mass to disconnected regions.

To avoid problems due to local modes and to ensure proper management of modes, an eigenvector tracking procedure is implemented. In the first iteration, the modes are calculated, sorted according to their eigenvalues, and saved. From then on, however, they are sorted based on their orthogonality with respect to the previous iteration. To this end, two possible algorithms can be used: the Normalized Cross Orthogonality (NCO) and the Modal Assurance Criterion (MAC) (Ewins, 2000). The NCO is based on checking the eigenvectors orthogonality between themselves. Despite its quick evaluation, it is not precise, as the eigenvectors are not necessarily orthogonal. To ensure correct sorting, the MAC is used. It functions similarly to the NCO; however, instead of evaluating the orthogonality of the eigenvectors, it verifies their $\mathbf{M}_g$-orthogonality.

At each iteration, the orthogonality of the eigenvectors is checked by performing the following procedure:

$$\mathbf{I}_{\text{MAC}} = \left| \mathbf{\Phi}_{(j-1)}^{T} \mathbf{M}_{g_{(j)}} \mathbf{\Phi}_{(j)} \right| \tag{2.50}$$

where the subscripts $(j-1)$ and j refer to the $(j-1)$th and jth iterations. $\mathbf{I}_{\text{MAC}}$ is the MAC matrix.

The previous equation can be used to sort eigenvectors by comparing them to Eq. (2.21). Assuming that, along with the iterations, the modes do not change significantly, the MAC matrix should remain close to an identity matrix with permuted columns. These permutations establish the ordering of the modes. The algorithm is defined in Algorithm 1.

With this algorithm, the modes from the current iteration are paired with the modes from the previous one. These paired modes are sorted according to the calculated permutation vector. Unpaired modes are treated as local modes and are not included in the objective function and sensitivity analysis. A parameter γ is defined to increase the number of calculated eigenpairs in the current iteration, ensuring a proper pairing.

2.2.5 Topology optimization algorithm

With all intermediary steps defined, the whole topology optimization algorithm can be described. The BESO method is a discrete topology optimization algorithm, based on successive updates of the domain in accordance with a sensitivity analysis. Due to being a discrete method, it allows for clear identification and definition of boundaries, which is especially im-

Input: γN_{modes} eigenvectors $\phi_{(j)}$ from current iteration, N_{modes} eigenvectors $\phi_{(j-1)}$ from previous iteration, $\mathbf{M}_{g_{(j)}}$ from current iteration
Calculate the MAC matrix: $\mathbf{I}_{\text{MAC}} = \left|\mathbf{\Phi}_{(j-1)}^{T}\mathbf{M}_{g_{(j)}}\mathbf{\Phi}_{(j)}\right|$
Create MAC permutation vector $\mathbf{p}_{\text{MAC}}$ with size $N_{\text{modes}} \times 1$
Create empty lists for rows and columns ($\mathbf{r}_{\text{MAC}}$ and $\mathbf{c}_{\text{MAC}}$)
Sort the MAC matrix in descending order and get the ordered indexes
$i = 0$
$j = 0$
while $i < N_{modes}$ **do**
  row = row of jth term from sorted $\mathbf{I}_{\text{MAC}}$
  $column$ = column of jth term from sorted $\mathbf{I}_{\text{MAC}}$
  if *row not in* $\mathbf{r}_{MAC}$ *and column not in* $\mathbf{c}_{MAC}$ **then**
    $\mathbf{p}_{\text{MAC}}(row) = column$
    Include row in $\mathbf{r}_{\text{MAC}}$
    Include $column$ in $\mathbf{c}_{\text{MAC}}$
    $i = i + 1$
    $j = j + 1$
  end
  else
    $j = j + 1$
  end
end
Output: Permutation indexes for current iteration $\mathbf{p}_{\text{MAC}}$

Algorithm 1: Eigenvector tracking algorithm

portant for fluid-structure formulations. Moreover, topologies from every iteration are a valid candidate for application, with little to no post-processing required.

The current implementation of the BESO is based on the formulation defined by (Huang; Xie, 2010). The BESO was programmed using Python and Cython (Behnel *et al.*, 2011). The algorithm is shown in Algorithm 2.

The BESO requires defining several parameters, some have already been presented, the others will be explained shortly. Regarding the interpolation scheme, the void design variable (x_{min}) and the penalization exponent (p) must be defined (Section 2.2.2). The variables N_{modes} is the number of calculated natural frequencies, which, as previously discussed, must be set by taking into account the contribution of each mode (Section 2.2.1). The final volume (V^*) is set by the user and is based on design constraints.

This implementation requires the application of a sensitivity filter. It is done after the sensitivity analysis and is used to avoid mesh dependency in the final topology and checkerboard patterns (Huang; Xie, 2007). This procedure is divided into two steps: averaging the elemental sensitivities into the nodes and averaging them back into the elements. The first step

Input: Define parameters: $x_{\min}$, p, ER, $\text{AR}_{\max}$, V^*, $r_{\min}$, τ, N, N_{modes}
Define boundary conditions and mesh
Start iteration counter: $j = 0$
Calculate eigenvalues and eigenvectors
while $\varepsilon < \tau$ ***or*** $V^{(j)} \neq V^*$ **do**
  $j = j + 1$
  Evaluate sensitivities $\alpha_e^{(j)}$ (Eq. (2.41))
  Filter sensitivities (Eqs. 2.51 and 2.52)
  Perform historical average (Eqs. 2.53)
  BESO update (Algorithm 3)
  Calculate eigenvalues and eigenvectors (Eq. (2.17))
  Perform eigenvector tracking (Algorithm 1)
  Calculate $\varepsilon = \dfrac{\left| \sum_{o=j-2N}^{j-N} f(x_e^{(o)}) - \sum_{o=j-N}^{j} f(x_e^{(o)}) \right|}{\sum_{o=j-N}^{j} f(x_e^{(j)})}$
end
Output: Optimized topology $x_e^{(j)}$

Algorithm 2: BESO topology optimization algorithm

is defined as:

$$\alpha_n^{(nd)} = \sum_{e=1}^{N_{\text{el}n}} \frac{1}{N_{\text{el}n} - 1} \left(1 - \frac{r_{en}}{\sum_{e=1}^{N_{\text{el}n}} r_{en}} \right) \alpha_e \tag{2.51}$$

where $N_{\text{el}n}$ is the number of elements that have the node n. The value r_{en} is the distance between the center of the eth element and the nth node, and α_e is the elemental sensitivity calculated in Eq. (2.41). If $N_{\text{el}n}$ is equal to 1, then $\alpha_n^{(nd)}$ is defined as equal to α_e.

The nodal sensitivities are averaged back into the elements as follows:

$$\alpha_e = \frac{\sum_{n=1}^{N_{\text{nd}}} \max(0, r_{\min} - r_{en}) \alpha_n^{(nd)}}{\sum_{n=1}^{N_{\text{nd}}} \max(0, r_{\min} - r_{en})} \tag{2.52}$$

where N_{nd} is the total number of nodes. The parameter $r_{\min}$ is the filter thickness (or radius).

Finally, these sensitivities are averaged with the ones from the previous iteration (unless the current iteration is the first one), performing what is known as the historical average of the sensitivities:

$$\alpha_e = \frac{\alpha_e^{(j)} + \alpha_e^{(j-1)}}{2} \tag{2.53}$$

The historical average is used as a stabilization process. This is needed as an element can change between solid and void, and therefore, its sensitivity might vary significantly between iterations, potentially destabilizing the procedure.

The update procedure is done based on these filtered and stabilized sensitivities. Elements are changed to x_{min} or to 1 according to the sorted sensitivities while also respecting the two parameters ER and AR_{max}. The Evolutionary Rate (ER) gives the volume change of each iteration while the current volume is different from the final one V^*. The maximum Addition Ratio AR_{max} defines the maximum number of elements added in the current iteration. Algorithm 3 shows how the update procedure is done.

Input: Filtered and stabilized sensitivities α_e, ER, AR_{max}, final volume V^*, current volume $V^{(j)}$
Estimate the next iteration volume: $V^{(j+1)} = V^{(j)}(1 - ER)$
if $V^{(j+1)} < V^*$ **then**
  $V^{(j+1)} = V^*$
end
Define number of solid elements n_{solid} required to obtain volume $V^{(j+1)}$
Sort elements according to α_e in descending order
Calculate AR by counting void elements with $e \leq n_{\text{solid}}$
if $AR > AR_{max}$ **then**
  Get number of added elements: $n_{\text{add}} = AR_{\text{max}} \cdot V^{(j+1)}$
  Get number of removed elements: $n_{\text{rem}} = n_{\text{add}} + ER \cdot (V^{(j+1)} - V^{(j)})$
  Turn the n_{add} void elements with the greatest α_e to solid
  Turn the n_{rem} solid elements with the smallest α_e to void
end
else
  $x_e = 1, \quad e \leq n_{\text{solid}}$
  $x_e = x_{\text{min}}, \quad e > n_{\text{solid}}$
end
Re-calculate $V^{(j+1)}$
Output: Updated topology $x_e^{(j)}$

Algorithm 3: BESO update procedure

2.2.6 Imposing periodicity constraint

Whenever periodic structures are desired, the method proposed by Zuo *et al.* (2011) is applied. It is based on constructing a list of elements that are equivalent for each periodic cell, as shown in Figure 2.4.

To ensure that every cell will be equal, the sensitivity of every corresponding element is changed by:

$$\alpha_e = \frac{\sum_{c=1}^{N_{\text{cell}}} \alpha_{ec}}{N_{\text{cell}}} \tag{2.54}$$

where e is the element numbering according to the cell, c is the cell number, and N_{cell} is the number of cells.

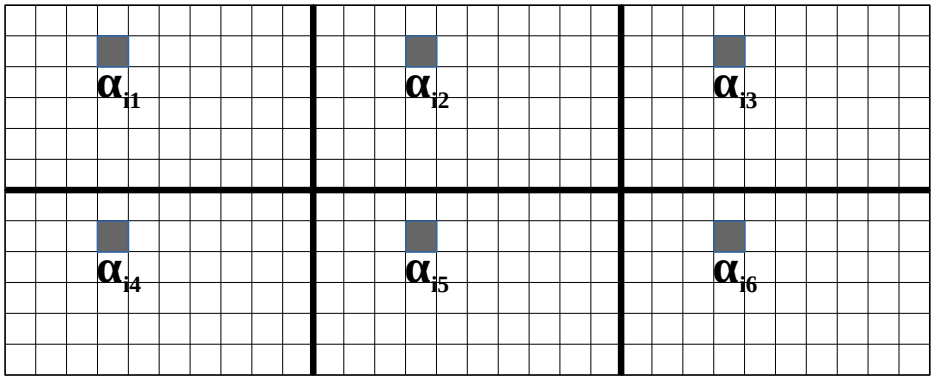

Figure 2.4 – Example of a periodic domain with 6 cells. Thick lines represent the edges of the cell, thin lines represent the elements. The highlighted elements are equivalent for each cell.

With these sensitivities, the update procedure can be done. Some important aspects to note are: this procedure must be the last one before updating the topology, these changes are not saved at the historical average of the sensitivities, and the number of removed/added elements must be divisible by the number of periodic cells.

2.3 Numerical results

This section presents the results from the analysis presented in this Chapter. The beam optimization results were published at *Structural and Multidisciplinary Optimization* (Lopes *et al.*, 2021), and the square domain was presented at the 14th World Congress on Computational Mechanics.

2.3.1 Optimization of a clamped-clamped beam

Initially, a clamped-clamped beam is studied. The domain comprises 400 x 40 bilinear quadrangular elements with equal size at the domain from Figure 2.5.

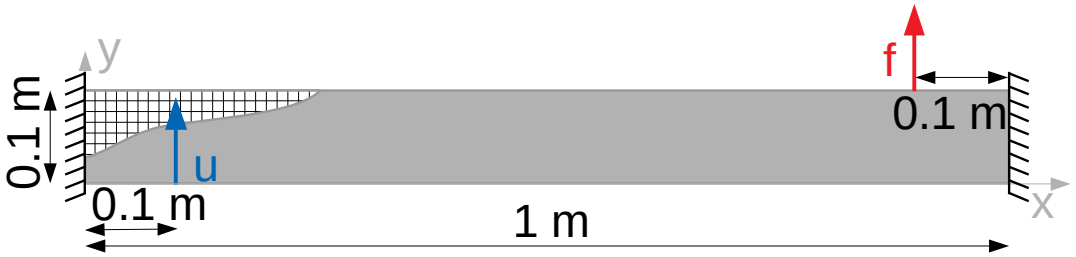

Figure 2.5 – Design domain for clamped beam optimization.

Material 1 is a steel with Young's Modulus $E_1 = 210$ GPa, density of $\rho_1 =$

7800kg/m^3 and Poison's ratio of $\nu_1 = 0.3$. Material 2 is a hypothetical material with $E_2 = 21$ GPa, $\rho_2 = 780$kg/m^3 and $\nu_2 = 0.3$. The properties of the second material were chosen as such to remove any effects due to changes in the stiffness-to-mass ratio between both materials.

The BESO parameters are: ER = 2%, AR$_{\text{max}}$ = 2%, final volume $V^* = 50\%$, $r_{\text{min}} = 10$ mm, penalty factor $p = 5$ and number of modes $N_{\text{modes}} = 40$. The operating frequency is set to 17 kHz, corresponding to a frequency between the 20$^{\text{th}}$ and 21$^{\text{st}}$ natural frequencies of the initial topology.

After 44 iterations the optimization stops, resulting in the topology from Figure 2.6a.

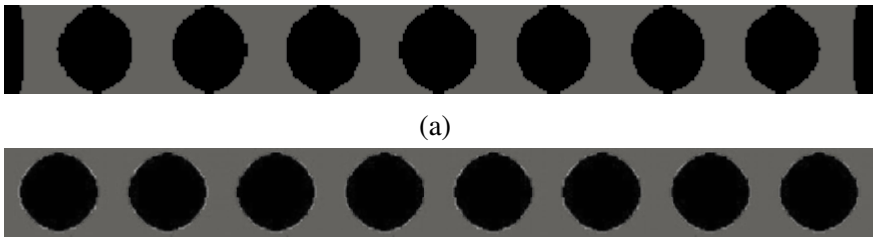

(a)

(b)

Figure 2.6 – Optimized topologies (a) without periodicity constraint (b) with periodicity constraint.

Though no periodicity constraint is imposed, the procedure obtained at a quasi-periodic configuration, resembling a phononic crystal. The main deviation from actual periodicity is the mass concentrations at the clamped boundaries.

To analyze the optimization process, the evolution of natural frequencies is shown in Figure 2.7.

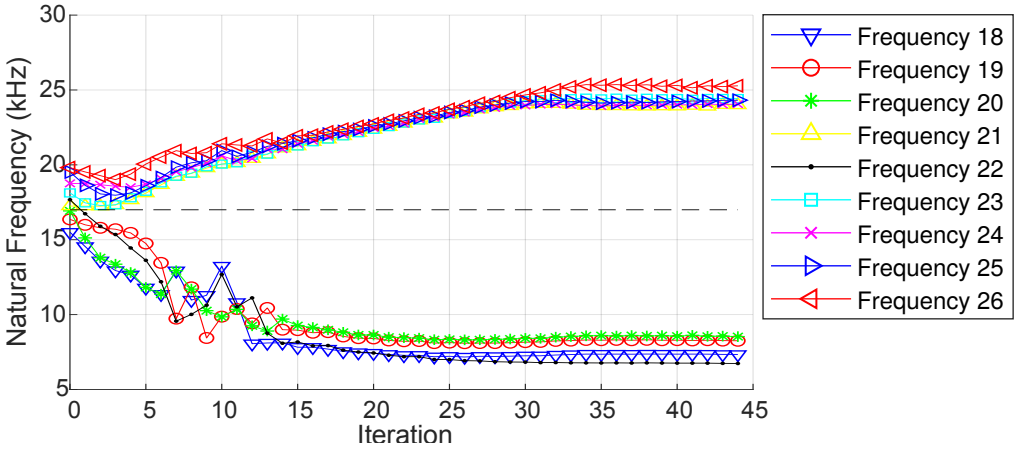

Figure 2.7 – Evolution of the natural frequencies closest to 17 kHz for clamped beam case.

The resulting interval corresponds to 15.4 kHz between 8.6 kHz and 24.0 kHz. Here, we see that not prescribing which eigenvalues must be maximized and which must be minimized is essential for obtaining this kind of topology. For instance, natural frequency 22 starts at 17.7 kHz (greater than the operating frequency) and ends at 6.8 kHz (less than the operating frequency).

To perform a dispersion analysis, we need to obtain a single periodic cell that optimizes the topology. To that end, the optimization procedure is repeated, while imposing periodicity constraints. Based on the previous topology, the domain is divided into 8 identical cells. This result is presented in Figure 2.6b.

This topology is similar to the previous one, except for the clamped boundaries. In the previous result, there is a concentration of material 1 around this area, while in this one, it is absent. Additionally, there is a slight change to the dimensions of the periodic disk-like features.

Such as before, we study the frequency separation by visualizing the behavior of the natural frequencies (Figure 2.8). The separation was 15.8 kHz, between 9.4 kHz and 25.25 kHz. This separation is slightly greater than the one obtained before, indicating that the differences in the boundaries do not result in increases to it.

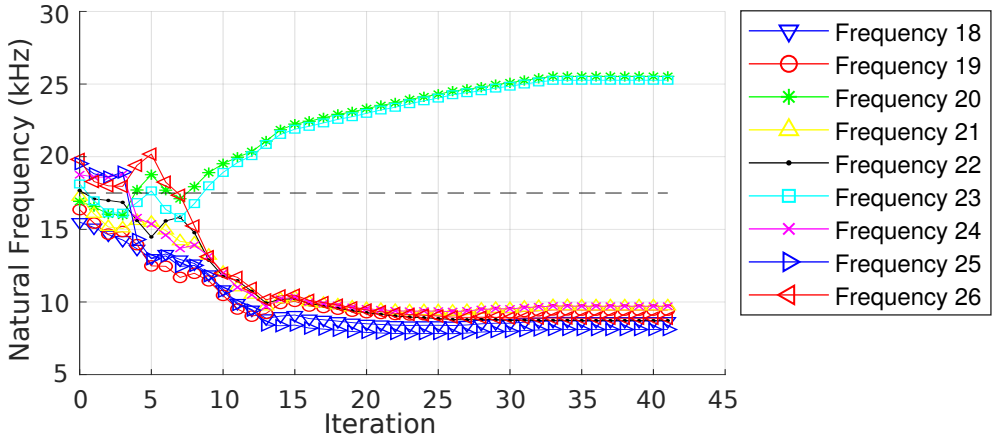

Figure 2.8 – Evolution of the closest natural frequencies to 17 kHz for the periodic optimization problem.

To compare both results, the Frequency Response Functions (FRFs) of both topologies are calculated and shown in Figure 2.9. The measurement and force application points are indicated in Figure 2.5.

As just mentioned, the difference between the lengths of the intervals is not notable. However, there is an observable offset between both of them. The interval from the non-periodic

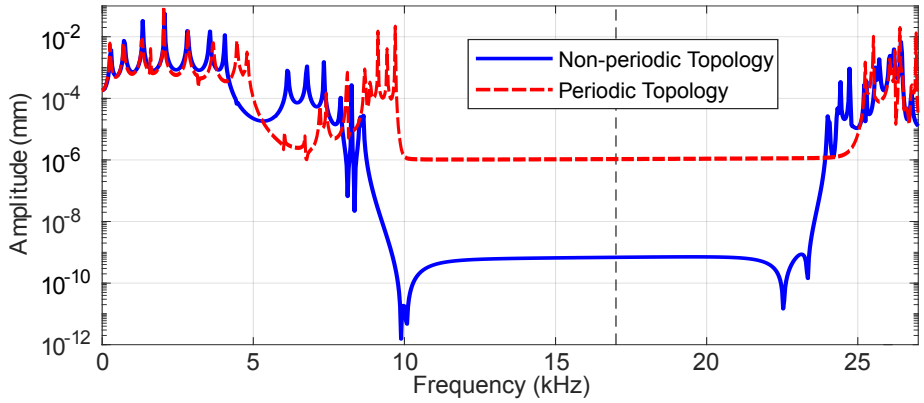

Figure 2.9 – Frequency response functions of the periodic and non-periodic optimized topologies on the 17 kHz optimization case.

optimization starts and ends at lower frequencies, while the periodic one starts and ends at higher frequencies.

With the cell obtained from the periodic optimization, a dispersion analysis is performed to better interpret the physical phenomenon behind this increased performance. Note that this topology, consisting of alternating stiff and flexible material is consistent with the literature of phononic band-gap optimization (Sigmund; Jensen, 2003). Assuming an infinite domain composed of this cell repeated indefinitely in the X and Y axes, Figure 2.10 shows the dispersion curve of this cell.

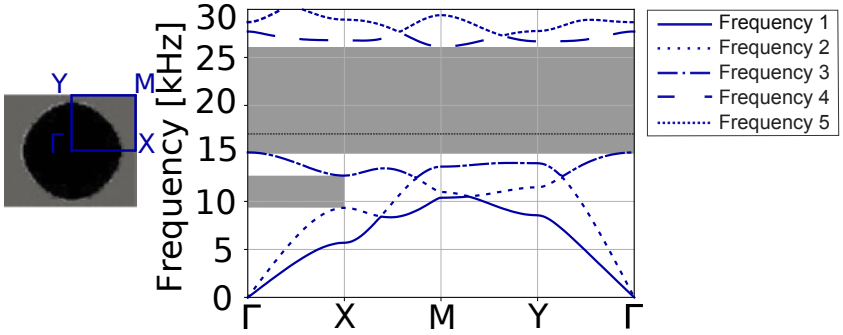

Figure 2.10 – Cell with edges of the first irreducible Brillouin zone and its dispersion curve. Band gaps are shown in gray.

This analysis shows a band gap on the interval spanning from 15.1 kHz to 26.1 kHz and a partial band gap on the x direction between 9.4kHz and 13.1 kHz. Interestingly, despite presenting wave modes between these band gaps and within the partial band gap interval, the structural response yielded no modes of vibration. This is due to the different hypotheses between wave propagation and vibration analyses.

Nonetheless, although performed exclusively on a structural scale, the topology op-

timization procedure produced results with characteristics commonly seen in band gap studies. That is, the optimized topology is composed of cells whose length is of the same order of magnitude as the wavelength of a wave with 17 kHz propagating through the material.

2.3.2 Optimization of a simply supported beam

Noting the material concentration on the final topology from Figure 2.6a around the clamped end, a second analysis is done to assess the influence of the boundary conditions. Here, both ends are supported as illustrated in Figure 2.11.

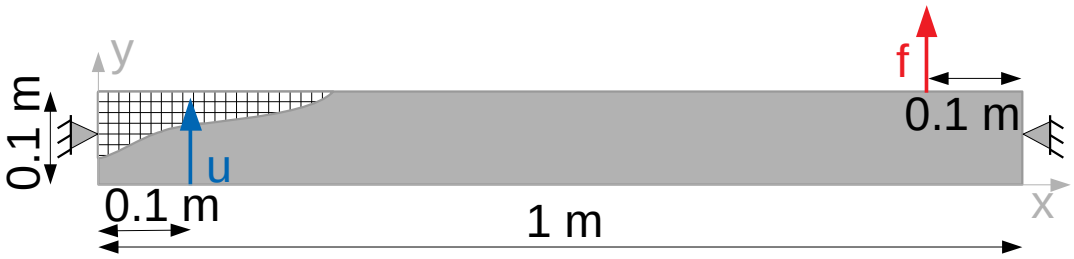

Figure 2.11 – Design domain for simply supported beam optimization.

The same optimization algorithm is run once again, keeping the same parameters as before. In the end, the topology from Figure 2.12a is obtained after 70 iterations.

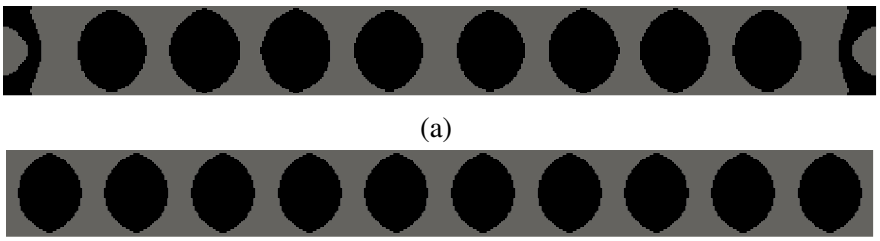

(a)

(b)

Figure 2.12 – Optimized topologies for supported case (a) without periodicity constraint (b) with periodicity constraint.

This topology is similar to the previously obtained one (Figure 2.6a), aside from two main differences. First, the number of stiff discs inside the topology is greater here, with eight discs instead of seven. Also, the optimizer left the region around the boundary conditions flexible, creating a stiff feature with a circular hole around the supports.

We can visualize the natural frequency evolution of the natural frequencies around 17 kHz in Figure 2.13. Here, the separation interval is 15.4 kHz, from 11.3 kHz to 26.7 kHz. Once again, the optimizer is able to open a wide separation around the operating frequency, granted it took it some additional iterations for that.

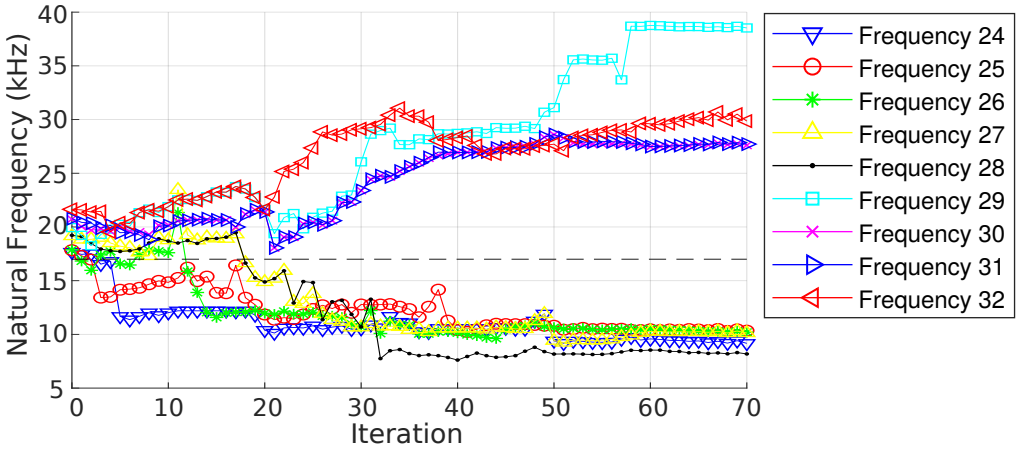

Figure 2.13 – Evolution of the natural frequencies closest to 17 kHz for simply supported beam case.

The same way that the previous study was repeated while imposing periodicity, this one is run while imposing 10 equal cells. Note that the number of cells is chosen by counting the features on the non-periodic topology (also counting the two irregular features). Figure 2.12b shows the final topology of this analysis.

The evolution of natural frequencies is shown in Figure 2.14. The natural frequency separation interval here is 16.6 kHz, from 10.5 kHz to 27.1 kHz. Note that, despite the additional constraint, the separation here is greater than the previous one. We should not draw any design conclusions, especially due to the high number of local minima that this problem possesses. However, this indicates that even if gains could be obtained by considering the boundary conditions, it would not lead to a significant increase.

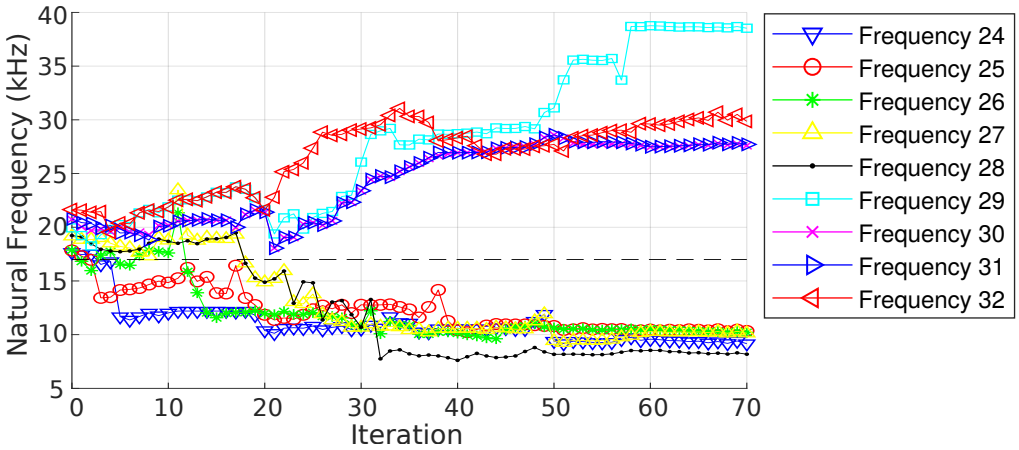

Figure 2.14 – Evolution of the natural frequencies closest to 17 kHz for simply supported periodic beam case.

Finally, given this low dependence on the boundary conditions, one could ponder

what would happen when comparing the results from the same topology but with different boundary conditions. For this end, the topology from the previous 8 cell periodic case (Figure 2.6b) is simulated under both clamped and simply supported boundary conditions. The FRFs from both cases are calculated and shown in Figure 2.15.

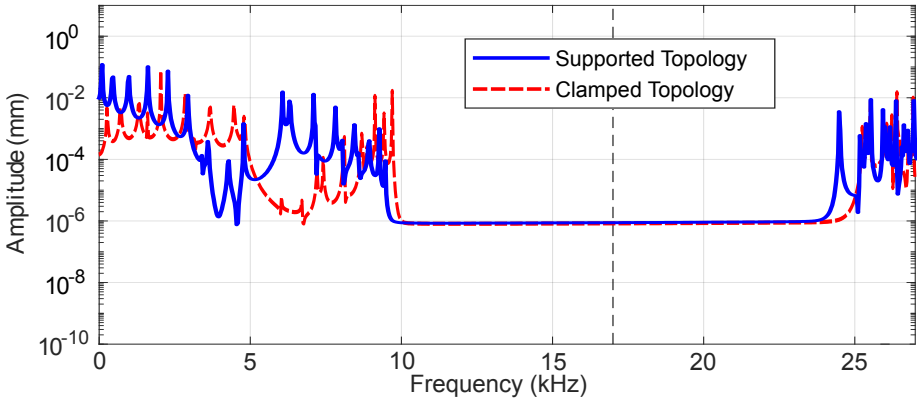

Figure 2.15 – Frequency response functions of 8-cell topology under supported and clamped boundary conditions.

Comparing both curves shows a very small difference when altering the boundary conditions. There is a small decrease on the start and end of the separation interval when applying supported boundary conditions, but it is minor, when compared to the total size of the interval.

In the end, the elements in the boundary condition regions have significant sensitivities, resulting in topologies with boundary condition dependent features. However, any change to the separation interval size is negligible when compared to the effects of the periodic components in the middle of the structure.

2.3.3 Optimization at a higher operating frequency

Now that an analysis involving the change of boundary conditions has been done, a study on the operating frequency is performed. For this end, the operating frequency is increased to 30 kHz. The domain is considered clamped, much like in Section 2.3.1. Every BESO parameter is kept the same as before, except for the number of modes, which is increased to $N_{\text{modes}} = 200$. This is due to the 200^{th} natural frequency being 63.8 kHz, more than double the operating frequency.

Running the optimization yields the topology from Figure 2.16a. Once again, it is a quasi-periodic topology. Note, however, how the periodic cell has significantly decreased when

compared to the previous cases. This is expected, as a higher frequency of vibration implies in the propagation of waves with lower wavelength. In this case, however, the optimized does not keep stiff material around the boundary condition, and seems to just ignore it.

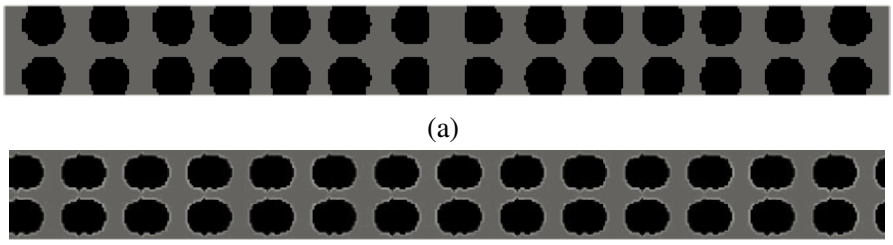

(a)

(b)

Figure 2.16 – Optimized topologies at 30 kHz (a) without periodicity constraint (b) with periodicity constraint.

The evolution of natural frequencies is shown in Figure 2.17. The natural frequency separation interval here is 22.3 kHz, between 20.9 kHz and 43.2 kHz. Note the more unstable evolution compared to the 17 kHz optimization cases. As the modes of vibration here tend to become periodic, they become increasingly more sensitive to single element topological changes; thus, this instability is seen. Finally, we can note that, in the end, the closest natural frequencies from 30 kHz start greater than 30 kHz, even those that end below this value. This is yet another indication of the importance of using Eq. (2.39) as the objective function, not imposing which natural frequencies to maximize or minimize.

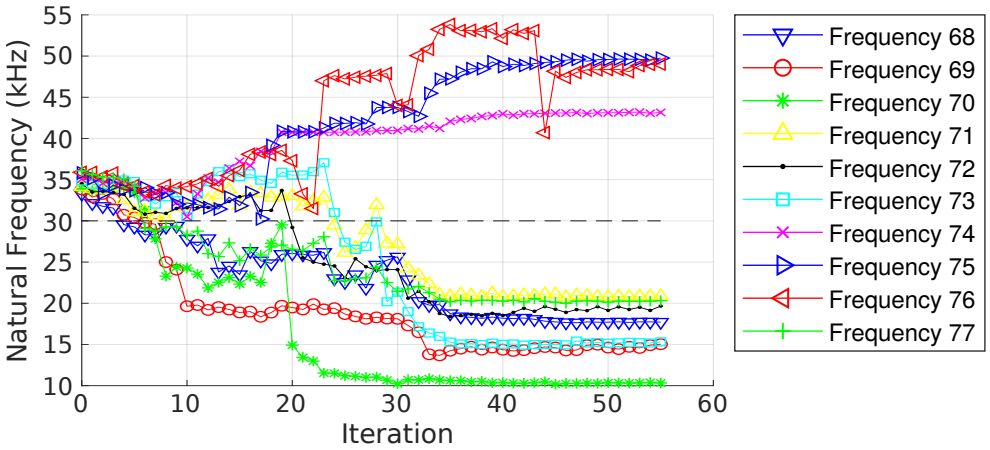

Figure 2.17 – Evolution of the natural frequencies closest to 30 kHz for the clamped beam case.

As before, this optimization is run once again, but while imposing a periodicity constraint. A grid of 14×2 cells is used here, in accordance to the topology from Figure 2.16a. In the end, the topology from Figure 2.16b is obtained. The cells here seem to be misaligned,

that is, instead of having their boundaries exclusively on soft material, it seems to break the stiff discs in two parts. This can be better visualized by looking at the boundaries of the structure.

Figure 2.18 shows the evolution of the natural frequencies. Compared to Figure 2.17, the interval here seems to be displaced to a higher frequency, from 24.3 kHz to 43.3 kHz, a total of 19 kHz.

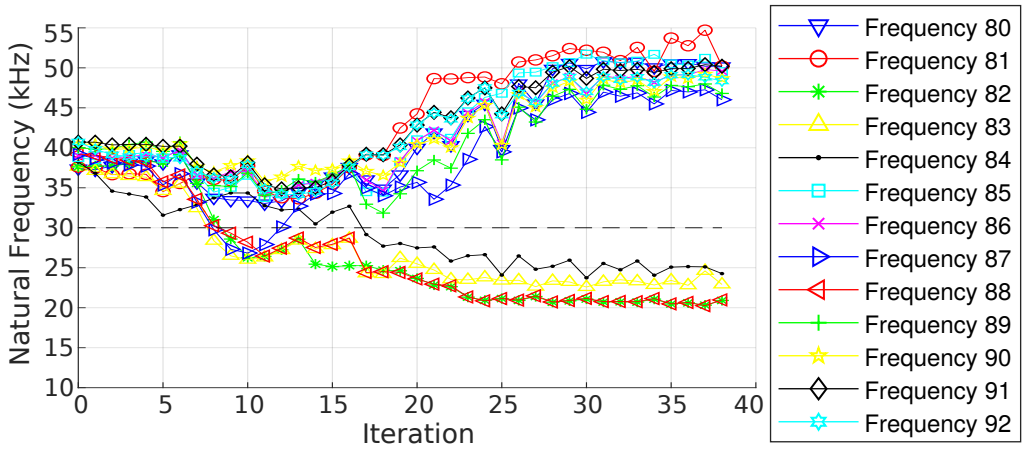

Figure 2.18 – Evolution of the natural frequencies closest to 30 kHz for the periodic clamped beam case.

Much like Section 2.3.1, this periodic cell is used to perform a dispersion analysis (Figure 2.19). A band gap is seen here from 26.2 kHz to 47.7 kHz, as well as a partial one from 17.1 kHz to 20.8 kHz. Once again, both the dispersion and the structural results had the same tendency, presenting, respectively, a band gap and a natural frequency separation around the same interval. Granted, some changes due to their different hypotheses were seen. However, both models seem to agree with each other.

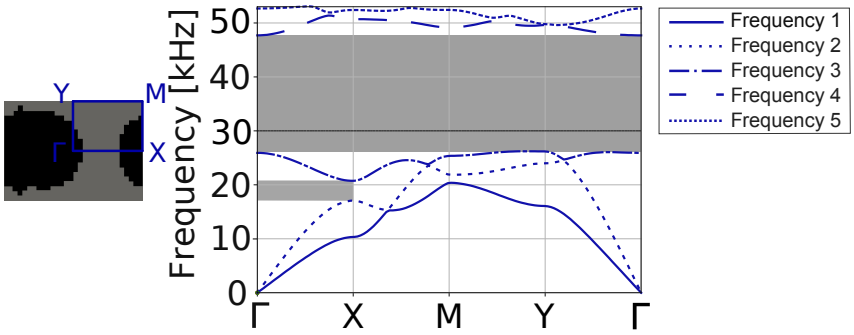

Figure 2.19 – Cell with edges of the first irreducible Brillouin zone and its dispersion curve. Band gaps are shown in gray.

2.3.4 Optimization of a frame domain

In the previous cases, the initial domain was a beam-like structure whose modes could be classified as longitudinal or transversal. In this current analysis, we are interested in a structure with no symmetries and whose modes can not be easily categorized. The proposed domain is shown in Figure 2.20, along with its degrees of freedoms for the FRFs.

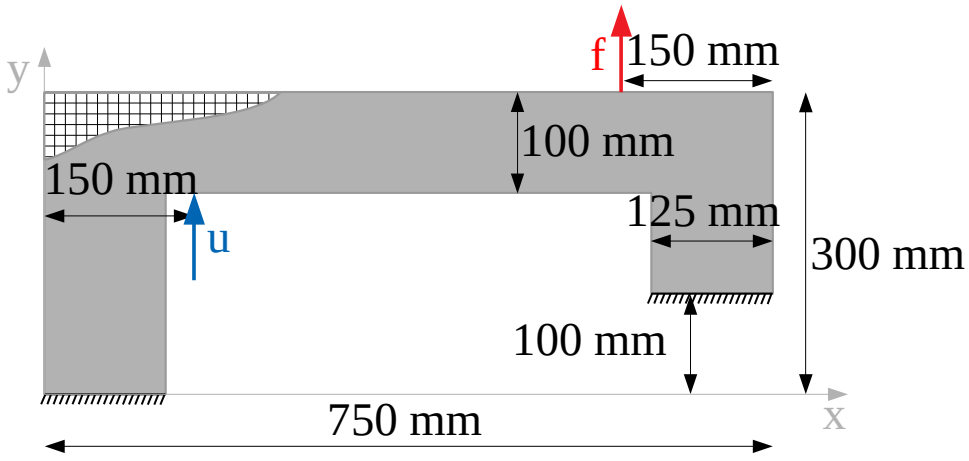

Figure 2.20 – Design domain for the frame topology optimization case.

As we are interested in a case where the optimized structure is comparable to those from Section 2.3.1, the operating frequency is maintained as 17 kHz. All other BESO parameters are kept unchanged.

The optimization study in this domain is performed without periodicity constraints and results in Figure 2.21a after 42 iterations.

Once again, the topology is quasi-periodic. While the features on the long horizontal part are mostly centered and equidistant, those on the edges are more offset from the center, connecting to the boundaries of the domain. This might be due to boundary effects, such as the reflection of waves from a horizontal direction to a vertical one and vice versa. Nonetheless, it is mainly composed of disks resembling those from Figure 2.6a.

The evolution of natural frequencies is shown in Figure 2.22. The separation span from 11.9 kHz to 24.3 kHz, a total of 12.4 kHz. Despite being less stable than the previous cases, the evolutionary procedure obtained a feasible topology that separates the natural frequencies.

Due to its similarity with the results from the preceding analysis, its cell is inserted in this domain to study how it would behave if it were periodic (Figure 2.21b). With both topologies, their FRFs can be compared (Figure 2.23).

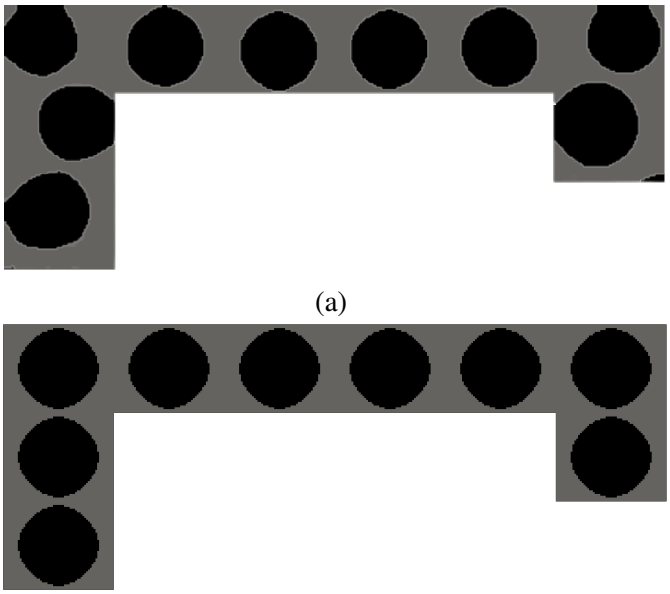

(a)

(b)

Figure 2.21 – Optimized topologies for frame domain (a) without periodicity constraint (b) inserting unit cells from Section 2.3.1.

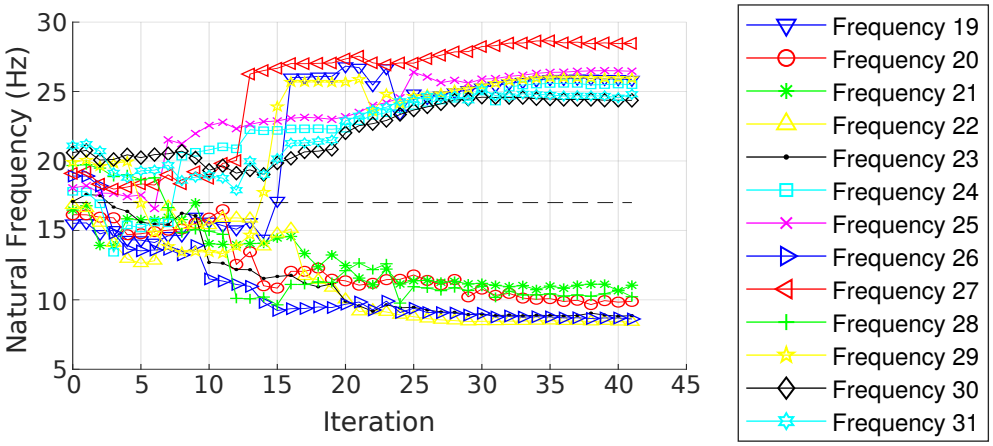

Figure 2.22 – Evolution of the closest natural frequencies to 17 kHz for the frame domain optimization problem.

Despite not being optimized for this case, the periodic structure presents a separation of 11.5 kHz, from 13.3 kHz to 24.8 kHz. This indicates that only assembling a cell with a band gap in this range is enough to obtain a satisfactory frequency separation in the structure. However, as the non-periodic topology provides a separation roughly 7.8 % greater than the periodic one, it indicates that the aforementioned changes to the placement of certain disks can increase the separation of the natural frequencies.

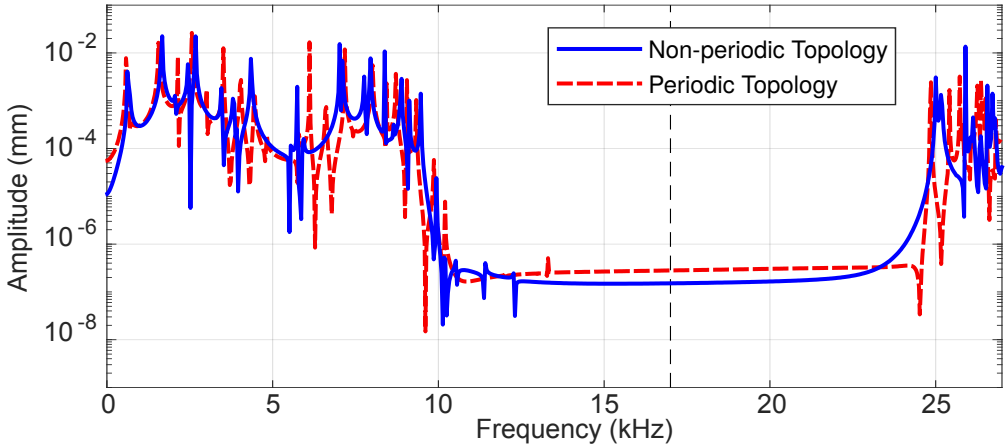

Figure 2.23 – Comparison between frequency responses for 17 kHz frame periodic and non-periodic domains.

2.3.5 Optimization with varying domain

For this analysis, the operating frequency is once again maintained at 17 kHz. The other BESO parameters are also unchanged. The domain, however, is defined with two changing dimensions L_x and L_y, as illustrated in Figure 2.24.

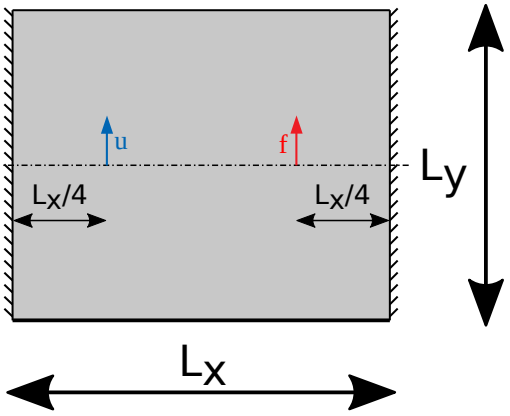

Figure 2.24 – Design domain for the varying topologies case.

All cases are composed of a mesh with quadrangular elements of 2 mm x 2 mm, and the number of elements is changed accordingly. The BESO parameters and the material parameters are kept the same from the previous two sections.

In total, six cases are optimized. Their dimensions are: 100 mm x 100 m, 200 mm x 100 m, 200 mm x 200 m, 400 mm x 100 m, 400 mm x 200 m and 400 mm x 400 m. The resulting topology for each case is shown in Figure 2.25.

A glance at these topologies shows that the periodic pattern previously observed in Sections 2.3.1 and 2.3.4 appear here once again. Also, these topologies are not strictly periodic,

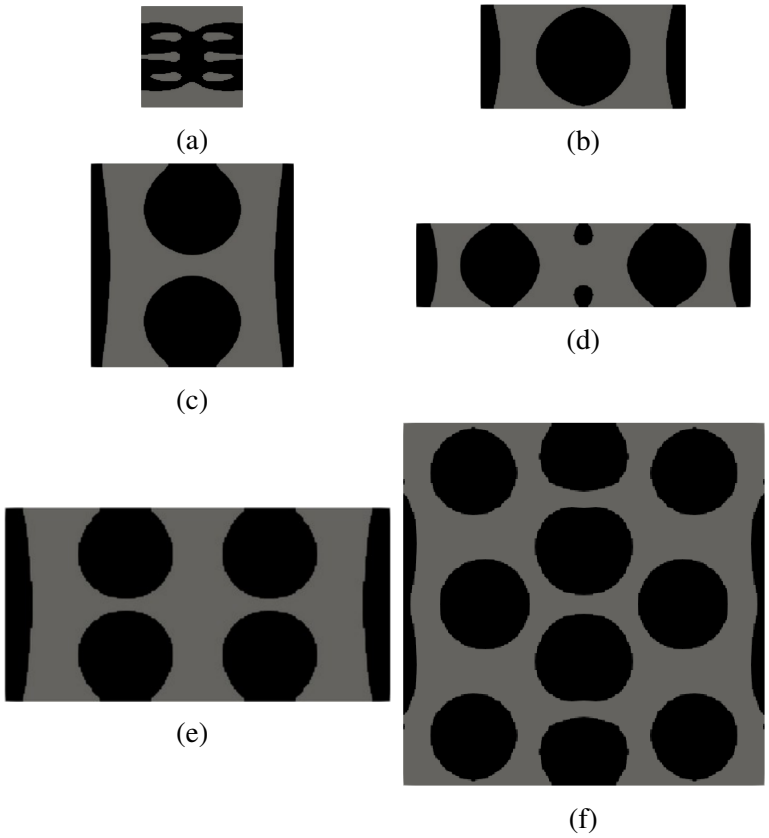

Figure 2.25 – Optimized topologies for clamped domain with (a) 100 x 100 mm^2, (b) 200 x 100 mm^2, (c) 200 x 200 mm^2, (d) 400 x 100 mm^2, (e) 400 x 200 mm^2 and (f) 400 x 400 mm^2.

as the position and number of cells change. Given the dimensions of case f, one would expect a 4x4 grid of cells, but instead, there are two columns with 3 cells separated by a column with 4 cells. Additionally, two tiny disks appear between both cells in case d. Finally, case a differs significantly from the other ones, resulting in a connected structure instead of disconnected cells. All topologies have reinforced the area around the boundary conditions. For further analysis, the FRFs for all optimized topologies are calculated in Figure 2.26.

We see an increase in the frequency separation for all cases, being more significant for larger domains. In these cases, we see that the quasi-periodic disk distribution is once again an optimal configuration, similar to the previous section (Figure 2.10). As the dimensions are increased, the natural frequencies are reduced, and thus, the number of natural frequencies below and around the operating frequency drastically raises.

Despite increasing the number of relevant modes in the objective function, the obtained frequency separation is large. When larger domains are involved, the effects that dictate the band gap phenomenon for periodic structures become more relevant. Thus, the final

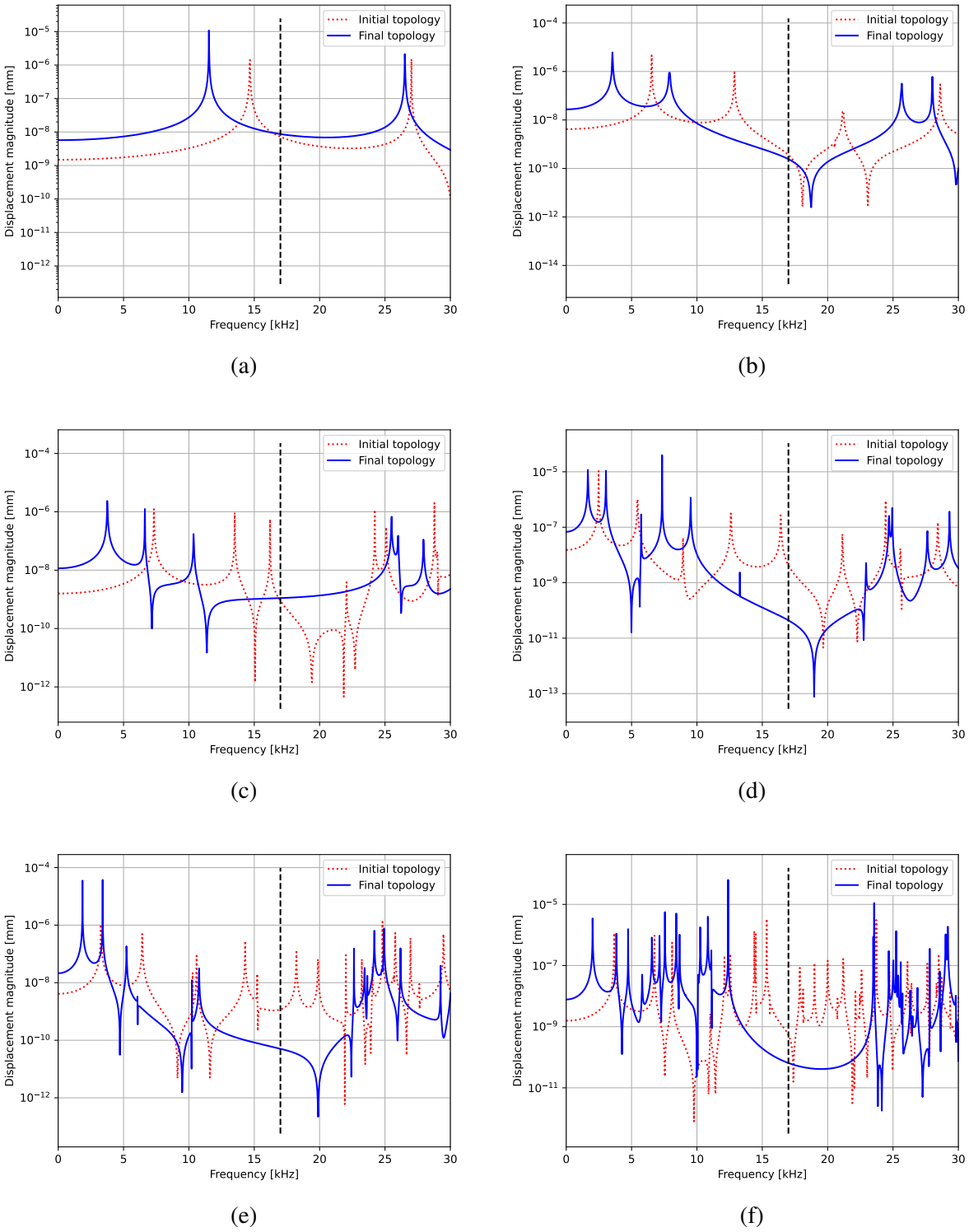

Figure 2.26 – FRFs of initial and final topologies for clamped domain with (a) 100 x 100 mm^2, (b) 200 x 100 mm^2, (c) 200 x 200 mm^2, (d) 400 x 100 mm^2, (e) 400 x 200 mm^2 and (f) 400 x 400 mm^2.

topologies only add disks and redistribute them. For smaller domains, such as the first one, the structural vibration phenomenon is more important, and thus, the topology tends to a beam-like

structure connected at both ends.

2.3.6 Optimization of a 3D clamped-clamped beam

Finally, a clamped-clamped domain, similar to that of Section 2.3.1, is studied. The domain is illustrated in Figure 2.27. It is discretized in a mesh of 100 x 10 x 10 hexahedric finite elements.

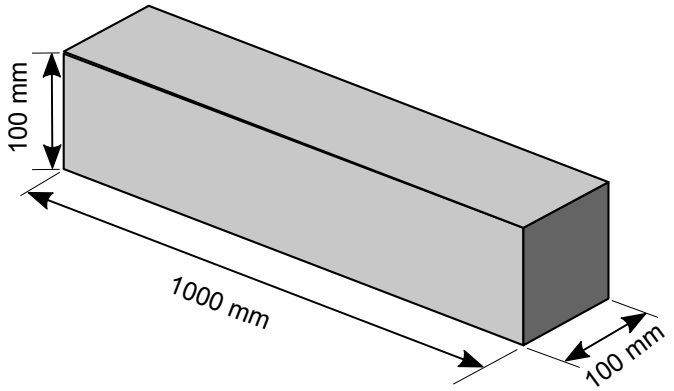

Figure 2.27 – Design domain for 3D clamped-clamped beam optimization.

The optimization is, once again, defined as the maximization of the natural frequency separation around 17 kHz. Most BESO parameters and material properties are the same from Section 2.3.1: ER = 2%, AR_{max} = 2%, $r_{min} = 10$ mm, $p = 5$, $E_1 = 210$ GPa, $E_2 = 21$ GPa, $\rho_1 = 7800$kg/m^3, $\rho_2 = 780$kg/m^3, and $\nu_1 = \nu_2 = 0.3$. The final volume is reduced to $V^* = 40\%$, and the number of calculated modes is $N_{modes} = 80$.

The final topology is shown in Figure 2.28. Once again, a quasi-periodic pattern emerges during the optimization. Furthermore, it is very similar to that from Figure 2.6a, even sharing the same number of stiff material concentration. Still, they are not all equal here, not even being the same geometric shape. Some of them are roughly spheres, while others seem closer to cuboids with a square hole.

The performance of this structure, compared to the full topology, can be seen in Figure 2.29. Once again, a clear natural frequency separation can be seen here, when comparing the initial and the optimized topologies. This shows, not only that this methodology is able to obtain this kind of frequency separation in 3D, where additional modes appear, such as torsional modes; but also that the quasi-periodic pattern obtained in 2D optimization is also optimal in 3D.

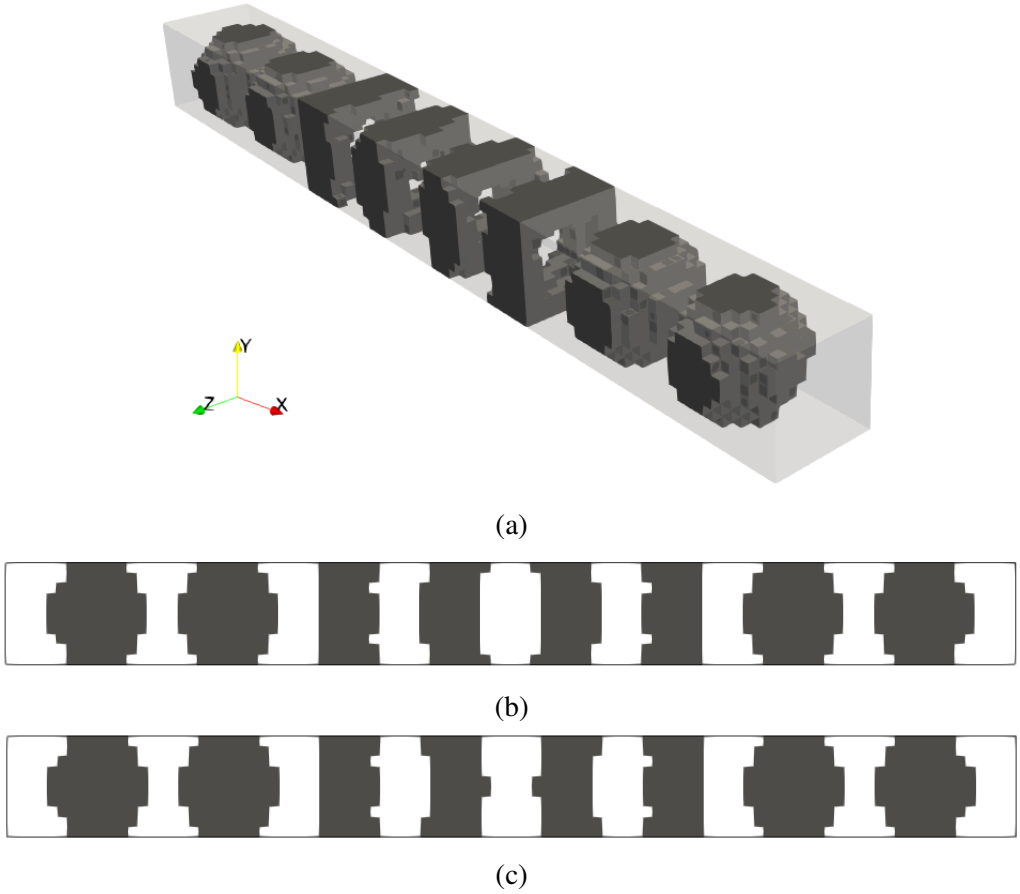

(a)

(b)

(c)

Figure 2.28 – Final topology of 3D clamped-clamped beam optimization (a) 3D view (b) view from x-y plane (c) view from x-z plane.

2.4 Conclusions

In this chapter, a topology optimization procedure to maximize the natural frequency separation of two-material structures was presented. In these cases, mode-shifting is an important problem, which is solved by using an objective function that takes into account several modes and by using an eigenvector tracking procedure. Although more critical in one material and void, local modes can also be a nuisance in the two-material optimization of natural frequencies. The eigenvector tracking procedure also helped to confront this challenge.

To illustrate the functioning of this method, distinct domains were optimized using the same parameters. In all cases, the non-periodic optimization study resulted in similar topologies composed of a quasi-periodic pattern. This pattern was shown to result in the band gap phenomenon when infinitely repeated. Therefore, despite not strictly following the infinitely periodic hypothesis required for the dispersion study, an optimal topology obtained from such cases still improves the desired natural frequency separation. Then, when we change

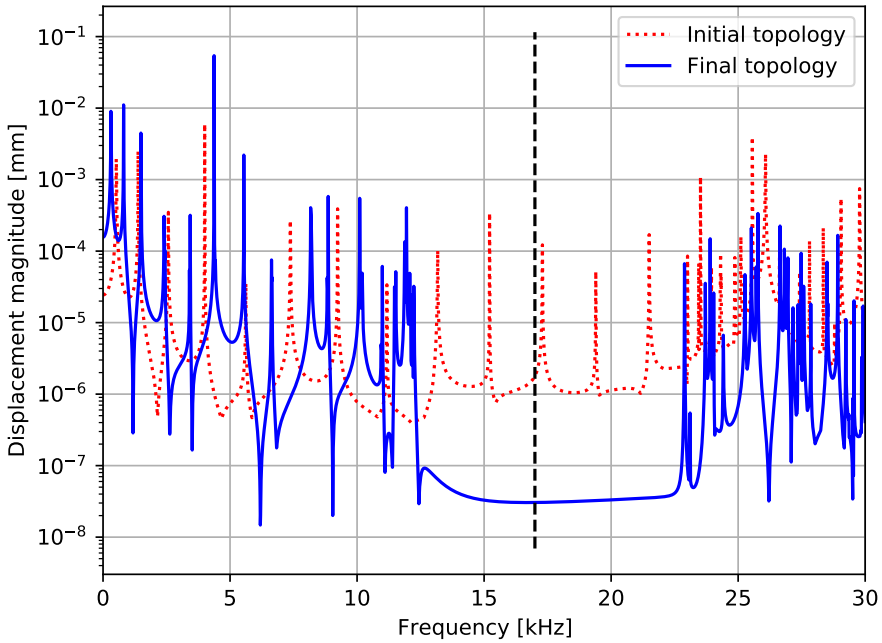

Figure 2.29 – Frequency response function for 3D clamped-clamped beam optimization.

boundary conditions, different topologies may be obtained, especially around the boundaries. Nevertheless, very little quantitative difference is seen on the separation interval.

Finally, a 3D optimization case was presented, illustrating the behavior of this type of problem when this dimension is added.

3 TOPOLOGY OPTIMIZATION WITH CONNECTIVITY CONSTRAINT

As seen in Chapter 2, optimization results from frequency separation problems are usually periodic with alternating stiff and flexible materials. As such, when we try to perform a topology optimization which admits void elements, it results in disconnected topologies. This chapter presents a methodology for maintaining connectivity based on a heat conduction problem. This contribution was published at *Mechanical Systems and Signal Processing* (Lopes *et al.*, 2022b) and presented at (Lopes *et al.*, 2022a). This section was done in collaboration with Prof. Jarir Mahfoud from INSA Lyon, in France.

3.1 Virtual Flux Method

In this section, the Virtual Flux Method (VFM) will be described. Initially, a method for measuring the connectivity of a point is described. Then, it is used to define an elemental connectivity parameter. Finally, an update procedure for the BESO is defined. Alternatively, an approach that reuses the factorization from the optimization is presented.

3.1.1 Point-wise measure of connectivity

The VFM is a method that operates in two steps: first, it measures the importance of each element in keeping the connectivity between two regions; then, it updates their sensitivities to prevent them from turning to void. To measure which regions are essential for the maintenance of connectivity, an analogy to the heat conduction problem is used (Figure 3.1).

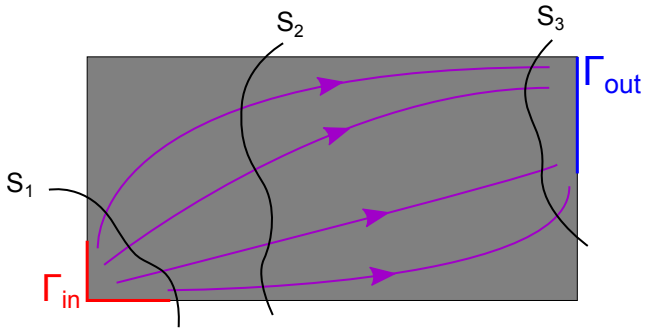

Figure 3.1 – Domain with heat flux flowing between an input surface Γ_{in} and an output surface Γ_{out}.

The main considerations are: solid regions are thermally conductive while void ones are insulators, and a unitary transfer rate enters the domain through a subdomain Γ_{in} and exits through another one Γ_{out}. Under these conditions, at every section that divides Γ_{in} and Γ_{out} (such as S_1, S_2 and S_3), a unitary heat flux must pass. This way, the thinner the bars that connect these two regions are, the greater the heat flux per unit area must be in these sections. Therefore, this formulation measures the importance of a region for connectivity. To compute this heat flux, the following heat conduction system is solved:

$$\begin{aligned} \nabla \cdot (k(\mathbf{r})\, \nabla T(\mathbf{r})) &= -q_{\text{V}}(\mathbf{r}) \quad &&, \text{for } \mathbf{r} \in \Omega \\ \nabla T(\mathbf{r}) \cdot \mathbf{n}(\mathbf{r}) &= 0 &&, \text{for } \mathbf{r} \in \partial\Omega, \end{aligned} \tag{3.1}$$

where $T(\mathbf{r})$ is the temperature field in a spatial point $\mathbf{r}$, $\mathbf{n}(\mathbf{r})$ is the unit normal vector to the boundary surfaces, the conductivity $k(\mathbf{r})$ is adopted as either 1, for solid regions, or x_{min} for void ones. The volumetric heat source $q_V(\mathbf{r})$ is defined as:

$$\begin{gathered} q_V(\mathbf{r}) = 0, \text{ for } \mathbf{r} \in \Omega / (\Gamma_{\text{in}} \cup \Gamma_{\text{out}}) \\ \int_{\Gamma_{\text{in}}} q_V(\mathbf{r})\, dV = 1 \\ \int_{\Gamma_{\text{out}}} q_V(\mathbf{r})\, dV = -1, \end{gathered} \tag{3.2}$$

This definition ensures that the total energy that enters and exits the system is equal to 1 W. Furthermore, it can only do it through the subdomains Γ_{in} and Γ_{out}.

For any section S that divides the system in such a way that both Γ_{in} and Γ_{out} are fully in each one of them, the following equilibrium must hold true:

$$\int_S \mathbf{q}''(\mathbf{r}) \cdot \mathbf{n}(\mathbf{r})\, dA = \int_{S_s} \mathbf{q}''(\mathbf{r}) \cdot \mathbf{n}(\mathbf{r})\, dA + \int_{S_v} \mathbf{q}''(\mathbf{r}) \cdot \mathbf{n}(\mathbf{r})\, dA = 1, \tag{3.3}$$

where $\mathbf{q}''(\mathbf{r})$ is the heat flux per unit area, which is obtained with Fourier's law.

Which, in turn, can be rewritten as:

$$A_s\, m_s + A_v\, m_v = 1, \tag{3.4}$$

where A_s and m_s are the surface of area of the section and the mean value of $\mathbf{q}''(\mathbf{r}) \cdot \mathbf{n}(\mathbf{r})$ within the solid domain, and A_v and m_v are the same but for the void domain.

Assuming that the conductivity of void elements is small enough so that any flux flowing through them is negligible, the following expression can be obtained:

$$m_s = \frac{1}{A_s}. \tag{3.5}$$

One could use the surface area A_s as a measure of connectivity; but, to avoid divisions by zero in void elements, the inverse measure m_s is adopted instead.

To measure the connectivity of a point $\mathbf{r}^*$, two hypotheses are applied: the mean value m_s can be approximated as its value evaluated at $\mathbf{r}^*$, and the surface S is normal to $\mathbf{q}''(\mathbf{r}^*)$. This last hypothesis can be interpreted as the surface S tending towards the isothermal plane that passes through $\mathbf{r}^*$ in its close neighborhood. With those hypotheses, then:

$$m_s(\mathbf{r}^*) = \frac{1}{A_s}\int_{S_s} \mathbf{q}''(\mathbf{r})\cdot\mathbf{n}(\mathbf{r})\,dA \approx \mathbf{q}''(\mathbf{r}^*)\cdot\mathbf{n}(\mathbf{r}^*) = \mathbf{q}''(\mathbf{r}^*)\cdot\frac{\mathbf{q}''(\mathbf{r}^*)}{\|\mathbf{q}''(\mathbf{r}^*)\|} = \|\mathbf{q}''(\mathbf{r}^*)\|. \tag{3.6}$$

These hypotheses may cause an overestimation or an underestimation of the mean value. Although undesirable, an underestimation is still acceptable when the main goal is preventing disconnection. However, one of the main advantages of the thermal conduction problem is that, whenever a component gets thinner, the flux not only increases in all points, but also tends to become uniform. Conveniently, those are the critical parts of the domain where the connectivity constraint should be activated.

3.1.2 Elemental connectivity measure

With a general connectivity measure, we can define an elemental value by calculating its mean along the element domain. For a given element e with volume V_e, a parametric extensive inverse measure of connectivity can be defined as:

$$q_e = \left[\tfrac{1}{V_e}\int_{\Omega_e} \|\boldsymbol{q}''(\boldsymbol{r})\|^m\,dV\right]^{\frac{1}{m}},\ m\in\mathbb{R}^*_+, \tag{3.7}$$

where the previous expression describes the generalized mean of the function $\|\boldsymbol{q}''(\boldsymbol{r})\|$ over the domain of the element. The parameter m sets the degree of the mean. In the case where $m\to\infty$, the mean becomes the maximum operator. The other case used in this thesis corresponds to when $m=2$. These two special cases are convenient for bilinear square elements, as $m=2$ can be integrated analytically, and $m\to\infty$ can be calculated by evaluating the heat flux at the four nodes of the element. These properties are presented in Appendix C.

To apply the connectivity constraint in the BESO, two parameters must be defined. The first one is the limit area A_{lim}, representing the minimum admissible area. The second one comes from the fact that the BESO is a discrete optimization method; as such, to make the constraint activate softly, an activation area $A_{\text{act}} \geq A_{\text{lim}}$ is also defined. With both parameters, and based on Eq. (3.5), the following inverse activation parameters can be defined:

$$q_{\text{act}} = \frac{1}{A_{\text{act}}}, \tag{3.8}$$

$$q_{\text{lim}} = \frac{1}{A_{\text{lim}}}. \tag{3.9}$$

On two-dimensional problems, since one of the dimensions that compose this area is the out of plane thickness, both areas will be referred as widths. This way, an activation parameter can be defined as a polynomial activation function:

$$c_e = \begin{cases} 0 & , \; q_e \leq q_{\text{act}} \\ \left(\frac{q_e - q_{\text{act}}}{q_{\text{lim}} - q_{\text{act}}}\right)^s & , \; q_{\text{act}} < q_e < q_{\text{lim}} \\ 1 & , \; q_e \geq q_{\text{lim}}, \end{cases} \tag{3.10}$$

where s is an exponent which determines the degree of the activation.

With this parameter, we can define the degree in which the method is activated for each element. If it is close to 1, then the element is necessary to maintain the desired connectivity. If it is between 0 and 1, then it is not yet indispensable, but it is still important for this connectivity and some consideration has to be done. If it is 0, then there are no connectivity issues in this region, and it can be continued to be treated normally by the optimizer. This activation parameter is used in the sensitivity update, shown in Section 3.1.5; but before that, some more details on the finite element formulation of this problem are shown.

With this method, we can measure the connectivity between to subdomains Γ_{out} and Γ_{in}. Nonetheless, it can be applied in a more general setting, maintaining multiple connectivity constraints active. For a set of N_{con} desired imposed connectivities, there is a set of subdomain pairs $\left\{\left(\Gamma_{\text{in}}^{[1]}, \Gamma_{\text{out}}^{[1]}\right), \left(\Gamma_{\text{in}}^{[2]}, \Gamma_{\text{out}}^{[2]}\right), ..., \left(\Gamma_{\text{in}}^{[N_{\text{con}}]}, \Gamma_{\text{out}}^{[N_{\text{con}}]}\right)\right\}$, each with their own limit area $(A_{\text{lim}}^{[1]}, A_{\text{lim}}^{[2]}, ..., A_{\text{lim}}^{[N_{\text{con}}]})$ and activation area $(A_{\text{act}}^{[1]}, A_{\text{act}}^{[2]}, ..., A_{\text{act}}^{[N_{\text{con}}]})$. We can define a total activation parameter with the maximum operator:

$$c_e = \max\left(c_e^1, c_e^2, ..., c_e^{N_{\text{con}}}\right), \tag{3.11}$$

where each of the $c_e^{N_{\text{con}}}$ is calculated from Eq. (3.10) for each set of imposed connectivity.

By using this total activation parameter, we guarantee that every connectivity is observed on every element.

3.1.3 Finite Element formulation of the Virtual Flux Method

Starting from the system from Eq. (3.1), we can apply the FEM similarly to the procedure from in Section 2.1.1, leading to the following equation:

$$\mathbf{R}_g \mathbf{t} = \mathbf{q}_{\mathbf{h}g} \tag{3.12}$$

where $\mathbf{R}_g$ is the global thermal conductivity matrix, $\mathbf{q}_{\mathbf{h}g}$ is the global thermal heat flux vector, and $\mathbf{t}$ is the nodal temperature vector. This vector is given by:

$$T(\mathbf{r}) \approx \mathbf{N_t} \mathbf{t} \tag{3.13}$$

where $\mathbf{N_t}$ is the matrix of shape functions for the heat conduction problem, which, for a 4-node isoparametric quadrilateral element is given by:

$$\mathbf{N}_t = \begin{bmatrix} N_1 & N_2 & N_3 & N_4 \end{bmatrix} \tag{3.14}$$

The global matrix $\mathbf{R}_g$ is assembled from elemental ones:

$$\mathbf{R}_e = k_e \int_{\Omega_e} \mathbf{B_t}^T \mathbf{B_t} d\Omega \tag{3.15}$$

where k_e is the thermal conductivity of element e and is assumed constant and equal to x_e. The matrix of the derivatives of the shape functions $\mathbf{B_t}$ is defined as:

$$\mathbf{B}_t = \begin{bmatrix} \frac{\partial N_1}{\partial x} & \frac{\partial N_2}{\partial x} & \frac{\partial N_3}{\partial x} & \frac{\partial N_4}{\partial x} \\ \frac{\partial N_1}{\partial y} & \frac{\partial N_2}{\partial y} & \frac{\partial N_3}{\partial y} & \frac{\partial N_4}{\partial y} \end{bmatrix} \tag{3.16}$$

This system, however, has two main problems. It lacks Dirichlet boundary conditions, so the stiffness matrix is non-invertible. There is also a difficulty in defining the heat flux vector $\mathbf{q}_{\mathbf{h}g}$, as the total heat flux must be equal to 1 W. To solve this problem, two nodes are added to the domain, and each is connected to every node of each surface (Figure 3.2).

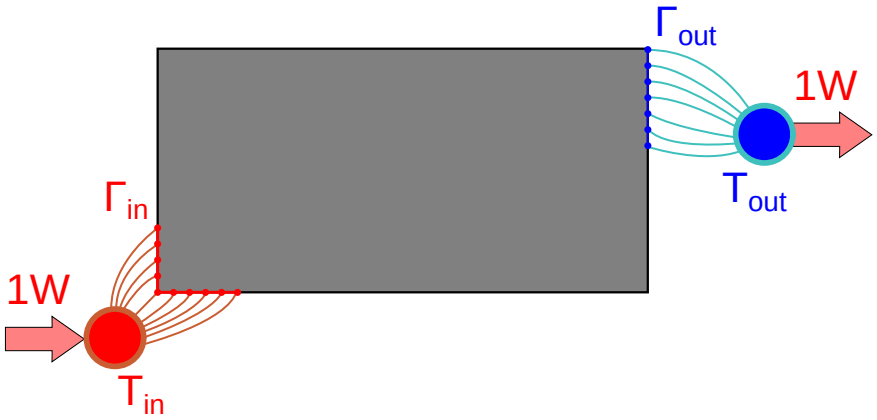

Figure 3.2 – Two nodes added to the VFM domain for the input and output flux.

The link between an additional node and a node of the domain is done via a one-dimensional heat conductor element with conductivity ξ. This element adds the following equations:

$$q_i = \xi \left(T_{\text{in}} - T_i \right) \quad , \quad i \in \{1, \dots , N_{\text{in}}\} \tag{3.17}$$

$$q_i = \xi \left(T_i - T_{\text{out}} \right) \quad , \quad i \in \{1, \dots , N_{\text{out}}\} \tag{3.18}$$

where N_{out} and N_{in} are the number of nodes in the output and input surfaces, respectively.

Assuming that the conductivity of all one-dimensional elements tends to infinity, then the temperature of all nodes connected to the same virtual node become equal (T_{out} or T_{in}).

Regarding the absence of a Dirichlet boundary condition, we can impose a temperature value for any single degree of freedom. For instance, we can impose $T_{\text{out}} = 0$. Choosing either the input or output temperature simplifies the formulation, as it leads to fewer calculations for assembling the matrices). This can be done since we are only interested in the flux, not in the temperature values. The main drawback from this is that, in the event of multiple connectivity constraints, each matrix will be different; and, as such, we cannot reuse the matrix factorization from one problem to solve the other one.

Regarding the input surface, we impose that all nodes have the same temperature. This implies adding all rows and columns of the stiffness matrix corresponding to these nodes. This leads to the following system:

$$\tilde{\mathbf{R}}_g \tilde{\mathbf{t}} = \tilde{\mathbf{q}}_g \tag{3.19}$$

where $\tilde{\mathbf{q}}_g$ is a vector with 1 at the location of the input temperature and 0 elsewhere. The matrix $\tilde{\mathbf{R}}_g$ is the stiffness matrix with the Dirichlet boundary conditions applied.

By solving this system, we obtain the nodal temperature vector $\mathbf{t}$, which can be used to get the heat flux per unit area of each element:

$$\mathbf{q}_e''(\mathbf{r}) = -k_e \mathbf{B}_\mathbf{t}(\mathbf{r})\mathbf{t}. \tag{3.20}$$

Which is the value used in 3.7 to obtain the inverse connectivity parameter, and then, the activation.

3.1.4 Morphological filtering

With the aforementioned techniques, only the total connectivity between both domains is constrained. That is, a domain with only one singular connection or with many thin connections are equally valid (Figure 3.3). However, such connections are not desired, as they may bring the same problems that motivated the use of filtering techniques (Section 2.2.5), such as mesh dependency and checkerboard designs.

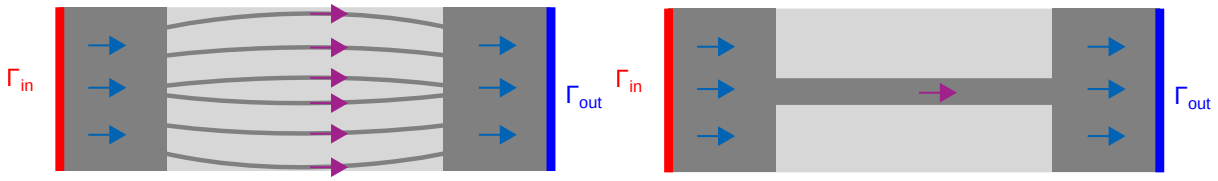

(a) Capillary connection. (b) Singular connection.

Figure 3.3 – Two different types of connection with similar connectivity measure.

Furthermore, should the connection between both regions become thinner than A_{lim}, the method does not guarantee an increase of this connection until this minimum threshold.

To correct both problems, a morphological "dilate" filter (Sigmund, 2007) is applied to the topology before simulating the heat conduction:

$$\hat{x}_e = \frac{1}{\iota} \ln \left(\frac{1}{N_i} \sum_i e^{\iota x_i} \right), \tag{3.21}$$

where i refer to elements inside a filter radius r_{dil}, and ι is a filtering parameter. In the examples presented here, it is used as $\iota = 0.5$. In order to maintain the limit area, it is increased by considering two dilation radii.

Note that on the heat conduction mesh, gray elements may be present, and their conductivity is interpolated via SIMP (Section 3.2). The procedures from Section 3.1.3 are then performed on this configuration.

3.1.5 Sensitivity update scheme

Given a certain activation parameter for each element of the mesh, their sensitivities can be updated via the following formulation:

$$\alpha_e^c = \alpha_e + c_e \left[\max(\alpha_e) - \alpha_e\right] \tag{3.22}$$

With this formulation, if the heat flux of an element is equal to or greater than q_{lim}, then its sensitivity is changed to the highest sensitivity of that iteration. This way, this element will not be removed, ensuring connectivity. For every other case, the VFM is activated according to the activation function (Eq. (3.10)).

Since this procedure may drastically change the sensitivities of some elements and since it is needed to maintain the connectivity, it must be the last operation on the BESO procedure. Therefore, the updated BESO algorithm is illustrated in Algorithm 4.

Input: Define parameters: x_{min}, p, ER, AR_{max}, V^*, r_{min}, τ, N, N_{modes}, A_{lim}, A_{act}, r_{dil}, ι
Define boundary conditions and mesh
Start iteration counter: $j = 0$
Calculate eigenvalues and eigenvectors
while $\varepsilon < \tau$ ***or*** $V^{(j)} \neq V^*$ **do**
  $j = j + 1$
  Evaluate sensitivities $\alpha_e^{(j)}$ (Eq. (2.41))
  Filter sensitivities (Eqs. 2.51 and 2.52)
  Perform historical average with $\alpha^{(j-1)}$ without VFM (Eqs. 2.53)
  Perform the VFM update (Eq. (3.22))
  BESO update (Algorithm 3)
  Calculate eigenvalues and eigenvectors (Eq. (2.17))
  Perform eigenvector tracking (Algorithm 1)
  Calculate $\varepsilon = \dfrac{\left| \sum_{o=j-2N}^{j-N} f(x_e^{(o)}) - \sum_{o=j-N}^{j} f(x_e^{(o)}) \right|}{\sum_{o=j-N}^{j} f(x_e^{(o)})}$
end
Output: Optimized topology $x_e^{(j)}$

Algorithm 4: BESO topology optimization algorithm with VFM

3.2 Interpolation scheme between solid and void structural elements

As previously mentioned in Section 2.2.2, a continuous function that interpolates the material properties must be defined. In this chapter, an interpolation between solid and void elements will be used. The most common interpolation scheme is the SIMP:

$$\rho(x_e) = \rho_0 x_e \tag{3.23}$$

$$E(x_e) = E_0 x_e^p \tag{3.24}$$

where ρ_1 and E_1 are the density and the Young's modulus of the base material.

This interpolation scheme, however, is not suited for dynamic optimization, as it produces local modes with no physical meaning in void regions (Pedersen, 2000). An alternative interpolation scheme was proposed by Huang and Xie (2010) to circumvent this problem in the BESO:

$$\rho(x_e) = \rho_0 x_e \tag{3.25}$$

$$E(x_e) = E_0 \left[\frac{x_{\text{min}} - x_{\text{min}}^p}{1 - x_{\text{min}}^p}(1 - x_e^p) + x_e^p \right] \tag{3.26}$$

This formulation does not generate spurious changes on the eigenvalues and eigenvectors of the system, as it does not change the stiffness to mass ratio of solid and void elements.

With this definition, the derivatives of the mass and stiffness matrices are obtained:

$$\frac{\partial \mathbf{M}_g}{\partial x_e} = \mathbf{M}_e^0 \tag{3.27}$$

$$\frac{\partial \mathbf{K}_g}{\partial x_e} = \frac{1 - x_{\text{min}}}{1 - x_{\text{min}}^p} p x_e^{p-1} \mathbf{K}_e^0 \tag{3.28}$$

where $\mathbf{M}_e^0$ and $\mathbf{K}_e^0$ are the mass and stiffness matrices of the eth element assuming it is made of the base material.

3.3 Numerical results

In this section, the optimization results using the VFM will be presented. The BESO is implemented as shown in Algorithm 4, with the procedures shown in Chapter 2. The opti-

mization and experimental results of the cantilever beam were published at *Mechanical Systems and Signal Processing* (Lopes *et al.*, 2022b).

3.3.1 Optimization of first natural frequency

A first case of a cantilever beam is run to illustrate the functioning of the VFM. The optimization domain is similar to the one in Figure 2.5, except that the right end is free. The optimization parameters and material parameter are also similar to the ones from Section 2.3.1. In this case, however, the one material and void interpolation scheme is used, with $x_{\text{min}} = 10^{-6}$ and $p = 5$. Additionally, the objective function is the maximization of the first natural frequency. The final volume is set to 40%.

Without the VFM, the final topology is the one shown in Figure 3.4a. This result is expected, as the trivial solution to the maximization of the first frequency of a cantilever beam is reducing its length, which is exactly what the optimizer did in every iteration.

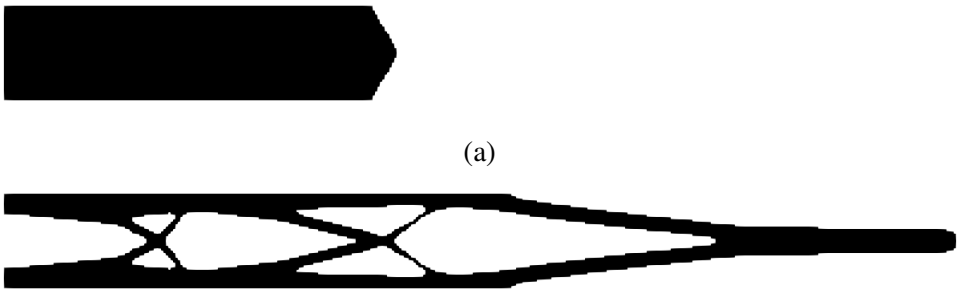

(a)

(b)

Figure 3.4 – Cantilever beam with maximized first frequency (a) without VFM (b) with VFM.

In contrast, we can impose a connectivity between the left surface and the right central node of the domain by classifying them as, respectively, output and input domains for the VFM. The activation length is defined as 100 mm and the limit one is 20 mm. The dilation radius is $r_{\text{dil}} = 7$ mm. The final topology of the optimization is shown in Figure 3.4b. Note that, in this case, connection between both edges of the domain is maintained during the entirety of the optimization procedure.

Without the VFM, the first natural frequency increased from 83 Hz to 224 Hz. With the VFM, it increased only to 126 Hz. The increased in the constrained case is evidently much lower than the one on the unconstrained problem, however, this is one of the expected consequences of imposing the geometric restriction.

This example shows that the method is effective in guaranteeing the connectivity in one of its motivation problems. Further analyses on the method itself will be done in the following examples.

3.3.2 Optimization of a compliant mechanism

This section illustrates the robustness of the VFM by applying it to a different kind of problem. Here, it is used for maximizing a compliant mechanism, more specifically, the inverter mechanism. While it may seem an abrupt change of subject, the goal of this section is to study the behavior of the VFM when applied in a different setting, not to extensively analyze compliant mechanisms.

The main difficulty in the optimization of compliant mechanism is the appearance of thin hinges, which destabilizes the methodology. Several ways to avoid them have been developed in the literature. Such as using an additional compliance term on the objective function, effectively penalizing any sort of drastic loss of stiffness (Li *et al.*, 2014). Also, the use of morphological filters can also help, by applying the robust optimization formulation (Sigmund, 2009). It consists of simulating three topologies: the current one, an eroded one and a dilated one. These three configurations are considered in the optimization analysis. Any thin hinge is broken on the eroded design, and thus, it is reinforced. In this work, the VFM is used to illustrate its effectiveness in maintaining connectivity.

The inverter mechanism consists of the domain from Figure 3.5. Its functioning is characterized by its behavior when applying a horizontal force at the center of its left end. The desired response is a horizontal displacement at the other end on the opposite direction. Note that, for a fully solid topology, the response is on the same direction of the force. Therefore, the optimizer must be able to invert the sign of the displacement.

The optimization problem here is, thus, described as follows:

$$\begin{aligned} \max \quad & f(x_e) = u_{\text{out}}, \\ \text{s.t.} \quad & V^* - \textstyle\sum_{e=1}^{N_{\text{el}}} V_e x_e = 0, \\ & x_e = 1 \text{ or } x_{\text{min}}, \end{aligned} \tag{3.29}$$

where u_{out} is the output displacement on the degree of freedom whose behavior we desire to control.

An important aspect to notice is that, usually, using only the displacement as the objective function is not feasible. That is, TO algorithms usually only work with other objective

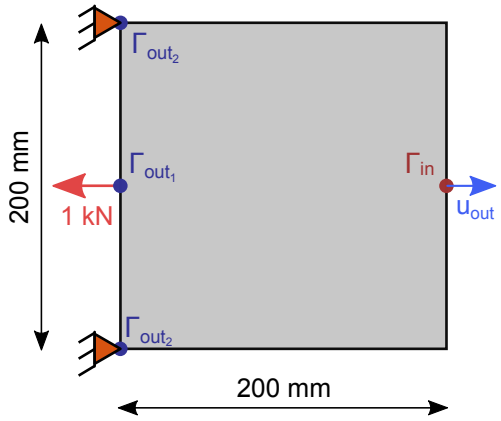

Figure 3.5 – Design domain of compliant mechanism optimization.

functions, such as the mechanical advantage (Sigmund, 1997; Ansola *et al.*, 2010), using geometrical advantage and compliance (Li *et al.*, 2014) or using a mutual potencial energy (Ansola *et al.*, 2007). The VFM, in this case, makes using this objective function possible.

The sensitivity analysis of this problem can be perfomed by differentiating Eq. (3.29):

$$\alpha_e = -\frac{1}{2}\mathbf{u}_j^T \frac{\partial \mathbf{K}_g}{\partial x_e}\mathbf{u}, \tag{3.30}$$

where $\mathbf{u}_j$ is a virtual displacement vector, obtained by considering a unit virtual load on the output degree of freedom.

Finally, since this is a static problem, the regular interpolation scheme from SIMP is used (Eq. (3.24)).

The optimization is run with the BESO, following the Algorithm 2. The BESO parameters are chosen as: ER $= 2\%$, $\text{AR}_{\text{max}} = 2\%$, V^* = 15%, $x_{\text{min}} = 10^{-3}$, $p = 3$, $N = 5$, $\tau = 0.01\%$. The domain is discretized in a 200×200 mesh. The domain is composed of steel, with: $E = 210$ GPa and $\nu = 0.3$.

Without the VFM, the optimization does not lead to a feasible design. The optimizer is even unable to obtain a topology that inverts the displacement. Note that this is due to the objective function being only the displacement (Eq. (3.29)). Solutions of this problem can be obtained with the BESO using different techniques.

Here, two VFM problems are defined, one connecting the boundary conditions nodes to the output displacement node and another one connecting the force-application node to the output displacement node (Figure 3.5). They are imposed simultaneously by employing

the strategy from Eq. (3.11). For both VFM definitions r_{dil} = 2 mm (two elements), and A_{act} = 40 mm and A_{lim} = 10 mm.

The optimization leads to the topology in Figure 3.6a. The evolution of the displacement is shown in Figure 3.7. At the start of the optimization, the displacement is slightly negative, meaning that the displacement is on the same direction as the force. The evolution is very unstable up to about iteration 40. At this point, a traditional inverter mechanism topology has already been achieved, the optimization is just fine-tuning its shape. Note that on iteration 94, the output displacement is at its maximum value with a feasible volume fraction, meaning that this should be the optimal solution. However, due to the influence of the VFM, the shape keeps changing, decreasing the output displacement. Figure 3.6b shows the design at iteration 94.

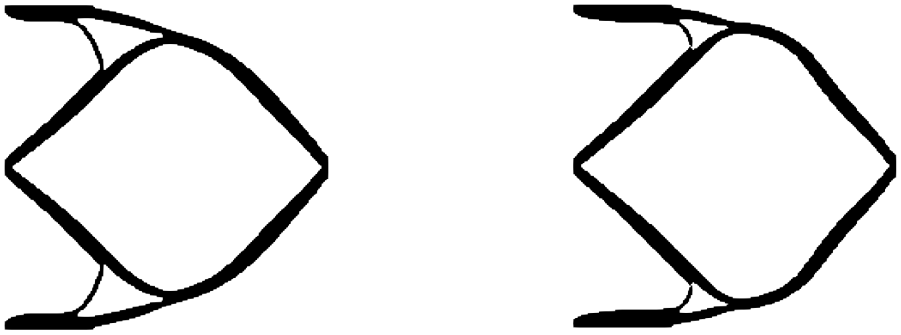

(a) (b)

Figure 3.6 – Compliant mechanism optimization (a) Final topology (b) Iteration 94.

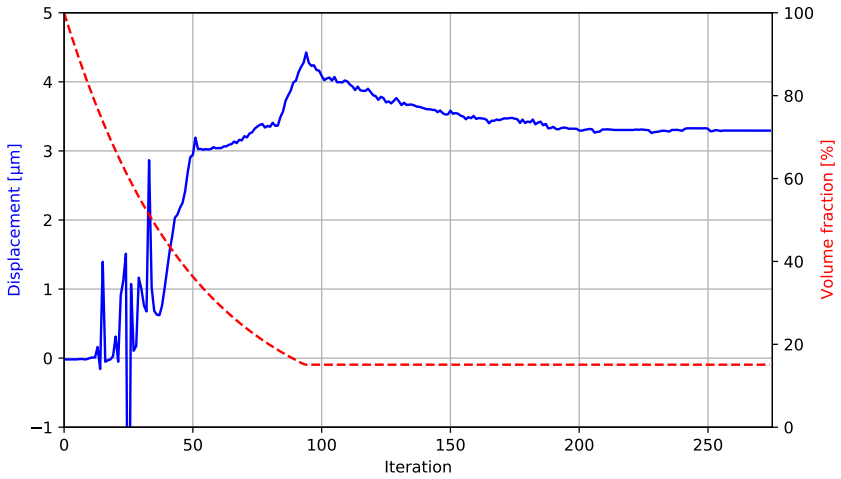

Figure 3.7 – Evolution of output displacement of compliant mechanism.

Finally, we can check the activation parameter. Figure 3.8 shows it for the final

topology. In this case, the volume constraint is tighter than in the previous results. Thus, the activation is close to one in the whole topology. On each of the components, we can clearly see the path that the heat flows from one subdomain to the other.

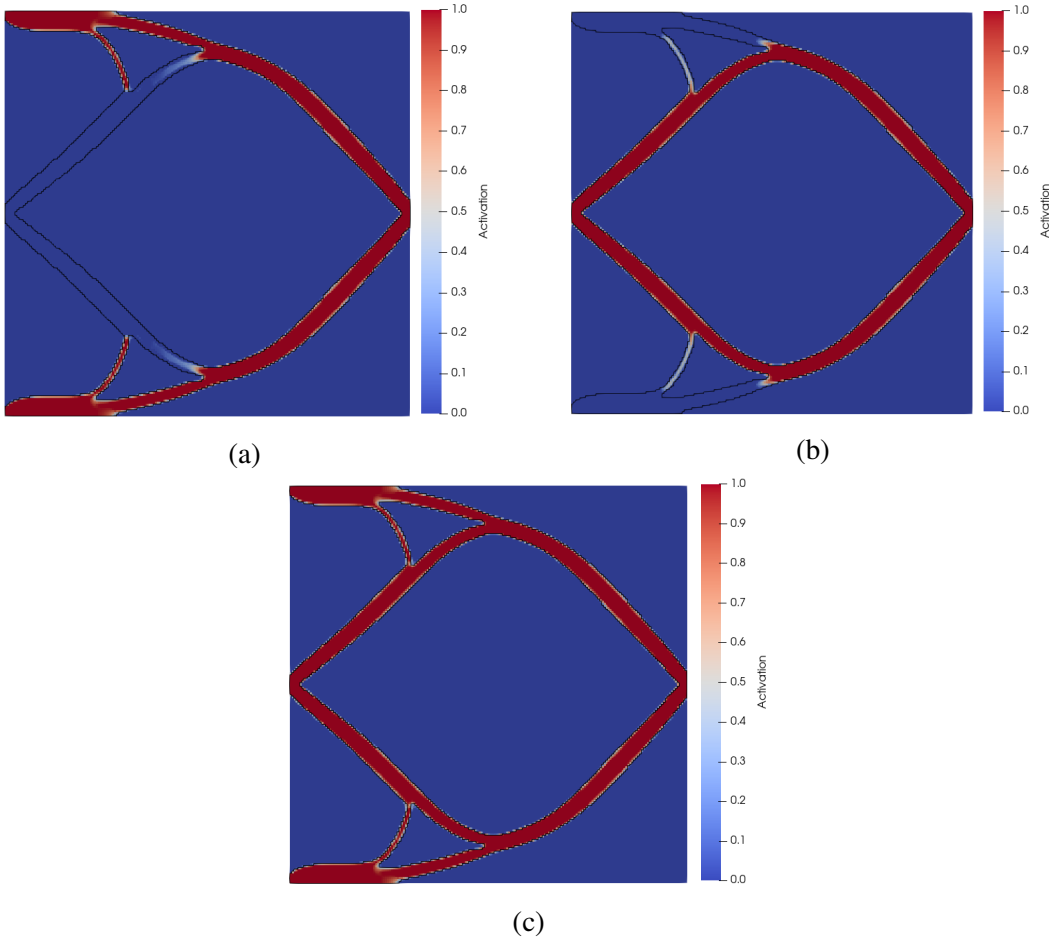

Figure 3.8 – Compliant mechanism activation parameter (a) Connection to force (b) Connection to supports (c) Both connectivities.

In the end, we can measure the width of each of the bars in this topology, to verify whether the geometric constraint of 10 mm was met. These sizes are estimated as the necessary dilation filter diameter necessary to make the feature disappear. First, the central bars (the ones in red in Figure 3.8b), have a 5 mm width each. The very thin bars (beige in Figure 3.8b and red in Figure 3.8a) have a 2 mm width, and the bar above it has 4 mm, totaling about 6 mm on each side. In the end, adding the connection widths on both sides yield at least 10 mm. This means that the constraint is met.

This analysis showed that the VFM worked in the design of compliant mechanisms. However, in order to be used in practical applications, further studies must be done. For example, while a minimal thickness was maintained, no hinges are seen in the final topology. Note

that only thin single-element hinges are a problem in this type of problem, hinges themselves are usually necessary to ensure the large displacement of the system.

3.3.3 Optimization of a cantilever beam

In this section, the VFM is applied once again to the optimization of an elongated cantilever beam. The dimensions for this problem are shown in Figure 3.9.

Figure 3.9 – Domain for optimization of cantilever beam with VFM.

The structure is modeled using the properties of Polylactic Acid (PLA), which has the following properties: $E = 3.5$ GPa, $\nu = 0.36$ and $\rho = 1250$ kg/m^3. The BESO parameters are set to: ER = 2%, AR$_{\text{max}}$ = 2%, final volume $V^* = 60\%$, $r_{\text{min}} = 2$ mm, penalty factor $p = 5$ and number of modes $N_{\text{modes}} = 10$.

The operating frequency is set to $f_0 = \omega_0/2\pi$ = 400 Hz, which is, for the initial topology, between the first and second modes.

To apply the VFM, an input and an output surfaces are defined, which are illustrated in Figure 3.9. The activation area is based on the width of the domain ($A_{\text{act}} = 18$ mm^2), while the limit area is defined as $A_{\text{lim}} = 4$ mm^2, which means we desire a minimum width of 4 mm.

With these parameters, the optimization procedure is performed. After 40 iterations, the stop criterion is met, yielding the topology from Figure 3.10.

Figure 3.10 – Optimized cantilever beam with VFM.

In this topology, the two main regions where the VFM operates the most are circled. These two locations have a width of roughly 3.7 mm, which is around the imposed minimum width. For further investigation, the connectivity parameter of the final topology is presented in Figure 3.11.

The contrast of this parameter along the topology shows the functionality of this process. The parameter is high in the regions where it is necessary to maintain connectivity, but

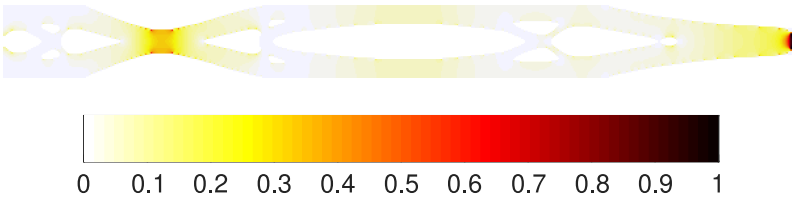

Figure 3.11 – Connectivity parameter for optimized cantilever beam.

it remains low elsewhere, meaning it doesn't compromise the optimization process outside the critical regions.

The frequency response of this structure is calculated to evaluate its performance and is shown in Figure 3.12. The natural frequency separation around f_0 is increased by 28%, going from 611.3 Hz to 785.4 Hz.

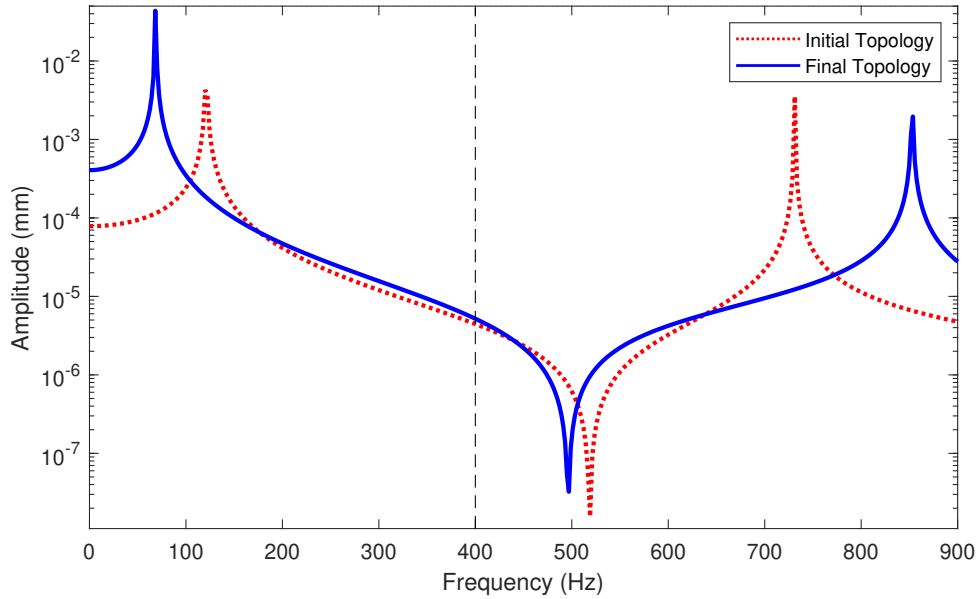

Figure 3.12 – Frequency response of the initial and final topologies of the cantilever beam optimization with VFM.

3.3.4 Optimization and experimental analysis of a cantilever beam

In the previous section, the topology optimization procedure with VFM generated a feasible topology that maximized the natural frequency separation. In this section, another topology is generated and tested experimentally to validate the optimization process.

The optimization domain for this case is the same as the previous one. To guarantee standardized testing for both initial and final topologies, a layer of non-design domain of thick-

ness 2 mm is added to the outer surfaces of the domain. Additionally, the sensitivity filter radius r_{min} is changed to 1.5 mm. All other parameters are kept unchanged from the previous result.

Due to the non-design domain layer, one could assume that the VFM would be unnecessary in this case, due to the impossibility of loss of connection. To prove otherwise, an initial optimization procedure is performed without the VFM (Figure 3.13).

Figure 3.13 – Optimized cantilever beam with non-design domain layer without VFM.

This topology is not a feasible solution. Its thin connections would make the manufacturing process challenging and could lead to structural problems in practical applications. Thus, the VFM is necessary even when adding this layer.

To be consistent with the filter radius, the limit connectivity area A_{lim} is changed to 1.5 mm^2. After 33 iterations, the optimized topology is shown in Figure 3.14. Additionally, the connectivity parameter is shown in Figure 3.15.

Figure 3.14 – Optimized cantilever beam with non-design domain layer with VFM.

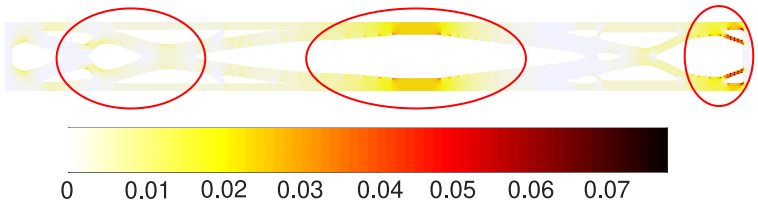

Figure 3.15 – Connectivity parameter for optimized cantilever beam with layer.

In this case, the connectivity parameter values are not as high as those from the previous optimization. Even so, they significantly affect the topology. There are three regions where the VFM activated the most, which are circled in Figure 3.15. Therefore, despite not being necessary to maintain connectivity in this case, the VFM guarantees that we obtain a feasible topology.

The evolution of natural frequencies is shown in Figure 3.16.

The first natural frequency barely changes during the evolution; however, the second one increases more. At iteration 5, we observe that the process rapidly removed elements from two of the marked regions, which remained connected due to the VFM. Around iteration 25,

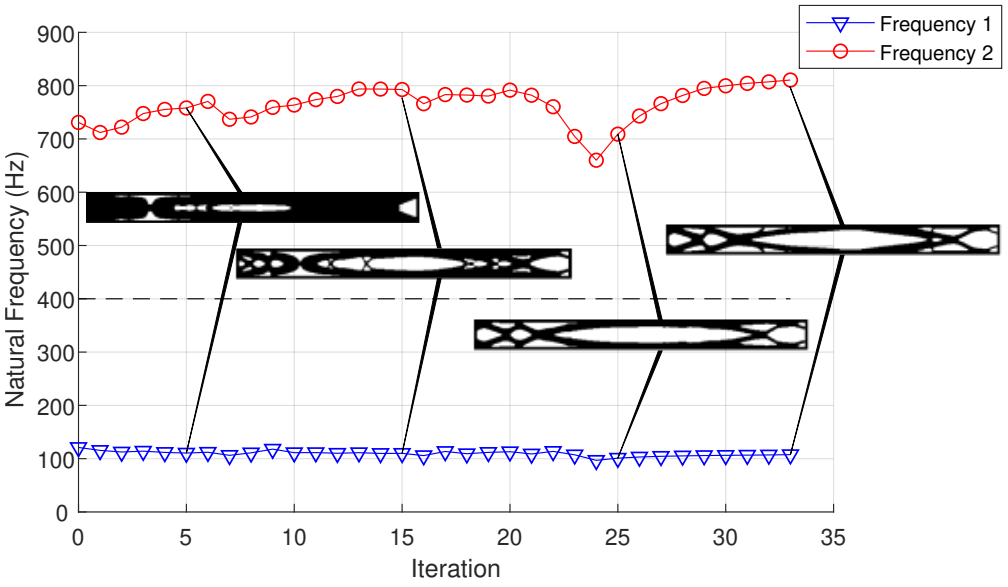

Figure 3.16 – Evolution of the first two natural frequencies for cantilever beam with VFM and non-design domain.

a large decrease in the second natural frequency is observed as a consequence of the removal of internal bars. Despite that, the procedure manages to increase it again by reinforcing other regions of the topology. The final natural frequency separation is also observed in Figure 3.17.

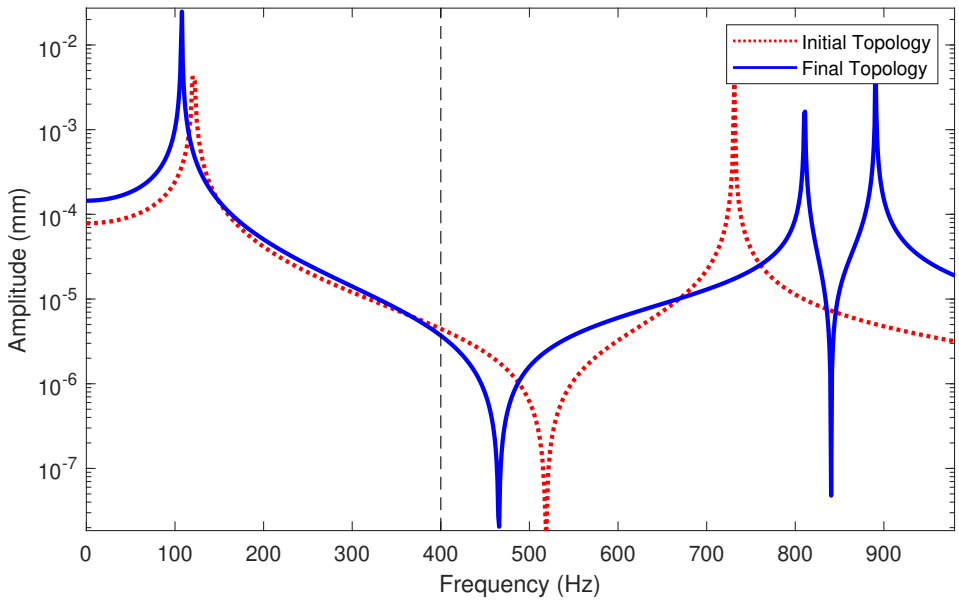

Figure 3.17 – Harmonic response of cantilever beam with VFM and non-design domain.

The natural frequency separation changed from 610 Hz to 703 Hz, an increase of 15%. This topology presents a satisfactory trade-off between the imposed design constraints and performance. Therefore, it is chosen for the experimental analysis.

To manufacture and experiment on this topology, it must be extended into a three-

dimensional model. It is done by extruding it along the Z axis by a thickness of 20 mm (Figure 3.18). Some small adjustments have been done to it, including the smoothing of sharp edges and the removal of small features.

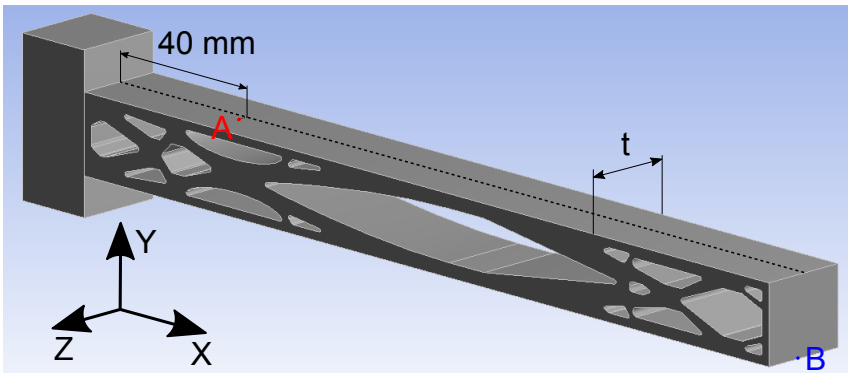

Figure 3.18 – Three-dimensional model of the optimized structure with VFM. A and B represent the points of force application and displacement measurement, respectively.

The commercial software Ansys® Workbench 17.0 was used to simulate the system and to generate the appropriate STL files for the 3D printing. The responses of both initial and optimized structures are shown in Figure 3.19.

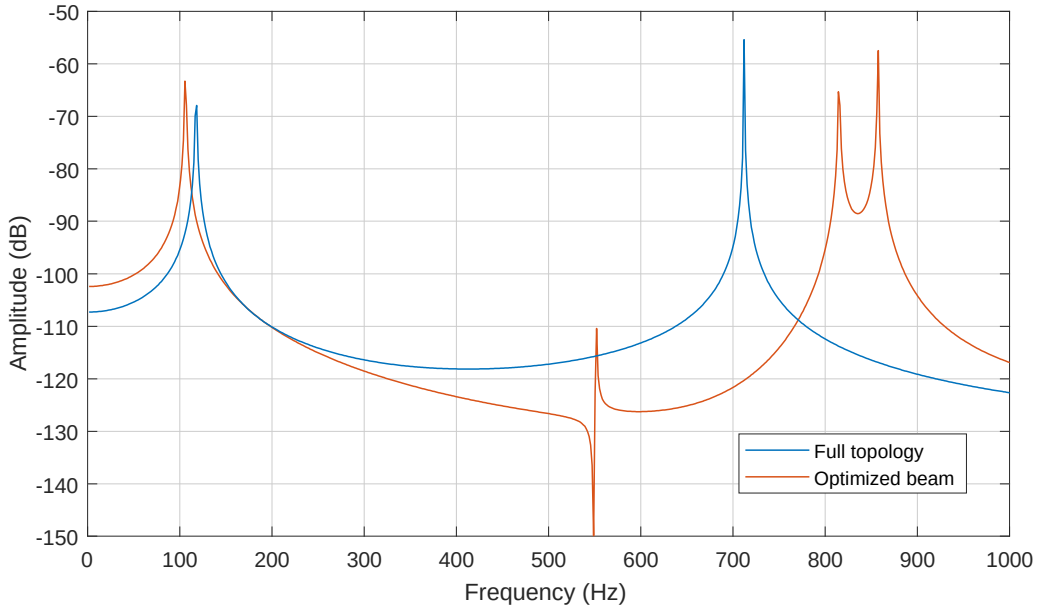

Figure 3.19 – Simulated FRFs from 3D initial and optimized structures.

Comparing this response with the optimized two-dimensional one, no significant difference is seen around the first resonance, which is still around 104.5 Hz. The two resonances at 789.2 Hz and 850.2 Hz are still present; however, their values have slightly changed here. Two new peaks are observed at 551.1 Hz and 716.0 Hz. These are due to out-of-plane modes, as can be seen in the mode shapes of the 3D model (Figure 3.20).

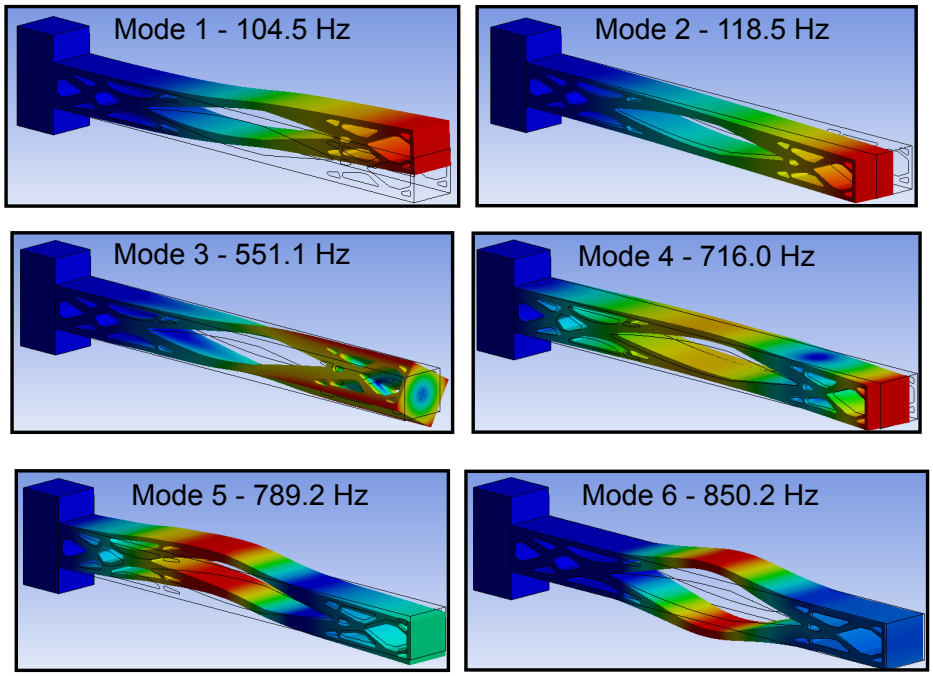

Figure 3.20 – Mode shape for the simulated model.

With this three-dimensional topology, we can print the samples. For that, a Lulzbot® Taz 6 printer was used. The two manufactured structures are shown in Figure 3.21.

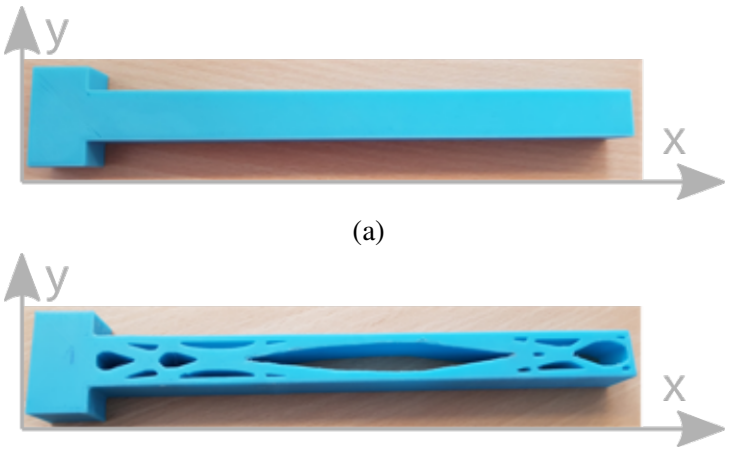

Figure 3.21 – Initial (a) and optimized (b) structures.

To perform the experiments, they were clamped at one end and excited by an electromagnetic shaker 40 mm from the clamped end (Figure 3.22). A force transducer was placed between the push-rod and the structure. The shaker was suspended by elastic links.

The laser vibrometer was set to sweep through several points of the structure. These points correspond to a 13 $\times$ 5 grid along the surface (Figure 3.23). The vibrometer was placed 1.5 m from the surface of the samples and its lens was aligned at 50 mm from the clamped

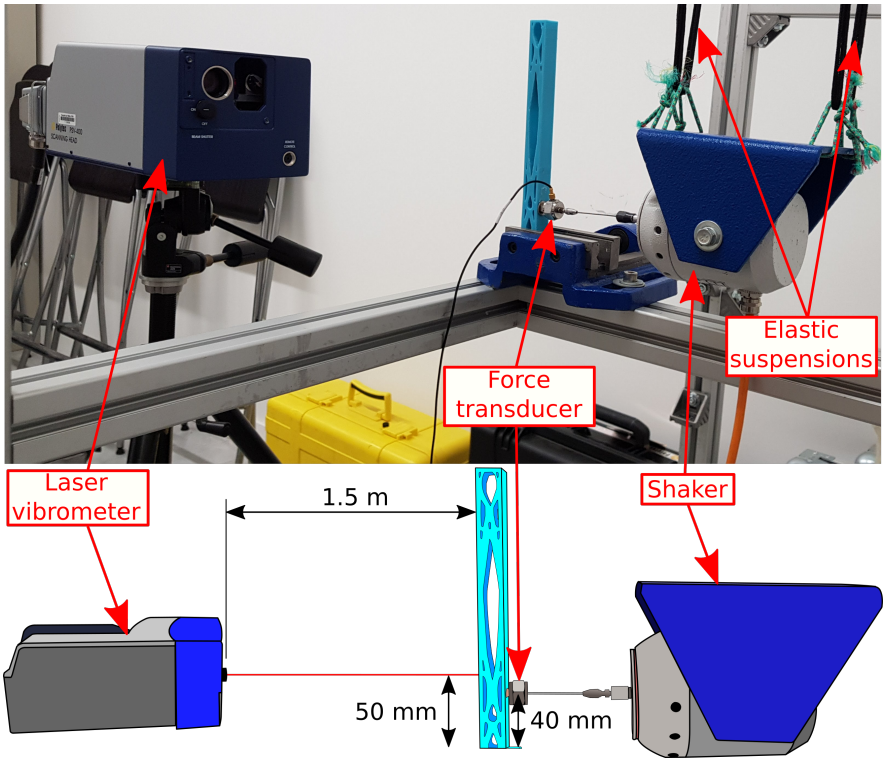

Figure 3.22 – Representation of the experimental setup of cantilever experiment.

end. White noise from 0 to 2000 Hz, with a sampling frequency of 2.5 kHz, was used for measurement. The process was repeated ten times for each point, and the final responses were obtained by averaging each measurement. The list of equipment is shown in Table 3.1, and a general view of the setup is illustrated in Figure 3.23.

Table 3.1 – List of equipment for VFM experiment

Equipment	**Model**
Laser Doppler Vibrometer	Polytec PSV-400
Force Shaker	TIRA Vibration Exciter S 50018
Power Amplifier	TIRA Power Amplifier BAA 60
Force Transducer	Bruel & Kjaer Type 8200
Signal Conditioner	Nexus Charge Conditioning Amplifier 2692-A

The experimental response had a more complex behavior than the simulation and several modes that had not been observed previously emerged. Those were due to the supports and equipment. At the considered frequency range, numerical and measured resonances of the optimized structure were similar, as shown in Table 3.2. Furthermore, their harmonic responses were also similar, as indicated in Figure 3.24.

With the results, the mode shape of the resonances that were measured can be

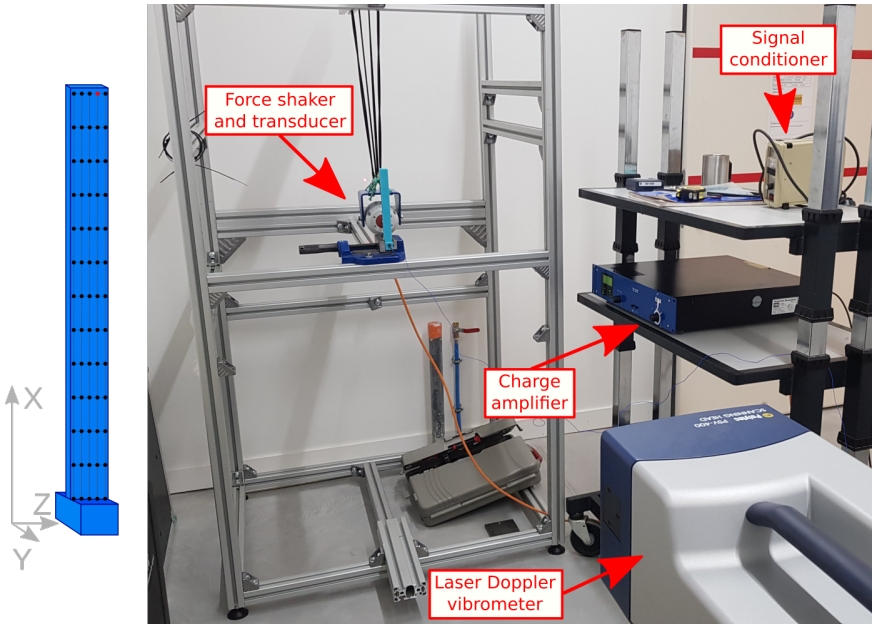

Figure 3.23 – General view of the experimental setup of cantilever beam.

Table 3.2 – First two bending frequencies (Hz) for experimental analysis with VFM

Numerical Simulation	Experiment	Difference
104.5	107.0	2.4%
789.2	790.0	0.1%

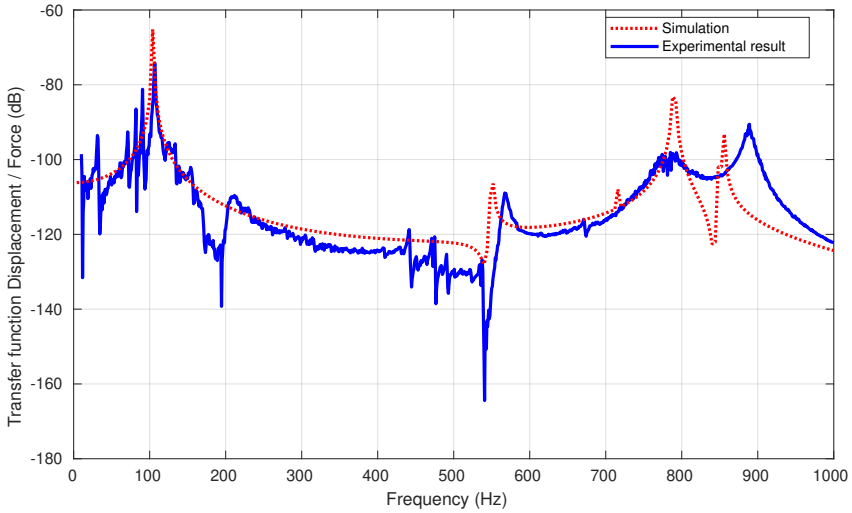

Figure 3.24 – Comparison between experimental and simulated FRFs of optimized structure.

graphed, as indicated in Figure 3.25.

Comparing the mode shapes obtained experimentally with those from the simulation indicates a good agreement between themselves. The modes that are perpendicular to the direction of the measurement can not be seen in this experimental setup.

Finally, the measured responses from both initial and optimized structures are com-

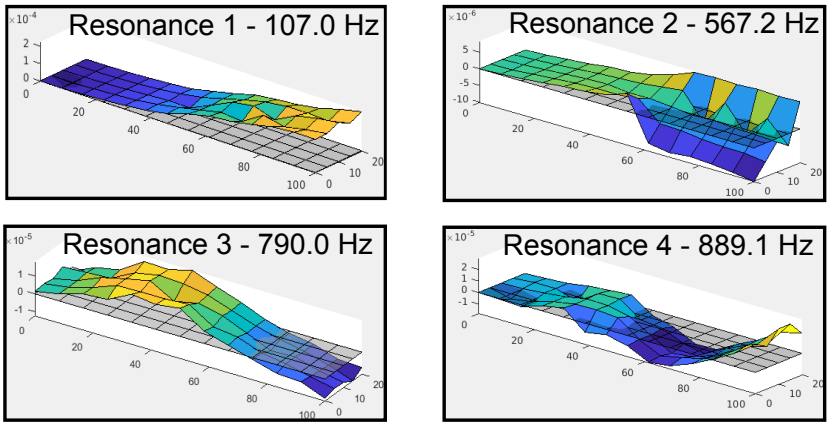

Figure 3.25 – Mode shape of the studied resonances.

pared in Figure 3.26.

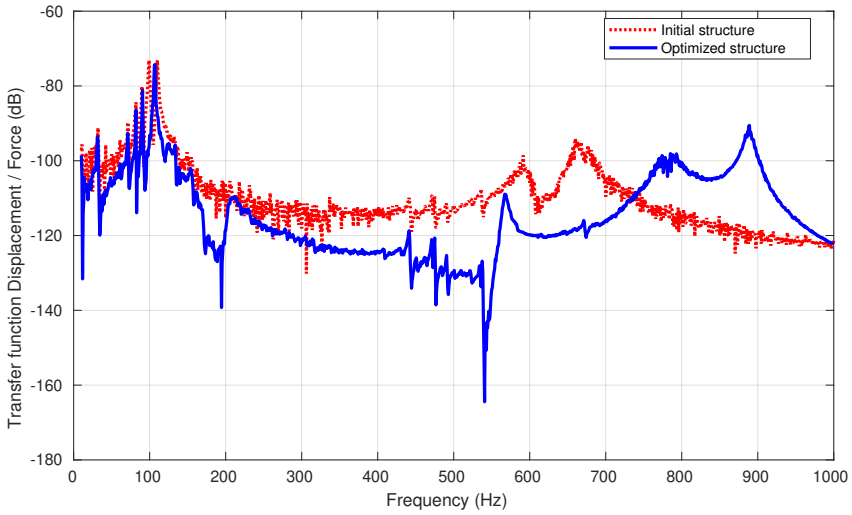

Figure 3.26 – FRFs of the optimized and the initial structures.

The topology optimization method produced a clear improvement on the desired dynamic behavior on these manufactured structures, the first resonance frequency changed from 110.2 Hz to 107.0 Hz, while the second one increased from 660.2 Hz to 790.0 Hz. This corresponds to a 24% increase in the frequency separation.

3.3.5 Optimization of a clamped-clamped beam

Finally, a system equivalent to the one from Section 2.3.1 is optimized. As evidenced then, when optimizing this problem, the procedure leads to a quasi-periodic and disconnected topology. This means that a one material and void optimization would lead to a non-physical solution, as islands of solid material would form.

Thus, the optimization from Section 2.3.1 is done here with one material and void. The final volume here is changed to 70%, considering that the amount of solid material here will be greater, as we expect the islands of solid material to be connected. To obtain a smoother optimization, the parameters ER and AR_{max} are also changed to 1%. The interpolation parameters x_{min} and p are set to 10^{-6} and 5. The other parameters are kept the same from the two material optimization.

The VFM is used to connect both clamped edges of the structure. The activation and limit widths are 60 mm and 20 mm, respectively. The dilation radius is $r_{dil} = 5$ mm. The final topology is shown in Figure 3.27.

Figure 3.27 – Final topology in frequency separation problem with VFM.

A direct comparison between Figure 3.27 and Figure 2.6a shows great similarity between both topologies. Pointedly, the quasi-periodic pattern is present in both topologies, and both present the same number of disks. The only notable difference is the presence of connections between them.

The resulting frequency separation interval corresponds to 8.7 kHz between 12.5 kHz and 21.2 kHz. The evolution of some frequencies can be seen in Figure 3.28.

This frequency separation is significantly lower than the one obtained in Section 2.3.1. This was, nonetheless, expected, as the alternation between stiff and flexible material is the optimal way to induce this kind of behavior. Despite this, connectivity was maintained, and only one material is used in this design. Additionally, this design is much stiffer than the two-material one, as we can see by comparing their FRFs (Figure 3.29).

3.3.6 Optimization of a ring structure

This next structure is a ring structure, as shown in Figure 3.30. Its radii are $R_1 = 270$ mm and $R_2 = 370$ mm. Note the similarity of this structure from the one from Section 3.3.5, they have the same widths and this one has roughly double the length of the previous one. The domain is discretized by a mesh of elements defined along the polar coordinates of this ring. The mesh is composed of 600 x 30 elements, and, for the sensitivity analysis, they are assumed to have roughly the same areas.

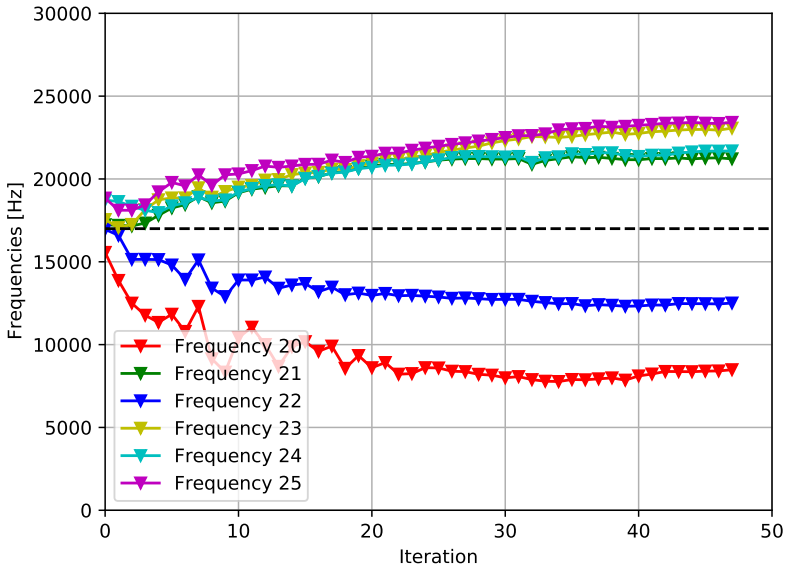

Figure 3.28 – Evolution of the natural frequencies closest to 17 kHz for clamped beam case with VFM.

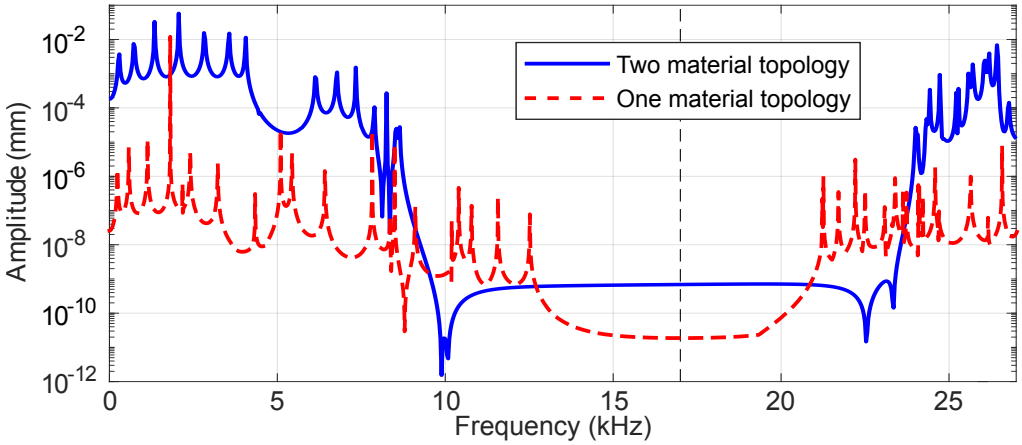

Figure 3.29 – Frequency response functions of the two-material and one-material optimized topologies on the 17 kHz optimization case.

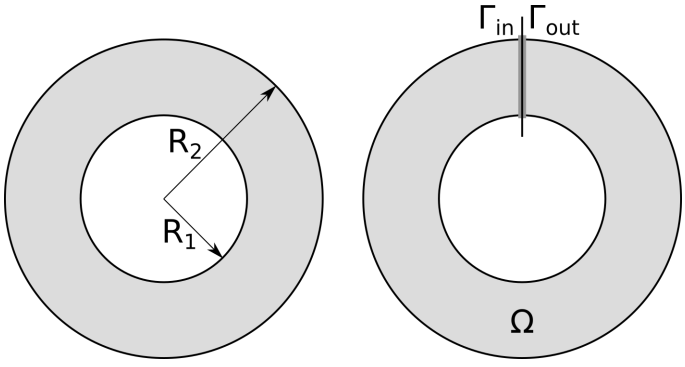

Figure 3.30 – Design domain of ring structure optimization.

Due to the circularity of this domain, it may not be clear which surfaces to use for the VFM. For that, the domain for the heat conduction problem is similar, apart from having a duplicate section, which are considered disconnected (Figure 3.31). That is, the input heat in one of them has to go all the all around the ring to reach the other one. One could also argue about using the inner and outer radii of the ring as input and output surfaces. However, this would only connect those two surfaces, not guaranteeing a full connection all around the disk.

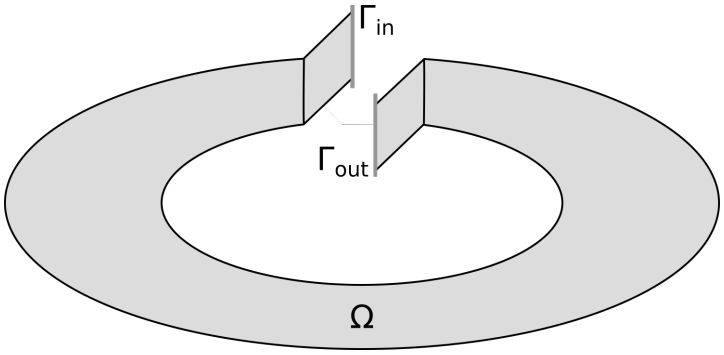

Figure 3.31 – VFM domain with duplicate section.

Finally, due to the perfect symmetry of this domain, the optimization would have difficulties in starting the procedure. Every single element along a given radius would have the same sensitivity. Thus, the optimization would either only ever remove all elements of a radius simultaneously, leaving only a thinner disk; or remove random elements based on numerical errors until the axissymmetry is lost, removing the deterministic nature of the method. To solve this, a non-symmetric initial topology is adopted, in this case, the one from Figure 3.32, with four holes of 30 mm of diameter.

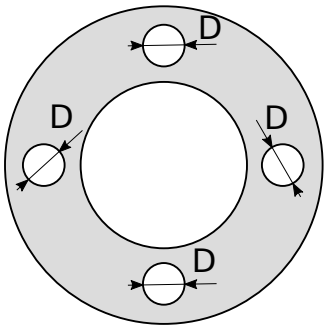

Figure 3.32 – Initial design for ring structure optimization.

The first optimization case is with an operating frequency of 17 kHz. The BESO parameters are kept the same from the previous cases. This optimization is done with two materials, with similar properties to Section 2.3.1. The final volume is 60%. Without the VFM,

the final topology is shown in Figure 3.33a. When applying the VFM, the activation length is 50 mm, and the limit one is 20 mm, leading to the final topology from Figure 3.33b.

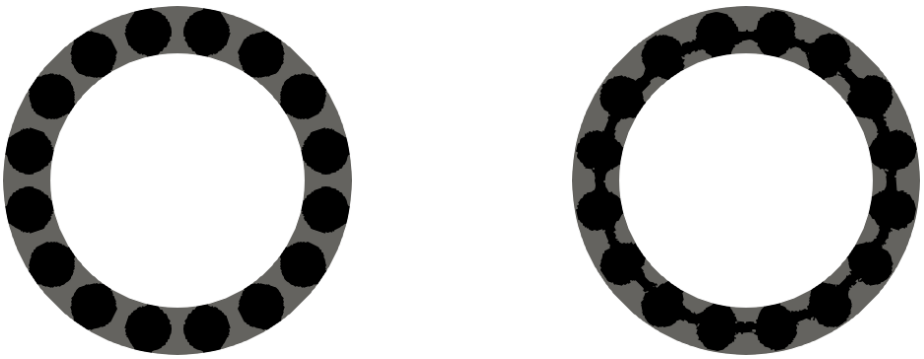

(a) (b)

Figure 3.33 – Final design in 17 kHz ring domain optimization (a) Without VFM (b) With VFM.

Once again, a set of periodic disks is obtained, both with and without the VFM. With is, all of them are connected by bars. We can verify the VFM activation parameter in this case in Figure 3.34.

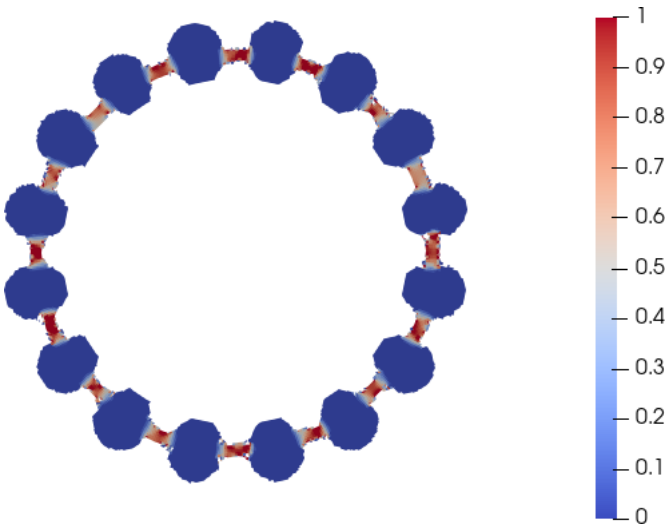

Figure 3.34 – VFM activation parameter for the optimization of ring structure.

Without the VFM, the final natural frequency separation is 14.7 kHz, while with it, it becomes 9.9 kHz. Expectedly, when adding a new constraint, the objective function increases less after the optimzaition.

Finally, we can verify how the optimization performs in lower operating frequencies. The process is repeated for both 12 kHz and 5 kHz. The topologies with and without VFM are shown, respectively in Figures 3.35 and 3.36.

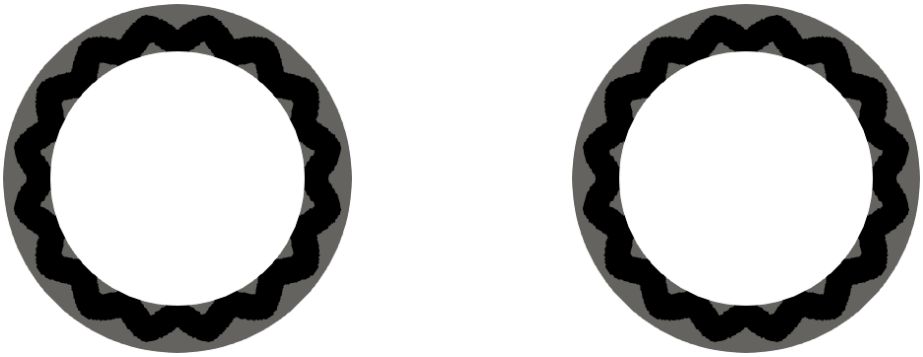

(a) (b)

Figure 3.35 – Final design in 12 kHz ring domain optimization (a) Without VFM (b) With VFM.

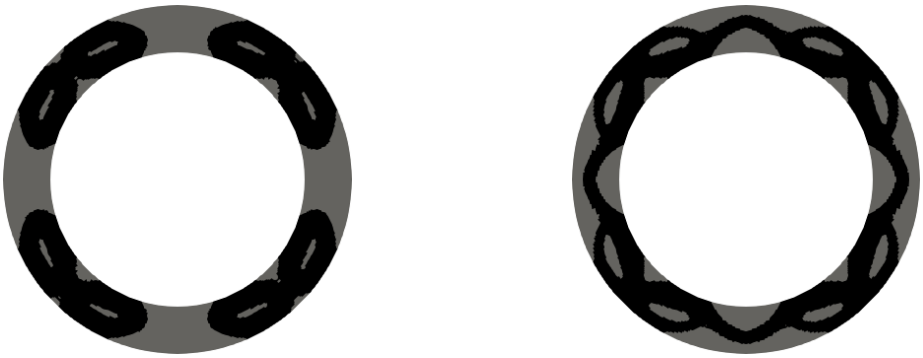

(a) (b)

Figure 3.36 – Final design in 5 kHz ring domain optimization (a) Without VFM (b) With VFM.

In general, when decreasing the operating frequency, the number of periodic cells decrease, as previously discussed in Chapter 2. This phenomenon repeats here.

Curiously, for the operating frequency of 12 kHz, both topologies are equal. That is, even without the VFM, the final topology is already connected. In that case, if we activate the VFM, it should continue giving the same result. Fortunately, that is what we observed here. This means that the VFM does not interfere with the optimization unless it is necessary. For this frequency, the obtained separation interval is 3.9 kHz.

Finally, for an operating frequency of 5 kHz, the structure is, once again, disconnected. With the VFM, a similar topology is obtained, only with connections between the solid regions. Nevertheless, note that these connections are not strictly lines connecting these regions, showing that even if the VFM seems to just connect the regions, the performance of this connection is also taken into account. In the end, the separation intervals are 3.0 kHz and 2.2 kHz for the topologies without and with the VFM, respectively.

3.3.7 Optimization of a 3D clamped-clamped beam

In this last case, a 3D clamped-clamped beam is optimized. The domain corresponds to a 3D structure clamped at both ends (Figure 3.37). It is discretized into a 500 x 60 x 24 mesh of hexahedral elements.

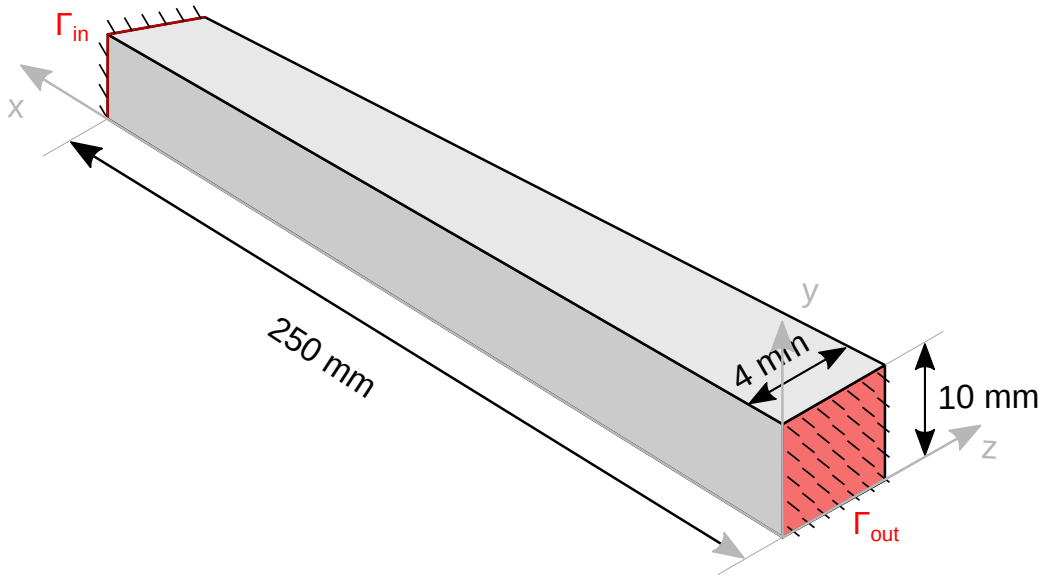

Figure 3.37 – Domain for optimization of 3D clamped-clamped beam with VFM.

The material properties are of a maraging steel alloy: $E = 150$ GPa, $\nu = 0.3$ and $\rho = 8000$ kg/m^3. The BESO parameters are set to: ER = 2%, AR$_{\text{max}}$ = 2%, final volume $V^* = 40\%$, $r_{\text{min}} = 0.5$ mm and penalty factor $p = 5$. It is desired to maximize the natural frequency separation around 5 kHz. For this frequency range, the number of calculated eigenvalues N_{modes} is set to 60. The input and output surfaces of the VFM are set as both extremities. The activation and limit areas are set to $A_{\text{act}} = 40$ mm^2 and $A_{\text{lim}} = 10$ mm^2.

The optimization ends after 54 iterations, at the topology from Figure 3.38.

In this topology, the main places where the VFM activated were the center and the thin connections throughout the topology. Without the connectivity constraint, the system would become disconnected, much like the previously presented cases.

The evolution of the closest natural frequencies from the operating frequency can be seen in Figure 3.39. This clearly shows that, despite the constraint, a clear separation was opened on the natural frequencies. Furthermore, it is important to note that, unlike the results from Sections 3.3.3 and 3.3.4, every single mode is considered here. That is, all transversal modes, from the x-y and x-z planes, and the torsion modes. Thus, it is expected that the ex-

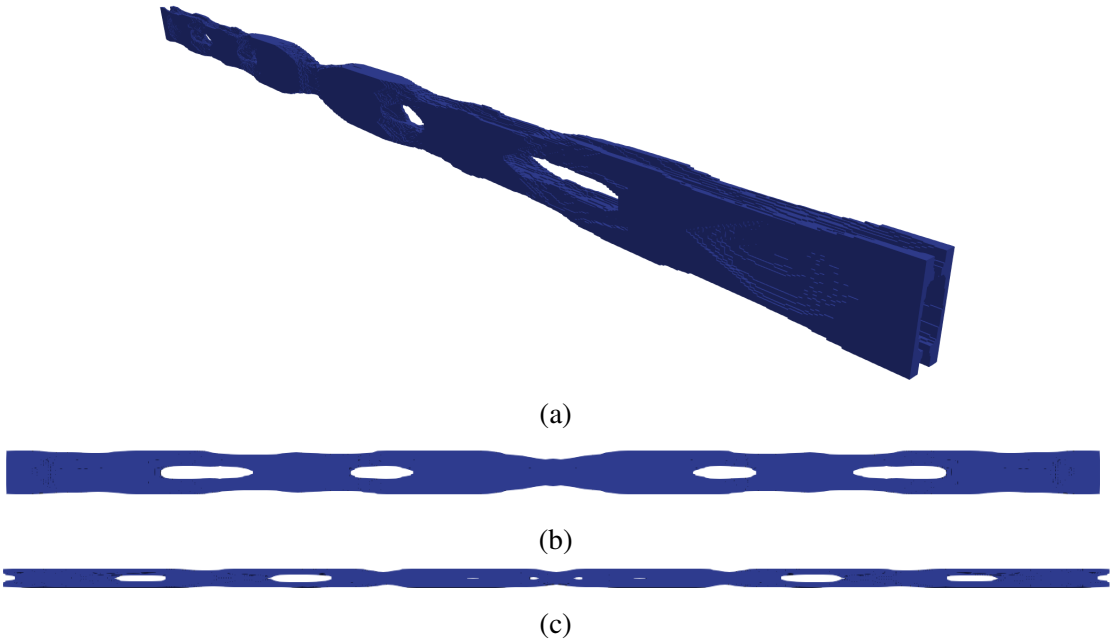

Figure 3.38 – Optimized topologies for clamped-clamped domain: (a) isometric view, (b) view from x-y plane, (c) view from x-z plane.

perimental result will preset less error regarding unexpected appearance of modes within the separation range.

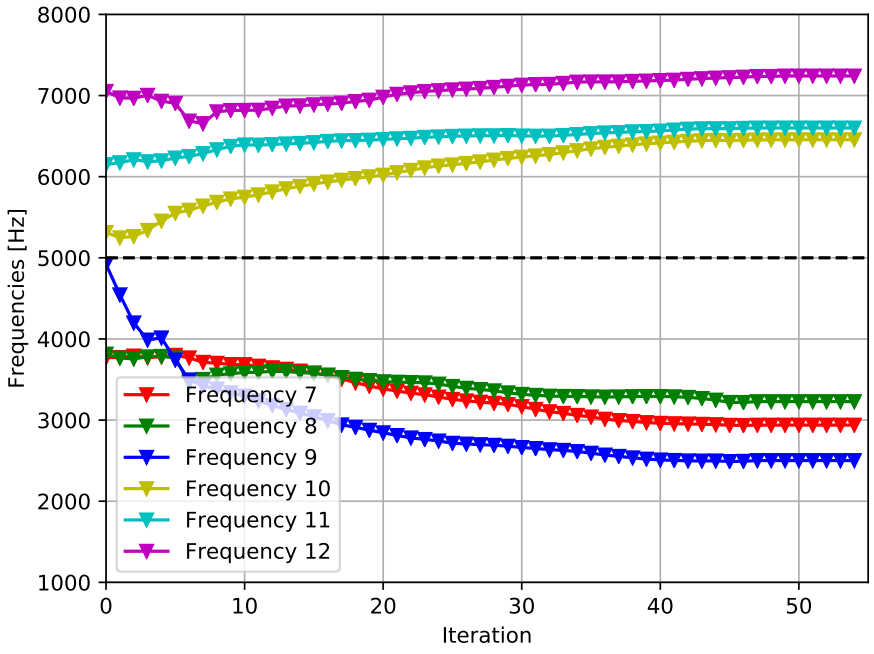

Figure 3.39 – Evolution of the closest natural frequencies to 5 kHz for the 3D clamped-clamped optimization with VFM.

Finally, the FRF from this structure is evaluated (Figure 3.40). The increase in

the natural frequency separation around 5 kHz was of roughly 2835 from 392 Hz to 3227 Hz. This is a significant increase in the interval without resonance, which is clearly seen in both Figure 3.39 and Figure 3.40. Furthermore, unlike the previous cases, all modes are considered here, even torsional ones and out of plane ones; thus, there is lower risk of unaccounted modes appearing, as they did in Section 3.3.4.

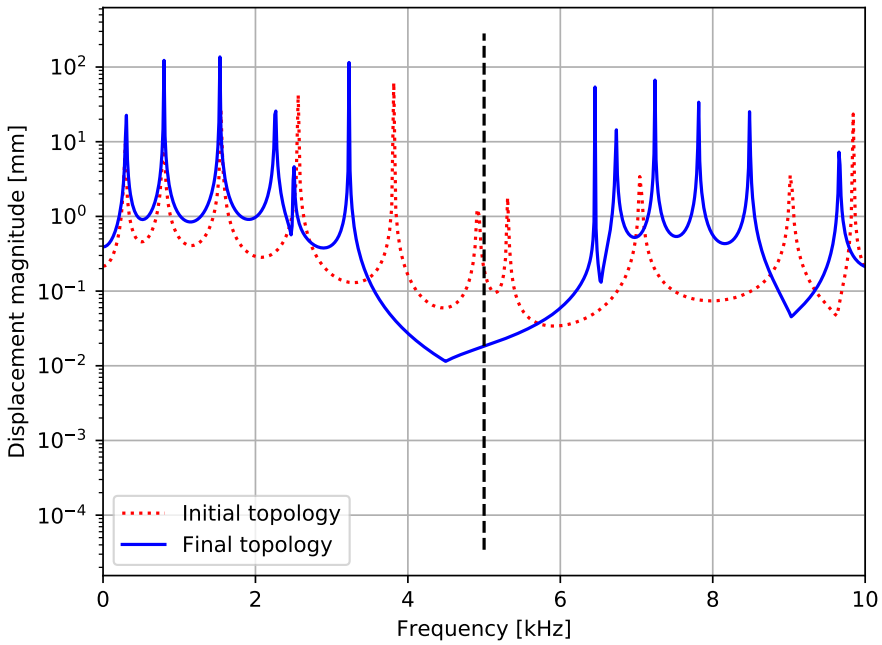

Figure 3.40 – Frequency response of the initial and final topologies for the 3D clamped-clamped optimization with VFM.

3.4 Conclusions

In this chapter, a connectivity algorithm designated as the Virtual Flux Method was proposed. It functions by guaranteeing that two regions defined by the user are maintained connected throughout the optimization. Their connectivity was preserved by bars whose areas are proportional to the user-given parameters.

To show this method in action and to validate it, seven problems were presented. The first one was the optimization of the first natural frequency of a cantilever beam. Here, we showed that the VFM was able to stop the optimization into going towards the trivial solution of reducing the length of the beam. In the second one, we changed the physics and the objective function, showing how the VFM can be extended to other kinds of problem. The third one

was the optimization of the natural frequencies of a cantilever beam. In this case, the optimization procedure would tend to reduce its length and disconnect it close to the clamped region. The VFM guaranteed its connectivity. The fourth case was similar, however, it was optimized considering the appropriate parameters and constraints for an experimental analysis, which was subsequently carried out to validate the numerical procedures. The fifth case corresponds to the same problem as Section 2.3.1. Here, a similar topology was obtained, compared to the two-material optimization counterpart, but the VFM guaranteed that the connectivity between the two clamped ends was maintained. Similarly, for the sixth case a different domain was chosen for the optimization, a ring structure. The VFM showed to be able to connect the structure here, but it also showed that it did not interfere with the optimization when it is not required for maintaining connectivity. Finally, a full 3D optimization case was presented, illustrating how the VFM works in a higher dimension.

4 OPTIMIZATION OF ACOUSTIC-STRUCTURE COUPLED SYSTEMS

Given a successful implementation of high natural frequency optimization for connected structures, we now focus on including a fluid phase, to extend the results to acoustic applications. Thus, this chapter presents the acoustic-structure formulation necessary so solve these kinds of problems and some analyses on the coupling between both phases.

4.1 Formulation of the acoustic-structure domain

This section presents the formulation for the acoustic domain used in this work. It is then combined with the structural formulation from Chapter 2 to obtain a coupled system.

4.1.1 Acoustic domain

The acoustic domain is indicated in Figure 4.1.

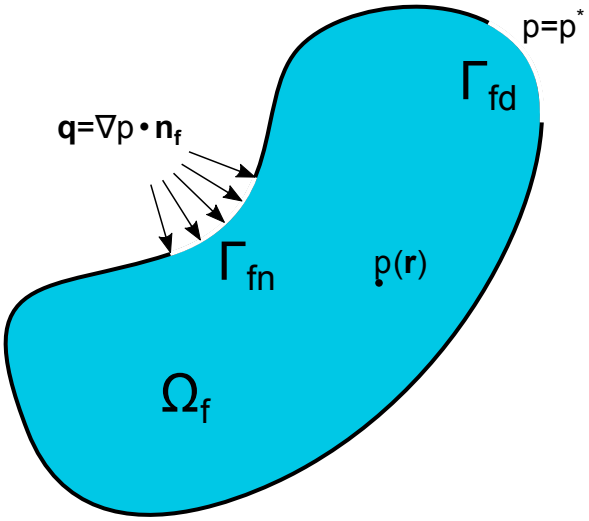

Figure 4.1 – Acoustic domain.

The acoustic domain is composed of an incompressible, inviscid fluid with negligible convective acceleration effects. When applied to the Navier-Stokes equation, these hypotheses lead to the following wave equation:

$$\begin{cases} \frac{1}{c_f^2}\ddot{p} - \nabla \cdot (\nabla p) = \mathbf{b_f} & \text{, on } \Omega_f \\ p(\mathbf{r}) = p^* & \text{, on } \Gamma_{fd} \\ \mathbf{q} = \nabla p \cdot \mathbf{n_f} & \text{, on } \Gamma_{fn}, \end{cases} \tag{4.1}$$

where c_f is the speed of sound on the medium, and p^* is the set pressure for the Dirichlet boundary condition.

After applying the Finite Element Method, the acoustic domain system becomes:

$$\mathbf{Q}_g\ddot{\mathbf{p}} + \mathbf{H}_g\mathbf{p} = \mathbf{q}_{\mathbf{p}g}, \tag{4.2}$$

where $\mathbf{Q}_g$ and $\mathbf{H}_g$ are, respectively, the compressibility and kinetic matrices, which can be assembled from their elemental counterparts:

$$\mathbf{Q}_g = \sum_{e=1}^{N_{el}} \mathbf{Q}_e, \tag{4.3}$$

$$\mathbf{H}_g = \sum_{e=1}^{N_{el}} \mathbf{H}_e, \tag{4.4}$$

$$\mathbf{q}_{\mathbf{p}g} = \sum_{e=1}^{N_{el}} \mathbf{q}_{\mathbf{p}e}, \tag{4.5}$$

$$\mathbf{H}_e = \int_{\Omega_s} \frac{1}{c_f^2} {\mathbf{N_f}}^T \mathbf{N_f} d\Omega, \tag{4.6}$$

$$\mathbf{Q}_e = \int_{\Omega_s} {\mathbf{B_f}}^T \mathbf{B_f} d\Omega, \tag{4.7}$$

$$\mathbf{f}_e = \int_{\Gamma_{sn}} {\mathbf{N_s}}^T \left(\nabla p \cdot \mathbf{n_s}\right) d\Gamma + \int_{\Omega_s} {\mathbf{N_s}}^T \mathbf{b_f} d\Omega, \tag{4.8}$$

where $\mathbf{N_f}$ is the matrix of shape functions, and $\mathbf{B_f}$ is the matrix of shape function derivatives for the acoustic domain.

Once again, problems are modeled either as two-dimensional or three-dimensional. Two-dimensional cases are discretized in 4-node isoparametric quadrilateral elements with the following matrices:

$$\mathbf{N_f} = \begin{bmatrix} N_1 & N_2 & N_3 & N_4 \\ N_1 & N_2 & N_3 & N_4 \end{bmatrix}, \tag{4.9}$$

$$\mathbf{B_f} = \begin{bmatrix} \frac{\partial N_1}{\partial x} & \frac{\partial N_2}{\partial x} & \frac{\partial N_3}{\partial x} & \frac{\partial N_4}{\partial x} \\ \frac{\partial N_1}{\partial y} & \frac{\partial N_2}{\partial y} & \frac{\partial N_3}{\partial y} & \frac{\partial N_4}{\partial y} \end{bmatrix}. \tag{4.10}$$

For the three dimensional cases, the matrices are:

$$\mathbf{N_f} = \begin{bmatrix} N_1 & N_2 & & N_7 & N_8 \\ N_1 & N_2 & \cdots & N_7 & N_8 \\ N_1 & N_2 & & N_7 & N_8 \end{bmatrix}, \tag{4.11}$$

$$\mathbf{B_f} = \begin{bmatrix} \frac{\partial N_1}{\partial x} & \frac{\partial N_2}{\partial x} & & \frac{\partial N_7}{\partial x} & \frac{\partial N_8}{\partial x} \\ \frac{\partial N_1}{\partial y} & \frac{\partial N_2}{\partial y} & \cdots & \frac{\partial N_7}{\partial y} & \frac{\partial N_8}{\partial y} \\ \frac{\partial N_1}{\partial z} & \frac{\partial N_2}{\partial z} & & \frac{\partial N_7}{\partial z} & \frac{\partial N_8}{\partial z} \end{bmatrix}. \tag{4.12}$$

The matrices are assembled via numerical integration using the Gauss-Legendre quadrature.

4.1.2 Acoustic-structure interaction

The coupled acoustic-structure problem is represented by Figure 4.2.

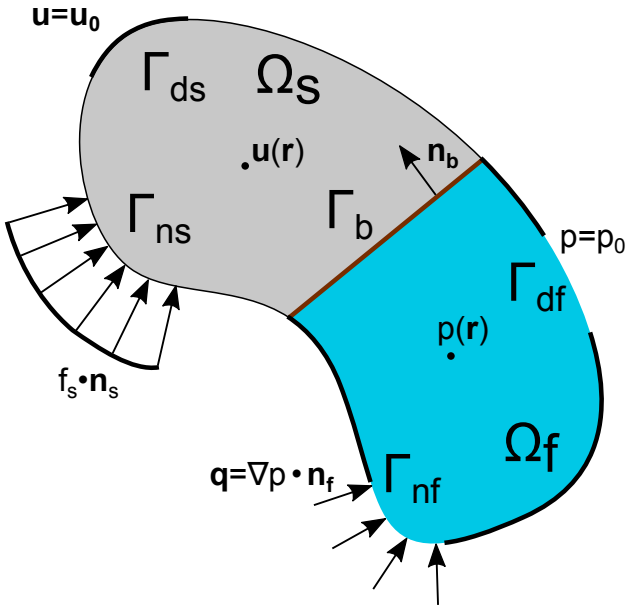

Figure 4.2 – Acoustic-structure domain.

This coupled system is formulated by using the segregated u/p model (Zienkiewicz; Bettess, 1978), where each domain is separately modeled by the formulation from either Section 2.1.1 or Section 4.1.1. The interactions between both domains are represented by forces:

$$\mathbf{f_{fs}} = p\mathbf{n_b}, \tag{4.13}$$

$$\mathbf{g_{sf}} = -\rho_f \mathbf{n_b} \cdot \ddot{\mathbf{u}}, \tag{4.14}$$

where $\mathbf{f_{fs}}$ and $\mathbf{q_{sf}}$ are, respectively, the force the fluid exerts on the structure and the force the structure exerts on the fluid. This relation leads to the following Finite Element formulation:

$$\mathbf{f_{fs}} = \int_{\Gamma_b} \mathbf{N_s}^T \mathbf{n_b} \mathbf{N_f} d\Gamma_b \; \mathbf{p} = \mathbf{L}\mathbf{p} = -\mathbf{L}_p \mathbf{p}, \tag{4.15}$$

$$\mathbf{g_{sf}} = -\int_{\Gamma_b} \rho_f \mathbf{N_f}^T \mathbf{n_b}^T \mathbf{N_s} d\Gamma_b \; \ddot{\mathbf{a}} = -\rho_f \mathbf{L}^T \ddot{\mathbf{a}} = -\mathbf{L}_u \ddot{\mathbf{a}}. \tag{4.16}$$

Applying these forces on the models from the solid and fluid domains, Eq. (2.3) and Eq. (4.2), the following system results:

$$\begin{cases} \mathbf{M}_g \ddot{\mathbf{a}} + \mathbf{K}_g \mathbf{a} - \mathbf{L}\mathbf{p} = \mathbf{f}_g \\ \mathbf{Q}_g \ddot{\mathbf{p}} + \mathbf{H}_g \mathbf{p} + \rho_f \mathbf{L}^T \ddot{\mathbf{a}} = \mathbf{q_p}_g \end{cases}. \tag{4.17}$$

This equation can be rewritten in a matricial form:

$$\begin{bmatrix} \mathbf{M}_g & \mathbf{0} \\ \mathbf{L}_u & \mathbf{Q}_g \end{bmatrix} \begin{Bmatrix} \ddot{\mathbf{a}} \\ \ddot{\mathbf{p}} \end{Bmatrix} + \begin{bmatrix} \mathbf{K}_g & \mathbf{L}_p \\ \mathbf{0} & \mathbf{H}_g \end{bmatrix} \begin{Bmatrix} \mathbf{a} \\ \mathbf{p} \end{Bmatrix} = \begin{Bmatrix} \mathbf{f}_g \\ \mathbf{q_p}_g \end{Bmatrix}, \tag{4.18}$$

$$\mathbf{G}_g \ddot{\mathbf{y}} + \mathbf{A}_g \mathbf{y} = \mathbf{w}_g. \tag{4.19}$$

With this equation, we can obtain the corresponding eigenproblems by assuming a free-response:

$$\omega_k^2 \mathbf{G}_g \phi_{\mathbf{k}} = \mathbf{A}_g \phi_{\mathbf{k}}, \tag{4.20}$$

$$\omega_k^2 \psi_{\mathbf{k}}{}^T \mathbf{G}_g = \psi_{\mathbf{k}}{}^T \mathbf{A}_g, \tag{4.21}$$

where $\psi_{\mathbf{k}}$ is the kth left eigenvector. As the matrices are non-hermitian, in this case, the eigenvectors from the left and the right are different. These equations can be rewritten in a matricial form:

$$\mathbf{G}_g \mathbf{\Phi} \mathbf{\Lambda} = \mathbf{A}_g \mathbf{\Phi}, \tag{4.22}$$

$$\mathbf{\Lambda} \mathbf{\Psi}^T \mathbf{G}_g = \mathbf{\Psi}^T \mathbf{A}_g, \tag{4.23}$$

where $\mathbf{\Psi}$ is the left eigenvector matrix, defined as:

$$\mathbf{\Psi} = \begin{bmatrix} \psi_{\mathbf{1}} & \psi_{\mathbf{2}} & \cdots & \psi_{\mathbf{n}} \end{bmatrix}. \tag{4.24}$$

In this case, the eigenvectors can be normalized so that:

$$\mathbf{I}_{N_{\text{dof}}} = \mathbf{\Psi}^T \mathbf{G}_g \mathbf{\Phi}, \tag{4.25}$$

$$\mathbf{\Lambda} = \mathbf{\Psi}^T \mathbf{A}_g \mathbf{\Phi}. \tag{4.26}$$

This eigenproblem, is once again, solved using the SLEPc library using the Krylov-Schur algorithm. The intermediate linear systems are solved by the LU factorization from the Intel® MKL PARDISO library. For faster computational times during the optimization, the pairs of eigenvectors obtained from the previous iteration are used as the initial space at the next iteration.

The eigenvectors from this system represent both the pressure field for the acoustic domain and the displacement for the structural one. Regarding the assembly of the coupling matrix, despite it only existing at the Γ_b surface, it does not require a boundary identification algorithm. Appendix D shows how this process can be conducted via an assembly procedure on the entire domain.

When compared to the mixed u/p formulation (Wang; Bathe, 1997), the most significant drawback of the segregated formulation is the asymmetry of the matrices $\mathbf{G}_g$ and $\mathbf{A}_g$, which increases the computational cost of both linear system and eigenvalue solvers. Its advantage, however, is the non-singularity of the mass matrix, and the clear separation between elastic and fluid phases.

4.2 Formulation of the acoustic-structure optimization

In this section, the main differences between solely structural optimization and acoustic-structure integrated one will be presented.

4.2.1 Changes to the sensitivity analysis

In the acoustic-structure optimization formulation, the objective function remains the same that was presented in Eq. (2.39). This way, the sensitivity analysis can be performed

similarly to what was done in Section 2.2.2, aside from the two different eigenvectors and the new terms.

The sensitivity analysis of this objective function is given by Eq. (2.41), which is repeated here:

$$\alpha_e = \frac{\partial f(x_e)}{\partial x_e} = \left[\sum_{k=1}^{N_m} \frac{1}{\left(\omega_k^2 - \omega_0^2\right)^2}\right]^{-\frac{3}{2}} \sum_{k=1}^{N_m} \frac{1}{\left(\omega_k^2 - \omega_0^2\right)^3} \frac{\partial(\omega_0^2)}{\partial x_e}. \tag{4.27}$$

The derivatives of the eigenvalues are given by the Rayleigh quotient:

$$\omega_k^2 = \frac{\psi_k^T \mathbf{A}_g \phi_k}{\psi_k^T \mathbf{G}_g \phi_k}. \tag{4.28}$$

Unlike the previous optimization studies, there is a difference between left and right eigenvectors. Thus, the derivative becomes:

$$\frac{\partial(\omega_k^2)}{\partial x_e} = \psi_k^T \left(\frac{\partial \mathbf{A}_g}{\partial x_e} - \omega_k^2 \frac{\partial \mathbf{G}_g}{\partial x_e}\right) \phi_k. \tag{4.29}$$

This expression can be expanded into a form with the structural and acoustic matrices:

$$\begin{aligned}\frac{\partial(\omega_k^2)}{\partial x_e} = {\psi_{\mathbf{k_s}}}^T \left(\frac{\partial \mathbf{K}_g}{\partial x_e} - \omega_k^2 \frac{\partial \mathbf{M}_g}{\partial x_e}\right) \phi_{\mathbf{k_s}} + {\psi_{\mathbf{k_f}}}^T \left(\frac{\partial \mathbf{H}_g}{\partial x_e} - \omega_k^2 \frac{\partial \mathbf{Q}_g}{\partial x_e}\right) \phi_{\mathbf{k_s}} \\ - \omega_k^2 {\psi_{\mathbf{k_f}}}^T \frac{\partial \mathbf{L}_u}{\partial x_e} \phi_{\mathbf{k_s}} + {\psi_{\mathbf{k_s}}}^T \frac{\partial \mathbf{L}_p}{\partial x_e} \phi_{\mathbf{k_f}},\end{aligned} \tag{4.30}$$

where the eigenvectors with the subscript s refer to the displacement degrees of freedom and the ones with the subscript f refer to the pressure degrees of freedom.

This shows that the sensitivities for an acoustic-structure interaction system possess terms corresponding to each characteristic of the fluid, the solid material, and their interface.

4.2.2 Modifications for void enclosed holes

In some cases, the optimization analysis is done considering that the fluid is only on the exterior part of the design domain. That is, if an enclosed hole appear during the optimization procedure, it is neither solid nor fluid, instead, it is void. Numerically, this can be done by setting the properties of this element to so that both the solid and the acoustic domains possess void properties ($x_e = x_{\min}$ for solid and $x_e = 1$ for void).

Nonetheless, the main challenge in this formulation, is finding which elements are within an enclosed void, and which ones are directly connected to the fluid domain. To do so, the Breadth-first search algorithm is employed (Cormen *et al.*, 2022). It functions by recursively checking the neighboring elements from the starting seed ones, stopping when a barrier is encountered. In the end, all elements not separated by the seed by barriers are detected. Figure 4.3 Illustrates the procedure.

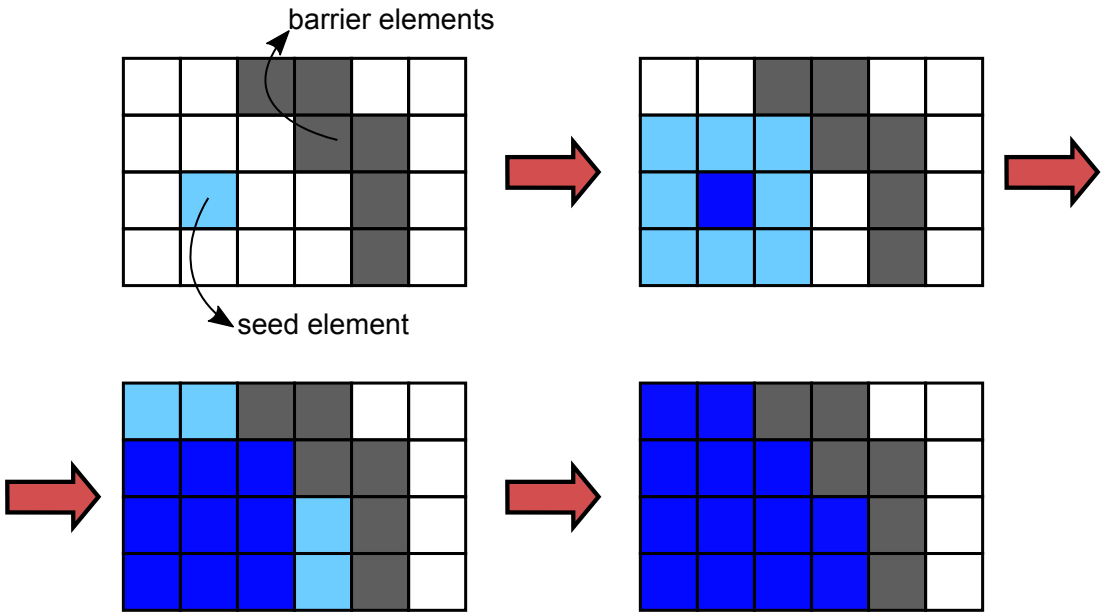

Figure 4.3 – Breadth-first search algorithm done to detect connected elements from seed.

From the point of view of the mathematical formulation of the system, a second design variable y_e is added. Whenever the Breadth-first search algorithm is employed, this variable is set to $y_e = 1$ on fluid elements, and to $y_e = x_{\text{min}}$ on solid or void ones. On the other hand, when performing a fluid-structure optimization with no voids, the Breadth-first search algorithm is not used and y_e is defined as:

$$y_e = 1 - x_e + x_{\text{min}}. \tag{4.31}$$

In the end, this design variable is used to interpolate the fluid-related parameters.

4.2.3 Interpolation scheme between structural and acoustic materials

The sensitivity analysis of an acoustic-structure system depends on the differentiation of several matrices, as previously shown in Eq. (4.30). Thus, an interpolation scheme for each one of them must be formulated (Jensen, 2019). The elastic properties are formulated

similar to Section 3.2. The fluid properties are interpolated based on the aforementioned fluid design variable y_e:

$$\mathbf{M}_e(x_e) = \mathbf{M}_e^1 x_e, \tag{4.32}$$

$$\mathbf{K}_e(x_e) = \mathbf{K}_e^1 \left[\frac{x_{\text{min}} - x_{\text{min}}^p}{1 - x_{\text{min}}^p}(1 - x_e^p) + x_e^p \right], \tag{4.33}$$

$$\mathbf{L}_{u_e}(x_e) = \mathbf{L}_{u_e}^1 \frac{1 - x_e}{1 - x_{\text{min}}} = \mathbf{L}_{u_e}^1 \frac{y_e - x_{\text{xmin}}}{1 - x_{\text{min}}}, \tag{4.34}$$

$$\mathbf{Q}_e(x_e) = \mathbf{Q}_e^1 \left(1 + x_{\text{min}} - x_e\right) = \mathbf{Q}_e^1 y_e, \tag{4.35}$$

$$\mathbf{H}_e(x_e) = \mathbf{H}_e^1 \left(1 + x_{\text{min}} - x_e\right) = \mathbf{H}_e^1 y_e, \tag{4.36}$$

$$\mathbf{L}_{p_e}(x_e) = \mathbf{L}_{p_e}^1 \frac{1 - x_e}{1 - x_{\text{min}}} = \mathbf{L}_{p_e}^1 \frac{y_e - x_{\text{xmin}}}{1 - x_{\text{min}}}, \tag{4.37}$$

where $\mathbf{M}_e^1$ and $\mathbf{K}_e^1$ are the elemental matrices assuming the element is structural, while $\mathbf{Q}_e^1$ and $\mathbf{H}_e^1$ are the elemental matrices assuming the element is acoustic. $\mathbf{L}_{u_e}^1$ and $\mathbf{L}_{p_e}^1$ are the matrices considering an interface at every border of the element, following the formulation from Appendix D.

With this definition, if $x_e = 1$, then the structural properties are solid, and the acoustic ones are rigid. If $x_e = x_{\text{min}}$ (and $y_e = 1$), then the structural properties are void and the acoustic ones are fluid. When considering the possibility of fully void elements, the direct relationship between x_e and y_e is lost, and void elements have $x_e = y_e = x_{\text{min}}$.

With these, the derivatives of the matrices can be calculated:

$$\frac{\partial \mathbf{M}_g}{\partial x_e} = \mathbf{M}_e^1, \tag{4.38}$$

$$\frac{\partial \mathbf{K}_g}{\partial x_e} = \frac{1 - x_{\text{min}}}{1 - x_{\text{min}}^p} p x_e^{p-1} \mathbf{K}_e^1, \tag{4.39}$$

$$\frac{\partial \mathbf{L}_u}{\partial x_e} = -\frac{1}{1 - x_{\text{min}}} \mathbf{L}_{u_e}^1, \tag{4.40}$$

$$\frac{\partial \mathbf{Q}_g}{\partial x_e} = -\mathbf{Q}_e^1, \tag{4.41}$$

$$\frac{\partial \mathbf{H}_g}{\partial x_e} = -\mathbf{H}_e^1, \tag{4.42}$$

$$\frac{\partial \mathbf{L}_p}{\partial x_e} = -\frac{1}{1 - x_{\text{min}}}\mathbf{L}_{p_e}^1. \tag{4.43}$$

Once again, when we consider void elements, the sensitivity terms of the coupling matrices and of the acoustic matrices change. Since most solid elements change to void elements in this case, these terms are not computed on the sensitivity when $y_e = x_{\text{min}}$.

With these expressions, we have all the necessary terms for the sensitivity analysis.

4.3 Sensitivity analysis on different components

In this section, the different terms of sensitivity are calculated for different types of structures and materials for the elastic and fluid phases. The domain of analysis is shown in Figure 4.4 is chosen.

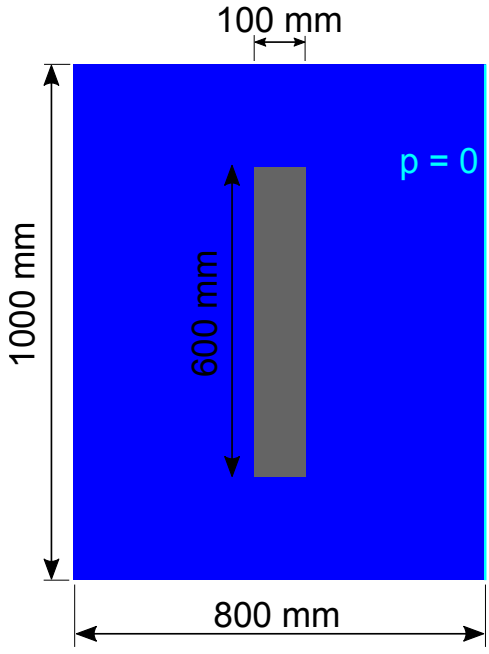

Figure 4.4 – Sensitivity analysis domain. Blue region represents fluid and gray region represents the design domain, which is initially solid.

Two studies are performed considering different fluids in the acoustic domain. In the first case, the fluid is air, with $c_f = 343$ m/s and $\rho_f = 1$ kg/m^3. The structural material has

the properties: $E = 70$ GPa, $\rho_s = 2700$ kg/m^3 and $\nu = 0.3$. This type of configuration may sometimes be referred to as a system with "weak coupling". This means that the modes from the system can be easily divided into acoustic and structural. In other words, the interactions between each domain can be treated as happening in one-way.

To verify the weakly-coupled behavior of the system, the 80 first eigenvalues are calculated under two conditions. In the first one, the system is purely acoustic, that is, modeled by the formulation of Section 4.1. In the second one, it is modeled with the acoustic-structure formulation (Section 4.2) with the aforementioned elastic properties. Table 4.1 shows the eigenvalues from both systems.

Table 4.1 – Comparison between natural frequencies of acoustic and acoustic-structure for weak coupling. The four modes without fluid values are structural.

Mode	Coupled	Fluid	Difference	Mode	Coupled	Fluid	Difference	Mode	Coupled	Fluid	Difference	Mode	Coupled	Fluid	Difference
1	24.9			21	862.5	862.5	0.00%	41	1287.5	1287.5	0.00%	61	1589.7	1589.7	0.00%
2	27.2			22	868.2	868.2	0.00%	42	1288.7	1288.7	0.00%	62	1626.4	1626.4	0.00%
3	32.5			23	887.4	887.4	0.00%	43	1309.8	1309.8	0.00%	63	1653.7	1653.7	0.00%
4	84.9	84.8	0.08%	24	909.9	909.9	0.00%	44	1333.0			64	1665.4	1665.4	0.00%
5	193.3	193.3	0.00%	25	978.6	978.6	0.00%	45	1344.9	1344.9	0.00%	65	1684.5	1684.5	0.00%
6	270.8	270.7	0.03%	26	992.7	992.7	0.00%	46	1353.0	1353.0	0.01%	66	1695.7	1695.7	0.00%
7	347.7	347.6	0.01%	27	1007.4	1007.4	0.00%	47	1383.4	1383.4	0.00%	67	1709.6	1709.6	0.00%
8	355.8	355.8	0.00%	28	1013.2	1013.2	0.00%	48	1406.3	1406.3	0.00%	68	1720.0	1720.0	0.00%
9	427.2	427.2	0.01%	29	1024.9	1024.9	0.00%	49	1407.5	1407.4	0.01%	69	1722.8	1722.8	0.00%
10	521.7	521.7	0.00%	30	1051.4	1051.4	0.00%	50	1436.4	1436.4	0.00%	70	1740.4	1740.4	0.00%
11	525.6	525.6	0.01%	31	1063.1	1063.1	0.00%	51	1456.0	1456.0	0.00%	71	1744.0	1744.0	0.00%
12	526.5	526.5	0.00%	32	1098.3	1098.3	0.00%	52	1461.0	1461.0	0.00%	72	1757.0	1757.0	0.00%
13	604.5	604.5	0.00%	33	1128.2	1128.2	0.00%	53	1473.9	1473.9	0.00%	73	1762.8	1762.8	0.00%
14	610.0	610.0	0.00%	34	1143.9	1143.9	0.00%	54	1484.1	1484.1	0.00%	74	1791.8	1791.8	0.00%
15	693.2	693.2	0.00%	35	1187.5	1187.5	0.00%	55	1540.1	1540.0	0.00%	75	1809.5	1809.5	0.00%
16	698.6	698.5	0.00%	36	1188.4	1188.4	0.00%	56	1549.9	1549.9	0.00%	76	1817.1	1817.1	0.00%
17	747.8	747.8	0.00%	37	1220.5	1220.5	0.00%	57	1552.2	1552.2	0.00%	77	1829.7	1829.7	0.00%
18	757.1	757.1	0.00%	38	1222.1	1222.1	0.00%	58	1561.4	1561.4	0.00%	78	1837.1	1837.1	0.00%
19	792.6	792.6	0.00%	39	1236.5	1236.5	0.00%	59	1581.5	1581.5	0.00%	79	1861.1	1861.1	0.00%
20	804.7	804.7	0.00%	40	1271.7	1271.7	0.00%	60	1586.0	1586.0	0.00%	80	1861.9	1861.9	0.00%

The comparison between fluid and coupled domains shows clearly that the modes from both cases are the same. The only four differences seen in Table 4.1 are related to structural modes (which evidently don't appear in the fluid analysis). The first three modes are the rigid-body modes of the structure, whose eigenvalues are not zero here because of the fluid.

The sensitivity analysis of the acoustic-structure interaction system is performed to evaluate the influence of each term from Eq. (4.30). In this study, the operating frequency is adopted as 900 Hz. These terms are presented separately in Figure 4.5.

A quick analysis of these sensitivities indicate that, for this system, the influence of the structural and coupling terms are negligible compared to the acoustic ones. This can be understood as a logical conclusion from the modes being nearly identical to the purely acoustic ones, as it would also imply that they are not dependent on the elastic properties of the structure (as long as they remain within the weak-coupling hypothesis).

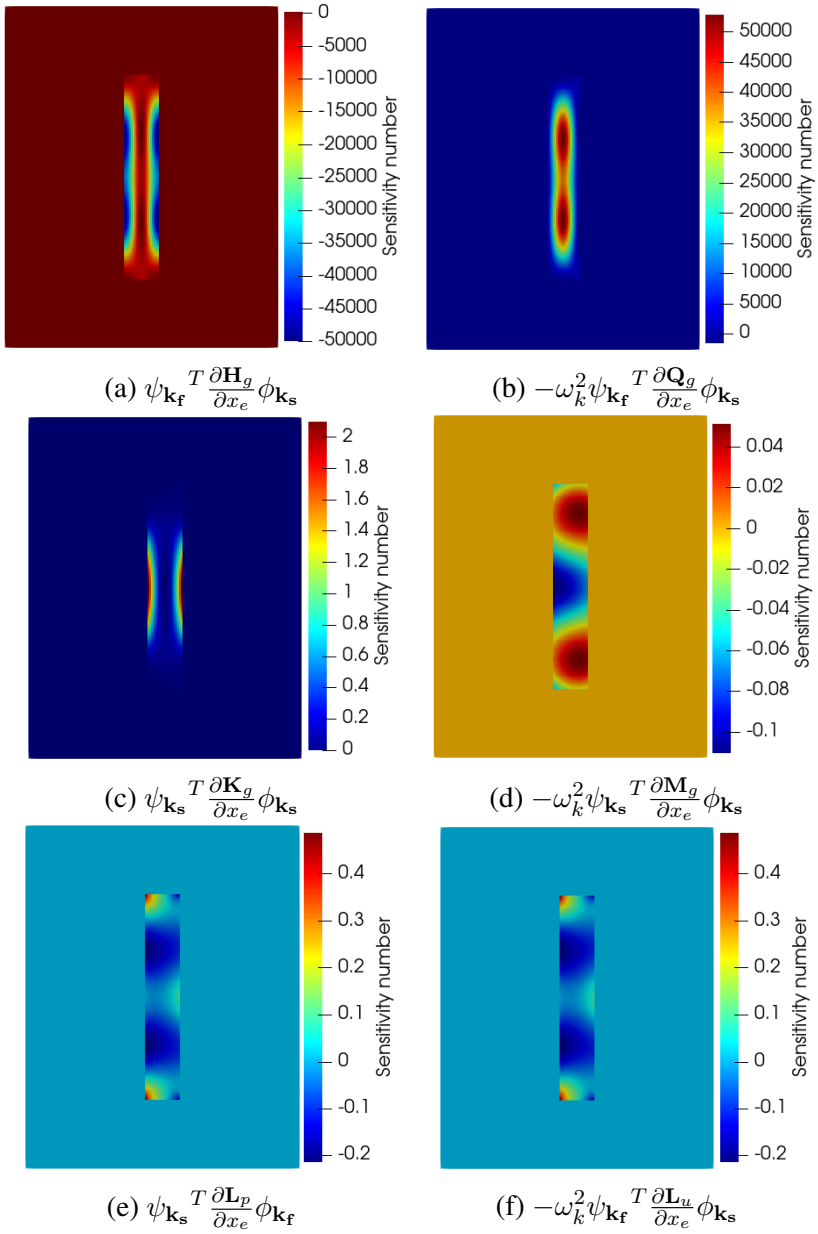

(a) $\psi_{\mathbf{k_f}}{}^T \frac{\partial \mathbf{H}_g}{\partial x_e} \phi_{\mathbf{k_s}}$ (b) $-\omega_k^2 \psi_{\mathbf{k_f}}{}^T \frac{\partial \mathbf{Q}_g}{\partial x_e} \phi_{\mathbf{k_s}}$

(c) $\psi_{\mathbf{k_s}}{}^T \frac{\partial \mathbf{K}_g}{\partial x_e} \phi_{\mathbf{k_s}}$ (d) $-\omega_k^2 \psi_{\mathbf{k_s}}{}^T \frac{\partial \mathbf{M}_g}{\partial x_e} \phi_{\mathbf{k_s}}$

(e) $\psi_{\mathbf{k_s}}{}^T \frac{\partial \mathbf{L}_p}{\partial x_e} \phi_{\mathbf{k_f}}$ (f) $-\omega_k^2 \psi_{\mathbf{k_f}}{}^T \frac{\partial \mathbf{L}_u}{\partial x_e} \phi_{\mathbf{k_s}}$

Figure 4.5 – Sensitivity terms corresponding to each component of the stiffness and mass matrices for weak coupling.

This, however, should not be understood as if this will always be the case for any configuration with those materials. Figure 4.6 shows an example where these terms are not negligible, despite using these same fluid and elastic properties. This is due to the thin components of this topology, which vibrate locally with lower natural frequencies, compared to the previously presented full topology.

Thus, since there is no way to know ahead of time whether the topology will extrapolate this hypothesis throughout the evolution, we have two possibilities: either we adopt the hypothesis and verify it at the end of the optimization, or we don't adopt it and consider fluid-

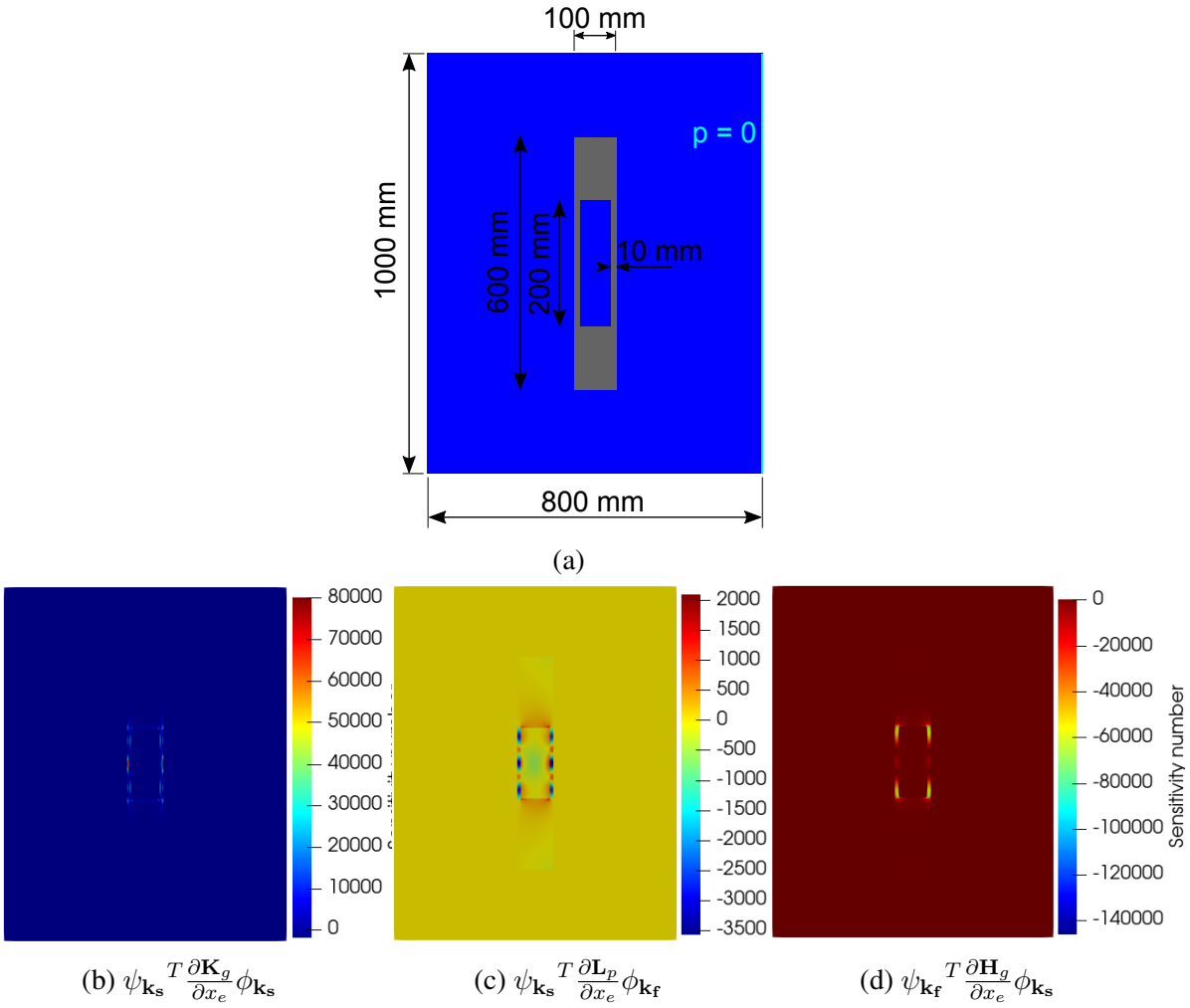

Figure 4.6 – Some sensitivity terms for a structure with thin components.

structure interaction. A lot of works in topology optimization of acoustic-structure systems do the first one (Picelli *et al.*, 2015a; Pereira *et al.*, 2022), assuming that the system will remain weakly-coupled throughout the optimization. However, that may not be necessarily the case, as illustrated here.

Finally, there is a different kind of problem, often called a "strongly-coupled" system, where the elastic and acoustic properties are so that the interactions between solid and fluid cannot be ignored, and therefore, the modes can not be separated between acoustic and structural. In this case, the fluid has the properties $c_f = 1450$ m/s and $\rho_f = 1000$ kg/m^3. The structural material has the properties: $E = 70$ GPa, $\rho_s = 2700$ kg/m^3 and $\nu = 0.3$.

As before, the 80 first eigenvalues are calculated considering a purely acoustic system and an acoustic-structure one. The results are shown in Table 4.2.

Since the first three modes on the coupled system are very small, they are assumed to be rigid-body modes, and thus, are not counted for the comparison. Despite that, the differences

Table 4.2 – Comparison between natural frequencies of acoustic and acoustic-structure for strong coupling.

Mode	Coupled	Fluid	Difference	Mode	Coupled	Fluid	Difference	Mode	Coupled	Fluid	Difference	Mode	Coupled	Fluid	Difference
1	18.1			21	3363.6	3645.2	8.37%	41	5148.6	5442.6	5.71%	61	6600.9	6871.1	4.09%
2	40.9			22	3504.0	3669.9	4.74%	42	5231.4	5446.2	4.11%	62	6671.1	6990.4	4.79%
3	47.6			23	3652.4	3751.0	2.70%	43	5295.1	5535.5	4.54%	63	6727.8	7037.7	4.61%
4	445.8	358.6	19.57%	24	3656.5	3845.6	5.17%	44	5438.1	5685.1	4.54%	64	6793.4	7118.8	4.79%
5	841.6	817.2	2.91%	25	3875.1	4136.8	6.75%	45	5476.2	5717.1	4.40%	65	6811.4	7167.7	5.23%
6	1083.8	1144.2	5.57%	26	3906.8	4195.6	7.39%	46	5515.1	5845.1	5.98%	66	7009.5	7225.1	3.08%
7	1331.1	1469.5	10.40%	27	3924.4	4257.9	8.50%	47	5547.2	5943.0	7.13%	67	7012.3	7264.2	3.59%
8	1505.6	1503.9	0.11%	28	4161.0	4282.9	2.93%	48	5747.7	5947.7	3.48%	68	7098.4	7278.7	2.54%
9	1526.1	1805.8	18.33%	29	4247.7	4332.0	1.99%	49	5765.2	6070.3	5.29%	69	7125.8	7350.5	3.15%
10	1939.3	2205.2	13.71%	30	4298.6	4444.3	3.39%	50	5901.7	6152.6	4.25%	70	7197.8	7365.8	2.33%
11	2204.1	2221.6	0.79%	31	4308.1	4492.7	4.29%	51	5917.7	6175.3	4.35%	71	7205.6	7425.9	3.06%
12	2306.6	2225.5	3.52%	32	4388.6	4642.8	5.79%	52	6008.4	6229.4	3.68%	72	7264.0	7450.3	2.56%
13	2318.5	2555.2	10.21%	33	4449.5	4768.1	7.16%	53	6070.6	6272.7	3.33%	73	7346.6	7567.9	3.01%
14	2532.6	2578.7	1.82%	34	4557.7	4834.2	6.06%	54	6151.2	6509.8	5.83%	74	7350.5	7642.6	3.97%
15	2661.6	2929.9	10.08%	35	4697.5	5019.7	6.86%	55	6213.1	6547.3	5.38%	75	7384.3	7681.4	4.02%
16	2736.4	2952.7	7.91%	36	4762.7	5021.7	5.44%	56	6214.4	6559.9	5.56%	76	7498.0	7732.8	3.13%
17	2939.8	3160.7	7.51%	37	4800.2	5157.4	7.44%	57	6290.4	6598.4	4.90%	77	7522.1	7761.1	3.18%
18	3146.7	3200.3	1.70%	38	4991.4	5165.3	3.48%	58	6491.5	6681.3	2.92%	78	7553.6	7864.4	4.11%
19	3198.4	3350.6	4.76%	39	5017.2	5226.4	4.17%	59	6547.5	6702.6	2.37%	79	7642.6	7868.2	2.95%
20	3250.2	3401.4	4.65%	40	5136.3	5375.4	4.65%	60	6569.2	6719.7	2.29%	80	7732.8	7898.2	2.14%

between coupled and fluid modes are so significant that there is no easy way to directly correlate them. This shows that the solid domain influences every eigenvalue, and thus, we must perform the full fluid-structure analysis.

Once again, we perform the sensitivity analysis of the acoustic-structure interaction system. In this analysis, the operating frequency is adopted as 3600 Hz. This frequency was chosen because it is around the same mode (at least when counting them in ascending order) from the previous analysis. The terms from the sensitivity are presented separately in Figure 4.7.

Here, we see that the sensitivity terms from the elastic and interaction properties are not irrelevant, when compared to the fluid ones. Admittedly, they are not as close as one would expect; however, they indicate that throughout the optimization (where these other parameter might increase in importance) we must account for these terms.

Thus, in theory, one should account for the full sensitivity terms. However, while these analyses indicated a higher accuracy on the sensitivity estimation, the only way to see how they perform during optimization is testing.

4.4 Optimization of sliding-fixed beam

In this section, some optimization results are presented. The acoustic-structure formulation from chapter, and the optimization algorithms from Chapters 2 and 3 are used. The following domain is taken from Jensen (2019). On their work, they perform the optimization of dynamic compliance of a sliding-fixed domain Figure 4.8, with two identical harmonic forces

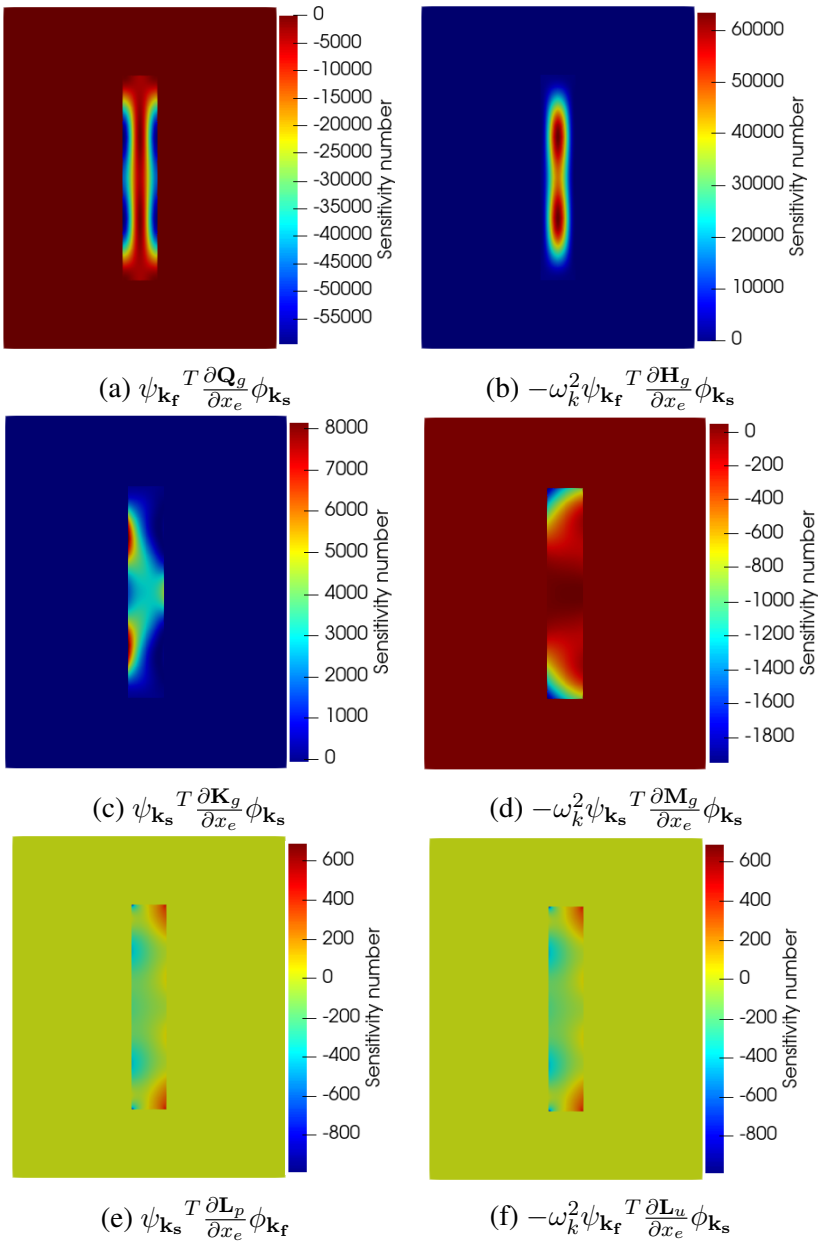

(a) $\psi_{\mathbf{k_f}}{}^T \frac{\partial \mathbf{Q}_g}{\partial x_e} \phi_{\mathbf{k_s}}$ (b) $-\omega_k^2 \psi_{\mathbf{k_f}}{}^T \frac{\partial \mathbf{H}_g}{\partial x_e} \phi_{\mathbf{k_s}}$

(c) $\psi_{\mathbf{k_s}}{}^T \frac{\partial \mathbf{K}_g}{\partial x_e} \phi_{\mathbf{k_s}}$ (d) $-\omega_k^2 \psi_{\mathbf{k_s}}{}^T \frac{\partial \mathbf{M}_g}{\partial x_e} \phi_{\mathbf{k_s}}$

(e) $\psi_{\mathbf{k_s}}{}^T \frac{\partial \mathbf{L}_p}{\partial x_e} \phi_{\mathbf{k_f}}$ (f) $-\omega_k^2 \psi_{\mathbf{k_f}}{}^T \frac{\partial \mathbf{L}_u}{\partial x_e} \phi_{\mathbf{k_s}}$

Figure 4.7 – Sensitivity terms corresponding to each component of the stiffness and mass matrices for strong coupling.

at the edges of the sliding end. Additionally, they consider the fluid boundary conditions as absorbing surfaces. For simplicity (to maintain an undamped system), we consider them as surfaces with an imposed pressure.

The design domain is the beam-like region, which, once again, starts fully structural in the optimization study. The elastic region is made of a hypothetical material with $E_s = 500$ MPa, $\rho_s = 1200$ kg/m^3, and $\nu = 0.4$. The acoustic region is filled with water, with $\rho_f = 1000$ kg/m^3, and $c_f = 1450$ m/s. These properties are enough for the coupling to be strong. The design domain is discretized in a 400×80 mesh. Finally, the BESO parameters are set to: ER

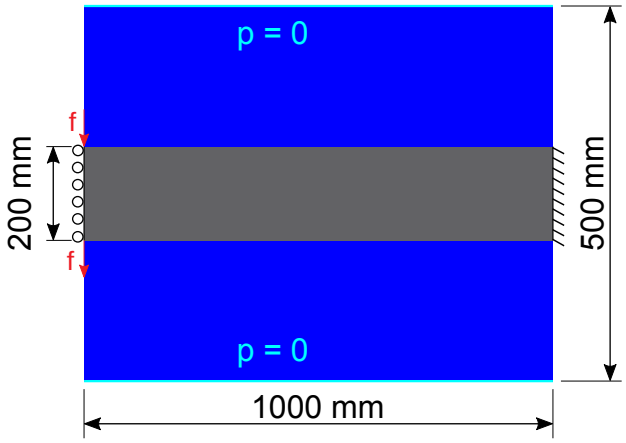

Figure 4.8 – Design domain for sliding-fixed problem surrounded by fluid.

= 1%, AR_{max} = 1%, final volume $V^* = 40\%$, $r_{\text{min}} = 12$ mm, penalty factor $p = 3$.

Much like Jensen (2019) does in his work, we start with the pure static compliance optimization. On this case and the subsequent dynamic compliance case, there are two vertical forces, applied on the edges of the sliding end (as indicated in Figure 4.8), and only the design domain is simulated.

After 117 iterations, the topology from Figure 4.9a is obtained. Furthermore, the evolution of the compliance and volume are shown in Figure 4.9b.

(a)

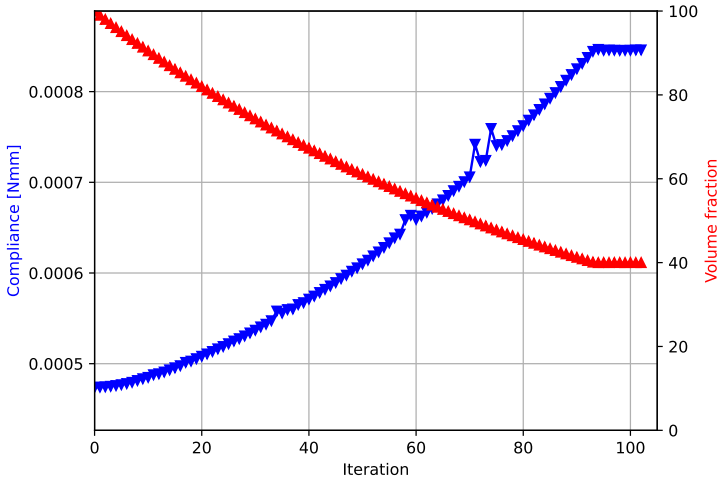

(b)

Figure 4.9 – Compliance optimization of sliding-fixed beam. (a) Final topology (b) Objective function.

This optimization is very stable, and the topology is similar to the one from Jensen (2019). Despite the non-symmetric boundary conditions, the final topology is symmetrical. Furthermore, very little instability is seen on the objective function during the optimization.

The second optimization case is a dynamic compliance optimization case, considering an excitation frequency of 30 Hz (note that the first natural frequency of the fully solid design is about 33.8 Hz). The final topology is shown in Figure 4.10a. Additionally, the objective function and volume are in Figure 4.10b.

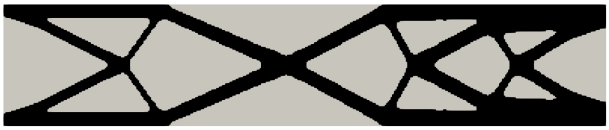

(a)

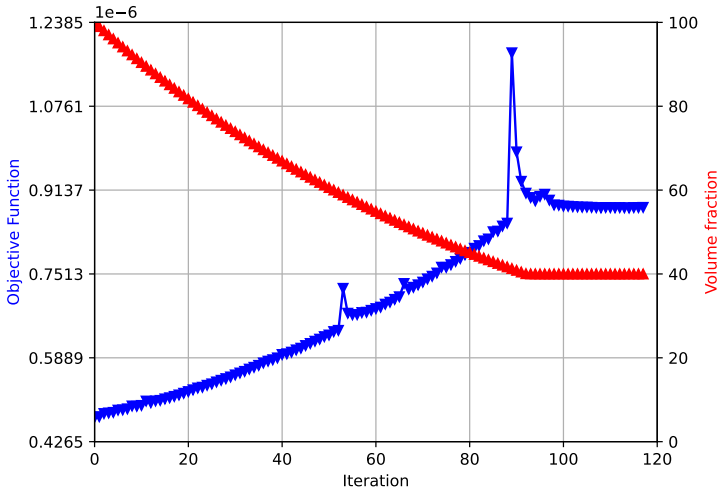

(b)

Figure 4.10 – Dynamic compliance optimization of sliding-fixed beam. (a) Final topology (b) Objective function.

Once again, a great level of similarity can be drawn between this topology and the one from Jensen (2019). When employing a dynamic model, the symmetry is lost during the optimization (at least one of them). The left part in the end is made more compliant, while the right one is stiffened.

Now, the same domain is used for the optimization of the first natural frequency. Much like the optimization from Section 3.3.1, connectivity between both edges is lost at some point during the optimization, leaving only a cantilever beam. Then the optimization goes towards the trivial solution of reducing its length. For this reason, the VFM is employed here and on all subsequent cases. The activation length is set to 100 mm, and the critical one to 50

mm. The connectivity is imposed between the right and left extremities, and the dilation radius is $r_{\text{dil}} = 6$ mm. The final topology and objective function are shown in Figures 4.11a and 4.11b.

(a)

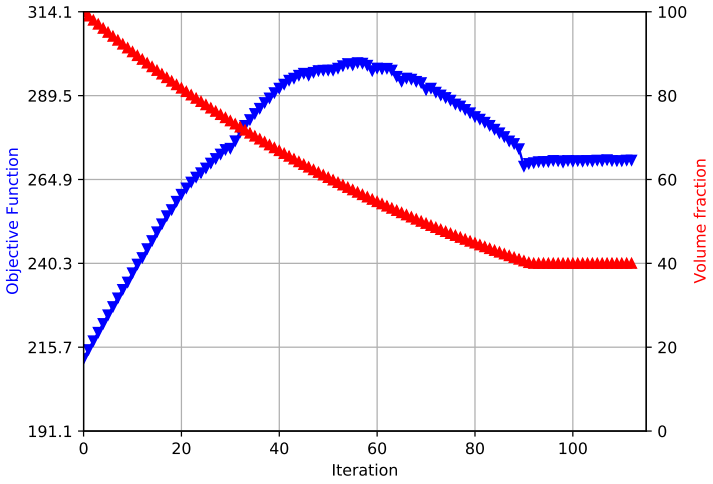

(b)

Figure 4.11 – Fundamental frequency optimization of sliding-fixed beam. (a) Final topology (b) Objective function.

The first natural frequency increased from 33.8 Hz to 43.1 Hz. Much like the previous case, there is a concentration of material on the right side of the structure, leaving the left one more flexible. Nevertheless, compared to the previous topologies, this one has a much rounder shape.

Looking at Figure 4.11b, we can also see that the imposed volume fraction is actually hindering the performance of the structure. If one desired a topology with maximum fundamental frequency no matter the volume, this curve indicates that using around 60% of material would be better. Although a precise assessment would require complete optimization analyses with different volume constraints. Note also that the VFM parameters are also very influential in this case, as the external outline of the structure is mostly maintained by it.

Having performed the preliminary analyses of this case, we can now run some acoustic-structure optimization studies. Initially, we consider the presence of void elements with the Breadth-first search algorithm (Section 4.2.2). The fluid phase is imposed at the top and bottom of the design domain (as shown in Figure 4.8). Any enclosed voids that end up

appearing inside the solid domain is considered as void. In all subsequent cases of this section, the optimization will be done in the first natural frequency. Note that the inclusion of the fluid domain decreases the initial value of the natural frequency to 23.6 Hz.

Initially, we perform an optimization case considering only the structural terms of the sensitivity (Eqs. (4.38) and (4.39)). With this in mind, after 102 iterations, the topology from Figure 4.12a is obtained. The objective function is shown in Figure 4.12b.

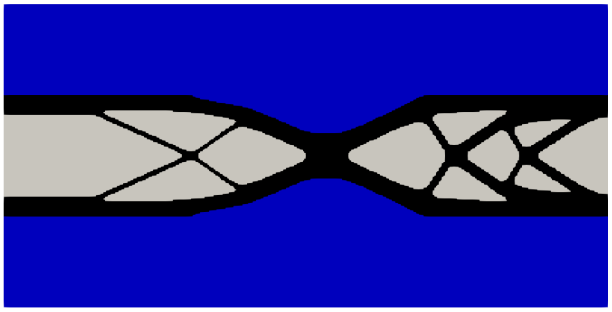

(a)

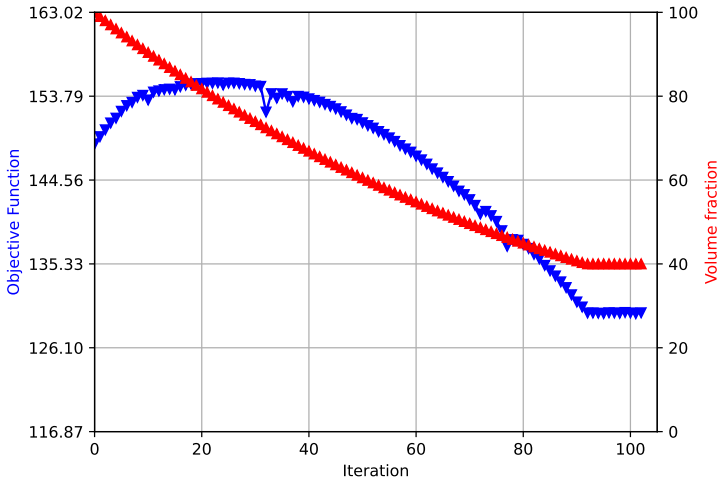

(b)

Figure 4.12 – Fundamental frequency optimization of sliding-fixed beam with acoustic-structure interaction, enclosed voids and solid sensitivities. (a) Final topology (b) Objective function.

This topology is very similar to the previous one (Figure 4.11a). However, unlike it, the natural frequency actually decreases from 23.6 Hz to 20.7 Hz. The objective function behaves as a curve with similar shape to Figure 4.11b, although below the initial value. In the end, a very stable evolution is seen, with very little points of sudden changes in the objective function throughout the optimization procedure.

We can compare this result to one obtained with the full sensitivity of the acoustic-

structure interaction. Note that, due to the enclosed-voids, we only consider the fluid and interaction terms of the sensitivity on the acoustic domain (as explained in 4.2.3). In the end, the topology from Figure 4.13a and evolution from Figure 4.13b are obtained.

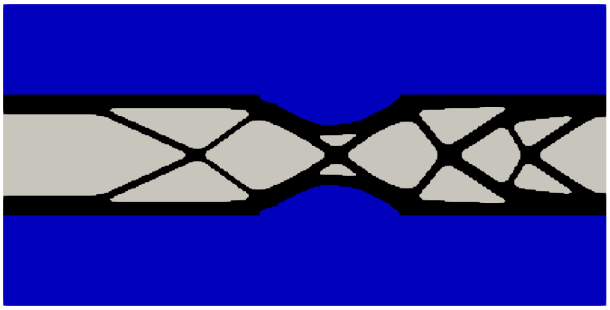

(a)

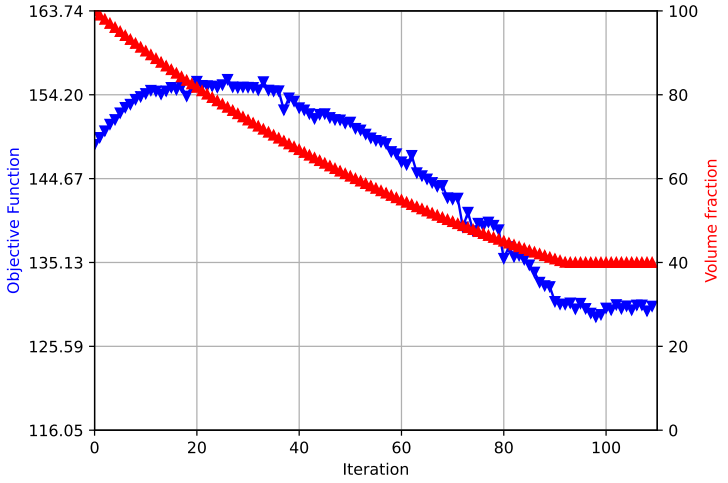

(b)

Figure 4.13 – Fundamental frequency optimization of sliding-fixed beam with acoutic-structure interaction, enclosed voids and full sensitivities. (a) Final topology (b) Objective function.

Once again, very little change on the topology, apart from the reinforcement of the central region. In this case, the evolution of the objective function is not as smooth, but the tendency of the curve can still be seen and is similar to both previous ones. Finally, the natural frequency decreases from 23.6 Hz to 20.7 Hz. Essentially, adding these sensitivity terms did not produce much quantitative change to the results, only altering the final topology and the evolutionary process.

Another way to verify these effects is by analyzing the FRF of these structures. In these FRFs the force is applied similarly to the compliance cases, and the displacement is measured at the central node of the left extremity. Four topologies are compared: the initial fully

solid one, the one from the purely structural natural frequency optimization, and both from the acoustic-structure optimization with enclosed voids. The curve is shown in Figure 4.14.

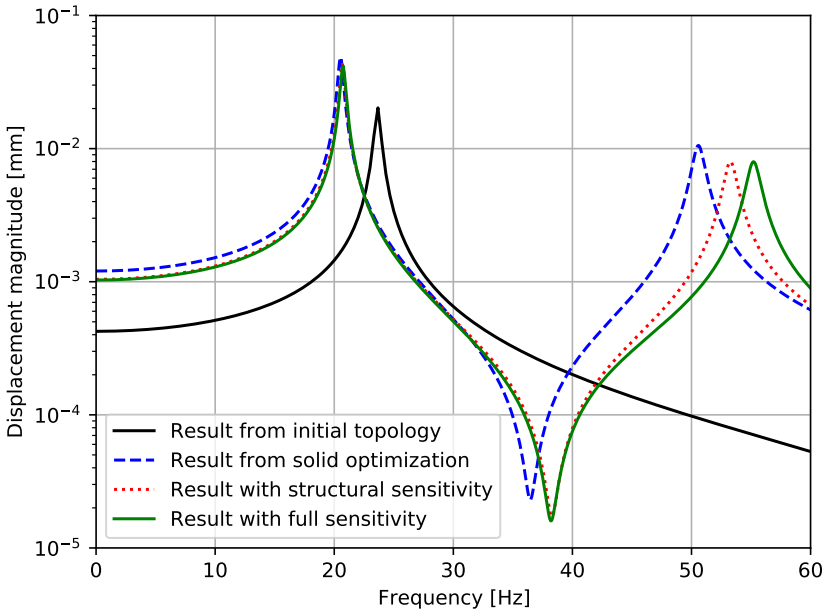

Figure 4.14 – Frequency response function of the four different topologies considering enclosed void.

Note that in this case, the topology from the purely structural optimization (Figure 4.11 (a)) also has a lower natural frequency than calculated before, now it is 20.5 Hz. From this case, we can see that the three optimized cases have very similar responses at the frequency of interest. If we consider the very small quantitative differences between them, we could conclude that very small gains were obtained with the successive additions in the formulation, but they are indeed negligible for this case. However, these effects could become more evident when increasing the frequency of optimization. Even though the second natural frequency was not considered here, we can see a substantial difference on the second resonances of each case.

Finally, the same study is repeated, but for an acoustic-structure optimization case without enclosed voids. All elements are either solid or fluid. Once again, we start with only the elastic sensitivity terms. Figure 4.15a shows the final topology, and Figure 4.15b, the objective function evolution.

Once again, a somewhat stable evolution is seen, with a similar final topology than the previous studies. There is a sudden drop in the objective function around iteration 100. This is due to some redistribution of material around the right side of the topology. In this case, the first natural frequency reduces from 23.6 Hz to 18.0 Hz. Note that this is an even

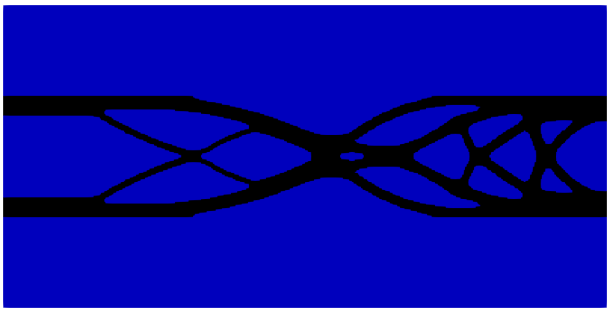

(a)

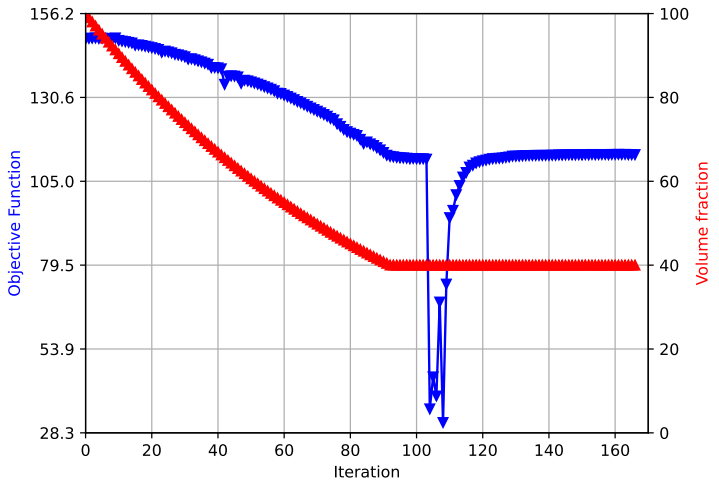

(b)

Figure 4.15 – Fundamental frequency optimization of sliding-fixed beam with acoustic-structure interaction, and solid sensitivities. (a) Final topology (b) Objective function.

greater decrease from the structural optimization, compared to the case with enclosed voids. The fact that the fluid also contributes to increasing the effective mass of the modes, but not as much to the effective stiffnesses, makes it increasingly harder for the optimizer to increase the natural frequencies. Note that while there is a slight increase in the objective function in the two previous cases (Figures 4.12b and 4.13b) roughly up to iteration 20, in this case, it already decreases from the start.

Lastly, an optimization with the full sensitivity can be performed. Unfortunately, no feasible topologies could be obtained for such case. Hence, we instead considered a similar case as before, considering the acoustic and interaction sensitivity terms only on the acoustic elements. Note that, unlike before, the internal holes here are fluid, and thus these terms are considered here. In the end, the topology and evolution from Figure 4.16a are obtained.

The most glaring characteristic of the topology is the presence of some appendix-

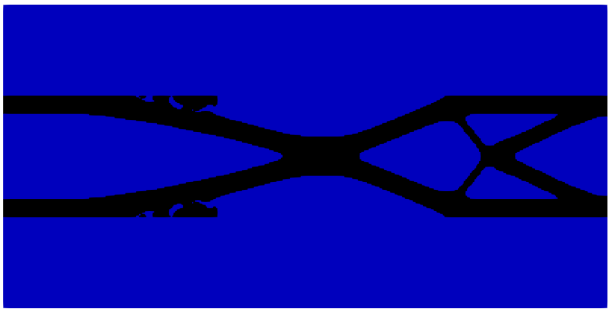

(a)

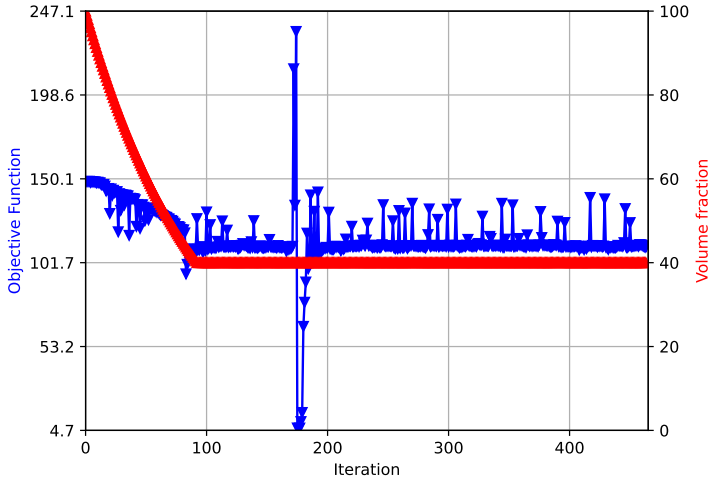

(b)

Figure 4.16 – Fundamental frequency optimization of sliding-fixed beam with acoustic-structure interaction, and full sensitivities. (a) Final topology (b) Objective function.

like solid regions on the left part. Additionally, we can see on the curve that the evolution is extremely unstable. The first natural frequency decreased from 23.6 Hz to 17.7 Hz.

In this case, the MAC (Section 2.2.4) has a lot of difficulties in identifying the local modes (there is an abundance of low-frequency acoustic modes in the holes), and thus these peaks are incorrectly identified on the curve. Thus, even though there are some points where it seems that the design improved significantly, it is not representative of what really happens. These problems with the acoustic modes also explains the appearance of these irregular surfaces.

We can compare the performance of the final topologies, once again, with an FRF. Figure 4.17 shows the response of the four topologies: initial topology, purely structural optimization, and the latest two ones.

As mentioned before, all three optimized results have a lower natural frequency than

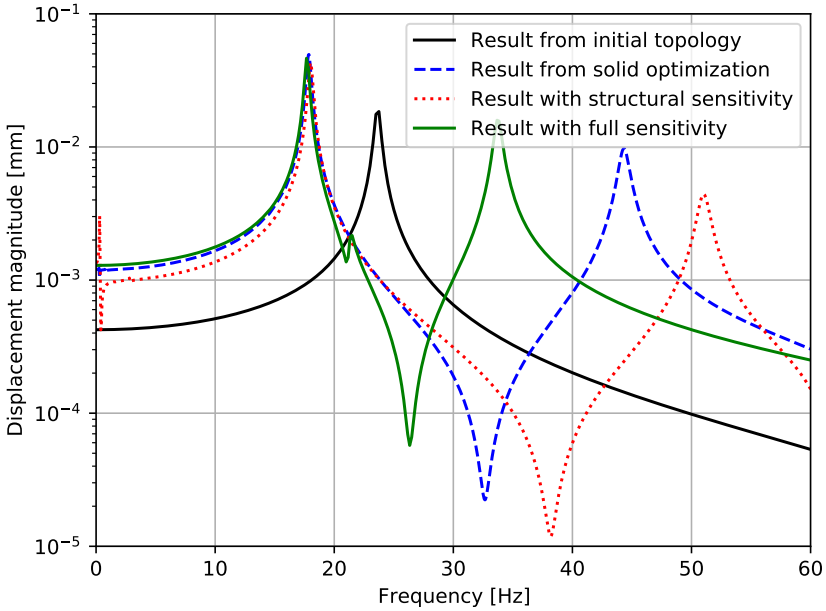

Figure 4.17 – Frequency response function of the four different topologies.

those with void holes. This is due to the additional mass of the fluid domain. The difference between the three optimized curves is even less noticeable. Their three natural frequencies are, respectively (following the order from the legend), 17.9 Hz, 18.0 Hz, and 17.7 Hz.

4.5 Conclusions

In this chapter, the formulation for acoustic-structure coupled systems is presented. The mathematical formulation for a similar kind of optimization as the ones done in Chapters 2 and 3 is presented. The sensitivity analysis for an acoustic-structure interaction optimization problem is derived. A preliminary analysis on the sensitivities and eigenvalues of different types of fluid-structure interaction problems illustrates that the level of interaction between both phases is dependent on the properties of both materials and on their topology. In some cases, the two phenomena (fluid and structure) can be treated separately and optimization can be done with only one formulation (as usually done in the literature). However, there may be cases where the coupling terms are not negligible, and thus, they must be fully implemented. This is tested in the optimization of the first natural frequency of a sliding-fixed beam. First, the optimization is done on a purely structural domain. The VFM from Chapter 3 had to be employed here to avoid loss of connectivity. Then, a first assessment was done considering void enclosed holes. Here, a small improvement was seen from the structural optimization. An even

smaller improvement was seen when also considering the acoustic and coupling sensitivities. In the second study, the holes were considered to be filled with fluid. A negligible quantitative difference was seen between the structurally optimized, and the acoustic optimized ones. In the latter, a lot of instability was also seen during the optimization procedure. Future works should assess this unstable evolution, as well as assess its effect on an increasing frequency domain.

5 BROADBAND OPTIMIZATION OF SOUND PROPAGATION OF FLOORS UNDER STRUCTURE-BORNE EXCITATION

Given the two types of problems presented in Chapter 4, we can now analyze a branch of problems in the weakly coupled formulation. Consider, for example, the first case from Section 4.3. If we consider that the fluid domain is a large room, then the number of natural frequencies in this domain might increase immensely, making a finite element modeling unfeasible. As an alternative, we can model the fluid domain with another model; in this case, the diffuse pressure field hypothesis can be adopted. The work presented in this chapter was done in KU Leuven, Belgium, in a collaboration with Prof. Mattias Schevenels and Prof. Edwin Reynders.

5.1 Diffuse field model

5.1.1 Acoustic system

In this chapter, we are interested in optimizing an acoustic-structure system in a higher frequency domain. To avoid having to calculate the eigenvalues of the acoustic domain, it is modeled using the diffuse pressure field model. Furthermore, the optimization problem to be solved is no longer the natural frequency separation, but one closer to the physical application of the system. More specifically, we minimize the sound transmission in a room due to an impact source on the floor of the room above. The vibration of the floor generates a diffuse pressure field in the receiving room directly below it, as illustrated in Figure 5.1.

This structural domain is once again modeled as linear elastic and isotropic, much like in Section 2.1.1. However, a hysteretic damping factor is added, to account for the energy that is dissipated before entering the room. Furthermore, two forces appear due to the interaction between the fluid and the structure. The equation that models the structure is shown below:

$$\left[\mathbf{K}_g\left(1+\mathrm{i}\beta\right)-\omega^2\mathbf{M}_g\right]\mathbf{a}=\mathbf{f}_{\mathbf{ext}}(\omega)-\mathbf{f}_{\mathbf{dir}}(\omega)-\mathbf{f}_{\mathbf{rev}}(\omega), \tag{5.1}$$

where β is a hysteretic damping, modeled by adding an imaginary factor to the stiffness. On the right side there are three terms: $\mathbf{f}_{\mathbf{ext}}(\omega)$ refers to the external mechanical forces applied to the domain, $\mathbf{f}_{\mathbf{dir}}(\omega)$ and $\mathbf{f}_{\mathbf{rev}}(\omega)$ are the reaction forces from the acoustic domain. These forces are divided in two terms, $\mathbf{f}_{\mathbf{dir}}(\omega)$ is the direct field forces, and $\mathbf{f}_{\mathbf{rev}}(\omega)$ is the reverberant field forces.

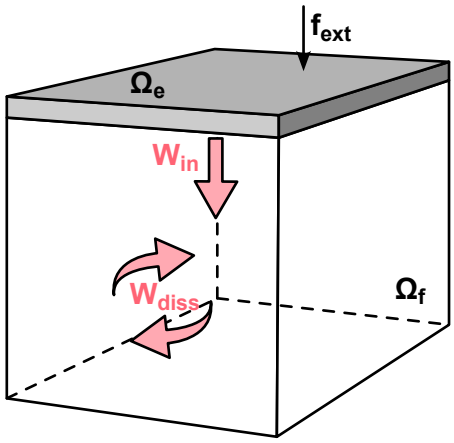

Figure 5.1 – System composed of a vibrating floor, generating a diffuse pressure field in the room below.

The direct field refers to the components of the pressure field that would occur assuming no reflection or scattering from the sound waves. The reverberant forces are the sum of all other components from the complete field.

Using the eigenmodes from the undamped structural domain (Section 2.1.2), we can rewrite the this system as:

$$\mathbf{\Phi}^{\mathrm{T}}\left[\mathbf{K}\left(1+\mathrm{i}\beta\right)-\omega^{2}\mathbf{M}\right]\mathbf{\Phi q}+\tilde{\mathbf{f}}_{\mathbf{dir}}(\omega)+\tilde{\mathbf{f}}_{\mathbf{rev}}(\omega)=\mathbf{\Phi}^{\mathrm{T}}\mathbf{f}_{\mathbf{ext}}(\omega), \tag{5.2}$$

where $\mathbf{q}$ is the modal displacement vector, and $\tilde{\mathbf{f}}_{\mathbf{dir}}(\omega)$ and $\tilde{\mathbf{f}}_{\mathbf{rev}}(\omega)$ are the direct field forces and the reverberant forces projected on the eigenvectors.

The reverberant forces are given from the acoustic domain:

$$\tilde{\mathbf{D}}_{\mathbf{dir}}(\omega)\mathbf{q}=\tilde{\mathbf{f}}_{\mathbf{dir}}(\omega), \tag{5.3}$$

where $\mathbf{D}_{\mathbf{dir}}(\omega)$ is the direct field dynamic stiffness matrix. This matrix is a result of the Rayleigh integral (Rayleigh, 1894), which can be numerically evaluated in many ways; in this thesis, the wavelet formulation (Langley, 2007) is used. Decraene *et al.* (2018) gives a simple description on how to calculate it (illustrated in Section 5.1.2). In this work, the most important aspect of this matrix is its independence on the thickness of the floor. This makes it so that it does not change throughout the optimization that will be done.

Regarding the reverberant forces, the diffuse field hypothesis makes it so that their mean value become zero.

The system is, thus, rewritten as:

$$\tilde{\mathbf{D}}_{\mathbf{tot}}(\omega)\mathbf{q} = \left[\tilde{\mathbf{D}}_{\mathbf{s}}(\omega) + \tilde{\mathbf{D}}_{\mathbf{dir}}(\omega)\right]\mathbf{q} = \mathbf{\Phi}^{\mathrm{T}}\mathbf{f}_{\mathbf{ext}}(\omega), \tag{5.4}$$

where $\tilde{\mathbf{D}}_{\mathbf{tot}}$ is the total dynamic stiffness matrix, and $\tilde{\mathbf{D}}_{\mathbf{s}}$ is its structural part of this matrix. From here on, the dependence on ω is suppressed for the sake of a simpler notation.

To aid in the energetic formulation that will be done in the following sections, we define the cross-spectrum of the response:

$$\mathbf{S}_{\mathbf{qq}} = \mathbf{q}\mathbf{q}^{\mathrm{H}} = \tilde{\mathbf{D}}_{\mathbf{tot}}^{-1}\mathbf{S}_{\mathbf{ff,ext}}\tilde{\mathbf{D}}_{\mathbf{tot}}^{-\mathrm{H}}, \tag{5.5}$$

where $\mathbf{S}_{\mathbf{ff,ext}}$ the cross-spectrum of the external force.

Usually, the cross-spectrum of the external force is a function of the frequency, and can be obtained experimentally or by employing a mass-impedance model (Reynders *et al.*, 2019; Wang *et al.*, 2020). For concrete floors, however, these values are mostly constant (within the frequency domain we are studying), thus, a constant value is adopted.

5.1.2 Wavelet formulation

To calculate the matrix $\tilde{\mathbf{D}}_{\mathbf{dir}}(\omega)$ from Eq. (5.3), we start from the solution of a vibrating baffled planar structure into an acoustic halfspace, which is given by the Rayleigh integral (Rayleigh, 1894):

$$p(\mathbf{r}) = -\left(\frac{\rho_f \omega^2}{2\pi}\right)\int_{\Omega_e}\left(\frac{e^{textik_a R}}{R}\right)u_n(\mathbf{r}')d\mathbf{r}', \tag{5.6}$$

where $p(\mathbf{r})$ is the complex pressure amplitude in the acoustic field at a location $\mathbf{r}$, due to a normal displacement of $u_n(\mathbf{r}')$ in the planar structure at the location $\mathbf{r}'$. The value k_a is the acoustic wave number, and R is:

$$R = \|\mathbf{r} - \mathbf{r}'\|. \tag{5.7}$$

The numerical integration of Eq. (5.6) is done by assigning a set of linear independent shape functions, similar to Eq. (2.2):

$$u_n(\mathbf{r}) \approx \sum_j \varphi_j(\mathbf{r})a_j, \tag{5.8}$$

where φ_j is the jth shape function.

One could use as shape functions a set of Lagrange polynomials, as commonly done in FEA. However, this does eventually lead to a complicated expression that must be numerically integrated. Langley (2007) proposed using a wavelet approach, using a set of radially symmetric jinc functions:

$$\varphi_j(\mathbf{r}) = \varphi(\mathbf{r} - \mathbf{r}_j) = \frac{2J_1(k_s R_j)}{k_s R_j} = 2\text{jinc}(k_s R_j), \tag{5.9}$$

where J_1 represents the Bessel function of the first kind and first order, and $\mathbf{r}_j$ represents the coordinates of the point where that shape function has its maximum value. These points are distributed in a rectangular grid with equal spacing between points in both directions (a spacing of Δr). The values of k_s and R_j are given by:

$$k_s = \frac{\sqrt{2}\pi}{\Delta r}, \tag{5.10}$$

$$R_j = \|\mathbf{r} - \mathbf{r}_j\|. \tag{5.11}$$

With this definition, substituting back into the Rayleigh integral, the direct field dynamic stiffness matrix is obtained as:

$$D_{mn}(\omega) = \frac{\mathrm{i}8\pi\omega\rho_f c_f k_a^2}{k_s^4} \left(\text{sinc}(k_a r_{mn}) + \mathrm{i}g(k_a r_{mn})\right), \tag{5.12}$$

$$g(x) = \frac{\cos(x) - 1}{x} + \frac{2}{x}\sum_{k=1}^{\infty} J_{2k+1}\left(x\frac{k_s}{k_a}\right), \tag{5.13}$$

$$r_{mn} = \|\mathbf{r}_m - \mathbf{r}_n\|, \tag{5.14}$$

where the indices m and n refer to the shape functions and their center points. The expression J_{2k+1} represent the $(2k+1)$th order Bessel function of first kind.

Finally, to obtain the matrix $\tilde{\mathbf{D}}_{\mathbf{dir}}(\omega)$ from Eq. (5.3), we must project the matrix $D_{mn}(\omega)$ (Eq. (5.12)) onto the eigenspace from the modal displacements $\mathbf{q}$.

5.1.3 Energy balance

Assuming that the system from Figure 5.1 is in stationary conditions, the energy that enters the receiving room must be equal to the energy dissipated in it:

$$W_{\text{diss}} = W_{\text{in}}, \tag{5.15}$$

where W_{diss} and W_{in} are, respectively, the dissipated and input powers. This formulation assumes that no energy exits the acoustic domain from its boundaries.

The dissipated power is formulated as a hysteretic damping inside the room:

$$W_{\text{diss}} = \omega \eta E_{\text{tot}}, \tag{5.16}$$

where E_{tot} is the total mean acoustic energy in the receiving room, and η is the loss factor (Vigran, 2008):

$$\eta = \frac{6\ln(10)}{\omega T_f}, \tag{5.17}$$

where T_f is the acoustic reverberation time.

The input power comes from the work of the direct field force:

$$W_{\text{in}} = \frac{1}{2}\text{Re}\left\{\text{i}\omega \mathbf{q}^{\text{H}} \mathbf{f}_{\mathbf{dir}}\right\} = \frac{\omega}{2}\left\langle \text{Im}\left\{\mathbf{D}_{\mathbf{dir}}\right\}, \mathbf{S}_{\mathbf{qq}}\right\rangle_F, \tag{5.18}$$

where the operator $\langle \square, \square \rangle_F$ represents the Frobenius inner product of two matrices.

Combining Eqs. 5.15, 5.16 and 5.18, we get the following expression for the total mean energy:

$$E_{\text{tot}} = \frac{1}{2\eta}\left\langle \text{Im}\left\{\mathbf{D}_{\mathbf{dir}}\right\}, \mathbf{S}_{\mathbf{qq}}\right\rangle_F. \tag{5.19}$$

Acoustic calculations are usually done in band-integrated values. We can approximate the total energy of the bth frequency band with numerical integration, leading to:

$$E_{\text{B}}^{(b)} = \frac{\Delta\omega_b}{2\eta_b}\left\langle \text{Im}\left\{\mathbf{D}_{\mathbf{dir}}\right\}, \mathbf{S}_{\mathbf{qq}}\right\rangle_F, \tag{5.20}$$

where $\Delta\omega_b$ is the band, and ω_b is the center frequency of the b band.

Finally, the normalized SPL in the receiving room can be described as (Reynders *et al.*, 2019):

$$L_{\mathrm{n,B}}^{(b)} = 10\log\left(\frac{E_{\mathrm{B}}^{(b)}\rho_f c_f^2}{V p_0^2}\right) + 10\log\left(\frac{A}{A_0}\right), \tag{5.21}$$

where ρ_f is the density of the fluid, V and A are the volume and the total absorption area of the receiving room, $p_0 = 2 \times 10^{-5}$ Pa is the reference pressure, and $A_0 = 10$ m^2 is the reference absorption area.

5.1.4 Floor modeling

The floor is modeled via the FEM by using four-node polyhedral shell elements coupling the membrane and plate components. Thus, each element has two components: a quadrilateral membrane part (Section 2.1.1), and a plate one, modeled with Kirchhoff plate theory. More specifically, the Discrete Kirchhoff Triangle (DKT) element formulated by Jeyachandrabose and Kirkhope (1986). In order to turn this triangle element into a square element (considering the symmetries), four triangle elements, each with a different combination of three nodes from the square, are added together. Thus, their matrices are added and then divided by two, to account for the overlap of the triangles.

To simulate ribbed floors, we intend to keep one of the surfaces flat. However, as we vary the thicknesses of the elements, they remain centered with respect to each other. Thus, a coordinate change is done to account for the offset between their local coordinates and the global one. For an element e, we define a fixed base b and a variable section h_e, totaling the thickness t_e (Figure 5.2).

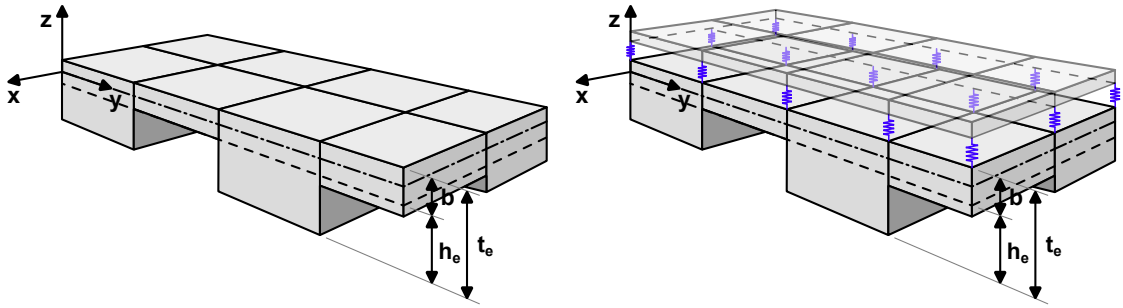

(a) (b)

Figure 5.2 – Mesh of shell elements. Dimensions are illustrated for the eth element. (a) Single slab floor (b) Floating floor.

For a regular shell element, the elemental matrices can be written as:

$$\mathbf{K}_{\textbf{shell}} = \begin{bmatrix} \mathbf{K}_{xx} & \mathbf{K}_{xy} & \mathbf{0} & \mathbf{0} & \mathbf{0} \\ \mathbf{K}_{yx} & \mathbf{K}_{yy} & \mathbf{0} & \mathbf{0} & \mathbf{0} \\ \mathbf{0} & \mathbf{0} & \mathbf{K}_{zz} & \mathbf{K}_{z\theta} & \mathbf{K}_{z\phi} \\ \mathbf{0} & \mathbf{0} & \mathbf{K}_{\theta z} & \mathbf{K}_{\theta\theta} & \mathbf{K}_{\theta\phi} \\ \mathbf{0} & \mathbf{0} & \mathbf{K}_{\phi z} & \mathbf{K}_{\phi\theta} & \mathbf{K}_{\phi\phi} \end{bmatrix}, \tag{5.22}$$

$$\mathbf{M}_{\textbf{shell}} = \begin{bmatrix} \mathbf{M}_{xx} & \mathbf{M}_{xy} & \mathbf{0} & \mathbf{0} & \mathbf{0} \\ \mathbf{M}_{yx} & \mathbf{M}_{yy} & \mathbf{0} & \mathbf{0} & \mathbf{0} \\ \mathbf{0} & \mathbf{0} & \mathbf{M}_{zz} & \mathbf{M}_{z\theta} & \mathbf{M}_{z\phi} \\ \mathbf{0} & \mathbf{0} & \mathbf{M}_{\theta z} & \mathbf{M}_{\theta\theta} & \mathbf{M}_{\theta\phi} \\ \mathbf{0} & \mathbf{0} & \mathbf{M}_{\phi z} & \mathbf{M}_{\phi\theta} & \mathbf{M}_{\phi\phi} \end{bmatrix}, \tag{5.23}$$

where each node has 5 degrees of freedom. The terms with the subscripts x and y refer to the membrane effects, and the ones with z, θ and ϕ refer to the plate effects.

We can transform this matrix by applying a change of coordinates so that the new coordinate system is centered in the middle of the fixed base b (Figure 5.2). Compared to the center of an element with thickness t_e, this implies applying an offset of:

$$e = \frac{t_e - b}{2}. \tag{5.24}$$

This results in the following transformation matrix:

$$\mathbf{T} = \begin{bmatrix} \mathbf{I} & \mathbf{0} & \mathbf{0} & \mathbf{0} & -\frac{t_e-b}{2}\mathbf{I} \\ \mathbf{0} & \mathbf{I} & \mathbf{0} & \frac{t_e-b}{2}\mathbf{I} & \mathbf{0} \\ \mathbf{0} & \mathbf{0} & \mathbf{I} & \mathbf{0} & \mathbf{0} \\ \mathbf{0} & \mathbf{0} & \mathbf{0} & \mathbf{I} & \mathbf{0} \\ \mathbf{0} & \mathbf{0} & \mathbf{0} & \mathbf{0} & \mathbf{I} \end{bmatrix} \tag{5.25}$$

Applying this coordinate change on the stiffness and mass matrices:

$$\mathbf{K}_e = \mathbf{T}^T \mathbf{K}_{\text{shell}} \mathbf{T}, \tag{5.26}$$

$$\mathbf{K}_e = \begin{bmatrix} t_e\hat{\mathbf{K}}_{xx} & t_e\hat{\mathbf{K}}_{xy} & \mathbf{0} & \frac{t_e^2-bt_e}{2}\hat{\mathbf{K}}_{xy} & -\frac{t_e^2-bt_e}{2}\hat{\mathbf{K}}_{xx} \\ t_e\hat{\mathbf{K}}_{yx} & t_e\hat{\mathbf{K}}_{yy} & \mathbf{0} & \frac{t_e^2-bt_e}{2}\hat{\mathbf{K}}_{yy} & -\frac{t_e^2-bt_e}{2}\hat{\mathbf{K}}_{yx} \\ \mathbf{0} & \mathbf{0} & t_e^3\hat{\mathbf{K}}_{zz} & t_e^3\hat{\mathbf{K}}_{z\theta} & t_e^3\hat{\mathbf{K}}_{z\phi} \\ \frac{t_e^2-bt_e}{2}\hat{\mathbf{K}}_{yx} & \frac{t_e^2-bt_e}{2}\hat{\mathbf{K}}_{yy} & t_e^3\hat{\mathbf{K}}_{\theta z} & t_e^3\hat{\mathbf{K}}_{\theta\theta} + \frac{t_e^3-2t_e^2b+t_eb^2}{4}\hat{\mathbf{K}}_{yy} & t_e^3\hat{\mathbf{K}}_{\theta\phi} - \frac{t_e^3-2t_e^2b+t_eb^2}{4}\hat{\mathbf{K}}_{yx} \\ -\frac{t_e^2-bt_e}{2}\hat{\mathbf{K}}_{xx} & -\frac{t_e^2-bt_e}{2}\hat{\mathbf{K}}_{xy} & t_e^3\hat{\mathbf{K}}_{\phi z} & t_e^3\hat{\mathbf{K}}_{\phi\theta} - \frac{t_e^3-2t_e^2b+t_eb^2}{4}\hat{\mathbf{K}}_{xy} & t_e^3\hat{\mathbf{K}}_{\phi\phi} + \frac{t_e^3-2t_e^2b+t_eb^2}{4}\hat{\mathbf{K}}_{xx} \end{bmatrix}, \quad (5.27)$$

$$\mathbf{M}_e = \mathbf{T}^T\mathbf{M}_{\text{shell}}\mathbf{T}, \quad (5.28)$$

$$\mathbf{M}_e = \begin{bmatrix} t_e\hat{\mathbf{M}}_{xx} & t_e\hat{\mathbf{M}}_{xy} & \mathbf{0} & \frac{t_e^2-bt_e}{2}\hat{\mathbf{M}}_{xy} & -\frac{t_e^2-bt_e}{2}\hat{\mathbf{M}}_{xx} \\ t_e\hat{\mathbf{M}}_{yx} & t_e\hat{\mathbf{M}}_{yy} & \mathbf{0} & \frac{t_e^2-bt_e}{2}\hat{\mathbf{M}}_{yy} & -\frac{t_e^2-bt_e}{2}\hat{\mathbf{M}}_{yx} \\ \mathbf{0} & \mathbf{0} & t_e\hat{\mathbf{M}}_{zz} & t_e\hat{\mathbf{M}}_{z\theta} & t_e\hat{\mathbf{M}}_{z\phi} \\ \frac{t_e^2-bt_e}{2}\hat{\mathbf{M}}_{yx} & \frac{t_e^2-bt_e}{2}\hat{\mathbf{M}}_{yy} & t_e\hat{\mathbf{M}}_{\theta z} & t_e\hat{\mathbf{M}}_{\theta\theta} + \frac{t_e^3-2t_e^2b+t_eb^2}{4}\hat{\mathbf{M}}_{yy} & t_e\hat{\mathbf{M}}_{\theta\phi} - \frac{t_e^3-2t_e^2b+t_eb^2}{4}\hat{\mathbf{M}}_{yx} \\ -\frac{t_e^2-bt_e}{2}\hat{\mathbf{K}}_{xx} & -\frac{t_e^2-bt_e}{2}\hat{\mathbf{M}}_{xy} & t_e\hat{\mathbf{M}}_{\phi z} & t_e\hat{\mathbf{M}}_{\phi\theta} - \frac{t_e^3-2t_e^2b+t_eb^2}{4}\hat{\mathbf{M}}_{xy} & t_e\hat{\mathbf{M}}_{\phi\phi} + \frac{t_e^3-2t_e^2b+t_eb^2}{4}\hat{\mathbf{M}}_{xx} \end{bmatrix}, \quad (5.29)$$

where the symbol ($\hat{\square}$) represents the matrix with unitary thickness.

In this chapter, the design variable of the optimization will be the thickness of each element. As such, we need the derivatives of the matrices with respect to them, which is given by:

$$\frac{\partial\mathbf{K}_e}{\partial t_e} = \begin{bmatrix} \hat{\mathbf{K}}_{xx} & \hat{\mathbf{K}}_{xy} & \mathbf{0} & \left(t_e-\frac{b}{2}\right)\hat{\mathbf{K}}_{xy} & -\left(t_e-\frac{b}{2}\right)\hat{\mathbf{K}}_{xx} \\ \hat{\mathbf{K}}_{yx} & \hat{\mathbf{K}}_{yy} & \mathbf{0} & \left(t_e-\frac{b}{2}\right)\hat{\mathbf{K}}_{yy} & -\left(t_e-\frac{b}{2}\right)\hat{\mathbf{K}}_{yx} \\ \mathbf{0} & \mathbf{0} & 3t_e^2\hat{\mathbf{K}}_{zz} & 3t_e^2\hat{\mathbf{K}}_{z\theta} & 3t_e^2\hat{\mathbf{K}}_{z\phi} \\ \left(t_e-\frac{b}{2}\right)\hat{\mathbf{K}}_{yx} & \left(t_e-\frac{b}{2}\right)\hat{\mathbf{K}}_{yy} & 3t_e^2\hat{\mathbf{K}}_{\theta z} & 3t_e^2\hat{\mathbf{K}}_{\theta\theta} + \frac{3t_e^2-4t_eb+b^2}{4}\hat{\mathbf{K}}_{yy} & 3t_e^2\hat{\mathbf{K}}_{\theta\phi} - \frac{3t_e^2-4t_eb+b^2}{4}\hat{\mathbf{K}}_{yx} \\ -\left(t_e-\frac{b}{2}\right)\hat{\mathbf{K}}_{xx} & -\left(t_e-\frac{b}{2}\right)\hat{\mathbf{K}}_{xy} & 3t_e^2\hat{\mathbf{K}}_{\phi z} & 3t_e^2\hat{\mathbf{K}}_{\phi\theta} - \frac{3t_e^2-4t_eb+b^2}{4}\hat{\mathbf{K}}_{xy} & 3t_e^2\hat{\mathbf{K}}_{\phi\phi} + \frac{3t_e^2-4t_eb+b^2}{4}\hat{\mathbf{K}}_{xx} \end{bmatrix}, \quad (5.30)$$

$$\frac{\partial\mathbf{M}_e}{\partial t_e} = \begin{bmatrix} \hat{\mathbf{M}}_{xx} & \hat{\mathbf{M}}_{xy} & \mathbf{0} & \left(t_e-\frac{b}{2}\right)\hat{\mathbf{M}}_{xy} & -\left(t_e-\frac{b}{2}\right)\hat{\mathbf{M}}_{xx} \\ \hat{\mathbf{M}}_{yx} & \hat{\mathbf{M}}_{yy} & \mathbf{0} & \left(t_e-\frac{b}{2}\right)\hat{\mathbf{M}}_{yy} & -\left(t_e-\frac{b}{2}\right)\hat{\mathbf{M}}_{yx} \\ \mathbf{0} & \mathbf{0} & \hat{\mathbf{M}}_{zz} & \hat{\mathbf{M}}_{z\theta} & \hat{\mathbf{M}}_{z\phi} \\ \left(t_e-\frac{b}{2}\right)\hat{\mathbf{M}}_{yx} & \left(t_e-\frac{b}{2}\right)\hat{\mathbf{M}}_{yy} & \hat{\mathbf{M}}_{\theta z} & \hat{\mathbf{M}}_{\theta\theta} + \frac{3t_e^2-4t_eb+b^2}{4}\hat{\mathbf{M}}_{yy} & \hat{\mathbf{M}}_{\theta\phi} - \frac{3t_e^2-4t_eb+b^2}{4}\hat{\mathbf{M}}_{yx} \\ -\left(t_e-\frac{b}{2}\right)\hat{\mathbf{M}}_{xx} & -\left(t_e-\frac{b}{2}\right)\hat{\mathbf{M}}_{xy} & \hat{\mathbf{M}}_{\phi z} & \hat{\mathbf{M}}_{\phi\theta} - \frac{3t_e^2-4t_eb+b^2}{4}\hat{\mathbf{M}}_{xy} & \hat{\mathbf{M}}_{\phi\phi} + \frac{3t_e^2-4t_eb+b^2}{4}\hat{\mathbf{M}}_{xx}. \end{bmatrix}. \quad (5.31)$$

Finally, a floating floor model is also used. It is composed of a base floor and a floating slab, connected by a resilient interlayer. The base floor is a heavy structural component, while the floating slab is usually a light load-bearing screed (Hongisto *et al.*, 2020).

In this thesis, floating floors are modeled as follows: the base floor is simulated as just described, with ribbed polyhedral shell elements; the floating slab is composed of plate

elements; and the interlayer are a series of springs connecting the vertical degrees of freedom of both slabs. These springs have their properties defined based on the geometry of the floor and the material properties of the interlayer material. This formulation was verified with Cremer's model (Cremer *et al.*, 2005; Schiavi, 2018):

$$\begin{bmatrix} \mathbf{D_p} + g\mathbf{P_{pp}} & -g\mathbf{P_{pb}} \\ -g\mathbf{P_{bp}} & \mathbf{D_b} + g\mathbf{P_{bb}} \end{bmatrix} \begin{Bmatrix} \mathbf{q_p} \\ \mathbf{q_b} \end{Bmatrix} = \begin{Bmatrix} \tilde{\mathbf{f}}_{\mathbf{ext}} \\ \mathbf{0} \end{Bmatrix}, \tag{5.32}$$

where $\mathbf{D_p}$ and $\mathbf{D_b}$ are the normalized dynamic stiffness matrices of the floating screed and the base floor, respectively. Both layers are connected by springs with stiffness g. This value is calculated based on the dynamic stiffness s' of the resilient layer (ISO 9052-1, 1989). The coupling matrices $\mathbf{P}$ are given by:

$$\mathbf{P}_{\mathrm{ij}} = \sum_n \boldsymbol{\phi}_n^{(i)} \otimes \boldsymbol{\phi}_n^{(j)}, \tag{5.33}$$

where the indices i and j can be p or b. The term $\boldsymbol{\phi}_n^{(i)}$ is the row of the eigenvector matrix that refer to the values for the nth degree of freedom.

5.2 Optimization of impact sound rating

5.2.1 Single number rating for impact floor sound propagation

There are several ways to assess the impact sound insulation of floors. ISO 717–2 (2012) describes several Single-Number Quantity (SNQ), among which, one is used as an objective. The one used here is an unweighted normalized impact pressure level with a spectral adaptation term (C_{I}). The SNQ is denoted as $L_{\mathrm{n},\omega} + C_{\mathrm{I}}$ and is given by:

$$C_{\mathrm{I}} = L_{\mathrm{n,sum}} - 15 - L_{\mathrm{n},\omega}, \tag{5.34}$$

with:

$$L_{\mathrm{n,sum}} = 10 \log \left(\sum_b 10^{\frac{L_{\mathrm{n,B}}^{(b)}}{10}} \right), \tag{5.35}$$

calculated for one-third-octave bands from 100 Hz to 2500 Hz.

This SNQ is used when defining the impact sound insulation standards of some European countries, like Switzerland and the Netherlands (Rasmussen; Machimbarrena, 2014). Also, compared to other SNQs, it is much more convenient to implement in gradient-based

optimization schemes, as it is defined from a continuous function. In the end, the optimization is defined as:

$$\begin{aligned} \text{Min} \quad & L_{\text{n},\omega} + C_{\text{I}} \\ \text{S. t.} \quad & t_{\text{min}} \leq t_e \leq t_{\text{max}} \\ & V \leq V^*, \end{aligned} \tag{5.36}$$

where t_{min} and t_{max} are the minimum and maximum admissible thickness for each element. In this case, the volume is defined so that, if every element has $t_e = t_{\text{min}}$, then $V = 0$; likewise, if every element has $t_e = t_{\text{max}}$, then $V = 100\%$. For every other configuration, it is defined linearly based on every thickness.

To make this optimization independent on the location of the excitation, the SNQ is calculated by averaging the value obtained by putting the force on every vertical degree of freedom of the system, that is:

$$L_{\text{n,sum}} = 10 \log \left(\sum_{p=1}^{N_{\text{p}}} \sum_{b} \frac{1}{N_{\text{p}}} 10^{\frac{L_{\text{n,B}}^{(b,p)}}{10}} \right) = 10 \log \left(\sum_{p=1}^{N_{\text{p}}} \sum_{b} \frac{E_{\text{B}}^{(b,p)} \rho_f c_f^2 A}{N_{\text{p}} V p_0^2 A_0} \right), \tag{5.37}$$

where p refers to the pth vertical degree of freedom, and N_{p} is the number of such degrees of freedom.

Unlike the previous case, this optimization procedure admits intermediary values for the design variable, and thus a continuous optimization method is used. The Globally Convergent Method of Moving Asymptotes (GC-MMA) is chosen for this case (Svanberg, 1987; Svanberg, 2002), more precisely, the publicly available implementation from NLopt (Johnson, 2024).

5.2.2 Filtering scheme

To avoid getting mesh-dependent structures, as well as to avoid getting thin components, a filtering technique is employed. Unlike the previous cases, a filtering of the design variables is done. In this case, each thickness passes through the following filtering expression (Sigmund, 1997):

$$\hat{t_e} = \frac{\sum_i \max\left(r_{\text{min}} - r_{ei}, 0\right) t_i}{\sum_i \max\left(r_{\text{min}} - r_{ei}, 0\right)}, \tag{5.38}$$

where $\hat{t_e}$ is the filtered thickness, which is employed on the FEA. Such as before r_{min} is a parameter from the user, and r_{ei} is the distance between the centroid of elements e and i.

5.2.3 Sensitivity analysis

To calculate the sensitivity of this objective function, we start by differentiating Eq. (5.37):

$$\frac{\partial L_{\text{n,sum}}}{\partial \hat{t_e}} = \frac{10}{\ln 10 \left(\sum_{b,p} E_{\text{B}}^{(b,p)} \right)} \frac{\partial \left(\sum_{b,p} E_{\text{B}}^{(b,p)} \right)}{\partial \hat{t_e}}, \tag{5.39}$$

where the sums were put together for simplicity.

Likewise, the total average mean energy can differentiated from Eq. (5.20). This process is similar to what has been done by Van den Wyngaert *et al.* (2020) when they differentiated the coupling loss factor of airborne sound transmission:

$$\frac{\partial \left(\sum_{b,p} E_{\text{B}}^{(b,p)} \right)}{\partial \hat{t_e}} = -\sum_{b,p} \frac{\Delta\omega_b}{\eta_b} \text{Re} \left\{ \left\langle \text{Im} \left\{ \tilde{\mathbf{D}}_{\mathbf{dir}} \right\}_b, \left(\tilde{\mathbf{D}}_{\mathbf{tot}}^{-1} \frac{\partial \tilde{\mathbf{D}}_{\mathbf{s}}}{\partial \hat{t_e}} \mathbf{S_{qq}}^{(p)} \right)_b \right\rangle_F \right\}. \tag{5.40}$$

Note that, since $\tilde{\mathbf{D}}_{\mathbf{dir}}$ does not depend on the thickness of the elements, its derivative is zero. Additionally, we don't consider the derivatives of the eigenvectors in this differentiation as they only represent a change of basis. That is, we could perform this differentiation in nodal basis and only then pass it to a modal one, resulting in the same expression. However, this is only exact when a full modal basis is adopted, which is evidently not possible. When using an approximate basis, this sensitivity will be approximated. To this author's knowledge, there is no analysis done on the errors from doing this. Nonetheless, every analysis performed in this study resulted in acceptable numbers for this error.

This expression can be further changed by using some properties from the Frobenius inner product:

$$\frac{\partial \left(\sum_{b,p} E_{\text{B}}^{(b,p)} \right)}{\partial \hat{t_e}} = -\sum_{b,p} \frac{\Delta\omega_b}{\eta_b} \text{Re} \left\{ \left\langle \left[\tilde{\mathbf{D}}_{\mathbf{tot}}^{\text{H}} \text{Im} \left(\tilde{\mathbf{D}}_{\mathbf{dir}} \right) \mathbf{S_{qq}}^{H(p)} \right]_b, \left(\frac{\partial \tilde{\mathbf{D}}_{\mathbf{s}}}{\partial \hat{t_e}} \right)_b \right\rangle_F \right\}. \tag{5.41}$$

We can substitute the terms of the derivative of $\tilde{D}_{\mathbf{s}}$, based on the structural matrices:

$$\frac{\partial \tilde{\mathbf{D}}_{\mathbf{t}}}{\partial \hat{t_e}} = \mathbf{\Phi}^{\mathrm{T}} \left[\frac{\partial \mathbf{K}_g}{\partial \hat{t_e}} (1 + \mathrm{i}\beta) - \omega^2 \frac{\partial \mathbf{M}_g}{\partial \hat{t_e}} \right] \mathbf{\Phi}, \tag{5.42}$$

where the expression of the derivatives are given in Section 5.1.4.

$$\begin{aligned} \frac{\partial \left(\sum_{b,p} E_{\mathrm{B}}^{(b,p)} \right)}{\partial \hat{t_e}} = -\mathrm{Re} \left\{ \left\langle \left[\sum_b \frac{\Delta\omega_b (1 + \mathrm{i}\beta_b)}{\eta_b} \mathbf{Y}_b \right], \left(\frac{\partial \mathbf{K}}{\partial \hat{t_e}} \right) \right\rangle_F \right\} \\ + \mathrm{Re} \left\{ \left\langle \left[\sum_b \frac{\Delta\omega_b \omega_b^2}{\eta_b} \mathbf{Y}_b \right], \left(\frac{\partial \mathbf{M}}{\partial \hat{t_e}} \right) \right\rangle_F \right\}, \end{aligned} \tag{5.43}$$

where the matrix $\mathbf{Y}_b$ is added for simplicity:

$$\mathbf{Y}_b = \tilde{\mathbf{D}}_{\mathbf{tot}}^{-\mathrm{H}} \mathrm{Im} \left(\tilde{\mathbf{D}}_{\mathbf{dir}} \right) \left(\sum_p \mathbf{S}_{\mathbf{qq}}{}^{H(p)} \right). \tag{5.44}$$

Note that this expression simplifies the calculation of this sensitivity. On each Frobenius inner product, only the term on the right depend on e, meaning that, for each iteration of the optimization process, the left term only has to be calculated once. This is specially convenient as the sums of the different force locations and the different frequencies are all on this left term. Finally, since the derivatives of the matrices have the size of the elemental matrices (in this case, 20 x 20); then, for each element, the increase in computational time (with respect to eigenvalue derivative) is only up to 400 scalar multiplications.

This derivative is done with respect to the filtered thicknesses. To convert it back into sensitivities of the design variable, we use the chain rule in Eq. (5.38). In the end, it means that we apply the same scheme from Eq. (5.38) to this sensitivity vector.

5.3 Numerical results

5.3.1 Optimization of single slab

The aforementioned optimization process is initially done for a single slab floor. It is formulated as linear elastic isotropic and homogeneous polyhedral shell structure, based on the formulation from Figure 5.1. The floor is composed of a reinforced concrete with $E = 34$ GPa, $\nu = 0.2$ and $\rho = 2427$ kg/m^3. The damping factor is adopted as $\beta = 0.02$. The floor has

dimensions of 3 m x 3 m, and the thickness of each element can vary from $t_{\text{min}} = 80$ mm to $t_{\text{max}} = 400$ mm.

The receiving room is formulated with the diffuse pressure field model. It is considered to have dimensions of 4.15 m x 4.12 m x 5.1 m, totaling a volume of 87.2 m^3. The air inside it has $c_{\text{f}} = 343$ m/s e $\rho_{\text{f}} = 1.2$ kg/m^3. The reverberation time is $T_{\text{f}} = 1.5$ s.

The discretization of both the FEA and the wavelet formulation for the integration of the acoustic matrices is a 50 x 50 mesh of identical square elements. The acoustic simulation is done inside the interval of 63 Hz to 4 kHz, with a discretization of 48 frequencies per octave band. The force is such that $\mathbf{S_{ff,ext}} = 4$ N/Hz. A maximum volume of $V^* = 0.3$ is adopted in the optimization, as well as a filter radius of $r_{\text{min}} = 100$ mm. A two-fold symmetry is imposed during the optimization process; additionally, a relative tolerance of 10^{-5} on the objective function is used. The optimization starts with a flat design with volume V^*.

The optimization ends after 515 inner iterations of the GC-MMA. The evolution of the objective function is shown in Figure 5.3. The iteration number is counted based on inner iterations (evaluations of objective function), but the markers only represent outer iterations. In this case, no significant improvements are seen, as the objective function only decreased from 66.4 dB to 64.7 dB.

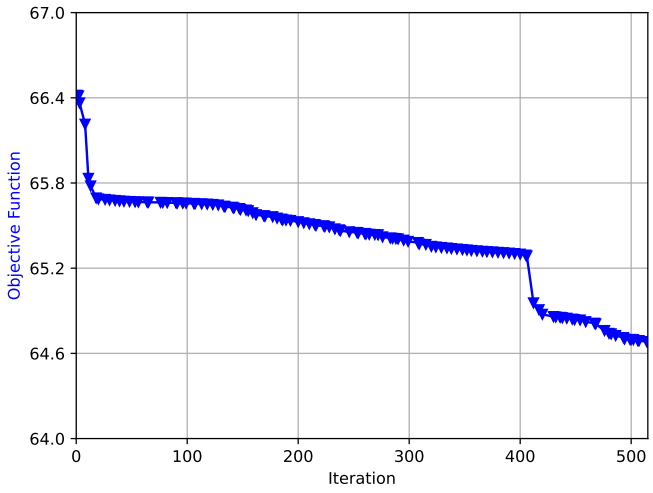

Figure 5.3 – Objective function of outer iterations throughout the optimization of single slab.

The objective function showed a peculiar behavior around iteration 406, where we see a steep drop. Around this iteration, there are some significant design changes, which helps to explain this behavior. Shortly after that, on iteration 515, the optimization reaches its stop

criterion. To confirm that no other abrupt changes would happen, we let the optimization run further, but no significant changes were seen beyond this point.

Figure 5.4 shows the final design. It is clear that this design is not physically viable, even if it resulted in significant decreases in the objective function. Its small features indicate that high frequency phenomena played an important role in the optimization process. The behavior of each frequency domain can be seen in Figure 5.5. There is a consistent decrease on most one-third-octave bands, indicating that the optimization procedure is able to consider all of them during the optimization. However, due to this broadband behavior, the decrease on each frequency was very low. For this reason, the objective function decreases very little.

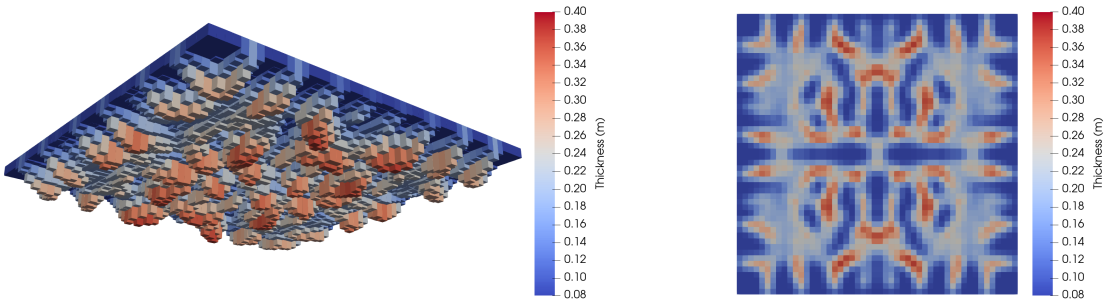

(a) (b)

Figure 5.4 – Final design in single slab optimization (a) 3D view and (b) bottom view.

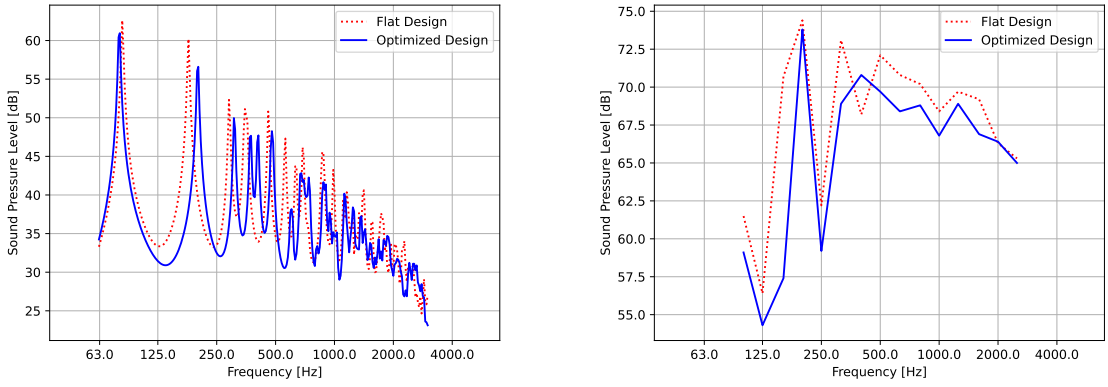

(a) (b)

Figure 5.5 – Sound pressure level curves for single slab flat and optimized designs. (a) Harmonic values and (b) 1/3 octave values.

5.3.2 Optimization of floating floor

A floating floor is added to the domain. It is modeled as described in Section 5.1.4. The floating slab is a 70 mm thick concrete screed with $E = 34$ GPa, $\nu = 0.2$, $\rho = 1500$ kg/m^3,

and $\beta = 0.02$. The interlayer connecting both slabs is a group of springs, composed of a layer of polyethylene foam, with $s' = 70$ MN/m^3 for a thickness of 5 mm, and a structural damping of 20%. The sum of their cross-section areas is assumed to be the surface area of the slabs.

To optimize this problem, only the thicknesses of the base floor are considered as design variables. Furthermore, the forces are only applied on the floating screed. Every optimization parameter is kept the same as the previous section. The evolution of the objective function in this optimization is shown in Figure 5.6. This case is much stabler than the previous one, going towards a certain design without difficulties. It needs some more inner iterations at the end because, since it is already close to the local minimum, the step has to be very small.

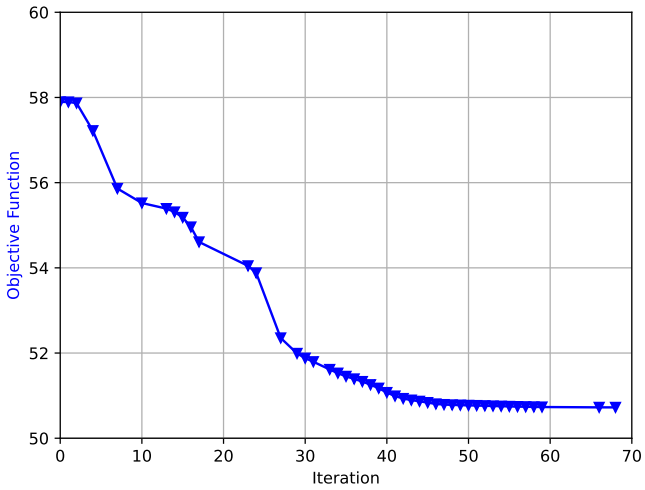

Figure 5.6 – Objective function of outer iterations throughout the optimization of floating floor.

Compared to the previous case, a much more significant decrease is observed. The SNQ decreased from 57.9 dB to 50.7 dB. We note that not only it is a significant decrease, but it also satisfies the building requirements of countries that adopt this descriptor: the Netherlands (54 dB), Switzerland (53 dB) (Rasmussen; Machimbarrena, 2014) and Brazil (55 dB) (Associação Brasileira de Normas Técnicas, 2013).

The final design is shown in Figure 5.7. Here, a much more discrete design is observed, as opposed to the previous section. We also see that, despite only imposing a two-fold symmetry, the optimizer opted to roughly maintain a four-fold one. The material concentration seen at the four edges is due to the boundary conditions of the system. Further discussion about this region is done in the next section.

Finally, we can more closely analyze the SPLs from both the flat and optimized designs (Figure 5.8). In this case, the reduction in SPL is seen only for low frequencies. However,

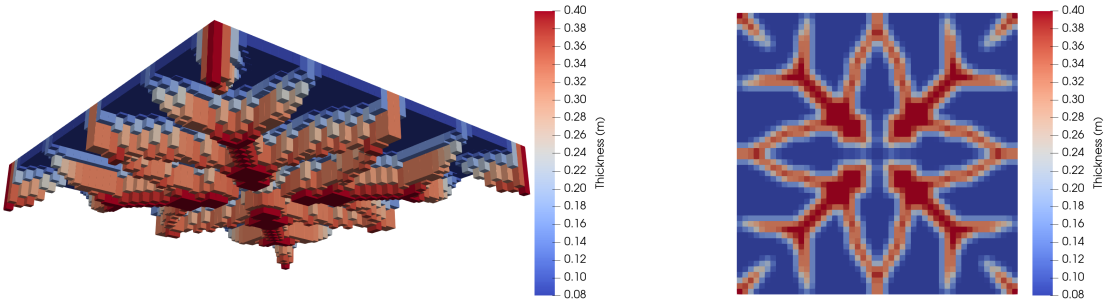

(a) (b)

Figure 5.7 – Final design in floating floor optimization (a) 3D view and (b) bottom view.

this does not negatively affect this design as much, since the floating floor reduces the transmission in high frequencies. Thus, there is combination from the effects of both phenomena: the floating floor minimizes the response in high frequency; while the optimization reduces it for low frequency, albeit sacrificing a bit of performance on higher ones. In this case, both curves cross at about 800-1000 Hz. Above this frequency, the optimized design performs worse than the flat one.

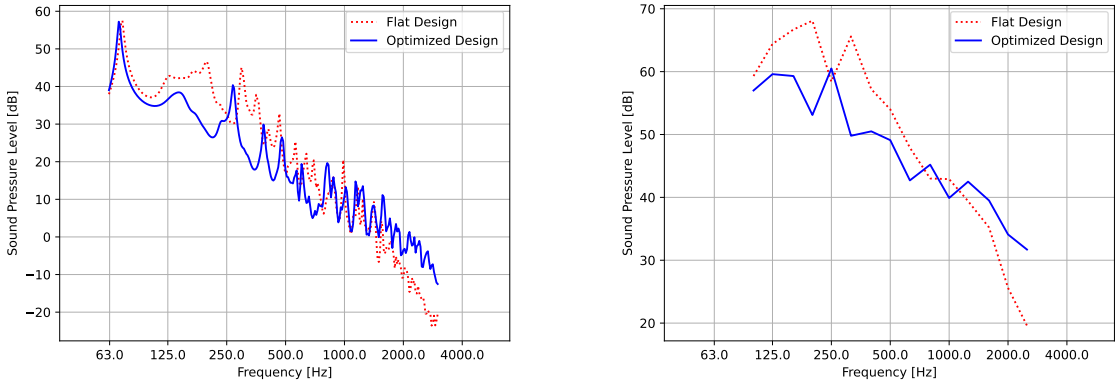

(a) (b)

Figure 5.8 – Sound pressure level curves for floating floor, flat and optimized designs. (a) Harmonic values and (b) 1/3 octave values.

To further assess this behavior, a unitary force is applied on coordinates (0.9, 1.2) m on the floating floor. The harmonic response of the structure at 600 Hz, 880 Hz and 1200 Hz are shown in Figure 5.9. Below 880 Hz, the base floor vibrates mostly on the reinforced regions (Figure 5.9a); while above it, vibration on the thin regions of the structure start to dominate its dynamic behavior(Figures 5.9b and 5.9c).

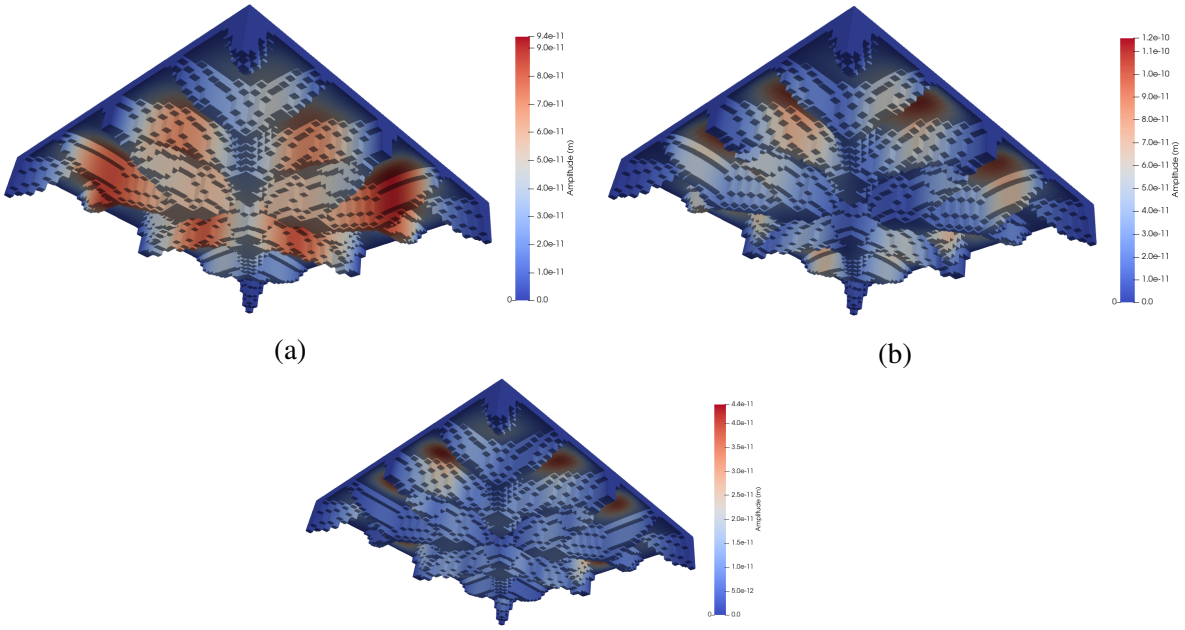

Figure 5.9 – Harmonic response of the floor for a point-load excitation at: (a) 600 Hz, (b) 880 Hz, (c) 1200 Hz.

5.3.3 Analysis over different ribbed floors

For the next analysis, the dimensions of the floor are increased to 6 m x 6 m. The number of elements in the mesh is increased to 100 x 100, as well as the number of evaluated modes, which is increased to 1000 on the floating screed and to 800 on the base floor. Finally, another polyethylene layer is added on the interlayer, totaling 10 mm, with half the stiffness.

To save on computational time, the next optimization cases are run only for one-third-octave bands between 100 Hz and 1000 Hz. Because of the floating floor, the total average energy in the room for high frequency bands is order of magnitudes lower than for lower frequency. The initial and final simulations, however, are done in the larger band. The volume constraint, as well as all other parameters are kept unchanged.

The optimization, in this case, leads to the evolution of objective function shown in Figure 5.10. The SNQ reduces from 58.0 dB on the flat design to 52.6 dB on the optimized one. Once again, the rating starts above the minimum requirements for the Netherlands, Switzerland and Brazil; but the optimization reduces it to an admissible value. The final design is shown in Figure 5.11. In this case, the four-fold symmetry is lost around iteration 70.

Before studying the SPL of this floor, other designs are simulated to enhance the analysis. Regular floors composed of a grid of perpendicular beams (Figure 5.12) are simulated

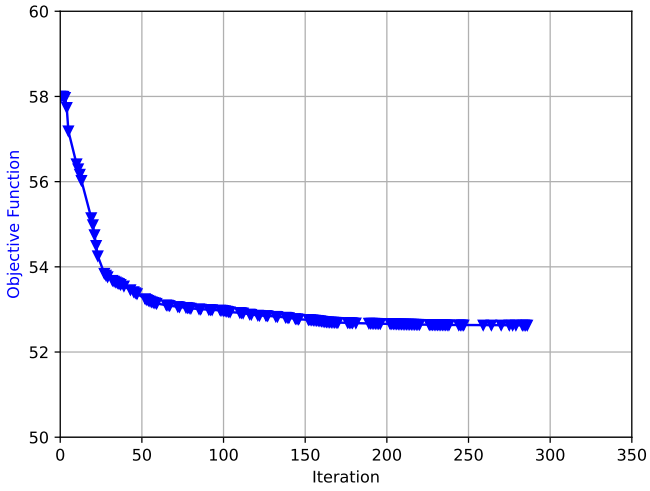

Figure 5.10 – Objective function of outer iterations throughout the optimization of floating floor with larger domain.

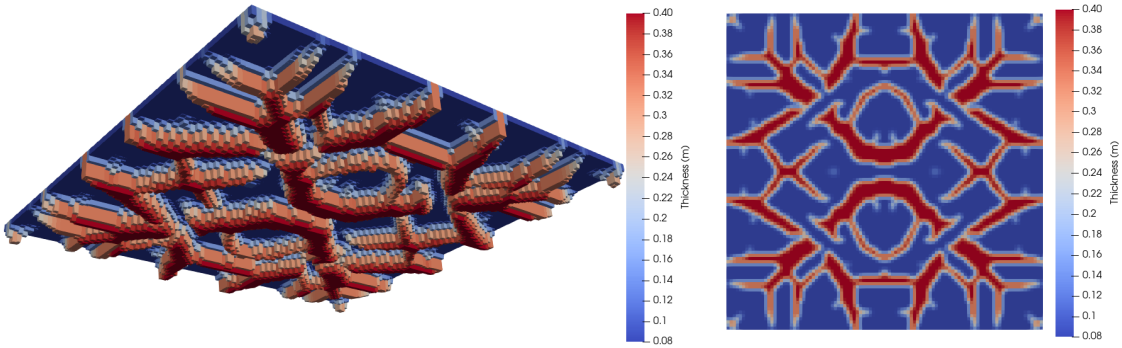

(a) (b)

Figure 5.11 – Final design in floating floor optimization with larger domain (a) 3D view and (b) bottom view.

for a varied number of beams between 1 and 10. The thickness of the beams and their height are chosen so that the same amount of material is used for all designs.

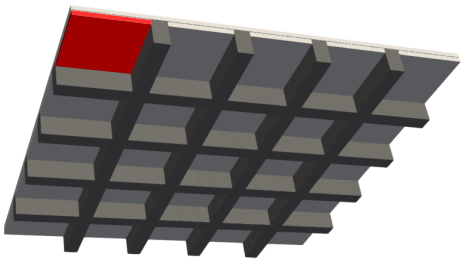

Figure 5.12 – Regular floor with a grid of beams. Example with four beams.

The one-third-octave SPLs from all the previous designs are shown in Figure 5.13. From the curves we see a clear pattern on the crossing of the regular designs with the flat one. As

the number of beams increase, the crossing frequency also increases; this is due to the vibration of the thin regions in between the beams.

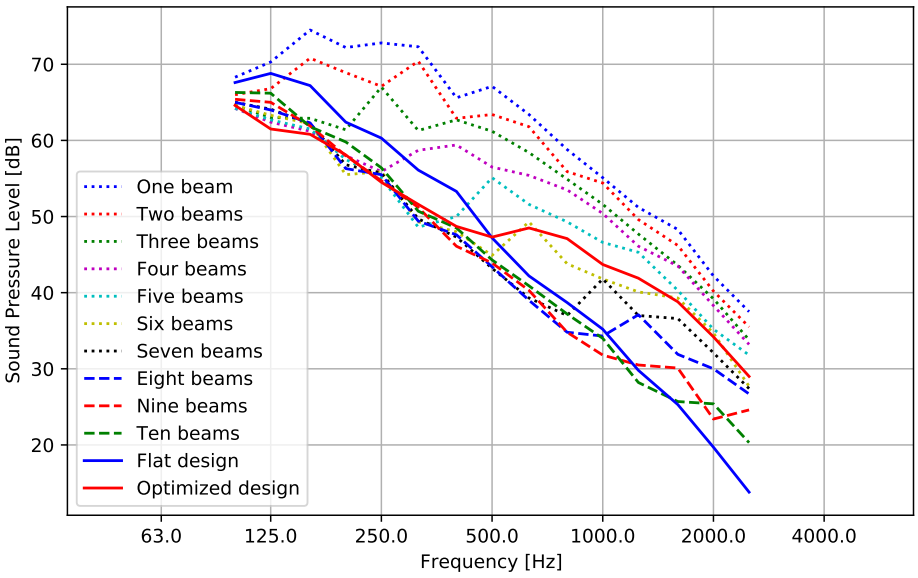

Figure 5.13 – Sound pressure level of regular, optimized, and flat designs.

The SNQ for each design is calculated and presented in Table 5.1. As the number of beams increase, the SNQ decreases. However, this is only true up to a certain point, above which, an inverse relationship is seen. From Figure 5.13, since the improvement on the increase of number of beams is on higher frequency, it is less significant the higher the frequency. On the other hand, if the structure becomes less stiff on low frequency domain, then the SNQ increases. We can see this for eight, nine, and ten beams.

Finally, the first natural frequency for supported and clamped plates with the same dimension as the edge thin plates (red region in Figure 5.12) is calculated. Table 5.2 shows the natural frequency values.

Looking at the values from Table 5.2 and the crossing frequencies and the peak right next to them on the curves from Figure 5.13, one could note that they occur roughly at the same frequencies for the same number of beams, that is, the peak occurs at a frequency between the supported and clamped analytical natural frequencies. This is another evidence for the importance of the vibration of those thin plates and the optimization of ribbed floors. Furthermore, this also indicates that a simple analysis on the natural frequencies of those regions could be a good indicator on the impact sound insulation performance of those floors.

Table 5.1 – Performance of designs with different number of beams

Number of beams	Single Number Quantity (dB)
Flat	58.0
1	65.3
2	61.9
3	57.5
4	54.2
5	53.2
6	53.2
7	53.5
8	53.5
9	54.0
10	54.9
Optimized	52.6

Table 5.2 – First natural frequency of plates

Beams	Supported frequency (Hz)	Clamped frequency (Hz)
1	56.0	102.4
2	114.5	209.5
3	197.3	361.2
4	303.7	555.8
5	433.3	793.2
6	586.2	1073.1
7	762.4	1395.6
8	961.8	1760.6
9	1184.5	2168.2
10	1430.4	2618.3

Finally, from Table 5.1 result with the lower SNQ is with five beams. To see if we can obtain better results starting with it, it is used as the initial design for an optimization study. The evolution of the objective function is shown in 5.14. The SNQ decreases from the starting 53.2 dB to 52.3 dB. In practice, it is not a meaningful improvement, compared to the previous optimization study.

The final design is shown in Figure 5.15. The main changes to the design compared to the initial one are at the edges of the structure. Material is removed at the four edges; this is due to the boundary conditions being supported instead of clamped, meaning that the structure is free to rotate at the extremities. For this region, material at those regions do not add to the general stiffness of the structure. The other main change is the addition of some material at the four vertices. This is because the four thin regions at the vertices are the most flexible ones, as

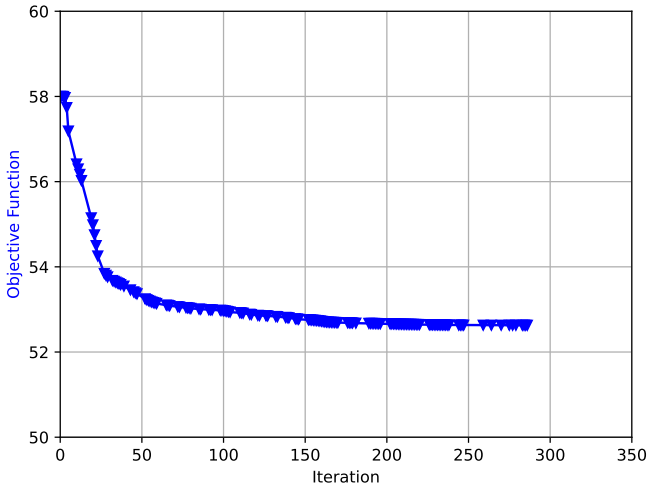

Figure 5.14 – Objective function of outer iterations throughout the optimization of floating floor with regular starting design.

two of their sides are free to rotate. These changes amount to very little change on the SPL, apart from at around 500 Hz, as indicated in Figure 5.16. This is mostly due to the material at the vertices.

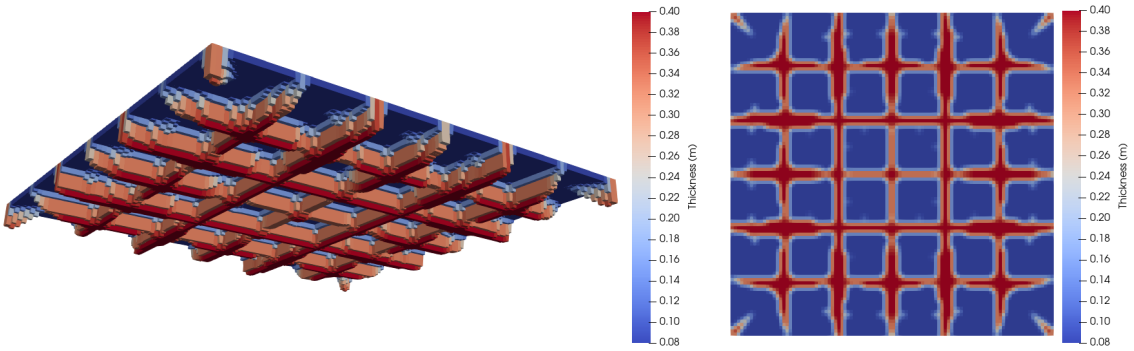

(a) (b)

Figure 5.15 – Final design in floating floor optimization with regular initial design (a) 3D view and (b) bottom view.

5.4 Conclusions

In this chapter, an optimization procedure for minimizing the SNQ related to impact sound insulation was presented and analyzed. A simple yet efficient expression is shown for calculating the sensitivities of this expression.

Optimizing a single slab did not result in good performance, as the optimizer was unable to find a good trade-off for low-frequency and high-frequency vibration that decreased

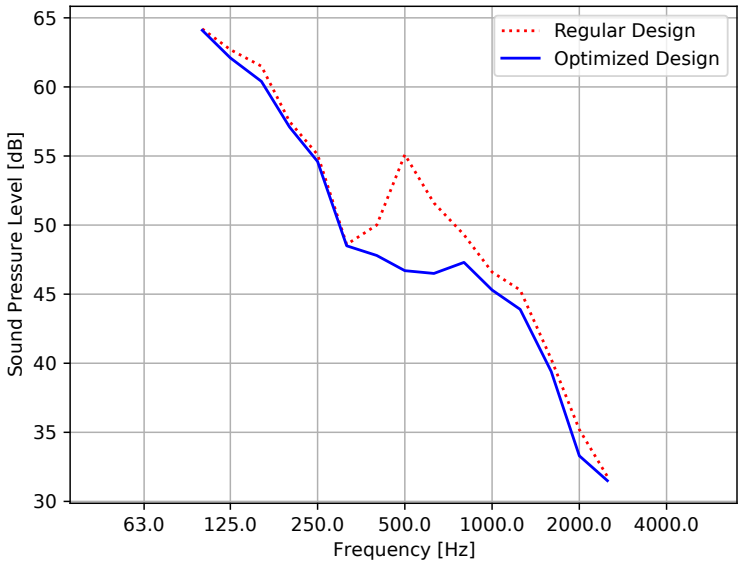

Figure 5.16 – Sound pressure level of regular and optimized designs.

both of them significantly. The addition of a floating floor, however, changed this scenario. As this component, by itself, already helps in decreasing high-frequency transmission, the optimizer was able the focus on lower ones, albeit sacrificing performance in high-frequency.

Analyses over the harmonic response of the structures indicated that the vibration of the thin sections made the response of the optimized structures in high frequency greater than the one in a flat structure with same amount of material. While this might seem troublesome, it should only be seen as a problem if this crossing frequency is too low, as in impact sound insulation systems with floating floor, the low frequency transmission is the most critical one. This is seen on the optimization of different regular designs, where gains were only seen up to a certain frequency.

6 CONCLUSIONS

In this work, methods for topology optimization of natural frequencies for systems in the low, medium and high frequency domain were presented. Different topics were addressed, each one of them related to a given challenge for these kinds of problem. Accordingly, this research was divided in four different chapters, in each one the problem was formulated, solved and discussed. A brief summary with concluding remarks and next steps are presented for each chapter as follows:

- *Chapter 2: High natural frequency separation maximization:* This chapter focused on formulating and discussing the general natural frequency separation maximization problem. An appropriate objective function was chosen, in which the phenomenon of mode shifting does not interfere with the arrangement of eigenvalues. Additionally, it manages to swap whether a given frequency is maximized of minimized based on its value relative to the operating frequency. Finally, a mode tracking procedure based on the MAC is introduced, in order to identify and remove local modes before they impair the evolutionary process. Several results were implemented to analyze this method. Initially, a clamped-clamped beam was optimized, showing that the proposed procedure managed to maximize the objective function, and that the final topology is quasi-periodic. Given this last result, a periodic optimization was performed, and with its resulting cell a dispersion analysis was performed, showing the presence of a band-gap within the separation interval. This indicates a correlation between the results from periodic dispersion analyses and finite structural ones. This conclusion was further corroborated by analyzing the responses from an optimized irregular domain and one assembled from repeated cells. Finally, a study of topologies with varying dimensions was performed. Except the smallest geometry, all the results were mostly variations of the same pattern: a number of disks with a fixed size spread within a flexible material.

- *Chapter 3: Topology optimization with connectivity constraint:* With two material optimization successfully performed at the last chapter, a way to do it with only one material was proposed here. With two materials, any combination of them has, in theory, a physical meaning. However, for one material, one should be concerned with disconnected islands of rigid material and disconnected regions. With this in mind, a connectivity pro-

cedure based on the heat flux of an auxiliary heat conduction problem was introduced, and named as Virtual Flux Method (VFM). It functions by assigning a limit and activation value for the heat flux per unit area for each element, which is used to penalize the sensitivities of these elements accordingly. Some numerical results are presented to exemplify this method. Initially, a cantilever beam is optimized for a low operating frequency. The VFM allows for the acquisition of a feasible optimized topology where the regions that would be disconnected without it remain connected. Then, a variation of this system is optimized, printed and tested experimentally, with the measurement from a laser doppler vibrometer. The experimental results showed an accordance between simulation and measured responses.

- *Chapter 4: Optimization of acoustic-structure coupled systems:* In this chapter, the formulation used in the natural frequency separation of structural domains was extended to a problem with acoustic-structure interaction. Additional terms appear in the simulation and on the sensitivity analysis. In this chapter, some assessments were done to show the difference between weakly coupled problems and strongly coupled ones. Finally, a study on a sliding-fixed beam indicated very little quantitative differences on the results when considering different sensitivity terms.

- *Chapter 5: Broadband optimization of sound propagation of floors under structure-borne excitation:* This chapter dealt with the optimization of floors when subjected to structure-borne impact excitation. To do so, a ribbed shell element formulation is presented, to better simulate ribbed floors. To model floating floors, an additional layer of plate elements, coupled with the base floor by spring elements, was added. To measure the impact sound insulation, a standardized single number rating was used. Results with a single slab did not show significant improvement. When adding a floating slab, we see that the combination of the high-frequency reduction from the floating floor and the low-frequency reduction from the optimization leads to better overall performance. Further analyses on waffle slabs indicate that the vibration on the regions between the ribs are the main source of sound transmission in high-frequency. Thus, one has to properly ponder that the structure should be stiff enough to reduce transmission in lower frequencies, while also mitigating the local vibration in high frequency.

In conclusion, this project approached the problem of maximizing the separation

between natural frequencies, proposing a solution to each one of the main challenges. Efficient and effective solutions were proposed and tested, showing that they are viable.

As a natural continuation of this project, the author proposes the assessment of the following challenges.

On the results from Chapter 2, the inclusion of either substructuring methods or of the dispersion analysis results could significantly reduce the computational costs and/or improve the results.

On Chapter 3, one could expand the VFM for maintaining separating walls between fluid and void phases. Furthermore, the removal of the morphological filter should be studied: if the auxiliary topology is the same as the optimization topology, we could potentially reuse the FEA results from the physics of the objective function on the VFM.

On Chapter 4, further studies on the instability observed during the optimization process should be done. Furthermore, analyses with increasing frequency should be done, assessing both the contribution from each sensitivity term and the stability of the process.

Finally, on Chapter 5, additional constraints could be added for improved manufacturability of the final designs. Additionally, one could study the effect of different interlayer composition, either by changing between traditional configurations and materials, or by performing a topology optimization study on it.

BIBLIOGRAPHY

Andreassen, E.; Ferrari, F.; Sigmund, O.; Diaz, A. R. Frequency response as a surrogate eigenvalue problem in topology optimization. **International Journal for Numerical Methods in Engineering**, v. 113, n. 8, p. 1214–1229, fev. 2018.

Ansola, R.; Veguería, E.; Canales, J.; Tárrago, J. A. A simple evolutionary topology optimization procedure for compliant mechanism design. **Finite Elements in Analysis and Design**, v. 44, n. 1-2, p. 53–62, dez. 2007.

Ansola, R.; Veguería, E.; Maturana, A.; Canales, J. 3D compliant mechanisms synthesis by a finite element addition procedure. **Finite Elements in Analysis and Design**, v. 46, n. 9, p. 760–769, set. 2010.

Associação Brasileira de Normas Técnicas. **NBR 15575-3: Edificações Habitacionais - Desempenho Parte 3: Requisitos Para Os Sistemas de Pisos. Rio de Janeiro**. 2013.

Balay, S.; Abhyankar, S.; Adams, M. F.; Benson, S.; Brown, J.; Brune, P.; Buschelman, K.; Constantinescu, E. M.; Dalcin, L.; Dener, A.; Eijkhout, V.; Faibussowitsch, J.; Gropp, W. D.; Hapla, V.; Isaac, T.; Jolivet, P.; Karpeev, D.; Kaushik, D.; Knepley, M. G.; Kong, F.; Kruger, S.; May, D. A.; McInnes, L. C.; Mills, R. T.; Mitchell, L.; Munson, T.; Roman, J. E.; Rupp, K.; Sanan, P.; Sarich, J.; Smith, B. F.; Zampini, S.; Zhang, H.; Zhang, H.; Zhang, J. **PETSc Web Page**. https://petsc.org/: [s.n.], 2022.

Behnel, S.; Bradshaw, R.; Citro, C.; Dalcin, L.; Seljebotn, D. S.; Smith, K. Cython: The Best of Both Worlds. **Computing in Science & Engineering**, v. 13, n. 2, p. 31–39, mar. 2011.

Bendsøe, M. P. Optimal shape design as a material distribution problem. **Structural Optimization**, v. 1, p. 193–202, 1989.

Bendsøe, M. P.; Kikuchi, N. Generating optimal topologies in structural design using a homogenization method. **Computer Methods in Applied Mechanics and Engineering**, v. 71, n. 2, p. 197–224, nov. 1988.

Brillouin, L. **Wave Propagation in Periodic Structures: Electric Filters and Crystal Lattices**. 2nd. ed. New York: Dover Publications, 1953.

Chen, B.-C.; Kikuchi, N. Topology optimization with design-dependent loads. **Finite Elements in Analysis and Design**, v. 37, n. 1, p. 57–70, jan. 2001.

Cormen, T. H.; Leiserson, C. E.; Rivest, R. L.; Stein, C. **Introduction to Algorithms**. Fourth edition. Cambridge, Massachusett: The MIT Press, 2022. ISBN 978-0-262-04630-5.

Cremer, L.; Heckl, M.; Petersson, B. A. T. **Structure-Borne Sound: Structural Vibrations and Sound Radiation at Audio Frequencies**. 3rd ed. ed. Berlin ; New York: Springer, 2005. ISBN 978-3-540-22696-3.

Cunha, D. C.; de Almeida, B. V.; Lopes, H. N.; Pavanello, R. Finite variation sensitivity analysis for discrete topology optimization of continuum structures. **Structural and Multidisciplinary Optimization**, v. 64, p. 3877–3909, out. 2021.

Decraene, C.; Dijckmans, A.; Reynders, E. P. Fast mean and variance computation of the diffuse sound transmission through finite-sized thick and layered wall and floor systems. **Journal of Sound and Vibration**, v. 422, p. 131–145, maio 2018.

Díaz, A.; Sigmund, O. Checkerboard patterns in layout optimization. **Structural Optimization**, v. 10, n. 1, p. 40–45, ago. 1995.

Díaz, A. R.; Kikuchi, N. Solutions to shape and topology eigenvalue optimization problems using a homogenization method. **International Journal for Numerical Methods in Engineering**, v. 35, n. 7, p. 1487–1502, out. 1992.

Du, Z.; Zhou, X.-Y.; Picelli, R.; Kim, H. A. Connecting Microstructures for Multiscale Topology Optimization With Connectivity Index Constraints. **Journal of Mechanical Design**, v. 140, n. 11, p. 111417, nov. 2018.

Emmendoerfer, H.; Maute, K.; Fancello, E. A.; Silva, E. C. N. A level set-based optimized design of multi-material compliant mechanisms considering stress constraints. **Computer Methods in Applied Mechanics and Engineering**, v. 391, p. 114556, mar. 2022.

Ewins, D. J. **Modal Testing: Theory, Practice, and Application**. 2nd ed. ed. Baldock, Hertfordshire, England ; Philadelphia, PA: Research Studies Press, 2000. (Mechanical Engineering Research Studies, 10). ISBN 978-0-86380-218-8.

Fahy, F. J. Statistical energy analysis: A critical overview. **Philosophical Transactions of the Royal Society of London. Series A: Physical and Engineering Sciences**, v. 346, n. 1681, p. 431–447, mar. 1994.

Ferrari, F.; Lazarov, B. S.; Sigmund, O. Eigenvalue topology optimization via efficient multilevel solution of the frequency response: Eigenvalue topology optimization. **International Journal for Numerical Methods in Engineering**, v. 115, n. 7, p. 872–892, ago. 2018.

Floquet, G. Sur les équations différentielles linéaires à coefficients périodiques. **Annales scientifiques de l'École normale supérieure**, v. 12, p. 47–88, 1883.

Gao, R.; Zhang, Y.; Kennedy, D. A hybrid boundary element-statistical energy analysis for the mid-frequency vibration of vibro-acoustic systems. **Computers & Structures**, v. 203, p. 34–42, jul. 2018.

Gao, R.; Zhang, Y.; Kennedy, D. Topology optimization of sound absorbing layer for the mid-frequency vibration of vibro-acoustic systems. **Structural and Multidisciplinary Optimization**, v. 59, n. 5, p. 1733–1746, maio 2019.

Gao, R.; Zhang, Y.; Kennedy, D. Optimization of mid-frequency vibration for complex built-up systems using the hybrid finite element–statistical energy analysis method. **Engineering Optimization**, v. 52, n. 12, p. 2125–2145, dez. 2020.

Giannini, D.; Schevenels, M.; Reynders, E. P. B. Optimization of material thickness distribution in single and double partition panels for maximized sound insulation. **Structural and Multidisciplinary Optimization**, v. 66, n. 12, p. 1–18, 2023.

Haftka, R. T.; Gürdal, Z. **Elements of Structural Optimization**. 3., rev. and expanded ed., reprinted with corr. ed. Dordrecht: Kluwer Acad. Publ, 1993. (Solid Mechanics and Its Applications, 11). ISBN 978-0-7923-1505-6 978-0-7923-1504-9.

Hashin, Z.; Shtrikman, S. A variational approach to the theory of the elastic behaviour of multiphase materials. **Journal of the Mechanics and Physics of Solids**, v. 11, n. 2, p. 127–140, mar. 1963.

Haug, E. J.; Rousselet, B. Design Sensitivity Analysis in Structural Mechanics.II. Eigenvalue Variations. **Journal of Structural Mechanics**, v. 8, n. 2, p. 161–186, jan. 1980.

Hernandez, V.; Roman, J. E.; Vidal, V. SLEPc: A scalable and flexible toolkit for the solution of eigenvalue problems. **ACM Transactions on Mathematical Software (TOMS)**, v. 31, n. 3, p. 351–362, set. 2005.

Hongisto, V.; Virjonen, P.; Maula, H.; Saarinen, P.; Radun, J. Impact sound insulation of floating floors: A psychoacoustic experiment linking standard objective rating and subjective perception. **Building and Environment**, v. 184, p. 107225, out. 2020.

Hopkins, C. **Sound Insulation**. 1st ed. ed. Amsterdam: Elsevier / Butterworth-Heinemann, 2007. ISBN 978-0-7506-6526-1.

Hu, J.; Yao, S.; Huang, X. Topology optimization of dynamic acoustic–mechanical structures using the ersatz material model. **Computer Methods in Applied Mechanics and Engineering**, v. 372, p. 113387, dez. 2020.

Huang, X. Smooth topological design of structures using the floating projection. **Engineering Structures**, v. 208, p. 110330, abr. 2020.

Huang, X.; Xie, Y. Convergent and mesh-independent solutions for the bi-directional evolutionary structural optimization method. **Finite Elements in Analysis and Design**, v. 43, n. 14, p. 1039–1049, out. 2007.

Huang, X.; Xie, Y. M. Optimal design of periodic structures using evolutionary topology optimization. **Structural and Multidisciplinary Optimization**, v. 36, n. 6, p. 597–606, nov. 2008.

Huang, X.; Xie, Y. M. **Evolutionary Topology Optimization of Continuum Structures: Methods and Applications**. Chichester: Wiley, 2010. ISBN 978-0-470-74653-0.

ISO 717–2. **International Organization for Standardization. ISO 717–2: Acoustics – Rating of Sound Insulation in Buildings and of Building Elements – Part 2: Impact Sound Insulation**. 2012.

ISO 9052-1. **International Organization for Standardization. ISO 9052-1: Acoustics - Determination of Dynamic Stiffness - Part 1: Materials Used under Floating Floors in Dwellings**. 1989.

Jensen, J. S. A simple method for coupled acoustic-mechanical analysis with application to gradient-based topology optimization. **Structural and Multidisciplinary Optimization**, v. 59, n. 5, p. 1567–1580, maio 2019.

Jensen, J. S.; Pedersen, N. L. On maximal eigenfrequency separation in two-material structures: The 1D and 2D scalar cases. **Journal of Sound and Vibration**, v. 289, n. 4-5, p. 967–986, fev. 2006.

Jeyachandrabose, C.; Kirkhope, J. Construction of new efficient three-node triangular thin plate bending elements. **Computers & Structures**, v. 23, n. 5, p. 587–603, jan. 1986.

Joannopoulos, J.; Villeneuve, P. R.; Fan, S. Photonic crystals. **Solid State Communications**, v. 102, n. 2-3, p. 165–173, abr. 1997.

Johnson, S. G. **The NLopt Nonlinear-Optimization Package**. http://github.com/stevengj/nlopt: [s.n.], 2024.

Kittel, C. **Introduction to Solid State Physics**. 5th. ed. New York: Wiley, 1976. ISBN 978-0-471-49024-1.

Kook, J. Evolutionary topology optimization for acoustic-structure interaction problems using a mixed u/p formulation. **Mechanics Based Design of Structures and Machines**, v. 47, n. 3, p. 356–374, maio 2019.

Kook, J.; Jensen, J. S. Topology optimization of periodic microstructures for enhanced loss factor using acoustic–structure interaction. **International Journal of Solids and Structures**, v. 122–123, p. 59–68, set. 2017.

Krog, L. A.; Olho, N. Optimum topology and reinforcement design of disk and plate structures with multiple stiffness and eigenfrequency objectives. **Computers and Structures**, p. 29, 1999.

Kushwaha, M. S.; Halevi, P.; Dobrzynski, L.; Djafari-Rouhani, B. Acoustic band structure of periodic elastic composites. **Physical Review Letters**, v. 71, n. 13, p. 2022–2025, set. 1993.

Langley, R. S. Numerical evaluation of the acoustic radiation from planar structures with general baffle conditions using wavelets. **The Journal of the Acoustical Society of America**, v. 121, n. 2, p. 766–777, fev. 2007.

De Leon, D. M.; Alexandersen, J.; O. Fonseca, J. S.; Sigmund, O. Stress-constrained topology optimization for compliant mechanism design. **Structural and Multidisciplinary Optimization**, v. 52, n. 5, p. 929–943, nov. 2015.

De Leon, D. M.; Gonçalves, J. F.; De Souza, C. E. Stress-based topology optimization of compliant mechanisms design using geometrical and material nonlinearities. **Structural and Multidisciplinary Optimization**, v. 62, n. 1, p. 231–248, jul. 2020.

Li, Q.; Chen, W.; Liu, S.; Tong, L. Structural topology optimization considering connectivity constraint. **Structural and Multidisciplinary Optimization**, v. 54, n. 4, p. 971–984, out. 2016.

Li, Q.; Wu, Q.; Dou, S.; Wang, J.; Liu, S.; Chen, W. Nonlinear eigenvalue topology optimization for structures with frequency-dependent material properties. **Mechanical Systems and Signal Processing**, v. 170, p. 108835, maio 2022.

Li, Q.; Wu, Q.; Liu, J.; He, J.; Liu, S. Topology optimization of vibrating structures with frequency band constraints. **Structural and Multidisciplinary Optimization**, v. 63, n. 3, p. 1203–1218, mar. 2021.

Li, W.; Meng, F.; Chen, Y.; Li, Y. fan; Huang, X. Topology optimization of photonic and phononic crystals and metamaterials: A review. **Advanced Theory and Simulations**, v. 2, n. 7, p. 1900017, jul. 2019.

Li, Y.; Huang, X.; Xie, Y.; Zhou, S. Evolutionary topology optimization of hinge-free compliant mechanisms. **International Journal of Mechanical Sciences**, v. 86, p. 69–75, set. 2014.

Lin, R.; Mottershead, J.; Ng, T. A state-of-the-art review on theory and engineering applications of eigenvalue and eigenvector derivatives. **Mechanical Systems and Signal Processing**, v. 138, p. 106536, abr. 2020.

Liu, S.; Li, Q.; Chen, W.; Tong, L.; Cheng, G. An identification method for enclosed voids restriction in manufacturability design for additive manufacturing structures. **Frontiers of Mechanical Engineering**, v. 10, n. 2, p. 126–137, jun. 2015.

Liu, W.; Yoon, G. H.; Yi, B.; Choi, H.; Yang, Y. Controlling wave propagation in one-dimensional structures through topology optimization. **Computers & Structures**, v. 241, p. 106368, dez. 2020.

Lopes, H. N.; Candeloro Cunha, D.; Pavanello, R. Topology optimization with connectivity constraint to separate natural frequencies of a ring structure. In: **Proceedings of the 8th International Symposium on Solid Mechanics**. [S.l.]: ABCM, 2022.

Lopes, H. N.; Cunha, D. C.; Pavanello, R.; Mahfoud, J. Numerical and experimental investigation on topology optimization of an elongated dynamic system. **Mechanical Systems and Signal Processing**, v. 165, p. 108356, fev. 2022.

Lopes, H. N.; Mahfoud, J.; Pavanello, R. High natural frequency gap topology optimization of bi-material elastic structures and band gap analysis. **Structural and Multidisciplinary Optimization**, v. 63, n. 5, p. 2325–2340, maio 2021.

Luo, Y.; Sigmund, O.; Li, Q.; Liu, S. Additive manufacturing oriented topology optimization of structures with self-supported enclosed voids. **Computer Methods in Applied Mechanics and Engineering**, v. 372, p. 113385, dez. 2020.

Lyon, R. H.; DeJong, R. G.; Lyon, R. H. **Theory and Application of Statistical Energy Analysis**. 2nd ed. ed. Boston: Butterworth-Heinemann, 1995. ISBN 978-0-7506-9111-6.

Ma, Z.-D.; Cheng, H.-C.; Kikuchi, N. Structural design for obtaining desired eigenfrequencies by using the topology and shape optimization method. **Computing Systems in Engineering**, v. 5, n. 1, p. 77–89, fev. 1994.

Ma, Z. D.; Kikuchi, N.; Hagiwara, I. Structural topology and shape optimization for a frequency response problem. **Computational Mechanics**, v. 13, n. 3, p. 157–174, dez. 1993.

Munk, D. J.; Vio, G. A.; Steven, G. P. A Bi-directional Evolutionary Structural Optimisation algorithm with an added connectivity constraint. **Finite Elements in Analysis and Design**, v. 131, p. 25–42, set. 2017.

Azari Nejat, A.; Held, A.; Trekel, N.; Seifried, R. A modified level set method for topology optimization of sparsely-filled and slender structures. **Structural and Multidisciplinary Optimization**, v. 65, n. 3, p. 85, mar. 2022.

Olhoff, N.; Du, J. Generalized incremental frequency method for topological designof continuum structures for minimum dynamic compliance subject to forced vibration at a prescribed low or high value of the excitation frequency. **Structural and Multidisciplinary Optimization**, v. 54, n. 5, p. 1113–1141, nov. 2016.

Olhoff, N.; Niu, B.; Cheng, G. Optimum design of band-gap beam structures. **International Journal of Solids and Structures**, v. 49, n. 22, p. 3158–3169, nov. 2012.

Pedersen, N. Maximization of eigenvalues using topology optimization. **Structural and Multidisciplinary Optimization**, v. 20, n. 1, p. 2–11, ago. 2000.

Pereira, A. D. A.; Cardoso, E. L. On the influence of local and global stress constraint and filtering radius on the design of hinge-free compliant mechanisms. **Structural and Multidisciplinary Optimization**, v. 58, n. 2, p. 641–655, ago. 2018.

Pereira, R. L.; Lopes, H. N.; Moura, M. S.; Pavanello, R. Multi-domain acoustic topology optimization based on the BESO approach: Applications on the design of multi-phase material mufflers. **Structural and Multidisciplinary Optimization**, v. 66, n. 1, p. 25, jan. 2023.

Pereira, R. L.; Lopes, H. N.; Pavanello, R. Topology optimization of acoustic systems with a multiconstrained BESO approach. **Finite Elements in Analysis and Design**, v. 201, p. 103701, abr. 2022.

Picelli, R.; Vicente, W.; Pavanello, R. Bi-directional evolutionary structural optimization for design-dependent fluid pressure loading problems. **Engineering Optimization**, v. 47, n. 10, p. 1324–1342, out. 2015.

Picelli, R.; Vicente, W.; Pavanello, R.; Xie, Y. Evolutionary topology optimization for natural frequency maximization problems considering acoustic–structure interaction. **Finite Elements in Analysis and Design**, v. 106, p. 56–64, nov. 2015.

Querin, O.; Steven, G.; Xie, Y. Evolutionary structural optimisation (ESO) using a bidirectional algorithm. **Engineering Computations**, v. 15, n. 8, p. 1031–1048, dez. 1998.

Rasmussen, B.; Machimbarrena, M. (Ed.). **Building Acoustics throughout Europe Volume 1: Towards a Common Framework in Building Acoustics throughout Europe**. [S.l.: s.n.], 2014. (COST Action TU0901).

Rayleigh, J. W. S. **The Theory of Sound**. 2nd. ed. New York: Dover Publications, 1894. v. 2.

Reynders, E. P.; Wang, P.; Van hoorickx, C.; Lombaert, G. Prediction and uncertainty quantification of structure-borne sound radiation into a diffuse field. **Journal of Sound and Vibration**, v. 463, p. 114984, dez. 2019.

Rozvany, G. I. N.; Zhou, M.; Birker, T. Generalized shape optimization without homogenization. **Structural Optimization**, v. 4, n. 3-4, p. 250–252, set. 1992.

Schiavi, A. Improvement of impact sound insulation: A constitutive model for floating floors. **Applied Acoustics**, v. 129, p. 64–71, jan. 2018.

Seyranian, A. P.; Lund, E.; Olhoff, N. Multiple eigenvalues in structural optimization problems. **Structural Optimization**, v. 8, n. 4, p. 207–227, dez. 1994.

Sigalas, M.; Economou, E. Elastic and acoustic wave band structure. **Journal of Sound and Vibration**, v. 158, n. 2, p. 377–382, out. 1992.

Sigmund, O. **Design of Material Structures Using Topology Optimization**. Tese (Thesis) — Technical University of Denmark, Lyngby, Denmark, dez. 1994.

Sigmund, O. On the Design of Compliant Mechanisms Using Topology Optimization. **Mechanics of Structures and Machines**, v. 25, n. 4, p. 493–524, jan. 1997.

Sigmund, O. Morphology-based black and white filters for topology optimization. **Structural and Multidisciplinary Optimization**, v. 33, n. 4-5, p. 401–424, fev. 2007.

Sigmund, O. Manufacturing tolerant topology optimization. **Acta Mechanica Sinica**, v. 25, n. 2, p. 227–239, abr. 2009.

Sigmund, O.; Clausen, P. Topology optimization using a mixed formulation: An alternative way to solve pressure load problems. **Computer Methods in Applied Mechanics and Engineering**, v. 196, n. 13-16, p. 1874–1889, mar. 2007.

Sigmund, O.; Jensen, J. S. Systematic Design of Phononic Band-Gap Materials and Structures by Topology Optimization. **Philosophical Transactions: Mathematical, Physical and Engineering Sciences**, v. 361, n. 1806,, p. 1001–1019, 2003.

Sivapuram, R.; Picelli, R. Topology optimization of binary structures using Integer Linear Programming. **Finite Elements in Analysis and Design**, v. 139, p. 49–61, fev. 2018.

Sun, J.-g. Multiple eigenvalue sensitivity analysis. **Linear Algebra and its Applications**, v. 137–138, p. 183–211, ago. 1990.

Svanberg, K. The method of moving asymptotes—a new method for structural optimization. **International Journal for Numerical Methods in Engineering**, v. 24, n. 2, p. 359–373, fev. 1987.

Svanberg, K. A Class of Globally Convergent Optimization Methods Based on Conservative Convex Separable Approximations. **SIAM Journal on Optimization**, v. 12, n. 2, p. 555–573, jan. 2002.

Torii, A. J.; Faria, J. R. D. Structural optimization considering smallest magnitude eigenvalues: A smooth approximation. **Journal of the Brazilian Society of Mechanical Sciences and Engineering**, v. 39, n. 5, p. 1745–1754, maio 2017.

Van den Wyngaert, J. C.; Schevenels, M.; Reynders, E. P. Broadband acoustic shape optimization of studs in double-leaf walls. **Journal of Sound and Vibration**, v. 485, p. 115562, out. 2020.

Van den Wyngaert, J. C.; Schevenels, M.; Reynders, E. P. Shape optimization of studs in double-leaf plasterboard walls for maximal broadband sound insulation and minimal material use. **Applied Acoustics**, v. 183, p. 108307, dez. 2021.

Vasseur, J. O.; Deymier, P. A.; Frantziskonis, G.; Hong, G.; Djafari-Rouhani, B.; Dobrzynski, L. Experimental evidence for the existence of absolute acoustic band gaps in two-dimensional periodic composite media. **Journal of Physics: Condensed Matter**, v. 10, n. 27, p. 6051–6064, jul. 1998.

Vicente, W.; Picelli, R.; Pavanello, R.; Xie, Y. Topology optimization of frequency responses of fluid–structure interaction systems. **Finite Elements in Analysis and Design**, v. 98, p. 1–13, jun. 2015.

Vigran, T. E. **Building Acoustics**. London ; New York: Taylor & Francis, 2008. ISBN 978-0-415-42853-8 978-0-203-93131-8.

Wang, C.; Xu, B.; Duan, Z.; Rong, J. Structural topology optimization considering both performance and manufacturability: Strength, stiffness, and connectivity. **Structural and Multidisciplinary Optimization**, v. 63, n. 3, p. 1427–1453, mar. 2021.

Wang, P.; Van hoorickx, C.; Lombaert, G.; Reynders, E. Numerical prediction and experimental validation of impact sound radiation by timber joist floors. **Applied Acoustics**, v. 162, p. 107182, maio 2020.

Wang, X.; Bathe, K.-J. Displacement/pressure based mixed finite element formulations for acoustic fluid-structure interaction problems. **International Journal for Numerical Methods in Engineering**, v. 40, n. 11, p. 2001–2017, jun. 1997.

Xia, Q.; Shi, T.; Wang, M. Y. A level set based shape and topology optimization method for maximizing the simple or repeated first eigenvalue of structure vibration. **Structural and Multidisciplinary Optimization**, v. 43, n. 4, p. 473–485, abr. 2011.

Xie, Y.; Steven, G. A simple evolutionary procedure for structural optimization. **Computers & Structures**, v. 49, n. 5, p. 885–896, dez. 1993.

Xie, Y.; Steven, G. A simple approach to structural frequency optimization. **Computers & Structures**, v. 53, n. 6, p. 1487–1491, dez. 1994.

Xie, Y.; Steven, G. Evolutionary structural optimization for dynamic problems. **Computers & Structures**, v. 58, n. 6, p. 1067–1073, mar. 1996.

Xiong, Y.; Yao, S.; Zhao, Z.-L.; Xie, Y. M. A new approach to eliminating enclosed voids in topology optimization for additive manufacturing. **Additive Manufacturing**, v. 32, p. 101006, mar. 2020.

Yang, X. Y.; Xie, Y. M.; Steven, G. P.; Querin, O. M. Topology optimization for frequencies using an evolutionary method. **Journal of Structural Engineering**, v. 125, n. 12, p. 1432–1438, dez. 1999.

Yao, D.; Zhang, J.; Wang, R.-q.; Xiao, X.-b.; Guo, J.-q. Lightweight design and sound insulation characteristic optimisation of railway floating floor structures. **Applied Acoustics**, v. 156, p. 66–77, dez. 2019.

Yoon, G. H.; Jensen, J. S.; Sigmund, O. Topology optimization of acoustic–structure interaction problems using a mixed finite element formulation. **International Journal for Numerical Methods in Engineering**, v. 70, n. 9, p. 1049–1075, maio 2007.

Zhao, C.; Steven, G.; Xie, Y. Evolutionary natural frequency optimization of two-dimensional structures with additional non-structural lumped masses. **Engineering Computations**, v. 14, n. 2, p. 233–251, mar. 1997.

Zhou, M.; Rozvany, G. The COC algorithm, Part II: Topological, geometrical and generalized shape optimization. **Computer Methods in Applied Mechanics and Engineering**, v. 89, n. 1-3, p. 309–336, ago. 1991.

Zhou, M.; Rozvany, G. On the validity of ESO type methods in topology optimization. **Structural and Multidisciplinary Optimization**, v. 21, n. 1, p. 80–83, mar. 2001.

Zienkiewicz, O. C.; Bettess, P. Fluid-structure dynamic interaction and wave forces. An introduction to numerical treatment. **International Journal for Numerical Methods in Engineering**, v. 13, n. 1, p. 1–16, 1978.

Zuo, Z. H.; Xie, Y. M.; Huang, X. An improved bi-directional evolutionary topology optimization method for frequencies. **International Journal of Structural Stability and Dynamics**, v. 10, n. 01, p. 55–75, mar. 2010.

Zuo, Z. H.; Xie, Y. M.; Huang, X. Optimal topological design of periodic structures for natural frequencies. **Journal of Structural Engineering**, v. 137, n. 10, p. 1229–1240, out. 2011.

Appendix

APPENDIX A – VALIDATION OF FINITE ELEMENT ANALYSIS

The methodology presented in Section 4.1.2 is tested to confirm its validity via comparison with the commercial software COMSOL Multiphysics®. This software was chosen as it possesses the same formulation for structural, acoustic, and acoustic-structure domains as presented in Section 4.1.2.

The first validation problem is shown in Figure A.1. The acoustic domain is made of water, with ρ_{f} = 1000 kg/m^3 and $c_{\mathrm{f}} = 1450$m/s. The structural domain is modeled as aluminum, with E = 70 GPa, ρ_{s} = 2700 kg/m^3 and ν = 0.3. Due to this geometry (the fluid domain is divided in two by the structural one) and to the material properties, this system is classified as a strongly coupled system; thus, its modes cannot be divided into structural or acoustic.

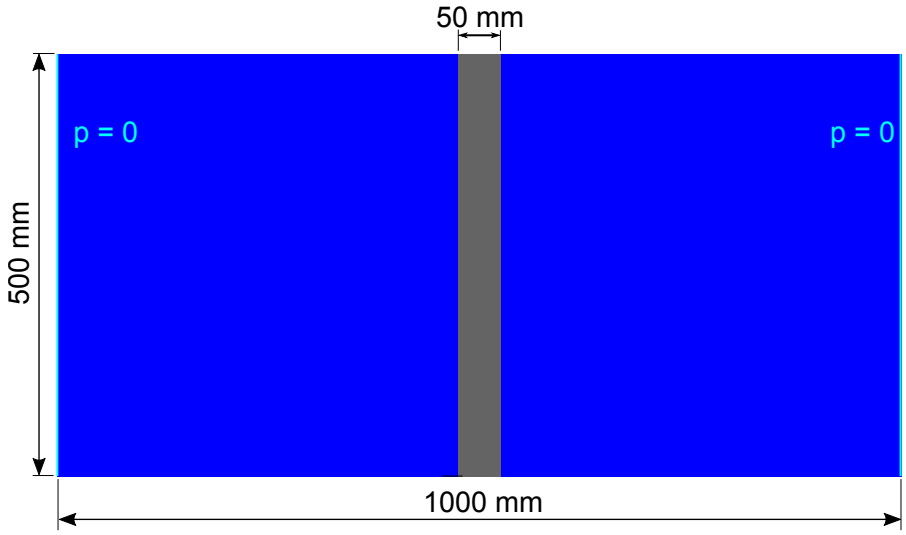

Figure A.1 – Acoustic-structure domain for finite element validation.

For the reference result from COMSOL Multiphysics®, the analysis is created by generating a component with both “Solid Mechanics” and “Pressure Acoustics, Frequency Domain” physics. They are coupled with an “Acoustic-Structure Boundary” multiphysics analysis. Elements are defined as quadrangular, with first-order Lagrange polynomials. The study is set to “Eigenfrequency Analysis” with 20 desired eigenfrequencies.

Table A.1 compares the results from COMSOL Multiphysics® (denoted as "Reference Frequency") and the calculated by the program developed for this thesis. Frequency errors are defined as the relative error between calculated and reference frequency. Eigenvector errors are defined as the Euclidean norm of the error.

Table A.1 – Comparison between reference and calculated frequencies

Mode	Reference frequency [Hz]	Calculated frequency [Hz]	Frequency error [%]	Eigenvector error [%]
1	361.728	361.728	2.48×10^{-4}	3.58×10^{-5}
2	762.099	762.099	3.86×10^{-6}	2.18×10^{-6}
3	1282.418	1282.418	2.55×10^{-5}	2.17×10^{-5}
4	1308.225	1308.225	4.34×10^{-5}	5.39×10^{-5}
5	1636.159	1636.159	8.43×10^{-7}	2.19×10^{-6}
6	2124.765	2124.765	1.26×10^{-5}	4.74×10^{-5}
7	2286.501	2286.501	4.29×10^{-7}	8.35×10^{-7}
8	2401.054	2401.054	5.47×10^{-6}	2.01×10^{-5}
9	2706.073	2706.073	3.09×10^{-7}	1.14×10^{-6}
10	2994.647	2994.647	2.56×10^{-7}	2.20×10^{-6}
11	2997.923	2997.923	5.18×10^{-6}	1.90×10^{-5}
12	3008.855	3008.855	4.22×10^{-6}	2.00×10^{-5}
13	3401.976	3401.976	3.10×10^{-6}	3.19×10^{-5}
14	3689.749	3689.749	1.66×10^{-7}	1.13×10^{-6}
15	3811.512	3811.512	1.55×10^{-7}	6.46×10^{-7}
16	4052.305	4052.305	1.01×10^{-6}	6.64×10^{-6}
17	4065.590	4065.590	2.12×10^{-6}	2.57×10^{-5}
18	4076.015	4076.015	1.43×10^{-7}	7.33×10^{-7}
19	4213.611	4213.611	3.39×10^{-6}	2.81×10^{-5}
20	4411.207	4411.207	1.22×10^{-7}	2.21×10^{-6}

The errors are significantly low, which indicates that they are due to numerical errors, instead of systematic ones. With this in mind, the finite element model is validated.

APPENDIX B – VALIDATION OF SENSITIVITY ANALYSIS

The Finite Difference Method is a numerical method for estimating the derivatives of a function without explicit differentiation. For instance, the first derivative of a function $f(x)$ evaluated at $x = x^*$ can be estimated as:

$$\left.\frac{df}{dx}\right|_{x=x^*} \approx \frac{f(x^* + \Delta x) - f(x^*)}{\Delta x} \approx \frac{f(x^*) - f(x^* - \Delta x)}{\Delta x} \approx \frac{f(x^* + \frac{\Delta x}{2}) - f(x^* - \frac{\Delta x}{2})}{\Delta x} \tag{B.1}$$

where Δx is a small step.

In theory, convergence should be inversely proportional to this variation, providing a better approximation for lower values of Δx. In practice, however, computational errors can create noisy results if this parameter is excessively low. Therefore, an appropriate value must be chosen based on this trade-off. The three distinct approximations shown in Eq. B.1 are known as forward, backward, and centered differences, respectively. The centered difference provides lower error than the forward and backward ones, and therefore, is chosen.

The sensitivity analysis developed in Section 2.2.2 is validated by comparing its values with the Finite Difference Method. Figure B.1 shows the domain chosen to perform this analysis.

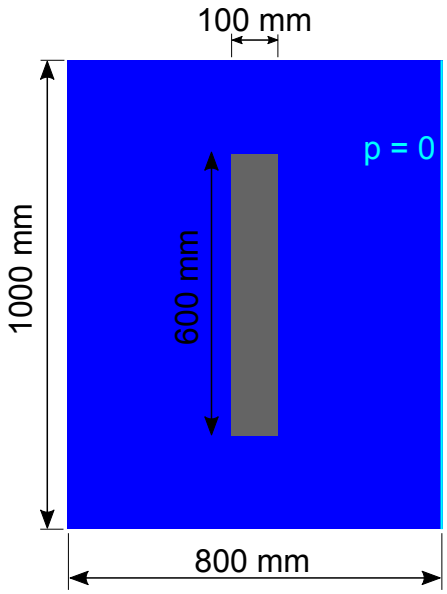

Figure B.1 – Acoustic-structure domain for sensitivity validation. The blue area a fluid non-design domain and the gray area is the design domain.

The domain is discretized in a 80 x 100 mesh of identical quadrilateral elements. The fluid is set to water, which has the properties $\rho_{\mathrm{f}} = 1000$ kg/m^3 and $c_{\mathrm{f}} = 1450$ m/s. The structure is set to a steel with $E = 70$ GPa, $\nu = 0.3$ and $\rho_s = 2700$ kg/m^3 and is modeled using the plane stress hypothesis.

The operating frequency is chosen as 2500 Hz, and the number of analyzed frequencies is set to 40, as the 40^{th} natural frequency is 5162 Hz. The interpolation parameters x_{min} and the penalization exponent p are set to 10^{-6} and 5, respectively.

Initially, we perform the analytical and numerical sensitivity analyses for a fully solid design domain. The behavior of the Finite Difference Method convergence is studied by sweeping through different values of Δx, as illustrated in Figure B.2.

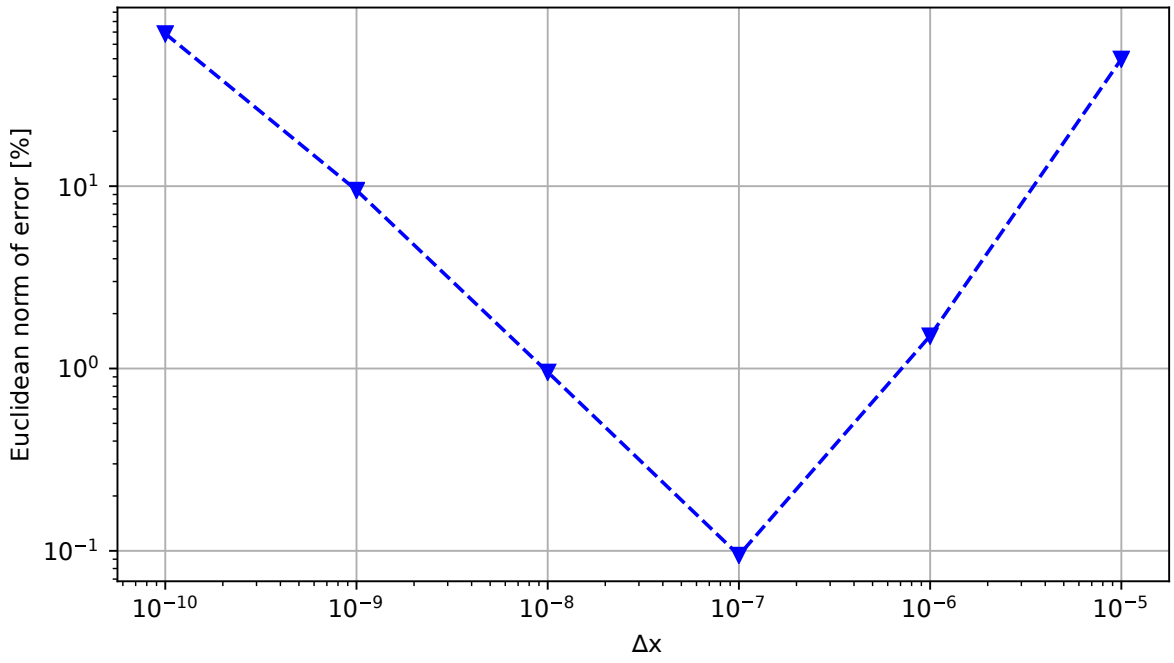

Figure B.2 – Influence of the error as a function of Δx.

This behavior of the error is expected. As previously mentioned, lowering Δx provides a better approximation up to a certain point. Lowering it further causes an increase in computational errors. The value with the smallest error occurs when $\Delta x = 10^{-7}$, and therefore, it is chosen for the subsequent analyses.

The numerical and analytical sensitivity maps for $\Delta x = 10^{-7}$ are shown in Figure B.3.

Two other cases are analyzed to check the validity of the sensitivity analysis. The

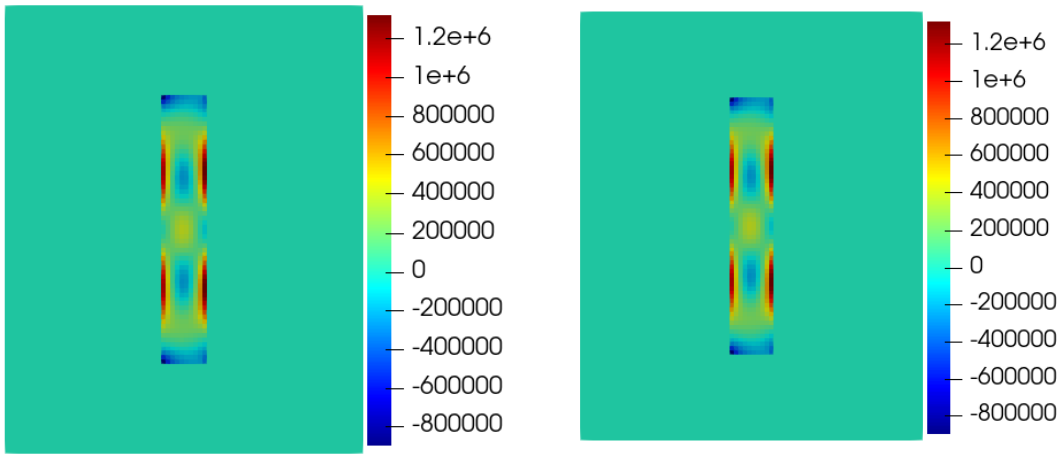

(a) (b)

Figure B.3 – Sensitivity maps for fully solid (a) numerical analysis and (b) analytical analysis.

first one is with a fully fluid design domain. Every parameter is kept the same as before. The sensitivity maps are shown in Figure B.4.

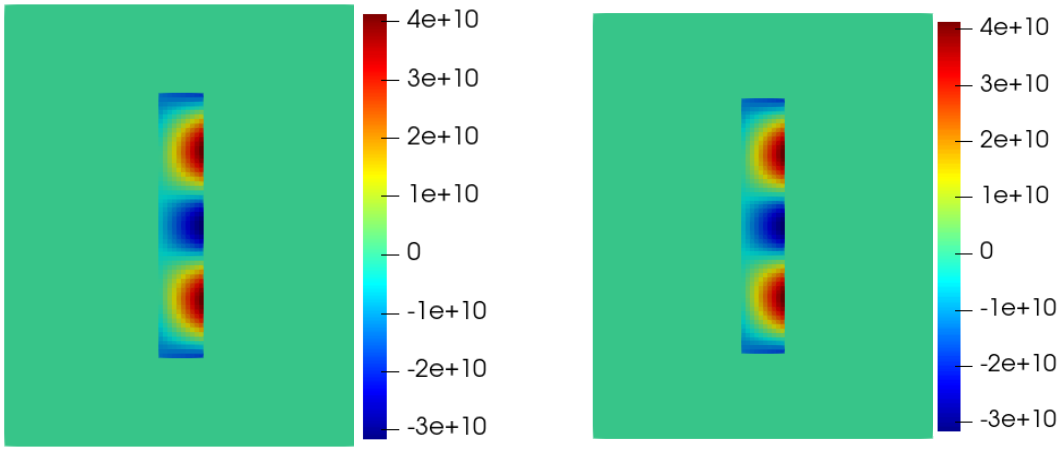

(a) (b)

Figure B.4 – Sensitivity maps for fully fluid (a) numerical analysis and (b) analytical analysis.

The Euclidean norm of the error is 0.0330%. This small value and the similarity between the two sensitivity maps indicate the validity of the analytical analysis.

Finally, the last analyzed case is a solid domain with a fluid hole with dimensions of 60 mm x 200 m. The sensitivity maps are shown in Figure B.5.

The Euclidean norm of the error is 0.304%. This small value and the similarity between the two sensitivity maps indicate the validity of the analytical analysis.

All three results show that the analytical development of the sensitivity analysis corresponds to the numerical calculation via the Finite Difference method.

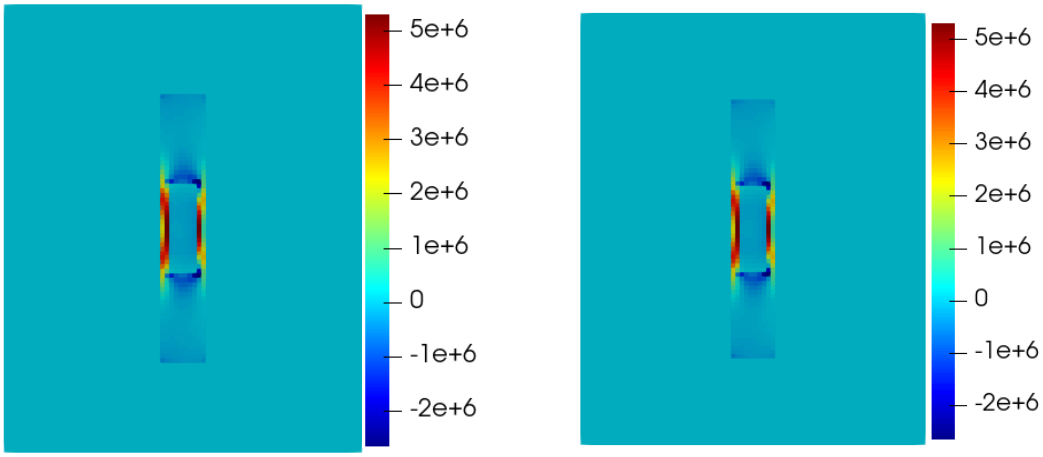

(a) (b)

Figure B.5 – Sensitivity maps for domain with hole: (a) numerical analysis and (b) analytical analysis.

APPENDIX C – ANALYTICAL SOLUTIONS FOR HEAT FLUX OF BILINEAR SQUARE ELEMENT

The norm of the heat flux per unit area of an element (Eq. 3.7) must usually be calculated via numerical integration, via the Gauss-Legendre quadrature. However, for a square element, we can deduce some analytical formulations that will reduce computational costs of the VFM.

Given a square element with local coordinates $\bar{x}$ and $\bar{y}$ (Figure C.1), where the local coordinates are only translated with respect to the global ones, the shape functions can be written as:

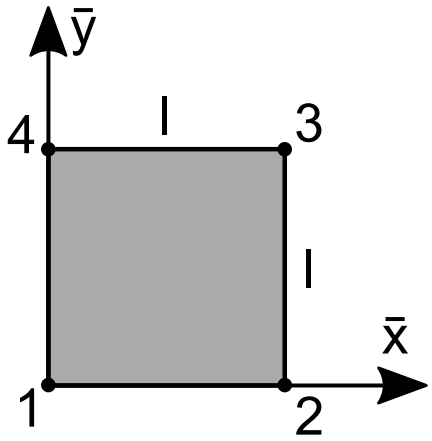

Figure C.1 – Square element in local coordinates.

$$N_1(\bar{x},\bar{y}) = \frac{1}{l^2}(l-\bar{x})(l-\bar{y}) \tag{C.1}$$

$$N_2(\bar{x},\bar{y}) = \frac{1}{l^2}\bar{x}(l-\bar{y}) \tag{C.2}$$

$$N_3(\bar{x},\bar{y}) = \frac{1}{l^2}\bar{x}\bar{y} \tag{C.3}$$

$$N_4(\bar{x},\bar{y}) = \frac{1}{l^2}\bar{y}(l-\bar{x}) \tag{C.4}$$

where l is the length of the element.

The matrix of the derivatives of the shape functions is given by:

$$\mathbf{B}_t = \begin{bmatrix} \frac{\partial N_1}{\partial x} & \frac{\partial N_2}{\partial x} & \frac{\partial N_3}{\partial x} & \frac{\partial N_4}{\partial x} \\ \frac{\partial N_1}{\partial y} & \frac{\partial N_2}{\partial y} & \frac{\partial N_3}{\partial y} & \frac{\partial N_4}{\partial y} \end{bmatrix} = \frac{1}{l^2} \begin{bmatrix} -(l-\bar{y}) & (l-\bar{y}) & \bar{y} & -\bar{y} \\ -(l-\bar{x}) & \bar{x} & \bar{x} & (l-\bar{x}) \end{bmatrix} \tag{C.5}$$

Then, the heat flux per unit area of an element can be written as:

$$\mathbf{q}_e(\bar{x},\bar{y}) = -k_e \mathbf{B_t t} = -k_e \frac{1}{l^2} \begin{Bmatrix} (T_1 - T_2 + T_3 - T_4)\bar{y} + l(T_2 - T_1) \\ (T_1 - T_2 + T_3 - T_4)\bar{x} + l(T_4 - T_1) \end{Bmatrix} = -\frac{k_e}{l^2} \begin{Bmatrix} A\bar{y} + lB \\ A\bar{x} + lC \end{Bmatrix} \tag{C.6}$$

where A, B and C are constants that are defined to simplify the expressions that will follow.

The norm with $m = 2$ is given by:

$$q_e = \sqrt{\frac{1}{l^2} \int_0^l \int_0^l \left[\frac{k_e^2}{l^4} (A\bar{y} + lB)^2 + \frac{k_e^2}{l^4} (A\bar{x} + lC)^2 \right] d\bar{x} d\bar{y}} \tag{C.7}$$

Integrating this expression analytically:

$$q_e = \frac{k_e}{l} \sqrt{\frac{2}{3} A^2 + AB + AC + B^2 + C^2} \tag{C.8}$$

With this, we have a simple expression for the $m = 2$ norm of a square element.

Likewise, for $m \to \infty$, the norm is equivalent to the maximum value of $\|\mathbf{q}_e(\bar{x},\bar{y})\|$, which must be at the same point as the maximum of $\|\mathbf{q}_e(\bar{x},\bar{y})\|^2$. For that, we analyze it expression:

$$\|\mathbf{q}_e(\bar{x},\bar{y})\|^2 = (\tilde{A}\bar{y} + \tilde{B})^2 + (\tilde{A}\bar{x} + \tilde{C})^2 \tag{C.9}$$

where the constants $\tilde{A}$, $\tilde{B}$ and $\tilde{C}$ are used for simplicity.

Considering $f(x,y) = \|\mathbf{q}_e(\bar{x},\bar{y})\|^2$ a function to be maximized, we can easily verify that it is convex, via its hessian matrix:

$$\mathbf{H} = \begin{bmatrix} 2\tilde{A}^2 & 0 \\ 0 & 2\tilde{A}^2 \end{bmatrix} \tag{C.10}$$

This matrix can be quickly verified as semi-positive definite, which implies that the function $f(x,y)$ is convex. Since the element is a square, problem of finding the maximum value of $f(x,y)$ is equal to maximizing it along a convex domain. In this case, the maximum value of

this function is equal to the maximum value between the vertices of the domain. Therefore, for each element, it is enough to evaluate the heat flux per unit area at the four nodes and use the highest value.

APPENDIX D – ASSEMBLING AND UPDATING THE COUPLING MATRIX

To assemble the coupling $\mathbf{L}$ matrix presented in Eq. (4.18), one would require the identification of the Γ_b surface. A simpler procedure, however, is presented here.

In an element-by-element analysis, assume that the surfaces of all acoustic elements are an acoustic-structure interface, while the surfaces of structural elements are not. This is illustrated in Eq. (D.1).

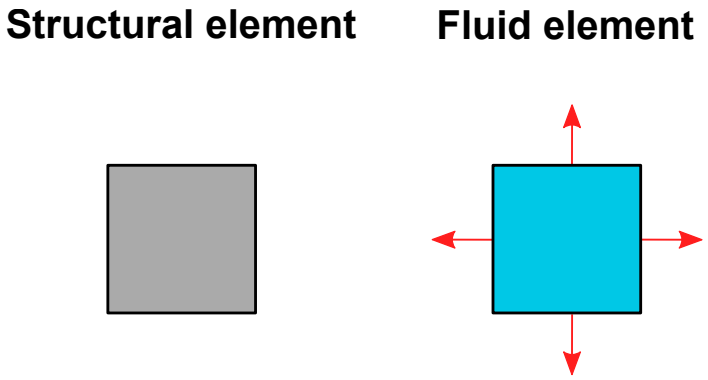

Figure D.1 – Representation of acoustic and structural elements according to their coupling matrix. The red arrows represent the presence of non-zero $\mathbf{L}$.

This way, the coupling matrix terms will cancel themselves wherever elements of the same type are connected (Figure D.2).

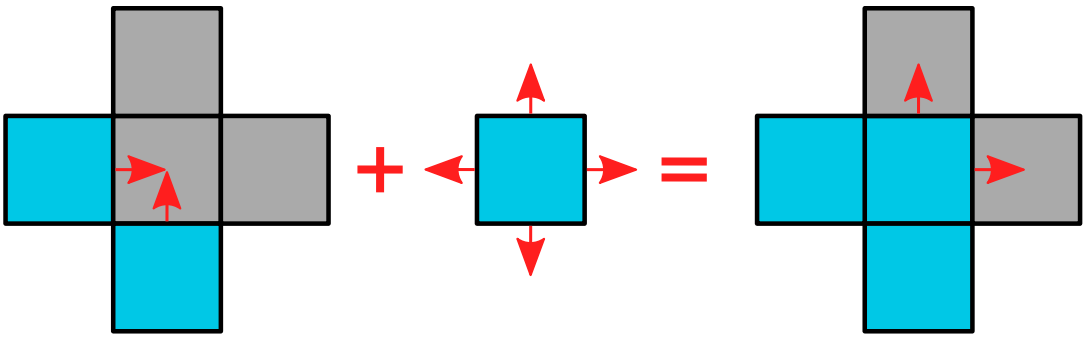

Figure D.2 – Representation of a mesh with acoustic and structural elements. Arrows represent the presence of non-zero $\mathbf{L}$.

With this procedure, the interaction effects can be taken into account correctly via a simple assembly process. This also simplifies the update of matrices due to changes from the topology optimization method, as these effects can be inserted in the material interpolation scheme.